Single-Frequency EYDFA with Polarization-Maintaining Fibers for Gravitational Wave Detection

Phillip Booker, M.Sc.

Abstract

In 2015, the space-time distortion caused by GW150914 was found - a pivotal event that inaugurated the era of interferometric gravitational wave astronomy. As of today, gravitational wave observations are routinely made with proper sky localization by the world-wide operating detector network of the second generation.

The implementation of cryogenic cooling can reduce the coating thermal noise in the next detector generation. In this case, optics made of fused silica are not suitable because of fused silica's large mechanical loss at low temperatures. Crystalline silicon is an alternative material but not transparent at 1064 nm; therefore, other laser wavelengths, e.g. 1.5 µm, must be used. Single-frequency EYDFAs[1] based on LMA[2] fibers can deliver the required output power at 1.5 µm. A PM[3] setup, however, has not been demonstrated on the desired ≈100 W power level so far; also, there has been no demonstration of any successful longterm operation (> hours) even of a non-PM setup. In this work, a prototype amplifier with PM fibers is presented on a laboratory- and advanced engineering-level.

A numerical FEM[4] analysis of the pump wavelength dependence of the Yb^{3+} ASE[5] and non-linear SBS[6] has been performed; off-peak pumping was found to suppress the unwanted Yb^{3+} ASE considerably. The achievable output power at 1.5 µm was limited by the Yb^{3+} ASE if the simulated amplifier was pumped from 880 nm to 990 nm; the onset of the Yb^{3+} ASE was linked to a deterioration of the Yb^{3+}-to-Er^{3+} energy transfer. The simulated amplifier was limited by SBS if pumped at wavelengths shorter than 880 nm or longer than 990 nm. The power threshold was approximatable by adapting a well-known threshold approximation for passive fibers.

Uncontrolled gain, e.g. resulting from a seed laser failure, must be prevented by interlocking the pumping process. In this work, the required reaction time has been studied with single-mode fibers by a combined experimental and numerical approach. It was found that a potential emergency-off system must switch-off the pumping process well below ≈100 µs and/or ≈300 µs to prevent catastrophic gain for the Yb^{3+} ASE and/or Er^{3+} ASE, respectively. An electronic circuit was designed; the board in PCB[7] format was found capable to meet this requirement. The PCB prototype was installed as part of the engineering-level amplifier.

A high-power single-frequency EYDFA made from 25/300 PM fibers is presented; the amplifier was implemented with low seed input power to match available GWD[8]-compatible seed laser sources. A pump wavelength of 940 nm was used. The pre-amplifier delivered 1.07 W output power with low ASE power levels and operated free of SBS. The maximum output power of the high-power amplifier was 110 W with 44.4±0.3 % optical-to-optical efficiency. The Er^{3+} ASE extinction ratio was 48.34 dB at maximum output power; the Yb^{3+} ASE was negligible. SBS-free operation was confirmed by monitoring the amplifier noise at MHz frequencies. The PER[9] ranged from 9.8 dB to 12.6 dB, probably owed to the used gain fiber. Further power scaling was limited by thermal fiber damage assumed to originate from photodarkening.

Moreover, an advanced prototype with a revised cooling approach is presented. The performance of two suitable 25/xxx gain fibers was compared at the ≈50 W level over a 2-week period. The *Nufern* fiber showed a growing attenuation, i.e. 14.7±2.2 % per 13 days, that was tentatively attributed to the formation of P1 type color centers from POHCs[10]; further research needs to be undertaken to confirm. The *iXblue* fiber seemed more heat resilient under operation. Furthermore, the PER from the *iXblue* fiber was in the range of 15.2 dB to 20.7 dB; the fundamental mode power was 95.7 %. It was concluded that the *iXblue* fiber is suited to be used in GWD-compatible laser sources.

Key words: Gravitational wave detection, Er^{3+}:Yb^{3+} doped fiber amplifier, Off-peak pumping, Single-frequency

---

[1] Er^{3+}:Yb^{3+} doped fiber amplifier (EYDFA), [2] Large-mode-area (LMA), [3] Polarization-maintaining (PM), [4] Finite-element-method (FEM), [5] Amplified spontaneous emission (ASE), [6] Stimulated Brillouin scattering (SBS), [7] Printed circuit board (PCB), [8] Gravitational wave detector (GWD), [9] Polarization extinction ratio (PER), [10] Phosphorous oxygen hole center (POHC)

Contents

Acronyms

AdVirgo Advanced Virgo.

aLIGO Advanced Laser Interferometer Gravitational-Wave Observatory.

AR anti-reflectance.

ASE amplified spontaneous emission.

BH black hole.

BS beam splitter.

BVP boundary-value-problem.

CAD computer-aided design.

CE Cosmic Explorer.

CLIO Cryogenic Laser Interferometer Observatory.

DBB *Diagnostic Breadboard*.

DFB distributed feedback.

ECDL external cavity diode laser.

EDFA Er^{3+} doped fiber amplifier.

EDFL Er^{3+} doped fiber laser.

EMO emergency-off.

ESA excited state absorption.

ET European Einstein Telescope.

EYDFA Er^{3+}:Yb^{3+} doped fiber amplifier.

FEM finite-element-method.

FRET Förster-resonance-energy-transfer.

FUT fiber under test.

GR general relativity.

GW gravitational wave.

GWD gravitational wave detector.

HOM higher-order mode.

I/OMC input- and output-mode-cleaner.

KAGRA Kamioka Gravitational Wave Detector.

LIDT light-induced damage threshold.

LIGO Laser Interferometer Gravitational-Wave Observatory.

LISA Light Interferometer Space Antenna.

LMA large-mode-area.

MCVD modified chemical vapor deposition.

MO master oscillator.

MOSFET metal-oxide-semiconductor field-effect transistors.

NA numerical aperture.

NPRO non-planar ring oscillator.

OSA optical spectrum analyzer.

OVD outside vapor deposition.

PA power amplifier.

PANDA polarization-maintaining and absorption-reducing.

PCB printed circuit board.

PDE partial differential equation.

PER polarization extinction ratio.

PM polarization-maintaining.

PMC pre-mode-cleaner.

QE quantum efficiency.

RIN relative intensity noise.

RPN relative power noise.

SBS stimulated Brillouin scattering.

SCD standard confined-doping model.

SUT system under test.

TEM transverse electro-magnetic.

VAD vapor axial deposition.

Chapter 1

Introduction

In 1916, Einstein demonstrated in his theory of general relativity (GR) that the solutions of the linearized weak-field equations describe transverse waves in the fabric of space-time [1]. Gravitational waves (GWs) are generated by the second time derivative of the mass quadrupole moment of their sources. GWs interact weakly with matter and can therefore travel long distances through space relatively undisturbed with the speed of light c. Contrary to photons, archaic GWs were already present shortly after the Big Bang and could thus provide information about the primordial eras of the universe [2, 3]. Furthermore, GW astronomy may give access to astrophysical objects with a red shift beyond $z \gtrsim 20$ [3] that cannot be observed on earth in the electro-magnetic domain due to Hubble's law [4]. The immense reach allows to determine the universe's binary black hole (BH) merger population and may uncover secrets that have remained hidden behind the observable universe [3]. These are the reasons why GWs are of particular interest for astronomers and many efforts were made to provide evidence. The GWs that arrive at earth, however, are typically so faint that their proof has been extraordinarily challenging. The first attempts were carried out by Joseph Weber in the 1960s based on massive aluminum bars [5]. The mechanical eigenfrequencies of the bars were in the audioband matching to the frequencies of GWs that are generated during the merging process of two BHs. The displacement of the bars was sensed by precise piezoelectrics and converted into an electrical signal. In this way, a number of events were recorded by Weber but finally dismissed as false due to a glitch during the data acquisition [6]. The more sophisticated Weber apparatus, namely ALLEGRO, was already operating at cryogenic temperatures but decommissioned in 2008 without any confirmed detections. In 1979, Taylor *et al.* discovered the first hint of a GW in the radio-frequency spectrum of a binary neutron star pulsar [7]. The authors reported a variance of PSR1913+16's pulse arrival time implying a chirp of the binary's inspiral frequency. The energy loss corresponded to the predictions of GR and was hence attributed to GW radiation. Large-scale earth-bound interferometric gravitational wave detectors (GWDs) in Michelson, L-shape or xylophone-like architecture were proposed as early as 1970. The working principle, an overview of their history and a roadmap of future detectors are outlined in the following.

1.1 Interferometric GWDs: the first and second generation

The setup of a GWD in Michelson configuration is shown in Fig. 1.1.1. The interferometer detects microscopic length perturbations by referencing the phase of two independently propagating laser beams [8, 9, 10]. The principle works as follows. A laser beam is generated by a non-planar ring oscillator (NPRO) made from an Nd:YAG crystal. The laser operates at a wavelength of 1064 nm with exceptional power and frequency noise properties, e.g. 1 kHz measured over 100 ms [11]. The laser beam is further amplified to the ≈100 W level in either Nd:YAG [12] or Nd:YVO$_4$ [13] crystals and injected into the interferometer. The amplified beam is split by a beam splitter (BS) at the inter-

ferometer's vertex in orthogonal directions denoted as x and y. The orthogonal laser beams propagate back and forth along the interferometer arms, are combined at the BS and aligned to a photo detector, where the beams interfere. The accumulated phase of each beam can differ in integer or fractional numbers depending on the lengths of the x- and y-arms:

$$\phi_{x,y} = \frac{2\pi f}{c} L_{x,y}, \tag{1.1}$$

where $f = 2.82\,\text{THz}$ is the optical frequency of the light and $L_{x,y}$ the beams' total propagation lengths. The interferometer is normally operated near the dark fringe

$$\underbrace{\phi_x - \phi_y = 2n\pi + \frac{\pi}{2}}_{\text{destructive interference}}, \tag{1.2}$$

i.e. no light hits the photo detector. The tidal field of a passing GW would change the relative lengths of the two arms, i.e. stretch or compress the interferometer. As a result, light falls on the photo detector and can be used to readout the GW signal.
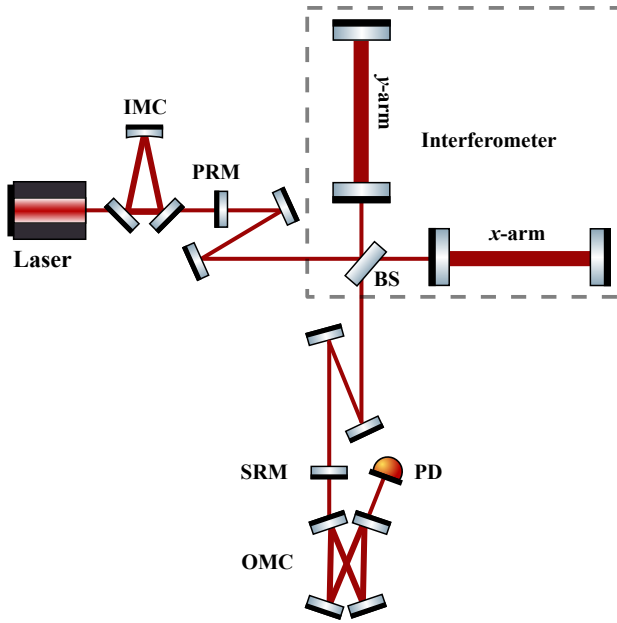
Figure 1.1.1: Interferometric GWD setup in Michelson architecture with laser source, input-mode-cleaner (IMC), power recycling mirror (PRM), beam splitter (BS), x- and y-arm cavities, signal recycling mirror (SRM), output-mode-cleaner (OMC) and photo detector (PD). Attribution to the component library by Alexander Franzen.

The relative length change, i.e. *strain*, is only in the order of $\Delta L/L \approx 10^{-20}$ so that sophisticated noise suppression is required. The following technical measures can be taken to isolate the interferometer from environmental influences (see Fig. 1.1.2) [10]; a more detailed discussion on the quantum and thermal noise can be found in Sec. 1.1.2. For example, optical components can be suspended on multi-stage pendulums with non-uniform fused silica fibers and active or passive noise damping [14]. Other key components can also be isolated from seismic ground motions by multi-stage isolation platforms [15]. Refractive index fluctuations by non-stationary gas pressure and stochastic transits of molecules through the laser beam can be reduced by enclosed and vented beam tubes. Additionally, the beam quality of the laser can be enhanced by optical cavities that filter higher-order modes (HOMs) from the laser beam. The cavities can also reduce residual beam jitter and suppress high-frequency power fluctuations. Furthermore, a filter cavity in triangular configuration can clean the polarization due to an additional phase shift of π for the polarization parallel to the cavity plane. Scattered light can be removed by special stray light apertures and the effective circulating laser power can be increased by using power recycling and intra-arm cavities. Moreover, signal recycling at the interferometer output can reduce the finesse of the arm cavities and ensure a broad response bandwidth of the detector [10].

The maturity of the detectors has grown rapidly in time; their evolution is therefore divided into three generations. In the first generation, the TAMA300 detector was operated from 1999 to 2004 as the first L-shaped Fabry-Pérot detector. TAMA300 used a 10 W injection-locked Nd:YAG laser amplifier at 1064 nm [16]. Cryogenic cooling was first introduced in the Cryogenic Laser Interferometer Observatory (CLIO) in Japan. CLIO's mirrors were cooled to 20 K to reduce the thermal noise

by around one order of magnitude [17]. The cryogenic operation required CLIO to use SiO_2:Ta_2O_5-coated Al_2O_3 substrates. CLIO used an Nd:YAG-based NPRO laser with 2 W output power and a wavelength of 1064 nm as a laser source. In the early 2000s, GEO600 (Hanover, Germany), Virgo (Cascina, Italy) and the LIGO twin-detectors (**L**aser **I**nterferometer **G**ravitational-Wave **O**bservatory in Hanford and Livingston, USA) launched their observation runs simultaneously as the last detectors of the first generation. The GEO600 detector used a 12 W injection-locked Nd:YAG laser system at 1064 nm; the master laser was an Nd:YAG-based NPRO laser with 0.8 W output power [18]. The x- and y-arms of the GEO600 detector are folded to increase the detector's effective arm lengths. The initial LIGO detectors used diode-pumped Nd:YAG lasers with 10 W output power at 1064 nm [19]. The laser system of the Virgo detector consisted of an Nd:YAG-based NPRO master laser at 1064 nm and an injection-locked laser stage with diode-pumped Nd:YVO_4 rods providing up to 20 W output power [20].
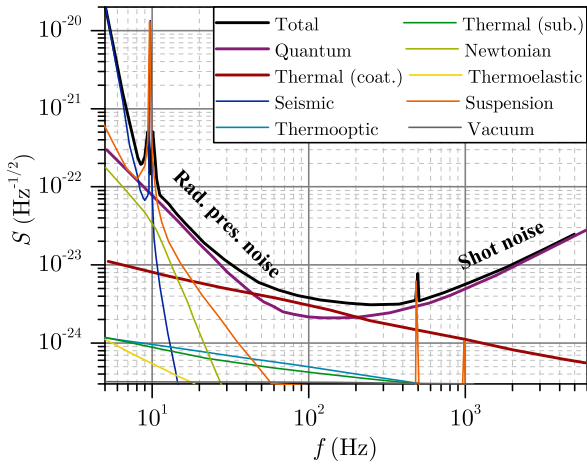

Figure 1.1.2: Modelled noise budget of aLIGO detectors with non-detuned signal recycling cavity at 125 W input power. Compiled from GWINC-v2 software simulations [21].

Until 2015 and 2017, the LIGO and Virgo detectors were subjected to major upgrades referred to as Advanced LIGO (aLIGO) and Advanced Virgo (AdVirgo). These upgrades marked the dawn of the second detector generation. In the aLIGO detectors, Nd:YAG-based NPRO lasers with a wavelength of 1064 nm were first pre-amplified to 35 W in single-pass Nd:YVO_4-rod-based amplifiers [22]. Subsequent injection-locked Nd:YAG ring oscillators provided up to 180 W output power at 1064 nm [12]. In late 2020, the Kamioka Gravitational Wave Detector (KAGRA) joined the detector network. KAGRA is located in the seismically quiet Kamioka mine in Japan with two 3 km-long arms. KAGRA inherited the technology of its progenitor CLIO; therefore, KAGRA also uses Al_2O_3 mirrors that are cryogenically cooled to 20 K to reduce the thermal noise [23]. In KAGRA, a 400 mW Nd:YAG-based NPRO laser with a wavelength of 1064 nm is amplified by a commercial fiber amplifier up to 40 W[1] [25].

1.1.1 Detections from the second generation

The aLIGO twin-detectors in Hanford and Livingston made the first GW detection (GW150914) in September 2015, which marked a major breakthrough in modern astronomy. The observatories simultaneously detected a GW signal that chirped upwards in frequency from 35 Hz to 250 Hz with a peak strain of 1.0×10^{-21} [26]. The signal matched a waveform that was predicted by numerical relativity calculations. The waveform described the inspiral and subsequent merger of a binary BH system in a distance of 410^{+160}_{-180} Mpc and the ring-down of the resulting BH with a final mass of $62^{+4}_{-4} M_\odot$ [26]. The binary BH system had initial masses of $36^{+5}_{-4} M_\odot$ and $29^{+4}_{-4} M_\odot$; the event generated GW radiation that was equivalent to $3.0^{+0.5}_{-0.5} M_\odot$ [26].

The observation of GW170817 by the joined aLIGO/AdVirgo network marked another milestone in the GW success story [27, 28]. GW170817 arose from the merger of two neutron stars in the galaxy NGC 4993 in the constellation Hydra. The previous inclusion of AdVirgo in the detector network increased the sky localization to 28 deg^2 and enabled the detection of the γ-ray burst GRB 170817A

---

[1]Amplification from 2 W up to 121 W was also demonstrated by Takeno *et al.* by using injection-locking based on two Nd:YAG rods [24]. The quality of the laser, however, was not sufficient for the requirements [24].

by the Fermi satellite as well as the discovery of the AT 2017gfo (SSS17) transient [29]. The observation of GW170817 sparked the era of multi-messenger astronomy and, in total, over 70 follow-up radio-band to X-ray studies were performed globally in the following weeks. A detailed catalogue of all GW detections from the first, second and third (incomplete) observation runs can be found in references [30] and [31].

1.1.2 Quantum and thermal noise

Fig. 1.1.2 shows the noise budget of the aLIGO detectors; the total noise (black curve) determinates the sensitivity of the detector. The dominant noise sources, namely quantum and thermal noise, are described in the following. Moreover, strategies to reduce the quantum and thermal noise are given. The resulting requirements on the laser sources of future detectors can be found in Sec. 1.2.1.

Quantum noise

The audio-band sensitivity of the aLIGO detectors is limited by the quantized nature of the laser light (see Fig. 1.1.2). The quantum noise is a direct manifestation of the Heisenberg uncertainty principle and results in detector noise through two different mechanisms: photon shot noise and radiation pressure noise. The photon shot noise is caused by the uncertainty of the arrival times of individual photons - and hence non-stationary photon flux - at the photo detector. The photon shot noise dominates at high frequencies and increases with the square root of the laser power. Thus, the relative photon shot noise, denoted as S_s, decreases with the square root of the laser power:

$$S_s \propto \sqrt{\frac{\lambda_{\text{laser}}}{P_{\text{laser}}}}.$$ (1.3)

Radiation pressure noise is caused by the random motion of the mirror surfaces that are exerted by the momentum of incoming photons. As a result, the mirrors are deflected from their neutral positions. The corresponding spatial displacement shifts the light's phase at the photo detector. The quantum nature of the light randomizes this effect resulting in mirror vibrations and phase noise. Radiation pressure noise is dominant at low frequencies and increases with laser power. Hence, laser power scaling in itself cannot solve the quantum issue over the complete frequency range[2].

The current aLIGO detectors use the squeezing technique to reduce the quantum noise [32]. Squeezed states have a redistributed quantum uncertainty either minimized in the phase or amplitude quadrature to either reduce the photon shot noise or the radiation pressure noise at the expense of the other. However, a low-loss quantum noise filter cavity can rotate the squeezed quadrature as a function of frequency and thus simultaneously reduce both [32]. Hence, frequency dependent squeezing is believed to mitigate the quantum noise barrier in the future. In that case, the coating thermal noise will dominate the detector's total sensitivity.

Thermal noise

Apart from quantum noise, thermal noise sets the second most dominant sensitivity limit. Thermal noise originates from the random motion of atoms or molecules in the optics' amorphous fused silica substrates and their μm-thin SiO_2/Ti:Ta_2O_5 coating layers. The atomic motions displace the optical surfaces and can distort the surface curvature, which affects the phase of the laser beam. The randomness of this process induces surface vibrations; the corresponding phase noise couples into

---

[2]Higher circulating laser power decreases the photon shot noise at high frequencies but increases the radiation pressure noise at low frequencies and vice versa.

detector noise. The thermal noise is temperature dependent and furthermore related to the mechanical loss through the fluctuation-dissipation theorem. The power spectral density of the thermal noise originating from a coated substrate with temperature T can be expressed by [33]:

$$S_x(f) = \frac{2k_B T}{\pi^{\frac{3}{2}} f \omega} \frac{1-\sigma}{Y} \left[\phi_{\text{sub}} + \frac{d}{\sqrt{\pi}\omega} \left(\frac{Y}{Y_\perp} \phi_\perp + \frac{Y_\parallel}{Y} \phi_\parallel \right) \right], \tag{1.4}$$

where f is the frequency, k_B is Boltzmann's constant and σ Poisson's ratio, ω the beam radius of a Gaussian beam, Y are Young's moduli and ϕ are the mechanical losses of the substrate in parallel and in orthogonal direction[3].

Eq. (1.4) shows that the thermal noise scales linear with T; thus, cryogenic cooling is a viable approach to reduce the thermal noise. However, the mechanical loss of fused silica peaks below room temperature [34] and cancels the benefits of the lower temperature. Cryogenically cooled detectors must therefore use alternative substrate materials like Al_2O_3 (see KAGRA) or crystalline silicon. Al_2O_3 suffers from thermoelastic noise due to its high thermal conductivity and requires to be operated at 20 K where the thermal expansion coefficient vanishes due to the Nernst heat theorem [35]. As a result, liquid He and sophisticated cooling systems are necessary if Al_2O_3 substrates are used. Such requirements are rather eased for crystalline silicon making it the preferred substrate choice. Moreover, crystalline silicon's thermal expansion coefficient already crosses zero at 123 K without inducing excess mechanical loss.

As a major disadvantage, crystalline silicon is opaque to light with a wavelength of 1064 nm making the use of the current laser technology as per Sec. 1.1 no longer feasible. The absorption coefficient of crystalline silicon, however, decreases towards longer wavelengths, e.g. to less than 10^{-6} cm^{-1} above 1.4 µm [36]. Compatible laser wavelengths can be provided by erbium (Er^{3+}, $\approx$1.5 µm), thulium (Tm^{3+}, $\approx$1.8 µm to $\approx$2.1 µm) or holmium (Ho^{3+}, $\approx$2.1 µm) based laser sources. The 2.0 µm wavelength range has the following advantages. For example, Tm^{3+} and Ho^{3+} doped fiber amplifiers can generate hundreds of W output power with a wavelength around 2.0 µm [37, 38, 39, 40]. Ho^{3+} can be pumped with good quantum efficiency (QE) around 1.95 µm from a Tm^{3+} doped laser source or at 1.15 µm. Tm^{3+} amplifiers also achieve excellent QEs due to the 2-for-1 cross-relaxation process. Furthermore, the optical scatter losses at the mirrors scale with $1/\lambda^2$; the wide-angle scattering loss is therefore $\approx$40 % less at 2.0 µm versus that at 1.55 µm [35]. Moreover, the SiO_2 coatings show less absorption at 2.0 µm (49 ppm versus $\approx$350 ppm, $d = 1$ µm [41]). Additionally, the two-photon absorption coefficient of crystalline silicon is lower at 2.0 µm than at 1.5 µm ($\approx$0.25 cmGW^{-1} versus $\approx$1.5 cmGW^{-1}, derived from reference [42]).

However, the low QEs of photo detectors at 2.0 µm, i.e. extended InGaAs (QE: 87 % [35]), HgCdTe (QE: 94 % [35]) or InAsSb (QE: 70 % [43]), limit the achievable squeezing quality; in contrast, InGaAs have a QE larger 99 % at 1.55 µm [35]. The photon shot noise also scales with $\sqrt{\lambda}$; hence, more circulating power is required at 2.0 µm versus 1.5 µm to achieve the same photon shot noise level. Moreover, the substrate absorption is expected to scale with λ^2 although it is a factor 3 less than the coating absorption [35]. Finally, optical components, e.g. optical coatings, photo detectors as well as electro- and acousto-optical modulators, are more matured around 1.5 µm due to the rapid advancement of the telecommunication industry. From the perspective of these considerations, a wavelength of 1.5 µm seems to be more qualified than 2.0 µm to be used in a cryogenically cooled GWD of the third generation.

1.2 Interferometric GWDs: the third generation

In the second generation of GWDs, the detection rate was limited to a few events per month[4] [44]. The network's sky localization was furthermore restricted by the lack of detector distribution. For

---

[3] Assuming Poisson's ratio is small.

[4] Depending on the type of the source.

these reasons, detector upgrades and an advanced third detector generation are already in the conceptual and/or technical design phase. The aLIGO detectors will be subject to gradual upgrades in the mid-twenties referred to as LIGO A+. The LIGO A+ upgrades include balanced homodyne detection, frequency dependent squeezing and Newtonian noise subtraction. Improved amorphous or AlGaP/GaP coatings have also been studied [45]. LIGO India, a replica facility of LIGO A+, is also planned to join the detector network in the mid-twenties. The LIGO A+ and LIGO India detectors, however, will continue to operate at room temperature. LIGO Voyager is already assigned to the third detector generation but will inherit the aLIGO facilities. LIGO Voyager is predicted to improve the detector's audio-band sensitivity by a factor of four with a myriad of instrumental upgrades. The upgrades include cryogenic cooling, crystalline silicon substrates and a laser wavelength around 1.5 μm or 2.0 μm with a circulating arm power of up to 3 MW [46]. The Cosmic Explorer (CE) detector will inherit the matured technologies of the previous generation in a new facility. CE is planned to have 40 km-long arms with an L-shaped architecture and is expected to operate mid 203x. CE is foreseen to use crystalline silicon substrates and will operate around 2.0 μm. The European Einstein Telescope (ET) will have a triangular facility with 10 km-long arms. The ET facility will house three xylophone-like dual-detectors: a low frequency interferometer (ET-LF) operating at cryogenic temperatures and a high frequency interferometer (ET-HF) operating at room temperature [47]. ET-LF is expected to use crystalline silicon substrates and operate with 18 kW circulating arm power around 1.5 μm. Finally, the Light Interferometer Space Antenna (LISA) will be the first spaceborne GWD. Three satellites will span six active laser links in triangular formation and the detector will be effectively shielded in a heliocentric orbit from seismic disruptions. LISA will operate at 1064 nm like detectors of the second generation.

1.2.1   Requirements on the laser source

The reduction of shot and thermal noise requires sufficient laser power and cryogenic cooling; a compatible laser source must therefore have a wavelength around 1.5 μm and preferably $\gtrsim 100$ W output power as the current 1064 nm laser systems. Additionally, the laser source must meet the following requirements[5]. Firstly, fluctuations of the power relative to the beam's mean power manifest as relative power noise (RPN). The RPN impinges on the mirrors' positions and thus couples through phase noise into detector noise. RPN can originate from the pump and/or seed laser with respect to the device's effective transfer function. RPN can be suppressed by tailored feedback loops e.g. fast pump power control as shown by Thies *et al.* [48]. Retrofitting of potential stabilization systems must be factored into the design process of the laser system[6]. Furthermore, the RPN can also arise from mechanical and/or thermal stress. The laser system must therefore be sufficiently shielded against environmental influences. Secondly, the laser power must be confined to the fundamental mode because the third detector generation will probably inherit the cavity technology from its predecessors including resonant arm cavities, HOM filtering[7] as well as power and signal recycling (see Fig. 1.1.1). The cavities are only resonant to the fundamental mode[8]; hence, the power in any other mode would be lost. Furthermore, residual mode fluctuations would induce excess RPN and therefore also require additional power stabilization. Thirdly, a stable linear polarization is required. The power in the incorrect polarization may be effectively filtered at the detector input; nevertheless, polarization fluctuations induce power noise that may require additional power stabilization. For this reason, mechanical and thermal shielding is required to preserve a stable polarization of the laser beam. In case of a fiber amplifier, polarization-maintaining (PM) fibers must be used. Fourthly, the laser frequency

---

[5]Note that the final design criteria are not concisely specified at the time of writing.

[6]aLIGO PSL design: RPN of $\leq 2 \times 10^{-9}$ Hz$^{-1/2}$ at 10 Hz [10].

[7]aLIGO: pre-mode-cleaner (PMC), input- and output-mode-cleaner (I/OMC).

[8]Equivalent to the LP_{01} fiber mode.

must be sufficiently stable[9] because the lengths of the x- and y-arms are not precisely equal but can differ by integers of the laser wavelength for a given phase relation. The frequency noise can therefore couple into phase noise at the photo detector. The laser linewidth can be reduced by active frequency stabilization if necessary. Fifthly, GWDs are supposed to work 24/7 without disruptions. Hence, a reliable and longterm stable laser design must be found. At some extent, the power stabilization may fail to compensate unrecoverable longterm drifts, for example as a result of photodarkening or diode aging. At this point, easy maintenance or repair procedures are desired; a non-complex laser architecture is therefore preferred. From a practical point of view, in situ monitoring of the optical and/or thermal properties should be possible. Furthermore, accessible diagnostic ports can provide early information on technical malfunctions and therefore minimize downtimes. In some cases, a suitable emergency-off (EMO) system may prevent imminent damage at all. It would also be desirable to avoid highly specialized or complex components with limited market availability. Instead, the components should be off-the-shelf available without significant effort to find replacement after a malfunction. Moreover, the components are desired to be available from different suppliers to prevent a spare part shortage.

1.2.2   Er^{3+}:Yb^{3+} doped fiber amplifiers

Er^{3+}-based laser systems are promising candidates to fulfil the requirements as stated in Sec. 1.2.1. The laser system can be implemented in either free-space or fiber format. The first free-space Er^{3+} laser with a wavelength of 1.54 μm was demonstrated by Snitzer *et al.* in 1965 [49] based on silicate glass; YAG [50], YLF [51], YALO [52], tungstates [53] and vanadates [54] are also possible host materials. Snitzer *et al.* also sensitized the glass with Yb^{3+} to achieve 1.54 μm emission at room temperature. The free-space format can be useful for high-power operation because the beam path through the laser material is too short to significantly trigger unwanted non-linear effects and/or ASE. Furthermore, in situ monitoring of the optical beam properties and fast replacement of damaged components are possible. Moreover, current detectors already established free-space Nd:YAG or Nd:YVO$_4$ laser amplifiers as well proven laser sources at a wavelength of 1064 nm. The free-space format, however, must be designed for a specific output power because of thermal lensing. Furthermore, the free-space format comes with a high degree of adjustability that can lead to pointing instabilities. Moreover, the low surface-to-volume ratio of an Er^{3+} laser crystal disqualifies the free-space configuration because of Er^{3+}'s large quantum defect and the associated heat load. A free-space Er^{3+}-based laser system is therefore not preferred.

In contrast, Er^{3+}:Yb^{3+} doped fiber amplifiers (EYDFAs) are rugged, reliable laser sources with good compactness and excellent thermal properties. Driven by applications mainly in the field of telecommunication, far-reaching foundations have already been laid for EYDFAs (see Sec. 2.2.3). For example, Yb^{3+} codoping eases the power scaling because it improves the Er^{3+} solubility. Yb^{3+} also increases the pump absorption at 9xx nm. Moreover, off-peak pumping was successfully tested to suppress the unwanted Yb^{3+} ASE [55]. The beam properties of the seed laser[10] - including laser wavelength, noise properties, beam quality and linewidth - are only marginally affected by the amplifier [56]. Moreover, EYDFAs with non-PM fibers have already been tested in references [55, 56, 57] to be compliant with some of the requirements from Sec. 1.2.1; for example, a fundamental mode content of ≈95 % with compatible noise properties and kHz linewidth has been shown with non-PM fibers in reference [56]. Using PM fibers, however, is inevitable if the laser is to be used in a GWD; a PM fiber setup has not been demonstrated on the desired ≈100 W power level so far. Furthermore, the thermal management and its potential impact on fiber (coating) damage is critical. For example, Matniyaz *et al.* had to immerse the fiber directly into water for cooling; power scaling was still lim-

---

[9]The required frequency stability of the pre-stabilized aLIGO laser is $1\,\text{Hz}/\sqrt{\text{Hz}}$ at 10 Hz [10].

[10]For example, the seed laser can be a temperature-stabilized fiber laser, a fiber-coupled distributed feedback (DFB) diode laser or an external cavity semiconductor laser. At the time of writing, NPRO lasers made from Er^{3+} laser crystals are not available.

ited by fiber damage [57]. There has also been no demonstration of any successful longterm operation (>hours) even of a non-PM setup.

A single-frequency EYDFA with PM fibers is presented in this work; the amplifier is compatible with the provisional laser source requirements at $1.5\,\mu m$ of a cryogenically cooled GWD as per Sec. 1.2.1. The work is structured in the following form. The fundamental principles for understanding are reviewed in Chap. 2. The achievable output power levels for pump wavelengths within the 9xx nm pump band can be found in Chap. 3; the Yb^{3+}-to-Er^{3+} transfer process is quantized by introducing the energy transfer efficiency. A protective EMO system is described in Chap. 4; the system interlocks the pumping process in case of a seed laser failure. A laboratory-level amplifier in PM format is presented in Chap. 5. A further advanced amplifier is presented in Chap. 6; a performance comparison of two potential gain fibers is given. The work is summarized in Chap. 7; also, pumping around $1480\,nm$ is suggested as a future line of investigation.

Chapter 2

Fundamentals of optical fibers and fiber amplifiers

Optical fibers are light-weight, small-footprint tools to safely manage, transmit or amplify light. The availability of compatible glass hosts and active ions as well as the advancements in highly efficient fiber coupled pump sources, e.g. high-brightness laser diodes or high-power Raman fiber lasers, stimulated the commercialization of fiber amplifiers. The all-fiber design can provide outstanding thermal management, good compactness and high durability with robust beam quality [58]. For these reasons, the fiber format has found its way into the internet and data transmission industry, application-oriented devices for medicine and security or harsh sensing environments. This chapter reviews the important properties and challenges of optical fibers and fiber amplifiers that are of relevance for this work.

Sec. 2.1 explains light guidance in optical fibers and defines the relevant fiber parameters. Sec. 2.1 also presents how the light's electric field $\vec{E}(r)$ is confined to the fiber core by total internal reflection at the core-cladding interface and derives a solution of $\vec{E}(r)$ from the radial Helmholtz equation. In this context, the LP_{mp} mode decomposition of the electric field is introduced. Sec. 2.2 explains the most common fiber manufacturing techniques and summarizes the important properties of Er^{3+} and Er^{3+}:Yb^{3+} (co)doped fibers. The energy levels that are relevant for this work, namely the $^4I_{15/2}$ to $^4I_{9/2}$ energy levels of Er^{3+} and the $^2F_{7/2}$ and $^2F_{5/2}$ energy levels of Yb^{3+}, are introduced and the important optical transitions are characterized by their effective emission and absorption cross-sections. Moreover, cooperative up-conversion and the Yb^{3+}-to-Er^{3+} energy transfer are described. Sec. 2.3 discusses relevant power scaling restrictions of fiber amplifiers. The non-linear process of stimulated Brillouin scattering (SBS) is presented and an expression for its critical power threshold is given. The amplification of the spontaneous luminescence is defined as amplified spontaneous emission (ASE); the corresponding rate and power propagation equations are described. Additionally, ASE suppression techniques such as off-peak pumping are introduced.

2.1 Light guidance in optical fibers

Most commercially available fibers on the market are made of silica and feature a dedicated centered area that is called the fiber core. The fiber core is surrounded by the cladding. The cladding has a lower refractive index than the fiber core[1] [59]:

$$n_{\text{core}} > n_{\text{clad}}. \tag{2.1}$$

---

[1] In practice, optical fibers typically do not have a discrete step as intended but a rather gradient-like or partly rippled refractive index profile due to the preform manufacturing process. Also, certain fiber types such as gradient index or hollow core fibers deliberately exploit refractive index profiles where the index transitions gradually between core and cladding or where the core is either gaseous or vacuum.

In the simplest case, i.e. a step index fiber, the refractive index increment at the core-cladding interface is a discrete step. The magnitude of the index step determines the number of guided modes and hence output beam quality of the fiber. The light ray model gives a simplified explanation for the guiding mechanism. The model is illustrated in Fig. 2.1.1. In the model, light that is coupled into the fiber core up to a particular incident angle, labelled as Θ_{NA}, experiences total internal reflection at the core-cladding interface as can be derived from the Fresnel equations. Hence, the light behaves like rays that are reflected at the cladding and bounce back and forth in the fiber core. The acceptance angle is given by the difference of the refractive indices of the core and cladding; furthermore, Θ_{NA} defines the numerical aperture (NA) of the fiber:

$$\text{NA} = \sqrt{n_{\text{core}}^2 - n_{\text{clad}}^2} = \sin\left(\Theta_{NA}\right). \tag{2.2}$$

The precise refractive indices of core and cladding can be carefully designed and controlled during the manufacturing process by the introduction of index-manipulating dopants such as GeO_2, Al_2O_3 or P_2O_5 [60]. More details on the fabrication process can be found in Sec. 2.2.
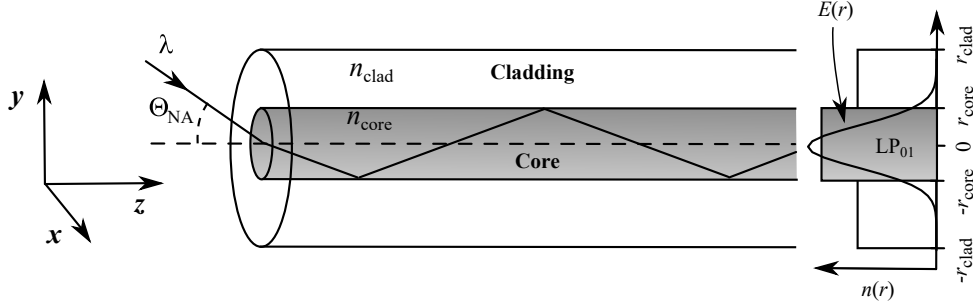

Figure 2.1.1: Total reflection of light rays in the core of a single-mode fiber. Fiber core and cladding radii are r_{core} and r_{clad} with refractive index $n(r)$ that includes n_{core} and n_{clad}. Θ_{NA} is the acceptance angle and $E(r)$ the electric field in the LP_{01} mode.

First principle calculations of Maxwell's equations give a precise solution of the electric field E in the fiber core [61]. Note that the electric field is a function of location (r, ϕ, z) and time t; the distance from the center of the fiber is r and ϕ is the azimuth angle. The z-axis corresponds to the propagation direction of the light and is aligned along the fiber. The corresponding wave equation can be expressed in cylindrical coordinates due to the radial symmetry of the fiber:

$$\nabla^2 E = \frac{1}{r}\frac{\partial}{\partial r}\left(r\frac{\partial}{\partial r}E\right) + \frac{1}{r^2}\frac{\partial^2}{\partial \phi^2}E + \frac{\partial^2}{\partial z^2}E. \tag{2.3}$$

The transversal and longitudinal propagation can be separated by applying the paraxial approximation. Hence, a separation ansatz can be applied:

$$E(r, \phi, z, t) = E_0 \mathcal{N}(r, \phi)\mathcal{Z}(z)\mathcal{T}(t). \tag{2.4}$$

E_0 is the electric field amplitude. The term $\mathcal{N}(r, \phi) = \mathcal{R}(r)\Phi(\phi)$ describes the transverse field distribution in the xy-plane in cylindrical coordinates. The expression

$$\mathcal{Z}(z) = e^{-i\beta z} \tag{2.5}$$

describes the longitudinal propagation of E along the z-axis as a plane wave. The propagation constant β is the longitudinal component of the wave vector $\vec{k}$. The transverse component is denoted as

$$\kappa = \sqrt{|\vec{k}|^2 - \beta^2}. \tag{2.6}$$

10

Such separation of the transverse and longitudinal components of $\vec{k}$ accounts for light that also propagates in transverse direction analogous to tilted rays. The term

$$\mathcal{T}(t) = e^{i\omega t} \tag{2.7}$$

describes the temporal evolution of the electric field as a complex exponential function with angular frequency ω. By using the separation ansatz, the following equation can be obtained from Eq. (2.3):

$$-\frac{1}{\Phi}\frac{\partial^2}{\partial\phi^2}\Phi = \frac{1}{\mathcal{R}}\left(r^2\frac{\partial^2}{\partial r^2}\mathcal{R} + r\frac{\partial}{\partial r}\mathcal{R} + r^2\left(k^2 - \beta^2\right)\mathcal{R}\right). \tag{2.8}$$

The terms E_0, $\mathcal{Z}(z)$ and $\mathcal{T}(t)$ have been eliminated from Eq. (2.8). Then, the right- and left-hand sides of Eq. (2.8) only depend on either r or ϕ, respectively, and must therefore be constant. Thus, two independent differential equations can be obtained for $\mathcal{R}(r)$ and $\Phi(\phi)$ by setting the right- and left-hand sides of Eq. (2.8) equal to a constant denoted as m^2:

$$r^2\frac{\partial^2}{\partial r^2}\mathcal{R}(r) + r\frac{\partial}{\partial r}\mathcal{R}(r) + \left(\kappa^2 r^2 - m^2\right)\mathcal{R}(r) = 0, \tag{2.9}$$

and

$$\frac{\partial^2}{\partial\phi^2}\Phi(\phi) + m^2\Phi(\phi) = 0. \tag{2.10}$$

Eq. (2.9) is known in literature as *Bessel's differential equation*. Its solutions are constrained to Bessel function $\mathrm{J}_m(\kappa_{\mathrm{core}}r)$ for the core and modified Bessel functions $\mathrm{K}_m(\kappa_{\mathrm{clad}}r)$ for the cladding by the following assumptions. Firstly, the light propagates mainly in the core of the step index fiber ($n_{\mathrm{core}} > n_{\mathrm{clad}}$). Secondly, the amplitude decays exponentially in the cladding. The solution of Eq. 2.10 is given by:

$$\Phi(\phi) = c_0\cos\left(m\phi + \phi_0\right) \tag{2.11}$$

with coefficients c_0 and ϕ_0. Such solution has to satisfy the continuity constraint at 2π:

$$\Phi(\phi) = \Phi(\phi + 2\pi), \tag{2.12}$$

and

$$\frac{\partial}{\partial\phi}\Phi(\phi) = \frac{\partial}{\partial\phi}\Phi(\phi + 2\pi). \tag{2.13}$$

Hence, m has to be an integer number ($m \in \mathbb{N}$) and can be interpreted as the number of nodes in azimuthal direction. In total, the transverse field distribution can be expressed as

$$\mathcal{N}_{\mathrm{core}}(r, \phi) = C_1\mathrm{J}_m(\kappa_{\mathrm{core}}r)\cos\left(m\phi + \phi_0\right) : \ r \leq r_{\mathrm{core}} \tag{2.14}$$

and

$$\mathcal{N}_{\mathrm{clad}}(r, \phi) = C_2\mathrm{K}_m(\kappa_{\mathrm{clad}}r)\cos\left(m\phi + \phi_0\right) : \ r \geq r_{\mathrm{core}}. \tag{2.15}$$

The continuity requirement at the core-cladding interface, i.e. $r = r_{\mathrm{core}}$, cannot be fulfilled for arbitrary variations of κ_{core} and κ_{clad}. As a result of this consideration, only certain regimes for κ_{core} - called *solution branches* - are allowed. Within such branch, κ_{clad} is determined by κ_{core}. The branches are enumerated with an integer $p \in \mathbb{N}$. The integer indicates the number of the branch's nodes in radial direction. The existence of a branch depends on the choice of m and requires a certain V-number of the fiber. The V-number is a dimensionless parameter and represents the relation between κ_{core} and κ_{clad}:

$$V = r_{\mathrm{core}}\sqrt{\kappa_{\mathrm{core}}^2 - \kappa_{\mathrm{clad}}^2} \tag{2.16}$$

$$= \frac{2\pi}{\lambda}r_{\mathrm{core}}\mathrm{NA}. \tag{2.17}$$

The total solution for a particular m and p is called LP_{mp} mode. Exemplarily, the LP_{01} mode - denoted as *fundamental mode* - has a Gaussian-like spatial beam profile and is desired for many applications. The set of all LP_{mp} modes provides a basis such that any arbitrary electric field can be represented as a superposition of individual LP_{mp} modes:

$$\mathcal{N}(r, \phi) = \sum_{m,p} c_{mp} \cdot \text{LP}_{mp}(r, \phi). \tag{2.18}$$

The propagation constant β can differ for each mode. The difference can be expressed in an effective refractive index n_{mp} for that mode, which satisfies:

$$n_{\text{core}} > n_{mp} > n_{\text{clad}}. \tag{2.19}$$

Practically, the V-number gives a figure of merit for the tendency of a fiber to support HOMs that can degrade the beam quality. For example, solutions of the first branch exist for every $V \in \mathbb{R}^+$ for $m = 0$; the second branch requires V to be ≥ 3.832. For $m = 1$, the first branch requires V to be ≥ 2.405. Consequently, fibers with $V \leq 2.405$ exclusively support the LP_{01} mode. Such single-mode fibers are limited to core diameters of $\approx 10\,\mu\text{m}$ because the following condition derived from Eq. (2.17) must be satisfied

$$\text{NA} \lesssim 1.2 \frac{\lambda}{\pi r_{\text{core}}}, \tag{2.20}$$

and the NA cannot be made any smaller at some point due to technical limitations of the fabrication process. Moreover, the V-number of a concrete fiber solely depends on the wavelength of the light because it has a fixed core diameter and NA^2. The wavelength at which the condition $V = 2.405$ is fulfilled is denoted as cut-off wavelength. A fiber only supports the fundamental mode at longer wavelengths but also HOMs at shorter wavelengths. Fibers with a V-number larger than 2.405 are termed few-mode or multi-mode fibers.

Double-cladding fibers

Optical fibers can have a second outer glass or polymer cladding with a lower refractive index compared to the first cladding:

$$n_{\text{clad},1} > n_{\text{clad},2}. \tag{2.21}$$

The light that is coupled in the first cladding is therefore also totally reflected at the cladding-cladding interface. Typical cladding diameters are above $\approx 100\,\mu\text{m}$ which results in large V-numbers that also allow higher LP_{mp} modes to propagate; the cladding is hence capable to guide pump light with low beam quality but high power levels. The large cladding area maintains moderate light intensities despite the high power levels and potential fiber damage can be avoided. The cladding modes overlap with the core area, where potential rare-earth dopants are confined. Hence, such dopants can still absorb the cladding light, albeit at a lower rate due to the decreased cladding-to-dopant overlap[3]:

$$\frac{A_{\text{core}}}{A_{\text{clad}}} \approx 1\,\%, \tag{2.22}$$

where A_{core} and A_{clad} are the core and cladding areas, respectively. Therefore, longer fibers are required for sufficient cladding absorption. As a second drawback, a circular cladding geometry also supports helical cladding modes which do not overlap at all with the fiber core. Such modes remain unabsorbed [62, 63] and degenerate the pump efficiency. Helical cladding modes can be suppressed

---

[2] Assuming that the wavelength dependency of the refractive index difference is negligible.

[3] Assuming that the diameter of the first cladding is in the range of hundreds of µm and the diameter of the core is around 10 µm.

by introducing non-circular or off-centered cladding geometries. The non-uniform symmetrical structures increase the inter-mode coupling and thus support the conversion of such pure helical modes into others that overlap with the core [64]. The introduction of stress rods next to the core achieves a similar effect.

Large-mode-area fibers

Large-mode-area (LMA) or few-mode fibers are a hybrid form of a multi-mode and single-mode fiber. LMA fibers are typically used in applications that require high power in the LP_{01} mode. Representative applications are short pulse amplification or high-power amplifiers. To withstand the associated high power levels, LMA fibers have large core diameters so that the intensity is reduced and the threshold for non-linearities or light-induced damage (LID, threshold power level: LIDT) is increased accordingly. The larger core diameter would result in a large V-number and must therefore be compensated by a low NA to maintain single-mode operation as can be seen from Eq. (2.20). However, achievable NAs are limited by the accuracy of the fabrication process. Additionally, the NA cannot be reduced arbitrarily because bending losses also increase with lower NAs [65]:

$$\alpha_{\text{bend,dB}} \approx 10 \log_{10} \left(1 + \frac{f(R, n_{\text{clad}})}{\text{NA}^2} \right). \tag{2.23}$$

The bending loss coefficient $\alpha_{\text{bend,dB}}$ is expressed in dB per m and $f(R, n_{\text{clad}})$ is a dimensionless function that depends on the bending radius R and the refractive index of the cladding. However, careful bending can be used to effectively suppress HOMs [66] because fiber modes with large diameter experience additional bending losses.
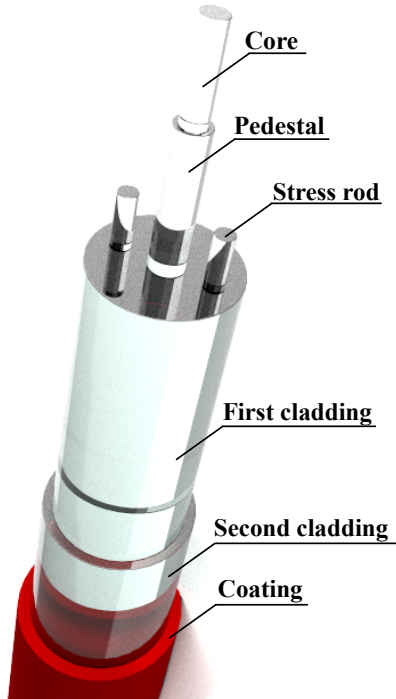
A reduction of the NA can also be hindered by additional dopants that raise the refractive index of the core such as phosphorus, Er^{3+} or Yb^{3+}. Some Er^{3+}:Yb^{3+} fibers are therefore made with an additional layer around the fiber core, denoted as *refractive index pedestal*, whose refractive index is tailored to achieve the desired NA [67].

Polarization-maintaining fibers

In fiber optics, random birefringence can cause significant cross-talk between orthogonal polarization modes, namely $LP_{mp,x}$ and $LP_{mp,y}$. The birefringence can be induced by impurities, stress or micro-bending and occurs unintendedly at random. The overall polarization therefore varies depending on the instant stress levels. As a result, standard fibers can show an unsatisfying degree of linear polarization and/or the polarization axis of a linearly polarized output beam can change in time for the following reason. The propagation constants of the $LP_{mp,x}$ and $LP_{mp,y}$ modes are equal in an unbent standard fiber due to its cylindrical geometry:

Figure 2.1.2: Computer-aided design (CAD) model of an optical PANDA fiber including the glass core, pedestal, stress rods (PANDA), first and second cladding as well as the coating.

$$\beta_{mp,x} = \beta_{mp,y}. \tag{2.24}$$

Hence, the light in the wrong polarization keeps its phase relation with the signal light during propagation. The power that is scattered in the wrong polarization therefore accumulates constructively over the entire fiber. High-birefringence fibers, denoted as PM fibers, have been developed to counteract this detrimental process. PM fibers have different refractive indices, namely $n_{\text{core,x}}$ and $n_{\text{core,y}}$, in x and y direction and thus different phase velocities along each transversal axis by design. A key parameter of a high-birefringence fiber is the beat length L_b over which one polarization experiences an additional phase shift of 2π:

$$L_b = \frac{\lambda}{n_{\text{core},x} - n_{\text{core},x}}. \tag{2.25}$$

The beat length is typically in the range of several mm and considerably shorter than the distances that are affected by the random cross-talk. The light that is cross-coupled at the position z_0 therefore interferes destructively with the light that is cross-coupled at $z_0 \pm L_b/2$. As a result, cross-talk over distances much larger than L_b can be avoided entirely. The birefringence is usually achieved by intentionally applying non-uniform stress to the fiber, for example via the inclusion of two glass rods opposite to each other made from different glass compositions (PANDA[4], bow-tie) or by using an elliptical core geometry. The polarization axis of the incoupled light must be aligned along or perpendicular to the birefringence axis to achieve the desired stability of the polarization.

2.2 Manufacturing of rare-earth doped optical fibers

Nowadays, commercially available optical fibers are a technologically refined product that imposes high expectations on purity and manufacturing accuracy. The production processes have been continuously improved to satisfy these quality demands and a variety of procedures were established. This section presents a brief overview on today's most popular manufacturing techniques. Furthermore, the most extensively studied dopants among the rare-earth family, i.e. Er^{3+} and Yb^{3+}, and their optical properties are introduced. The production process is divided into two steps: the preform preparation and the drawing process.

2.2.1 Preform preparation

First, the preform - a cylindrical glass rod with ultra-high purity - is produced. Typically, the preform has a diameter of tens of mm and is around 1 m-long with equivalent geometry, i.e. cladding-to-core ratio, to the final fiber [68, 61]. The choice of the preform is of significant importance because the composition of the glass host can significantly affect the performance of the final product, e.g. its absorption and scattering properties as well as the NA. The preform fabrication is based on the reactions of halides such as $SiCl_4$, $GeCl_4$, $POCl_3$, SiF_4 and BCl_3. The dominant reaction is an oxidation, here representatively written for the primary halide constituent $SiCl_4$:

$$SiCl_4 + O_2 \longrightarrow SiO_2 + 2\,Cl_2.$$
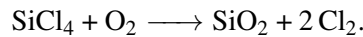
SiO_2 provides the bulk of the preform but is usually refined by the introduction of additional dopants. Al_2O_3 can act as a network modifier to open the silicate structure and enhance the rare-earth solubility [69, 70]. Also, GeO_2 and P_2O_5 are added to increase the refractive index of the glass material. The latter also ensures high uniformity and acts as control agent for the melt viscosity. The chemical reactions are typically conducted in an outside vapor deposition (OVD) [71], vapor axial deposition (VAD) [72] or modified chemical vapor deposition (MCVD) process.

Outside vapor deposition
In the OVD process, the gaseous chemicals are burned in a torch flame. The sub-microscopic glass

---

[4]A polarization-maintaining and absorption-reducing (PANDA) fiber is illustrated in Fig. 2.1.2.

14

particles of the soot are uniformly deposited on a constantly rotating Al_2O_3 rod. The required dopant compositions and refractive indices of the initially porous layers are controlled by the inflow of the gases. Residual gas entrapments and water residues are released through heating before the rod is sintered at $1500\,°C$. After the bulk has solidified, the Al_2O_3 rod is pulled out and the preform collapses into the final form [61].

Vapor axial deposition
The VAD method is a modification of the OVD technique but distinguishes by the fact that the reactants are deposited at the end of the target rod. During the VAD process, the preform is continuously pushed away from the heating zone. The product is consolidated as in the OVD process. With the VAD method, long preforms are feasible.

Modified chemical vapor deposition
In the MCVD process, the halide gas mixture is injected into a hollow silica tube that will later become the outer part of the cladding [61, 73, 74]. As a microwave cavity (IMCVD) or plasma torch (PCVD) traverses that tube, the gaseous reactants are deposited layer-wise on its inner surface. The process is driven by thermophoresis, a phenomenon that induces a net momentum to the reactants as a result of the temperature gradient between the center and wall of the tube. The refractive index of the current layer can be controlled by the mixture of the gaseous stream. Preforms that are made with the MCVD process do not contain gaseous or water residuals and the bake-out process is not required.

Solution doping technique
Rare-earth ions can be incorporated into a fiber's silicate lattice during the preform fabrication step by the solution-doping technique [75]. In a first step, the cladding preform is fabricated by the MCVD process but the inner silica layer remains unsintered i.e. porous. The porous layer is filled with an aqueous or alcoholic chloride solution where the corresponding rare-earth dopants are dissolved. The preform is purged with Cl_2 and O_2 and dried at $900\,°C$ so that the solution evaporates and only the rare-earth ions remain. Finally, the tube is sintered and collapsed into the actual preform. With this technique, rare-earth doping concentrations of up to several thousand parts per million are practicable prior to detrimental cluster formation and fluorescence quenching [72]. The absolute doping limit depends on the host material and dopant (see Sec. 2.2.3).

2.2.2 Fiber drawing

In a second step, the preform is heated and pulled to length to create the actual fiber. For this purpose, the preform is loaded at the top of a vertical drawing tower to take the advantage of the gravitational forces that pull down the fiber. The preform passes a furnace and is locally heated to $1950\,°C$ to $2250\,°C$ [61]. In the process, the preform shrinks in diameter and extends in length but keeps its relative core and cladding ratio. The process needs to be controlled by precise forces that are monitored and adjusted in real time. The geometrical properties can be controlled by the melting temperature and drawing speed that is typically several m per s [61]. A curable coating can be applied around the fiber immediately after cooling. The objective of the coating is to offer protection from mechanical damage and to shield the fiber from environmental disturbances. In some cases, the coating makes the low-index layer that guides the light in the cladding. The coating can consist of several temperature resistant acrylate layers. However, Lapointe *et al.* showed that coating temperatures exceeding $80\,°C$ can still harm the material and should be avoided entirely [76]. Other materials such as high-temperature acrylate (HTA), polyimide (PI), metals or carbon [77] may be used that reinforce stiffness, fracture toughness or damage tolerance of the fiber. The coating is illustrated in Fig. 2.1.2 in red to make it distinguishable from the cladding. At the end of the manufacturing process, a polymer jacket can be applied around the fiber that has merely protective purposes. The jacket's material

depends on the environment of the application but is typically made of (fluoro-)acrylate, polyvinyl chloride, polyethylene, polyurethane, polybutylene terephthalate or polyimide [78].

2.2.3 Rare-earth doping

Trivalent lanthanides, i.e. rare-earth ions, have particularly interesting optical properties because of their electronic structure[5] $[Xe]4f^{N-1}5s^25p^66s^0$. [Xe] represents the noble gas configuration of xenon. In this configuration, 1 and 2 electrons are missing in the $4f$ and $6s$ shells, respectively. As a result, the ions are trivalently charged. However, the remaining $N-1$ electrons in the $4f$ shell are effectively shielded by the outer $5s^25p^6$ electrons such that the $4f$-$4f$ transitions become relatively insensitive to external forces. The underlying physical mechanisms of the $4f$-$4f$ transitions are covered by the Judd-Ofelt theory at the atomic level [79, 80]. The Judd-Ofelt theory uses the static, free-ion and single configuration approximation[6] and models the electronic processes from a quantum point of view as a set of absorption and emission spectral structures.

Rare-earth dopants can be added to the fiber core during the manufacturing process as explained in Sec. 2.2 to interact with the guided light and trigger the $4f$-$4f$ transitions. The rare-earth ions Er^{3+} and Yb^{3+} are introduced in the following; the relevant energy levels, important optical transitions and the absorption and emission cross-sections are explained.

Er^{3+} doped fibers

The erbium(III)-ion, Er^{3+}, belongs to the rare-earth family and has a $[Xe]4f^{11}5s^25p^66s^0$ electron configuration. One of Er^{3+}'s $4f$-$4f$ transitions is located in the low loss window of fused silica around $1.5\,\mu m$ making Er^{3+} fibers good candidates as a laser-active material for cryogenically cooled GWDs [47, 81]. The key properties of Er^{3+} are summarized in this section.

The Er^{3+} energy levels $^4I_{15/2}$ (ground level), $^4I_{13/2}$ (laser-active level), $^4I_{11/2}$ and $^4I_{9/2}$ are shown in Fig. 2.2.1. Each level's energy degeneration is cancelled by the site-dependent electric field of the host matrix. Hence, the energy levels are not assigned to a distinct energy but split into Stark-manifolds. The strength of this effect depends on the host material and can thus vary from fiber to fiber. The individual Stark-levels, however, are affected by homogeneous broadening due to their finite lifetime via the energy-time uncertainty and thus merge to a broad energy band. The energy gap between the $^4I_{15/2}$ and $^4I_{13/2}$ energy levels is centered at $1.53\,\mu m$; the bandwidth of that transition, however, ranges from $\approx 1450\,nm$ to $\approx 1600\,nm$ as a result of the Stark-splitting, covering the S-, C- and L-band[7].

Fig. 2.2.2 shows the absorption and emission cross-sections of an Er^{3+} doped aluminosilicate fiber. Er^{3+} absorbs in the S-band and
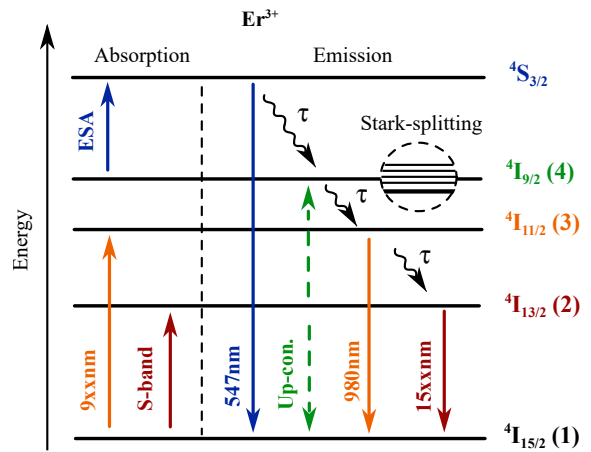
Figure 2.2.1: Energy level diagram of Er^{3+} including excited state absorption (ESA) to $^4S_{3/2}$ energy level. The $^4I_{15/2}$, $^4I_{13/2}$, $^4I_{11/2}$, $^4I_{9/2}$ and $^4S_{3/2}$ energy levels are shown in black, red, orange, green and blue. Relevant energy levels are enumerated from 1 to 4. Up-conversion is shown in dashed green and the non-radiative transitions are black. The detail illustrates the Stark-splitting.

---

[5]N numbers the sequence of the rare-earth ions.

[6]Static: influence of host ions is modelled as crystal field. Free-ion: influence of crystal field is treated as perturbation of the isolated ion. Single-configuration: electron interactions between configurations are neglected.

[7]The term *S-band* describes wavelengths from 1460 nm to 1530 nm, *C-band* from 1530 nm to 1565 nm and *L-band* from 1565 nm to 1625 nm.

emits in the C- and L-bands. Although the radiative transition from the $^4I_{13/2}$ to the $^4I_{15/2}$ level is forbidden by quantum mechanical parity consideration, it becomes available due to the following mechanisms [82]. If there is no inversion symmetry of the host field at the location of the ion, the wave functions of the $4f$-states contain components with opposite parity. Furthermore, vibrations of the host lattice also contribute to opposite parity components in the wave functions. The intensity of the transition then depends on the additional portions of opposite parity of the initial and final states. The fluorescence lifetime of the $^4I_{13/2}$ level is 8 ms in silica fibers [72, 83].

The S-band i.e. 1460 nm to 1530 nm has proven to be particularly advantageous in some aspects to pump the $^4I_{13/2}$ level; hence, remarkable achievements have been accomplished so far. Firstly, the quantum defect can be as low as a few percent. Secondly and as a result of that, the reduced heat load simplifies the thermal management. Thirdly, Raman lasers with high output power levels in the S-band (81 W, 32 % optical-to-optical efficiency [84]; 301 W, 42 % optical-to-optical efficiency [85]) and good beam quality have been demonstrated. Fujisaki *et al.* amplified a $^{13}C_2H_2$ (100 mW, 6 kHz) seed beam to 11.6 W output power (67.3 % optical-to-optical efficiency) by pumping an all-fiber Er^{3+} doped fiber amplifier (EDFA) at 1480 nm with a cascaded Raman-shifted Yb^{3+} fiber laser [86]. Supradeepa *et al.* also pumped the $^4I_{13/2}$ level of a 21 m-long Er^{3+} doped fiber with a cascaded Raman laser (142 W, 1480 nm) and achieved 101 W (71 % optical-to-optical efficiency) output power at 1554 nm [87]. Zhang *et al.* pumped a 15 m-long EDFL (LMA, Er60-20/125, *nLight Inc.*) at 1532 nm and demonstrated 88 W (59 % optical-to-optical efficiency[8]) at 1590 nm with off-the-shelf components [88].

The $^4I_{11/2}$ energy level can be pumped optically at 9xx nm. The transition to the laser-active $^4I_{13/2}$ level is a non-radiative multi-phonon transition. The lifetime of the $^4I_{11/2}$ level is 8 µs in silica fibers [83]; codoping with P_2O_4 reduces the lifetime [89] and consequently increases the population in the laser-active $^4I_{13/2}$ energy level. However, as stated in Sec. 2.2, P_2O_4 also raises the refractive index, thus limits the core's NA [90]. The non-radiative transition accounts to a quantum defect of $\approx 40\%$ and requires sophisticated thermal management in high-power systems. Kuhn *et al.* pumped an EDFA at 980 nm and reported 54 W output power (24 % optical-to-optical efficiency) with near-diffraction limited beam quality [91]. Later, the authors scaled the output power to 67 W (30 % optical-to-optical efficiency) with a 7.5 m-long LMA-EDF (Er60-40/140, *nLight Inc.*) pumped at 980 nm. Kuhn *et al.* also proved

Figure 2.2.2: Absorption (blue) and emission (red) cross-sections of an aluminosilicate Er^{3+} fiber compiled from *Liekki Application Designer* owned by *nLight Inc.* (Vancouver, WA, USA).

that photonic-crystal fibers (PCF, 40 µm core diameter, *NKT Photonics A/S*) pumped at 976 nm can generate more than 70 W (18.5 % optical-to-optical efficiency) output power with near-diffraction limited beam quality (TEM_{00} content of $\approx 80\%$, M^2 of ≈ 1) [92]. Kotov *et al.* optimized the Al_2O_3 and Er^{3+} doping content of a custom fiber by using core-pumped experiments and demonstrated a cladding-pumped EDFA (≈ 0.17 mol% Er_2O_3, ≈ 1.5 mol% Al_2O_3, 1 wt% fluorine) at 976 nm with 75 W (42 % optical-to-optical efficiency) output power [93].

Cooperative up-conversion arises from dipole-dipole interactions of proximate Er^{3+} ions in the $^4I_{13/2}$ energy level. One ion relaxes to the $^4I_{15/2}$ energy level and transfers the released energy to the
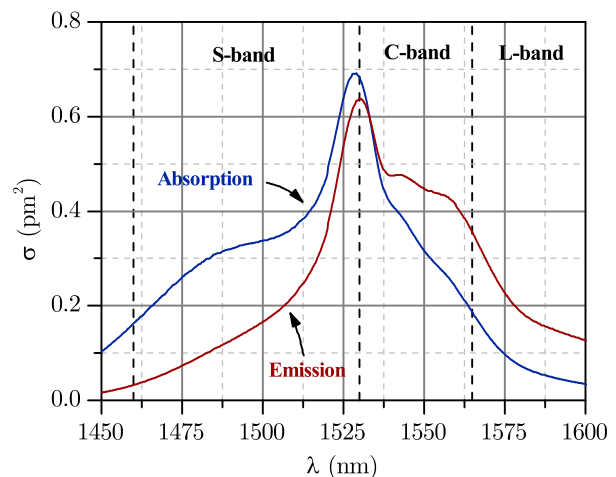
---

[8]The authors reported a record optical-to-optical efficiency of 69 % at lower power levels.

other, which is excited to the $^4I_{9/2}$ energy level. The transition from the $^4I_{9/2}$ to the $^4I_{11/2}$ energy level is radiation-free, which means that a considerable amount of energy is released in the form of heat and dissipated in the bulk. As a result, up-conversion effectively depletes the $^4I_{13/2}$ energy level and therefore limits the power scaling capacity of Er^{3+} doped fibers. On top of that, excited state absorption from the $^4I_{9/2}$ energy level to the $^4S_{3/2}$ energy level can further degrade the optical efficiency. The backtransition to the $^4I_{15/2}$ level is linked to the emission of a 547 nm photon, which gives Er^{3+} its characteristic green glow [94]. The up-conversion rate W_{up} (ions per s) depends on the mean distance of excited ions and is proportional to the squared population of the $^4I_{13/2}$ energy level:

$$W_{up} = C_{up} \cdot N^2_{\left(^4I_{13/2}\right)}. \tag{2.26}$$

C_{up} is the up-conversion coefficient and can be computed from the total Er^{3+} doping concentration:

$$C_{up} = C^0_{up} + k \left(N_{Er} - N^0_{Er} \right). \tag{2.27}$$

The parameters $C^0_{up} = 3.5 \cdot 10^{-24}$ m^{6}s^{-1}, $k = 2.41 \cdot 10^{-49}$ m^{9}s^{-1} and $N^0_{Er} = 4.4 \cdot 10^{25}$ m^{-3} are fit coefficients from an exemplary Er^{3+} doped fiber [95]. Up-conversion is particularly limiting when the detrimental cluster tendency of Er^{3+} during the manufacturing process is considered because the inter-ion distance in such Er^{3+} clusters shrinks significantly and the up-conversion probability becomes far more likely [96]. This phenomenon is called inhomogeneous up-conversion. Because of the up-conversion issue and Er^{3+}'s comparably low absorption at 9xx nm, power scaling of purely Er^{3+} doped fibers remains limited. The following section introduces Er^{3+}:Yb^{3+} codoped fibers; Yb^{3+} enhances the Er^{3+} solubility and increases the fiber's absorption at 9xx nm.

Er^{3+}:Yb^{3+} codoped fibers

The ytterbium(III)-ion, Yb^{3+}, has the electronic configuration $[Xe]4f^{13}5s^25p^66s^0$ and is one of the most versatile rare-earth dopants of silica glasses. Fig. 2.2.3 shows the energy level diagram of an Er^{3+}:Yb^{3+} doped fiber; the relevant Yb^{3+} energy levels are denoted as $^2F_{7/2}$ and $^2F_{5/2}$. The energy levels are non-degenerated but Stark-manifolds as a result of the different local electric field of the amorphous host. The fluorescence lifetime of the $^2F_{5/2}$ level is around 1 ms in silica fibers [72].
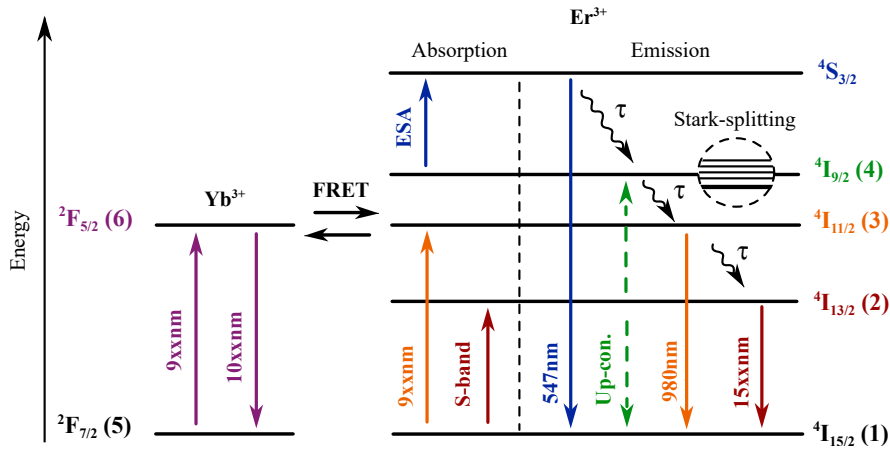
Figure 2.2.3: Energy level diagram of Er^{3+}:Yb^{3+}. The $^2F_{7/2}$ and $^4I_{15/2}$ levels are shown in black; the $^2F_{5/2}$, $^4I_{13/2}$, $^4I_{11/2}$, $^4I_{9/2}$ and $^4S_{3/2}$ levels are shown in purple, red, orange, green and blue including excited state absorption (ESA) to the $^4S_{3/2}$ level. Relevant energy levels are enumerated from 1 to 6. The arrows indicate the radiative transitions; up-conversion is shown in dashed green and the non-radiative transitions are black. The detail illustrates the Stark-splitting.

Fig. 2.2.4 shows the effective emission and absorption cross-sections of Yb^{3+} covering wavelengths from 850 nm to 1100 nm. Yb^{3+} has a sharp absorption peak at 976 nm; a broader absorption peak

emerges at $\approx 920\,$nm. The absorption cross-sections of Yb^{3+} are approximately ten times larger at 976 nm compared to Er^{3+}'s at that wavelength. Yb^{3+}'s emission cross-sections also peak at 976 nm but provide broad emission around 1030 nm.

Figure 2.2.4: Absorption (blue) and emission (red) cross-sections of an Er^{3+}:Yb^{3+} fiber compiled from *Liekki Application Designer* owned by *nLight Inc.* (Vancouver, WA, USA).
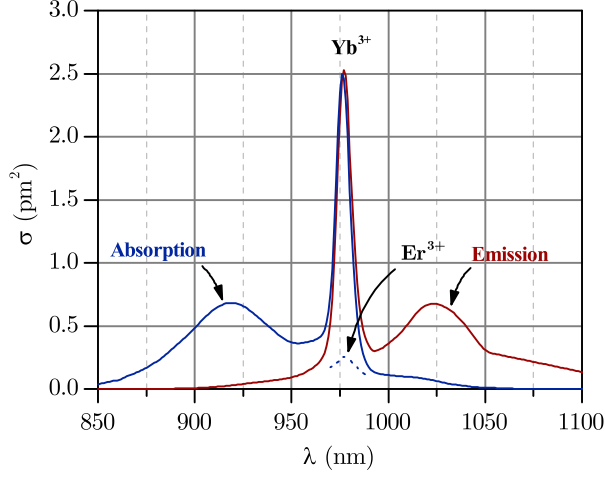
Yb^{3+} is often added to Er^{3+} fibers for three reasons: firstly, Yb^{3+} can be effectively embedded in the Er^{3+} doped lattice because the ion radii are similar ($r_{Yb}/r_{Er} \approx 0.98$ [97]).

Secondly, Yb^{3+} increases the solubility of Er^{3+} and prevents cluster formation. Hence, inhomogeneous up-conversion can be avoided and higher Er^{3+} doping concentrations become feasible.

Thirdly and most important, the absorption of Er^{3+} is relatively low at 9xx nm; and technical optimization of the fiber parameters to compensate Er^{3+}'s low absorption are not feasible for the given reasons. For instance, pure Er^{3+} silica fibers cannot simply be doped higher because such fibers would typically suffer from cluster formation and inhomogeneous up-conversion. Also, the choice of a longer fiber would trigger non-linear effects and overly large core sizes can degrade the beam quality. As a solution, Snitzer *et al.* introduced Yb^{3+} as a sensitizer [49]; the Yb^{3+} ions act as an absorption agent for the pump light but transmit the energy instantaneously to proximate Er^{3+} ions in the $^4I_{15/2}$ level. The fact that the associated Yb^{3+} cross-sections are one order of magnitude larger compared to Er^{3+} and that Yb^{3+} can be doped in larger quantity ensures that the pump light is mainly absorbed by the Yb^{3+} ions. The transfer mechanism is a dipole-dipole interaction called Förster-resonance-energy-transfer (FRET) process. The ion that provides the energy, here Yb^{3+}, is called the donor, while the one that receives the energy, here Er^{3+}, is called the acceptor. In this case, Yb^{3+} qualifies as a donor because several Yb^{3+} ions can surround each Er^{3+} ion, which increases the transfer probability. Förster found that the efficiency of the Yb^{3+}-to-Er^{3+} energy transfer, denoted as η, depends on the 6th power of the donor to acceptor distance $r_{Yb\text{-}Er}$ and can be expressed as [98]:

$$\eta = \frac{R_0^6}{R_0^6 + r_{Yb\text{-}Er}^6} \tag{2.28}$$

with

$$R_0^6 = \frac{9\ln(10)\kappa^2\Phi_D J}{128\pi^5 n^4 N_A}. \tag{2.29}$$

Here, κ is given by the dipole orientation of the donor and acceptor and varies between 0 and 2. Φ_D is the quantum yield of the donor in absence of the acceptor, n the refractive index and N_A the Avogadro constant. J is the overlap integral of the donor's emission and the acceptor's absorption cross-sections:

$$J = \int f_D(\lambda)\epsilon_A(\lambda)\lambda^4\partial\lambda. \tag{2.30}$$

$\epsilon_A(\lambda)$ is the molar extinction coefficient of the acceptor and $f_D(\lambda)$ the fluorescence spectrum of the donor. The latter is normalized on the wavelength scale:

$$f_D(\lambda) = \frac{F_D(\lambda)}{\int F_D(\lambda)\partial\lambda}. \tag{2.31}$$

19

The rate of the Yb^{3+}-to-Er^{3+} energy transfer, denoted as W_{FRET} (ions per s), is assumed to be proportional to the populations of the $^2F_{5/2}$ and $^4I_{15/2}$ energy levels [99]. R is the linear coefficient:

$$W_{FRET} = R \cdot N_{\left(^4I_{15/2}\right)} N_{\left(^2F_{5/2}\right)}. \tag{2.32}$$

The value of R can be approximated from the Yb^{3+} doping concentration:

$$R = R^0 + k\left(N_{Yb} - N_{Yb}^0\right), \tag{2.33}$$

where $R^0 = 1.0 \cdot 10^{-22}\,\text{m}^6\text{s}^{-1}$, $k = 4.00 \cdot 10^{-49}\,\text{m}^9\text{s}^{-1}$ and $N_{Yb}^0 = 1.0 \cdot 10^{25}\,\text{m}^{-3}$ are the linear fit parameters [100]. The probability of the Er^{3+}-to-Yb^{3+} backtransfer is significantly lower and often neglected because the non-radiative lifetime of Er^{3+}'s $^4I_{11/2}$ energy level is relatively short ($\approx 8\,\mu s$). Exemplarily, Jebali et al. reported an Er^{3+}:Yb^{3+} codoped fiber laser with 264 W ($\approx 74\,\%$ optical-to-optical efficiency) output power pumped at 1535 nm in the cladding of an 18 m-long fiber [101].

The Yb^{3+}-to-Er^{3+} energy transfer requires Er^{3+} partners in the $^4I_{15/2}$ energy level. The process can therefore saturate if the amplifier is pumped too hard. As a consequence, Yb^{3+} ions accumulate in the $^2F_{5/2}$ energy level and the unsaturated gain in the $1.0\,\mu m$-band can lead to excessive ASE (see Sec. 2.3.2). The Yb^{3+} ASE often restricts further power scaling of the amplifier. For example, Jeong et al. demonstrated an EYDFA with 151 W (33 % slope efficiency) output power and near diffraction-limited beam quality (M^2 of ≈ 1.1) [102]. The amplifier was implemented with a 30/650 multi-mode fiber with D-shaped inner cladding. The amplifier was tunable over the C-band but encountered Yb^{3+} ASE above 100 W output power. Jeong et al. also achieved 297 W (40 % optical-to-optical efficiency) laser power but had to accept Yb^{3+} colasing [103]. Bai et al. used a 25/300 PM fiber and achieved 56.4 W output power but had to implement three amplification stages [104]. Creeden et al. showed that the Yb^{3+} ASE can be significantly suppressed by pumping the amplifier off-peak around 940 nm (see Sec. 2.3.2). With this technique, 207 W (49.3 % optical-to-optical efficiency) output power at 1560 nm was demonstrated without notable Yb^{3+} ASE [55]. Furthermore, Varona et al. proved that off-peak pumped EYDFAs fulfil some of the stringent requirements of GW detection [56].

The heat coming from the quantum defect of the 9xx nm pump band poses another obstacle. For example, Alegria et al. demonstrated less than 3.2 % power in the ASE at 60 W using a multi-mode fiber but faced thermal fiber damage above 83 W output power [105]; fiber coating degradation originating from the high thermal load was identified as the failure mechanism. Matniyaz et al. partly solved the heat issue by immersing a 6.4 m long fiber (LMA-EYDF-25P/300-HE, Nufern Inc.) in water and reported 302 W (56 % optical-to-optical efficiency) output power at 1562 nm [57].

2.3 Non-linear processes in optical fibers

Non-linear processes that can limit the amplified power are described in the following. The electric field of a light wave couples to the polarization of a material that it is propagating through - in this case the fiber core - by forcing the electron shells out of neutral position. In linear optics, the polarization can be described with the model of a Lorentzian oscillator as a damped harmonic oscillator with the electric field as a driving force [106]. In this case, the polarization

$$\vec{P} = \epsilon \chi^{(1)} \vec{E} \tag{2.34}$$

depends linearly on the electric field amplitude; ϵ is the vacuum permittivity and the first-order susceptibility $\chi^{(1)}$ is analogous to the spring constant in Newtonian mechanics. For large amplitudes as found in ultra-short pulses or optical fibers, the linear dependency is no longer applicable and non-linear terms have to be considered. As a consequence, the polarization now contains terms of higher order and is given as a series expansion [107]:

$$\vec{P} = \epsilon\left(\chi^{(1)}\vec{E} + \chi^{(2)}\vec{E}^2 + \chi^{(3)}\vec{E}^3 + ...\right). \tag{2.35}$$

The susceptibility of n-th order $\chi^{(n)}$ is an $n + 1$ dimensional tensor whose values decrease with order and are hence only relevant at high intensities. However, the linear relationship from linear optics is once again recovered for low intensities. A number of non-linear phenomena such as the non-linear refractive index, which plays a crucial role in the theory of SBS, are derived from the higher-order terms. Beyond that, other non-linear phenomena such as Raman scattering or four-wave-mixing are of significant importance but not relevant for this work and are thus not discussed herein.

2.3.1 Stimulated Brillouin scattering

Brillouin scattering was first theoretically predicted in 1922 [108] and refers to the phenomenon that photons can scatter inelastically from acoustic phonon modes i.e. quantized states of lattice vibrations [109]. Spontaneous Brillouin scattering describes the conversion of a photon into a phonon and a frequency-shifted photon with respect to the law of energy conservation. Hence, the frequency shift is towards lower photon energies and accordingly denoted as Stokes:

$$\omega_{\text{Stokes}} = \omega_s - \Omega. \tag{2.36}$$

Here, ω_{Stokes} and ω_s are the Stokes and signal frequencies and Ω is the phonon frequency. The phonon frequency depends on the acoustic velocity v_A and is in the order of $10\,\text{GHz}$ to $20\,\text{GHz}$ in fused silica[9]. The spectra of two optical fibers obtained by self-heterodyne detection are exemplarily shown in Fig. 2.3.1.
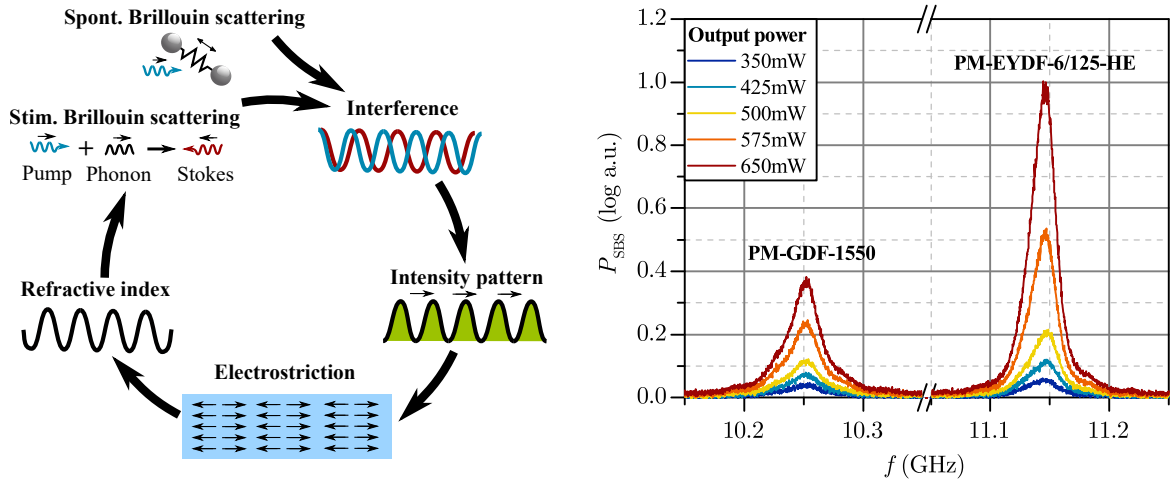
Figure 2.3.1: Left: scattering mechanism of SBS. The Stokes and signal waves interfere and form a moving intensity pattern that modulates the refractive index by electrostriction. The process becomes self-stimulated above the SBS power threshold. The process is initiated by spontaneous Brillouin scattering. Right: normalized heterodyne spectrum of output beam from an EYDFA at different output powers (see legend). The amplifier was seeded at 1556 nm and backward pumped at 940 nm. The fibers PM-EYDF-6/125-HE and PM-GDF-1550 from *Nufern Inc.* were used. The center frequency of the heterodyne spectrum was affected by the different dopant compositions and acoustic velocities of the fibers.

The scatter efficiency, here denoted as η, also depends on the acoustic velocity and can be expressed as follows:

$$\eta \approx 2\nu_A \frac{\omega_p n}{c} \sin \frac{\phi}{2}, \tag{2.37}$$

being c the speed of light, n the refractive index and ϕ the scattering angle. The efficiency vanishes at $\phi = 0$ but peaks at $\phi = \pi$ as per Eq. (2.37); Brillouin scattering therefore usually occurs in backward

---

[9]Acoustic velocity in fused silica is $v_{\text{Si}} = 5968\,\text{ms}^{-1}$ [110].

direction. However, forward scattering from transverse acoustic phonon modes was also observed in reference [111] and is referred to as guided acoustic wave Brillouin scattering.

If pumped hard enough, the scattering process becomes stimulated with a fixed phase relation between the scattered photons denoted as stimulated Brillouin scattering (SBS). SBS is an often undesired effect in high-power amplifiers as considerable amounts of signal power can be lost in the process. Moreover, the process imprints excess power noise on the signal [112]. The mechanism is shown in Fig. 2.3.1; the signal and Stokes waves interfere and form an intensity pattern, whose (anti-)nodes move in forward direction. The interference pattern modifies the refractive index of the glass by electrostriction, which describes the tendency of a material to change its density ρ through the interaction with an electric field $\vec{E}$:

$$\Delta\rho = \frac{1}{2}\epsilon_0\rho C\gamma_e\langle\vec{E}\cdot\vec{E}\rangle, \tag{2.38}$$

where γ_e is the electrostrictive constant, C the compressibility of the material and ϵ_0 the permittivity of vacuum. $\Delta\rho$ is related to the 3$^{\text{rd}}$-order susceptibility $\chi^{(3)}$ as shown in reference [107] that results in

$$\chi^{(3)} = \frac{1}{3}\epsilon_0 C\gamma_e^2. \tag{2.39}$$

On the other hand, $\chi^{(3)}$ is also related to the non-linear refractive index n_2 [107]:

$$n_2 = \left(\frac{3}{4}n_0^2\epsilon_0 c\right)\chi^{(3)}. \tag{2.40}$$

The product $\langle\vec{E}\cdot\vec{E}\rangle$ is therefore linked to the refractive index. This means that the moving interference pattern modifies the local refractive index. The index modification moves in the same direction as the signal and acts as a Bragg reflector. As a result, more light is reflected into the Stokes wave and the process is amplified. The SBS power threshold can be defined as the signal power at which the SBS power equals the signal output power[10]. The SBS threshold can be approximated by the following equation as shown in reference [114]:

$$P_{\text{thr}} \approx 21\frac{K_{\text{B}}A_{\text{eff}}}{L_{\text{eff}}g_0}. \tag{2.41}$$

A_{eff} and L_{eff} are the effective area and length of the fiber with

$$L_{\text{eff}} = \left[1 - \exp\left(-\alpha L\right)\right]/\alpha, \tag{2.42}$$

where L is the physical fiber length. K_{B} is a dimensionless correction factor as described in reference [72]. The scatter probability scales with the interaction length and is thus significant in optical fibers. However, the SBS power threshold also scales with the effective mode area thus making LMA fibers an excellent choice to increase the SBS power threshold. The propagation of signal and SBS power can be described by the following coupled differential equations:

$$\frac{\partial P_s}{\partial z} = -\frac{\gamma}{A_{\text{eff}}}\mathcal{L}(\nu, T)P_s P_{\text{SBS}} - \alpha P_s \tag{2.43}$$

and

$$\frac{\partial P_{\text{SBS}}}{\partial z} = -\frac{\gamma}{A_{\text{eff}}}\mathcal{L}(\nu, T)P_s P_{\text{SBS}} + \alpha P_{\text{SBS}}. \tag{2.44}$$

---

[10]Note that different definitions of the threshold power are used in practice. For example, the onset of excess noise at MHz frequencies can also represent a reasonable power threshold as argued in reference [113].

22

Here, $P_s(z)$ is the signal power, $P_{SBS}(z)$ the SBS power, γ is the Brillouin gain coefficient, α the bulk absorption and $\mathcal{L}(\nu, T)$ a Lorentzian-shaped envelope function, i.e. gain spectrum. The center frequency of $\mathcal{L}(\nu, T)$ is located relative to the signal at

$$\Delta\nu = \frac{2n\nu_A}{\lambda_s} + c_f \Delta T \tag{2.45}$$

and scales linearly (coefficient: c_f) with the temperature T [113]. Many applications in fiber optics try to prevent SBS by artificially manipulating $\mathcal{L}(\nu, T)$ so that the gain spectrum in the rear-end of the fiber is spectrally detuned from the Stokes waves that are generated in the front-end. For this purpose, temperature gradients can be applied to the fiber [115] or mechanical stress can be induced [116]. Also, pump phase modulation [117] and doping variations [118] have been successfully demonstrated to mitigate SBS. The bandwidth of $\mathcal{L}(\nu, T)$ depends on the phonon absorption of the host material, i.e. phonon lifetime. If the signal linewidth exceeds the SBS bandwidth, the scattering efficiency decreases significantly because the Bragg grating blurs out and individual frequency components of the Stokes wave do not affect each other. As a consequence, SBS is only relevant for sub-MHz signals in silica glasses[11].

2.3.2 Amplified spontaneous emission

Amplified spontaneous emission (ASE) describes the amplification of the luminescence from a laser gain material, for example from a laser crystal or a rare-earth doped fiber. The ASE can deteriorate the power scaling capacity of the device and/or dominate the noise figure. The ASE can even damage the device, e.g. through light-induced damage on coatings or end faces, because small back reflections may trigger Q-switching or the overall power levels of the ASE exceed the LIDT. Although the ASE is not caused by the susceptibility of the material, it typically scales non-linearly with the signal power and is thus listed in this chapter.

ASE is initiated by spontaneous emission, a random process that describes the transition between an excited energy level 2 and a lower energy level 1. The atom or molecule releases the quantized energy by emitting a photon. The photon wavelength corresponds to the energy difference of the levels:

$$\hbar\omega = E_2 - E_1. \tag{2.46}$$

Here, $\hbar$ is the reduced Planck constant and ω the photon frequency; E_1 and E_2 are the associated energies of the participating levels. The process occurs without external stimulus and the direction of the wave vector $\vec{k}$ is arbitrary i.e. isotropic emission. The probability of the spontaneous transition depends only on the quantum system and is described by the Einstein coefficient A_{21} [119]:

$$A_{21} = \frac{2\hbar}{\pi c^3} \omega^3 B_{21}. \tag{2.47}$$

The A_{21} coefficient is related to Einstein's B_{21} coefficient but is more dominant at short wavelengths. The emission rate W_{21} (transitions per s) scales proportionally with the population N_2 of the upper level:

$$W_{21} = \frac{N_2}{\tau_{21}}. \tag{2.48}$$

$\tau_{21} = A_{21}^{-1}$ is the fluorescence lifetime of the upper level. Moreover, the upper energy level can provide gain for the ASE via stimulated emission:

$$\frac{\partial P_{ASE}(z)}{\partial z} = (N_2 \sigma_{em} - N_1 \sigma_{abs}) P_{ASE}(z). \tag{2.49}$$

---

[11]SBS bandwidth is tens of MHz in silica glass.

Here, $P_{\mathrm{ASE}}(z)$ is the ASE power; N_1 and N_2 are the populations in the lower and upper energy levels. The coefficients σ_{abs} and σ_{em} are the corresponding absorption and emission cross-sections.

In an optical fiber, the ASE that aligns along the z-axis within the fiber's NA can extract large amounts of energy during propagation. The process depletes the excited energy levels - namely the $^4\mathrm{I}_{13/2}$ level of Er^{3+} and the $^2\mathrm{F}_{5/2}$ level of Yb^{3+} - so that ASE is generated at the expense of output power. Moreover, the randomness of the spontaneous process leads to excess power noise. Additionally, the ASE's electric field can beat with the electric field of the signal and contribute to the power noise of the laser system because of the arbitrary phase relation.

$\mathbf{Yb^{3+}}$ ASE suppression

ASE can arise in the 1.0 μm-band from the laser-active $^2\mathrm{F}_{5/2}$-to-$^2\mathrm{F}_{7/2}$ transition of the Yb^{3+} ions. The Yb^{3+} ASE can deteriorate the optical-to-optical efficiency (see references [102] and [103]) which exacerbates further power scaling of Er^{3+}:Yb^{3+} doped fibers. However, the Yb^{3+} ASE can be suppressed by reducing the population in the $^2\mathrm{F}_{5/2}$ energy level. The following techniques have been proposed.

Firstly, sufficiently high seed power stimulates Er^{3+}'s $^4\mathrm{I}_{13/2}$-to-$^4\mathrm{I}_{15/2}$ transition. Hence, the population in the $^4\mathrm{I}_{15/2}$ energy level increases and more Er^{3+} ions become available to participate in the Yb^{3+}-to-Er^{3+} energy transfer. The transfer process reduces the population in Yb^{3+}'s $^2\mathrm{F}_{5/2}$ energy level; the Yb^{3+} ASE is therefore suppressed.

Secondly, the Yb^{3+} ASE can be suppressed by co-seeding the amplifier with an auxiliary seed with a wavelength in the Yb^{3+} emission band. This technique has been experimentally demonstrated in references [120, 121, 122, 123] and numerically investigated in references [99, 124]. The auxiliary signal can be removed at the output by wavelength-selective filtering. Alternatively, the amplifier can be configured to reabsorb the co-seed along the fiber [123].

Thirdly, Er^{3+} can be pumped directly in the laser-active $^4\mathrm{I}_{13/2}$ energy level to avoid the Yb^{3+} ASE without waiving the increased Er^{3+} solubility coming from the Yb^{3+} codoping. This technique was successfully demonstrated in reference [101].

Fourthly, the Yb^{3+} ASE can be suppressed by pumping the amplifier off-peak, e.g. at 915 nm or 940 nm. Off-peak pumping lowers the pump absorption per unit length; thus, the absorbed pump energy is distributed more homogeneously along the fiber and bottlenecking of the Yb^{3+}-to-Er^{3+} energy transfer is prevented. Hence, the Yb^{3+} ions cannot accumulate in the $^2\mathrm{F}_{5/2}$ energy level. The effectiveness of off-peak pumping has been experimentally demonstrated in references [55, 56] at 940 nm, in reference [57] at 915 nm and in references [125, 126] at 1018 nm. A numerical analysis of different pump wavelengths can be found in Chap. 3. The use of a smaller pump-to-core overlap is a similar approach to reduce the absorption per unit length.

Chapter 3

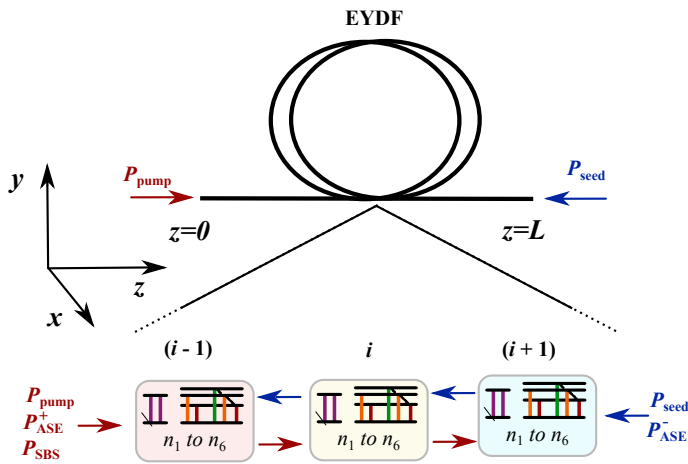# Pump wavelength dependence of ASE and SBS in single-frequency EYDFAs

Figure 3.0.1: Computation principle of the FEM solver. The energy level populations and transition rates in the i-th fiber node were calculated from the optical power levels. Vice versa, the optical power levels were calculated from the power propagation equations. When the algorithm reached the fiber end, the calculated power levels were kept and the power levels in reverse direction were computed. The procedure was repeated until the solution converged. A detailed description is given in the text.

Yb^{3+}-free EDFAs require long gain fibers because of Er^{3+}'s low pump absorption at 9xx nm. Furthermore, the achievable output power is limited by pair induced quenching as a result of Er^{3+}'s cluster tendency. Yb^{3+} sensitizing eases the power scaling process due to Yb^{3+}'s larger pump absorption and because higher Er^{3+} doping levels become possible without clustering. The Yb^{3+} ions, however, can emit detrimental ASE in the 1.0 μm-band. The Yb^{3+} ASE can derogate the optical efficiency or cause fiber damage by uncontrolled Q-switching. The Yb^{3+} emission can be avoided by pumping at 1480 nm. The 1480 nm pump band, however, waives the higher 9xx nm absorption, and thus also requires longer gain fibers for sufficient pump absorption. The lower nonlinear thresholds exacerbate power scaling of single-frequency signals; suitable pump sources around 1480 nm (see Sec. 2.2.3) suffer from either complexity [87] or low brightness [101].

In recent years, different techniques have been tested to suppress the Yb^{3+} ASE such as material optimization, auxiliary seeding [120, 99, 124, 121, 122, 123] or wavelength-selective filtering [99, 127]. In particular, off-peak pumping found considerable popularity because it maintains the preferred 9xx nm absorption band without adding complexity. In 2016, Creeden *et al.* demonstrated 207 W output power at 1560 nm with 49.3 % optical-to-optical efficiency by pumping at 940 nm [55]. In 2017, Varona *et al.* confirmed that off-peak pumped EYDFAs seem compliant with the requirements of GWD laser sources at 1.55 μm [56]. In 2020, Matniyaz *et al.* achieved the present record output power of 302 W with 58.3 % optical-to-optical efficiency by pumping at 915 nm [57]. Off-peak pumping, however, also requires longer gain fibers; thus, SBS may also prevent power scaling of single-frequency signals at some point. For example, Wang *et al.* observed SBS around 18 W out-

put power[1] from an 11.5 m-long 10/128 single-mode fiber pumped at 1018 nm [126]. Until recently, a systematic study on the ASE suppression and SBS mitigation trade-off and the pump wavelength of the EYDFA was missing.

The maximum ASE- and SBS-free output power is analyzed in this chapter for pump wavelengths from the 9xx nm pump band. The 9xx nm pump band was segmented in *in-band* and *off-band* wavelengths. The simulated EYDFA was limited by the Yb^{3+} ASE if pump wavelengths from the *in-band* regime were used. In contrast, the simulated EYDFA was limited by SBS if pump wavelengths from the *off-band* regime were used. A comparison of the pump wavelengths of 940 nm and 976 nm is presented; the power dependence of the Yb^{3+}-to-Er^{3+} transfer efficiency is discussed. Moreover, the pump power dependency of the SBS power is shown and an adaptation of the SBS power threshold formula to active Er^{3+}:Yb^{3+} fibers is discussed. This chapter concludes with the summary of the key findings. The results have been partly published in reference [128].

3.1 FEM model

The pump, signal, ASE and SBS power levels, labelled as $P_p(z)$, $P_s(z)$, $P_{ASE}^{\pm}(z)$ and $P_{SBS}(z)$, were numerically calculated by an in-house developed finite-element-method (FEM) solver from the rate and power propagation equations. The simulation parameters are summarized in Tab. 3.1. An overview of the computation principle including the power propagation directions is shown in Fig. 3.0.1 and described in the following.

Table 3.1: Summary of the simulation parameters.

Parameter	Value	Ref.	Parameter	Value	Ref.
λ_p	860 nm...1000 nm		T_0	298 K	
P_{pump}	variable		h	$10\,\mathrm{Wm^{-2}K^{-1}}$	[129]
λ_s	1556 nm	[56]	k	$1.38\,\mathrm{Wm^{-1}K^{-1}}$	[129]
P_{seed}	0.1 W...2.0 W		N_{Yb}	$3.53\times10^{26}\,\mathrm{m^{-3}}$	[99]
τ_{21}	10 ms	[99]	N_{Er}	$2.45\times10^{25}\,\mathrm{m^{-3}}$	[99]
τ_{32}	1 ns	[99]	r_{core}	12.5 µm	[130]
τ_{65}	1 ms	[131]	r_{clad}	150 µm	[130]
g_0	$5\times10^{-11}\,\mathrm{mW^{-1}}$	[72]	A_{core}	491 µm^2	[130]
Ω	58 MHz	[113]	NA	0.09	[130]
c_f	$2.25\,\mathrm{MHzK^{-1}}$	[113]	R_{63}	$5\times10^{-21}\,\mathrm{m^3s^{-1}}$	[95]
α_s	20 dB per km	[132]	$\Delta\lambda$	1 nm	
α_p	70 dB per km	[132]	R_{36}, C_{up}	0	

A typical LMA double-cladding 25/300 Er^{3+}:Yb^{3+} doped gain fiber with 0.09 NA was assumed. The fiber was orientated parallel to the z-axis and the fiber length L was segmented in equidistant nodes. A coupled 2- and 4-level system[2] was used to represent the energy levels of the Er^{3+} and Yb^{3+} ions at each node. The full energy level diagram can be found in Chap. 2.2.3. The populations of the $^4I_{15/2}$, $^4I_{13/2}$, $^4I_{11/2}$ and $^4I_{9/2}$ energy levels are labelled as n_1 to n_4. The populations of Yb^{3+}'s $^2F_{7/2}$ and $^2F_{5/2}$ energy levels are denoted as n_5 and n_6. The populations of the energy levels were normalized to reduce the computational cost:

$$1 = n_1 + n_2 + n_3 + n_4 \text{ and } 1 = n_5 + n_6. \tag{3.1}$$

Total Er^{3+} and Yb^{3+} doping concentrations of $2.45 \times 10^{25}\,\mathrm{m^{-3}}$ and $3.53 \times 10^{26}\,\mathrm{m^{-3}}$ were used as in reference [99]. The stimulated transition rates from energy level i to energy level j were determined

---

[1]The power threshold for SBS was substantially lower because of the smaller core area.

[2]The population of the $^4I_{9/2}$ level was set to zero as argued in the following.

by $P_\mathrm{p}(z)$, $P_\mathrm{s}(z)$, $P_{\mathrm{SBS},i}(z)$, $P^-_{\mathrm{ASE},i}(z)$ and $P^+_{\mathrm{ASE},i}(z)$:

$$W_{ij,\mathrm{s}}(z) = \frac{\Gamma_\mathrm{s}\lambda_\mathrm{s}\sigma_{ij}}{A_\mathrm{core}hc}P_\mathrm{s}(z), \quad W_{ij,\mathrm{ASE}}(z) = \frac{\Gamma_\mathrm{ASE}\sigma_{ij}}{A_\mathrm{core}hc}\left[\sum_i \lambda_{\mathrm{ASE},i}P^+_{\mathrm{ASE},i}(z) + \sum_i \lambda_{\mathrm{ASE},i}P^-_{\mathrm{ASE},i}(z)\right],$$

$$W_{ij,\mathrm{p}}(z) = \frac{\Gamma_\mathrm{p}\lambda_\mathrm{p}\sigma_{ij}}{A_\mathrm{core}hc}P_\mathrm{p}(z), \quad W_{ij,\mathrm{SBS}}(z) = \frac{\Gamma_\mathrm{s}\lambda_\mathrm{s}\sigma_{ij}}{A_\mathrm{core}hc}\sum_i P_{\mathrm{SBS},i}(z),$$

$$(3.2)$$

with core area A_core, pump, seed and ASE wavelengths λ_p, λ_s and $\lambda_{\mathrm{ASE},i}$, Planck constant h and speed of light c. The seed wavelength was 1556 nm as in reference [56]. The SBS wavelength can be approximated by $\lambda_\mathrm{SBS} \approx \lambda_\mathrm{s}$ because the Brillouin shift in fused silica glass is typically only $\approx 11.2\,\mathrm{GHz}$. The parameters σ_{ij} represent the associated cross-sections for absorption if $i < j$ or emission if $i > j$. The used cross-sections are plotted in Fig. 2.2.2 and Fig. 2.2.4. The factor Γ expressed the overlap of the LP_{01} mode with the doped core according to the standard confined-doping model (SCD) [133, 132]. The SCD neglects the radial energy level population in the xy-plane by approximating the light-to-dopant overlap via averaging across the illuminated area. Indeed, the SCD is only valid for doping areas substantially smaller than the LP_{01} mode-field area. Although this condition is not entirely fulfilled in LMA fibers, Canat *et al.* argued that the error introduced by the use of the SCD is in the range of other uncertainties for example from the cross-sections or doping concentrations [132]. The SCD is therefore reasonable to apply to reduce the computational cost of radial integration [132]. Γ was calculated with the core radius r_core and Gaussian mode radius ω for step-index fibers as shown by Marcuse [134]:

$$\Gamma = 1 - \exp\left(-2\frac{r^2_\mathrm{core}}{\omega^2}\right), \qquad \omega = r_\mathrm{core}\left(0.65 + \frac{1.619}{V^{1.5}} + \frac{2.879}{V^6}\right). \qquad (3.3)$$

In cladding pumped configuration, Γ was rescaled by the core-to-cladding area ratio as shown by Han *et al.* [99]:

$$\Gamma_\mathrm{pump} = \frac{A_\mathrm{core}}{A_\mathrm{clad}}\Gamma. \qquad (3.4)$$

This approximation practically represents a close to homogeneous pump light distribution across the cladding area i.e. $\Gamma_\mathrm{pump} \approx A_\mathrm{core}/A_\mathrm{clad}$ but neglects HOMs of the pump light as well as helical cladding modes.

The Er^{3+} and Yb^{3+} ions were linked by the Förster energy transfer process with bidirectional energy transfer. The Yb^{3+}-to-Er^{3+} energy transfer coefficient was assumed to be $5 \times 10^{-21}\,\mathrm{m}^3\mathrm{s}^{-1}$ as in reference [95]. The population of the $^4\mathrm{I}_{11/2}$ energy level was computed to be less than 0.1 %; the backward energy transfer coefficient was therefore set to zero to ease the computation. Additionally, the inclusion of up-conversion only marginally affected the results because n_4 was also close to zero. The up-conversion coefficient was therefore also set to zero. The fluorescence lifetime from the energy level i to j is denoted with τ_{ij}. The lifetimes τ_{21}, τ_{65} and τ_{32} were approximated to 10 ms, 1 ms and 1 ns [99]. However, τ_{32} merely affected the computation if τ_{32} was far shorter than the effective lifetime of the $^4\mathrm{I}_{13/2}$ energy level. Equilibrium conditions were assumed so that $\partial n_i/\partial t = 0$ applied. The rate equations from Han *et al.* [99] were simplified to:

$$0 = W_{12,\mathrm{s}}n_1 - W_{21,\mathrm{s}}n_2 + W_{12,\mathrm{SBS}}n_1 - W_{21,\mathrm{SBS}}n_2 - \tau^{-1}_{21}n_2 + \tau^{-1}_{32}n_3, \qquad (3.5)$$

$$0 = R_{63}N_\mathrm{Yb}n_1n_6 - \tau^{-1}_{32}n_3, \qquad (3.6)$$

$$0 = W_{56,\mathrm{p}}n_5 - W_{65,\mathrm{p}}n_6 + W_{56,\mathrm{ASE}}n_5 - W_{65,\mathrm{ASE}}n_6 - \tau^{-1}_{65}n_6 - R_{63}N_\mathrm{Er}n_1n_6. \qquad (3.7)$$

The pump power evolving in the positive z direction was calculated by the following equation:

$$\frac{\partial P_\mathrm{p}(z)}{\partial z} = \Gamma_\mathrm{p}N_\mathrm{Yb}\left(\sigma_{65}n_6 - \sigma_{56}n_5\right)P_\mathrm{p}(z) - \alpha. \qquad (3.8)$$

The background loss α arises from scattering loss or bulk absorption of the fiber core. The background loss was assumed to be 20 dB per km for the signal light[3] and 70 dB per km for the pump light as per Canat *et al.* [132].

The FEM solver calculated the bidirectional propagation of the Yb^{3+} ASE in positive and negative z direction. The propagation direction is denoted in the following by the $\pm$ superscript. The following nomenclature is used because the seed propagated in negative z direction: the ASE in positive z direction is referred to as *backward* ASE and the ASE in negative z direction as *forward* ASE. The forward and backward directed Yb^{3+} ASE power levels, denoted as $P_{\text{ASE}}^{\pm}(z)$, were subdivided in hundred individual channels from 1000 nm to 1100 nm. Each channel represented the power in a 1.0 nm-wide spectral sub-band. The power in the i-th ASE channel $P_{\text{ASE},i}^{\pm}(z)$ was computed by the equation:

$$\frac{\partial P_{\text{ASE},i}^{\pm}(z)}{\partial z} = \pm \, \Gamma_{\text{ASE}} N_{\text{Yb}} \left(\sigma_{65} n_6 - \sigma_{56} n_5 \right) P_{\text{ASE},i}^{\pm}(z) \, ...$$

$$... \mp \alpha \pm N_{\text{Yb}} \frac{2hc^2}{\lambda_{\text{ASE},i}^3} \sigma_{65} n_6 \Delta\lambda \Gamma_{\text{ASE},i}. \tag{3.9}$$

The last term accounted for the spontaneous emission in the Yb^{3+} emission band [99]. It was reasonable to assume that the power levels of the Er^{3+} ASE would be very small because sufficient seed saturation was assumed in the simulations. As a consequence, the Er^{3+} ASE would contribute only marginally to the transfer rates and would not affect the steady-state population densities. This assumption was verified by the simulations such that the Er^{3+} ASE was not included in the model. The signal power evolving in negative z direction was computed by the following formula:

$$\frac{\partial P_{\text{s}}(z)}{\partial z} = \Gamma_{\text{s}} \left(\sigma_{12} N_{\text{Er}} n_1 - \sigma_{21} N_{\text{Er}} n_2 + \sum_i g_{\text{SBS},i} P_{\text{SBS},i}(z) \right) P_{\text{s}}(z) + \alpha. \tag{3.10}$$

The term $\sum_i g_{\text{SBS},i} P_{\text{SBS},i}(z)$ incorporated SBS induced signal depletion in the model. The SBS power, denoted as $P_{\text{SBS},i}(z)$, evolved in the direction opposite to the signal light, hence positive z direction. The SBS power was calculated by the following equation:

$$\frac{\partial P_{\text{SBS},i}(z)}{\partial z} = \left[\Gamma_{\text{s}} N_{\text{Er}} \left(\sigma_{21} n_2 - \sigma_{12} n_1 \right) + g_{\text{SBS},i} P_s(z) \right] P_{\text{SBS},i}(z) - \alpha. \tag{3.11}$$

The SBS power was subdivided in 101 sub-bands with 3 MHz spacing. The first sub-band was allocated at 11.2 GHz off-set relative to $f_{\text{s}} = c/\lambda_{\text{s}}$. The total power in the i-th SBS channel is denoted as $P_{\text{SBS},i}(z)$ and $g_{\text{SBS},i}$ is the gain coefficient associated to that channel. The scattering gain was assumed to be frequency dependent with a Lorentzian shaped spectral gain profile (see Sec. 2.3.1) and Brillouin peak gain of g_0, full-width-at-half-maximum bandwidth of Ω, temperature coefficient c_f and Brillouin shift v_{B} [72, 113]:

$$g_{\text{SBS},i} = \frac{1}{4 A_{\text{core}}} \frac{g_0 \Omega^2}{\left[\nu_i - \left(\nu_{\text{B}} + c_f \Delta T \right) \right]^2 + \frac{1}{4} \Omega^2}. \tag{3.12}$$

The parameters $g_0 = 5 \times 10^{-11}$ mW^{-1}, $\Omega = 58$ MHz and $c_f = 2.25$ MHzK^{-1} were chosen as in references [72] and [113]. The Brillouin shift of 11.2 GHz corresponds to an acoustic velocity of 5.960 ms^{-1} typical for fused silica. Brown *et al.* described in detail how the temperature gradient, denoted as ΔT, along the fiber core of a double-cladding fiber can be computed from the optical power levels and the quantum defect [129]:

$$T_{\text{core}}(r) = T_0 + \frac{Q_0 a^2}{4k} \left[2 \ln \left(\frac{r_{\text{clad}}}{r_{\text{core}}} \right) + \frac{2k}{r_{\text{clad}} h} \right] + \frac{Q_0 a^2}{4k} \left(1 - \left(\frac{r}{r_{\text{core}}} \right) \right). \tag{3.13}$$

---

[3]Note that the losses are substantially higher in the rare-earth doped fiber compared to its passive counterpart (passive fibers: 0.2 dB per km [61]).

The ambient temperature T_0 and the convective heat transfer coefficient h of the surrounding air were 298 K and 10^{-3} Wcm^{-2}K^{-1}, respectively. The thermal conductivity coefficient k was assumed to be 1.38×10^{-2} Wcm^{-1}K^{-1} [129]. The heat load per volume, labelled as Q_0, was calculated from the quantum defect and the transition rate from the $^4\mathrm{I}_{11/2}$ energy level to the $^4\mathrm{I}_{13/2}$ energy level:

$$Q_0 = \frac{2\pi N_{\mathrm{Er}} \hbar c n_{32}}{\tau_{32} \Delta V} \left(\frac{1}{\lambda_{\mathrm{p}}} - \frac{1}{\lambda_{\mathrm{s}}} \right). \tag{3.14}$$

The parameter $\Delta V = \pi \times r_{\mathrm{core}}^2 \times \Delta L$ is the core volume per node. The localized non-fluctuation source model was used to initiate the SBS process [113]. The non-fluctuation source model assumes a single noise photon that is scattered at the fiber end from a thermally excited phonon.

Optical feedback, for example from Fresnel reflections, was neglected in the model. This simplification is justified because the fiber ends are typically slanted to reduce back reflections. The following nomenclatures are introduced to ease the readability:

$$\textbf{SBS power: } P_{\mathrm{SBS}} = \sum_i P_{\mathrm{SBS},i}(z = L), \tag{3.15}$$

$$\textbf{ASE power: } P_{\mathrm{ASE}} = \sum_i \left(P_{\mathrm{ASE},i}^+(z = L) + P_{\mathrm{ASE},i}^-(z = 0) \right), \tag{3.16}$$

$$\textbf{Output power: } P_{\mathrm{out}} = P_{\mathrm{s}}(z = 0). \tag{3.17}$$

The boundary conditions i.e. $P_{\mathrm{p}}(z = 0) = P_{\mathrm{pump}}$, $P_{\mathrm{s}}(z = L) = P_{\mathrm{seed}}$ and $P_{\mathrm{ASE},i}^+(0) = P_{\mathrm{ASE},i}^-(L) = 0$ constituted a two-point boundary-value-problem. The solution was computed by processing the power propagation equations satisfying the steady-state conditions according to Eq. (3.5) to Eq. (3.7) by an in-house developed iterative FEM solver until the optical power levels changed less than 10 nW per iteration. A node spacing of 2.5 mm per m was used; for example, a node-to-node distance of 5 mm was used for a 2 m-long fiber. For each pump wavelength, the fiber length was optimized by the FEM solver to 10 dB pump light absorption and the pump power was increased until the total power in either the ASE or SBS was more than 1 % of the output power. Fig. 3.2.1 presents the maximum ASE- and SBS-free output power[4] together with the used fiber length and the related cross-sections. Albeit arbitrary, the 1 % criterion is representative for practical applications because the energy level populations that are associated to it may already be enough to cause significant parasitic lasing from small back reflections. It was furthermore found that the simulated power limit is virtually independent of the break criterion as a result of the non-linear behavior of ASE and SBS.

3.2 Power scaling limitations

The simulated power limits are shown in Fig. 3.2.1; the results are discussed in the following for pump wavelengths from the *in-* and *off-band* domain. The *in-band* regime contains pump wavelengths from 880 nm to 990 nm. The pump wavelengths from the *in-band* regime led to fiber lengths shorter than 5.1 m. The *off-band* regime corresponds to pump wavelengths shorter than 880 nm or longer than 990 nm at the edges of the 9xx nm pump band. Pump wavelengths from the *off-band* regime led to fiber lengths longer than 5.1 m. In the following subsections, an in-depth performance analysis is given for the pump wavelengths of 940 nm and 976 nm at which high-power pump sources are available[5].

---

[4]Meaning that both the ASE power and the SBS power were less than 1 % of the output power.

[5]Pump sources are also available at 915 nm. However, the absorption and emission cross-sections of Yb^{3+} are similar at 915 nm and 940 nm. The following analysis focusses only on the performance at 940 nm; the basic results are transferable to a pump wavelength of 915 nm.
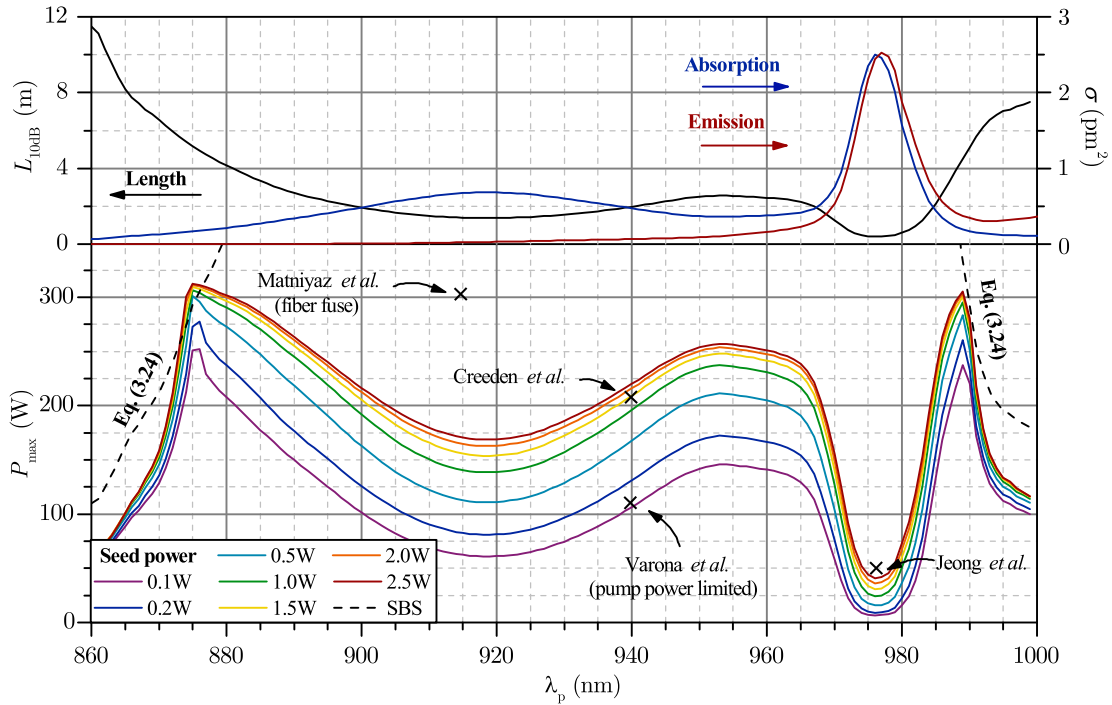
Figure 3.2.1: Top: Yb^{3+} absorption and emission cross-sections versus pump wavelength. The optimized fiber length, labelled as L_{10dB}, corresponds to 10 dB pump light absorption at each pump wavelength. Bottom: simulated power limit versus pump wavelength; the power limit is the maximum simulated output power with an ASE and SBS output below 1 % of the output power. The simulations were performed with seed input powers from 0.1 W to 2.5 W. The dashed line corresponds to Eq. (3.24) with 100 mW seed power. Experimental references: Matniyaz *et al.* (302 W output power, 1.9 W seed power [57]), Creeden *et al.* (207 W output power, 7.5 W seed power [55]), Varona *et al.* (111 W output power, 1.2 W seed power [56]) and Jeong *et al.* (100 W output power, 1.8 W seed power, 30 μm core diameter [102]).

3.2.1 ASE limitation for in-band wavelengths

The Yb^{3+} ASE onset defined the power limit in the *in-band* regime; the simulated power limit was primarily dependent on the Yb^{3+} absorption cross-sections, and thus on the pump wavelength[6]. The simulated power limit agrees reasonably well with the experimental results (see arrows in Fig. 3.2.1). Jeong *et al.* demonstrated 151 W output power at 1563 nm with 33 % slope efficiency from a large-core in-house fabricated 30/650 fiber by pumping at 976 nm. The Yb^{3+} ASE arose around $\approx$50 W output power (derived from publication), which is in fair agreement with the simulated power limit of $\approx$40.7 W. Matniyaz *et al.* demonstrated 302 W output power at 1562.3 nm by pumping a commercial off-the-shelf 25/300 fiber at 915 nm. A direct comparison to the simulated power limit is not possible because no information on the total Yb^{3+} ASE power was provided. Matniyaz *et al.*, however, noted that hardly any Yb^{3+} ASE was observed. Creeden *et al.* and Varona *et al.* achieved in fair agreement with the simulated power limit 207 W and 111 W output power virtually free of Yb^{3+} ASE from the very same 25/300 fiber by pumping at 940 nm. It must be noted, however, that further power scaling was limited for example by available pump power. Hence, no specific information on the Yb^{3+} ASE onset was provided.

---

[6]Indeed, both absorption and emission cross-sections affected the achievable ASE- and SBS-free output power. However, the emission cross-sections contributed only marginally to the simulated power limit because n_6 was much smaller than n_5. Thus, the following discussion refers primarily to the influence of the absorption cross-section.
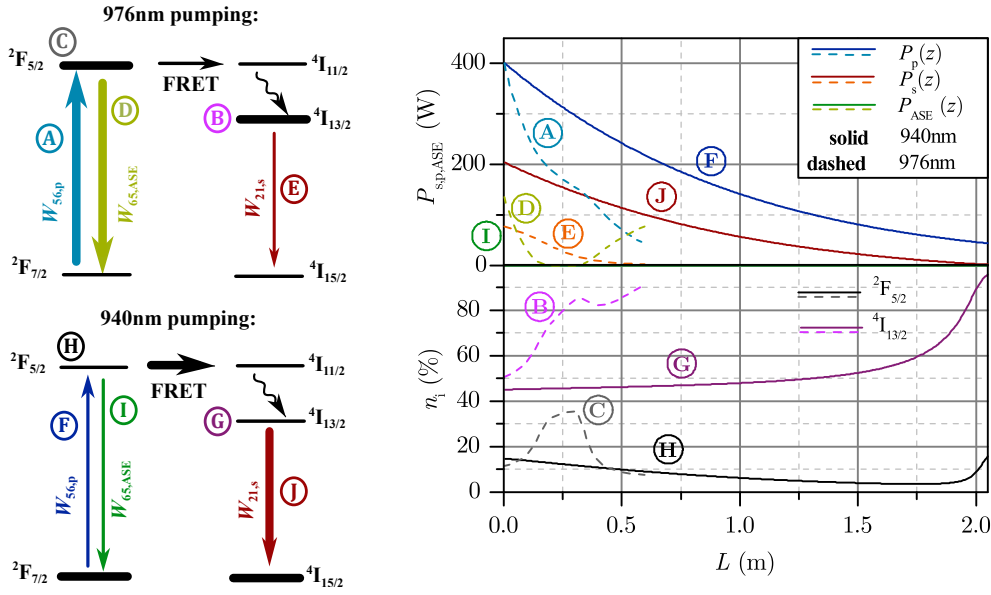
Figure 3.2.2: Left: schematic energy level diagram. The widths of the transition arrows and energy level bars show the magnitude of that transition or population, respectively. Right, top: power evolution of pump, signal and Yb^{3+} ASE with 400 W pump power. The pump power corresponds to the simulated power limit at a pump wavelength of 940 nm. Right, bottom: population of $^4I_{13/2}$ and $^2F_{5/2}$ energy levels for the pump wavelengths of 940 nm and 976 nm.

A detailed discussion on the underlying physical mechanism that is responsible for the pump wavelength dependency in the *in-band* regime is presented in the following. For the discussion, the pump wavelengths 940 nm and 976 nm are used, which are representative for small and large absorption cross-sections and of interest because of the market availability of suitable pump diodes at these wavelengths, for example as found in references [135] and [136]. The simulated power levels and the energy level populations are plotted in Fig. 3.2.2 for a pump power of 400 W. The SBS power was at the µW-level and is thus not depicted to increase the readability of the figure. The schematic energy diagram on the left side of the figure depicts the relevant transitions. The arrow size accords to the rate of the corresponding transition and the thickness of the energy level bars corresponds to the population in the respective level[7]. Important features are marked with alphabetical letters.

Pumping at 976 nm

The used pump power exceeded the simulated power limit at 976 nm and led to powerful Yb^{3+} ASE as explained as follows. The steep pump absorption (marker A) pumped between 50 % and 90 % of the Er^{3+} ions into the $^4I_{13/2}$ energy level (marker B), and thus depleted the $^4I_{15/2}$ energy level. The resulting shortage of transfer partners deteriorated the Yb^{3+}-to-Er^{3+} transfer efficiency. As a consequence, the Yb^{3+} ions in the $^2F_{5/2}$ energy level accumulated up to 36 % of the total Yb^{3+} doping concentration (marker C) giving large optical gain[8] for the Yb^{3+} ASE. The optical gain peaked around 1030 nm (see Fig. 3.2.3) because of the underlying maximum of the emission cross-sections; the Yb^{3+} ASE was therefore most powerful at this wavelength. The simulated total Yb^{3+} ASE output power (marker D) was

$$213.4\,\text{W} = \underbrace{135.6\,\text{W}}_{\text{forward}} + \underbrace{77.8\,\text{W}}_{\text{backward}} \qquad (3.18)$$

depleting the signal output power to 77.5 W accordingly (marker E).

---

[7]A thick arrow corresponds to a large transition rate and vice versa. The same applies for the bars of the energy levels.

[8]The term *optical gain* corresponds to the gain if g_{65} is positive or absorption if g_{65} is negative. An optical gain larger than zero can eventually lead to ASE.
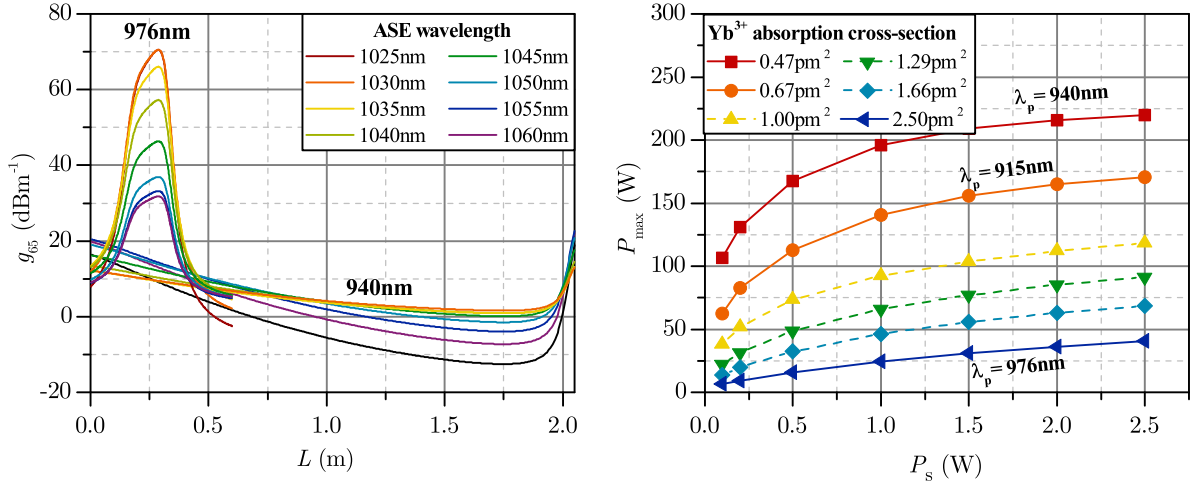
Figure 3.2.3: Left: optical gain at exemplary wavelengths in the 1.0 μm-band; the pump power was 400 W. The optical gain was substantially larger if a pump wavelength of 976 nm was used. An optical gain larger than zero can eventually lead to ASE. Right: simulated power limit versus seed input power at different absorption cross-sections i.e. pump wavelengths. The curves representing the pump wavelengths of 915 nm, 940 nm and 976 nm are solid. The simulated power limit increased with the seed power. Seed saturation was observed around 1.0 W seed power.

Pumping at 940 nm

The used pump power fell below the simulated power limit at 940 nm as explained as follows. The smaller absorption cross-section at 940 nm resulted in lower pump absorption per unit length that required a longer fiber to achieve 10 dB pump absorption. Therefore, overall more Er^{3+} ions, i.e. $L_{10dB} \times \pi r_{core}^2 \times N_{Er}$, participated in the absorption process, which were capable to receive in total more energy. As a result, the relative population in the $^4I_{13/2}$ energy level was generally lower at this pump wavelength compared to 976 nm pumping (marker G), albeit using the same pump power. The depletion of the $^4I_{15/2}$ energy level was mitigated. The availability of Er^{3+} ions in the ground state ensured an efficient Yb^{3+}-to-Er^{3+} energy transfer. Hence, a population of only 5 % to 15 % (marker H) was found in the $^2F_{5/2}$ energy level. The optical gain in the 1.0 μm-band was less than ≈20 dB per m and indeed negative in some cases. This is consistent with the fact that the simulations showed virtually no ASE output at the investigated pump power level. The ASE and signal output powers were 0.8 W (marker I) and 203.5 W (marker J) with 56.5 % optical-to-optical efficiency close to the quantum limit. The Yb^{3+} ASE output, however, increased steeply with pump power. For example, 22.5 W and 82.4 W Yb^{3+} ASE power levels were found with pump powers of 500 W and 600 W, respectively. This behavior is in agreement with the simulated power limit from Fig. 3.2.1 that found the Yb^{3+} ASE onset around ≈400 W pump power.

Seed power

The simulated power limit increased with more seed power as plotted in Fig. 3.2.3 if pump wavelengths from the *in-band* domain were used. The simulated amplifier was seed saturated around ≈1.0 W seed power. The underlying mechanism can be explained as follows. More seed power reduced the effective lifetime in the $^4I_{13/2}$ energy level; therefore, the mean population in the $^4I_{15/2}$ energy level increased. Thus, the efficiency of the Yb^{3+}-to-Er^{3+} energy transfer was sustained that prevented the accumulation of Yb^{3+} ions in the $^2F_{5/2}$ energy level. On a relative scale, the seed power dependency was found most striking at 976 nm at which *transfer bottlenecking* was more prevalent showing the immense importance of the transfer efficiency for ASE-free operation of the amplifier. The power dependency of the Yb^{3+}-to-Er^{3+} energy transfer efficiency is therefore discussed in the following.

32

Efficiency of the Yb^{3+}-to-Er^{3+} energy transfer

Excited Yb^{3+} ions can dissipate their energy via spontaneous or stimulated emission or through the Yb^{3+}-to-Er^{3+} energy transfer. The radiative dissipation processes produce Yb^{3+} ASE and are therefore detrimental to the efficiency of the transfer process[9]. The transfer efficiency can be written as the Yb^{3+}-to-Er^{3+} transfer rate per net pump absorption rate:

$$\eta_{\text{FRET}} = \frac{R_{63} N_{\text{Er}} n_1 n_6}{W_{56,\text{p}} n_5 - W_{65,\text{p}} n_6} \times 100\,\%. \tag{3.19}$$

$\eta_{\text{FRET}} = 100\,\%$ means that all Yb^{3+} ions that are pumped into the $^2F_{5/2}$ energy level undergo the transfer process. If η_{FRET} is less than 100 %, a fraction of the absorbed pump energy is emitted as Yb^{3+} ASE. It was therefore found by the simulations that high Yb^{3+} ASE outputs correspond to low transfer efficiencies, i.e. *transfer bottlenecking*, as shown in the right plot of Fig. 3.2.4. It is consequently reasonable to define the ASE power threshold, denoted as $P_{\text{ASE,thr}}$, on the basis of the transfer efficiency in the following way. The output power at which the transfer efficiency declines more than 0.1 % per W signal power is defined in the following as the ASE power threshold:

$$\left.\frac{\partial \eta_{\text{FRET}}}{\partial P_{\text{out}}}\right|_{P_{\text{ASE,thr}}} = 0.1\,\%/\text{W}. \tag{3.20}$$
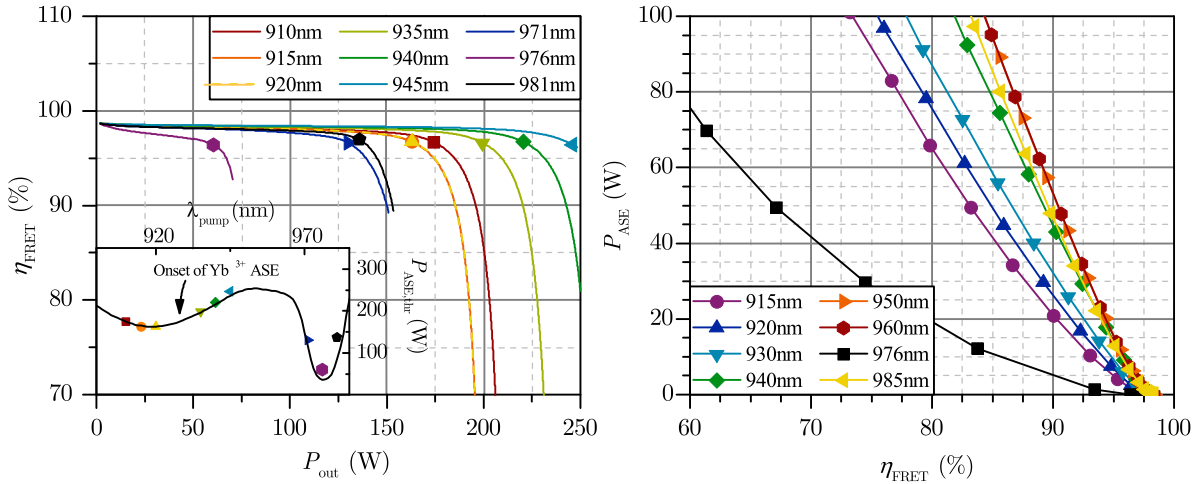

Figure 3.2.4: Left: energy transfer efficiency versus output power. The ASE power threshold is plotted with scattered symbols. The transfer efficiency dropped at power levels above the ASE power threshold. Inset: ASE power threshold versus pump wavelength. The solid line represents the simulated power limit from Fig. 3.2.1 and was in agreement with the ASE power threshold. Right: ASE output power versus transfer efficiency at different pump wavelengths. The data highlight the link between Yb^{3+} ASE generation and deterioration of the energy transfer. The Yb^{3+} ASE power at a specific transfer efficiency was lower at pump wavelengths with large pump absorption because the total power levels were generally lower at these wavelengths.

The left plot in Fig. 3.2.4 shows that this definition of the ASE power threshold ties in well with the onset at which the transfer efficiency deteriorates. Furthermore, this definition also coincides with the simulated power limit from Fig. 3.2.1 as depicted in the inset. It was also found that the ASE power threshold is almost independent from the threshold definition, i.e. 0.1 % per W, because of the non-linear behavior of the Yb^{3+} ASE and signal depletion, i.e. more pump power is required to scale the signal power by the same amount as a result of the power consumption of the prevalent Yb^{3+}

---

[9]The transfer efficiency depends on the local power levels and is thus depending on the position z in the fiber. In the following, the efficiency refers to the averaged efficiency.

ASE generation. This makes the definition used in Eq. (3.20) applicable in practice, although being arbitrary. In contrast, Dong *et al.* defined the ASE power threshold by

$$P_{\text{ASE,thr}} = R \frac{n_1 n_6}{n_5 \sigma_{56}} A h \nu_{\text{p}}, \tag{3.21}$$

where n_5 and n_6 represent only the fraction of the Yb^{3+} ions that are coupled to proximate Er^{3+} ions i.e. capable of transferring energy [137]. The definition from Eq. (3.21), however, turns out impractical because already the presence of small amounts of Yb^{3+} ASE meets such requirement.
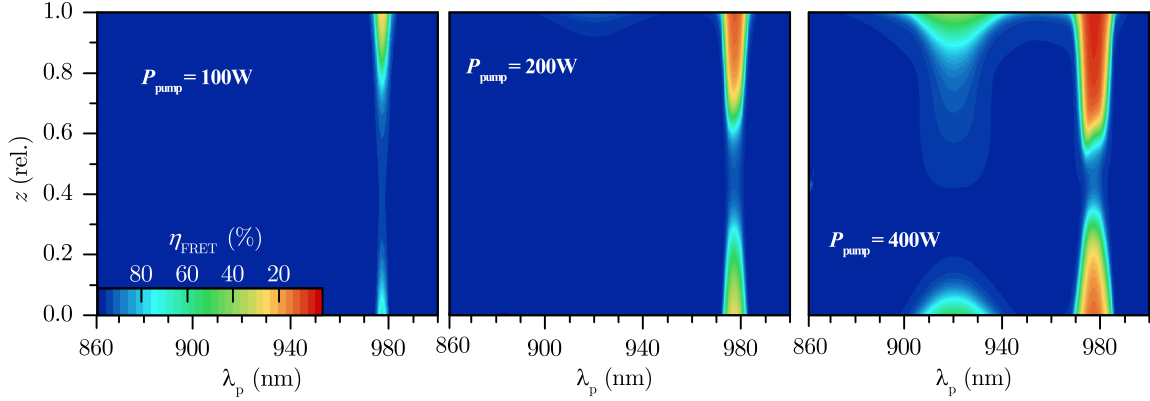

Figure 3.2.5: Energy transfer efficiency versus pump wavelength and fiber position from left to right at pump power levels of 100 W, 200 W and 400 W. The pump power levels correspond to ASE-free operation at 940 nm and 976 nm (100 W), ASE-free operation at 940 nm but not at 976 nm (200 W) and the ASE power threshold at 940 nm (400 W). The transfer efficiency decreased significantly along the fiber above the ASE power threshold of that wavelength.

At 976 nm, the ASE power threshold was 60.2 W and η_{FRET} tended towards 0 %, i.e. *transfer bottlenecking*, over the entire fiber length as depicted in Fig. 3.2.5. The efficiency degradation was found most notable at the fiber ends, i.e. $z = 0$ and $z = L$, due to either peak pump or minimal signal power levels. At 940 nm, the ASE power threshold was 220.6 W and, hence, approximately four times larger compared to pumping at 976 nm. This factor corresponds approximately to the larger absolute number of dopants in the longer gain fiber ($L_{10\text{dB}}$@940nm/$L_{10\text{dB}}$@976nm ≈ 5). The transfer efficiency at 940 nm was close to 100 % along the entire fiber leading to a higher Yb^{3+} ASE power threshold. The plots, however, also show that the transfer efficiency may also decrease around the fiber ends at 940 nm if pumped too hard. This ties in well with the results from Fig. 3.2.1 that show that pumping at 940 nm was also limited by the Yb^{3+} ASE at some point, albeit at higher power levels.

Nonetheless, pump wavelengths from the *in-band* regime resulted in output power levels of up to several hundreds of W and were merely limited by the Yb^{3+} ASE in some cases. In particular pumping at 940 nm was found to provide good power scalability without SBS; suitable pump diodes can be procured as off-the-shelf products that have been reliably tested. A pump wavelength of 940 nm was therefore used in the work outlined in Chap. 5 and Chap. 6.

3.2.2 SBS limitation for off-band wavelengths

The *off-band* regime contains pump wavelengths shorter than 880 nm or longer than 990 nm. The corresponding absorption cross-sections are considerably smaller compared to pump wavelengths from the *in-band* regime. The longer fiber lengths required for 10 dB pump absorption result in lower non-linear thresholds. The simulated output power was therefore limited by SBS. A threshold power level, denoted as $P_{\text{SBS,thr}}$, was found above which the SBS power increased steeply due to the non-linearity of the scattering process as shown in Fig. 3.2.6. The SBS power threshold decreased with the fiber length by $P_{\text{SBS,thr}} \approx 1/L_{\text{eff}}$ as per Eq. (2.41). Thus, the simulated power limit decreased

towards the edges of the 9xx nm pump band. The SBS slopes showed a roll-over particularly notable for long fibers because the associated signal depletion led to less gain from the scattering process.

The SBS power threshold is approximable by Eq. (2.41). The mode-field area of the studied fiber is $A_{\mathrm{eff}} = 327\,\mu\mathrm{m}^2$ at $1.55\,\mu\mathrm{m}$[10]. The factor K_{B} considers the relative orientation between the signal and SBS polarization [138]. For example, $K_{\mathrm{B}} = 1.5$ accounts for a non-PM fiber [139]. The effective fiber length accounts for the signal evolution of non-constant optical power along the fiber and can be calculated by

$$L_{\mathrm{eff}} = \left[1 - \exp\left(-\alpha L\right)\right]/\alpha. \tag{3.22}$$

Although being compiled for passive fibers with typically negligible α and $L_{\mathrm{eff}} \approx L$, the expression can be adopted by assuming an exponential-like signal evolution along the fiber:

$$\alpha = -\frac{1}{L} \ln \left[\frac{P_{\mathrm{out}}}{P_{\mathrm{seed}}} \right]. \tag{3.23}$$

Therefore, $P_{\mathrm{SBS,thr}}$ can be expressed with Eq. (2.41) as:

$$P_{\mathrm{SBS,thr}} \approx 21 \frac{K_{\mathrm{B}} A_{\mathrm{eff}}}{L g_0} \frac{\ln\left(\frac{P_{\mathrm{out}}}{P_{\mathrm{seed}}}\right)}{1 - \frac{P_{\mathrm{seed}}}{P_{\mathrm{out}}}}. \tag{3.24}$$

Eq. (3.24) is plotted for $100\,\mathrm{mW}$ seed power as the dashed line in Fig. 3.2.1. The approximation is in fair agreement with the simulated power limit in the *off-band* regime. The trends for the other seed power levels are equally fitting but are not plotted for clarity reasons. The agreement with the simulated power limit supports the validity of the definition of α. Furthermore, the comparison shows that Eq. (2.41) is also applicable to the studied $\mathrm{Er}^{3+}:\mathrm{Yb}^{3+}$ fiber even though Eq. (2.41) was developed for passive fibers.

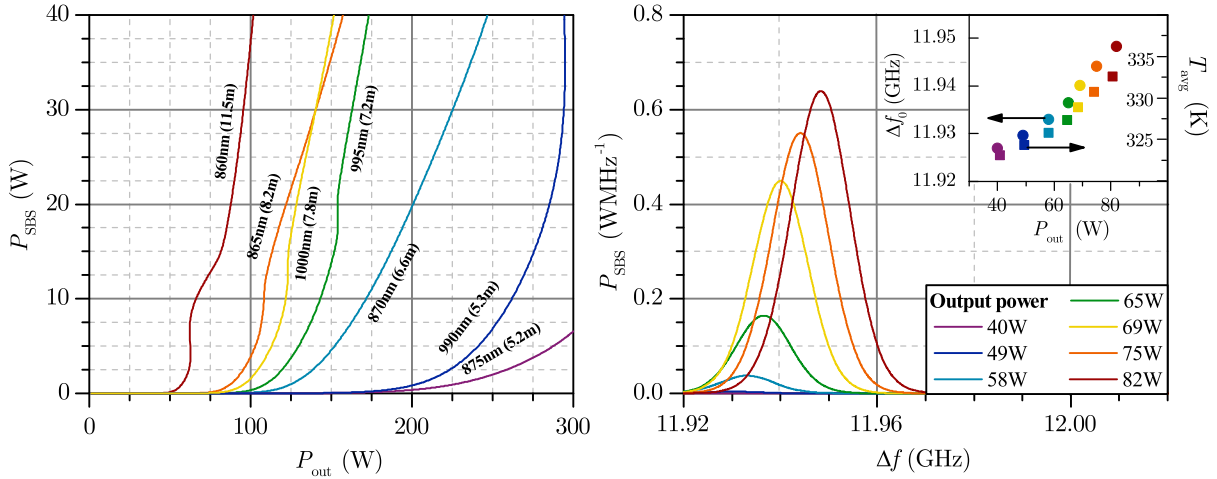**Figure 3.2.6:** Left: SBS power versus output power at different pump wavelengths. The corresponding fiber length is specified in brackets and accorded to $10\,\mathrm{dB}$ pump absorption. The output power from longer fibers already depleted at the investigated power levels, which resulted in a dip of the SBS power slopes. Right: spectrally resolved SBS power density at various output power levels at $860\,\mathrm{nm}$. Inset: central frequency and core temperature versus output power.

The simulated power limit in the *off-band* regime was found to be almost independent from the seed input power for the following reasons. Higher seed input power increases the total signal power levels and thus gain for the SBS from the non-linear scattering mechanism as per $\partial P_{\mathrm{SBS}}(z)/\partial z \approx$

---

[10]The mode-field area corresponds to a mode radius of $10.2\,\mu\mathrm{m}$.

$P_{\text{SBS}}(z)P_{\text{s}}(z)$. At the same time, the more powerful signal depletes the $^4I_{13/2}$ energy level. This reduces the optical gain for the SBS power from stimulated emission and cancels the increased gain from the scattering mechanism.

The simulated power limit peaked at the junction of the *in-* and *off-band* domain. The 1 % break criterion used in Fig. 3.2.1, however, is - although reasonable to calculate the onset of the ASE - rather insensitive to define the SBS onset power because in practice already much lower SBS power levels might imprint excess noise on the signal beam making the amplifier incompatible as a GWD laser source. The formula derived in Eq. (3.24) is even more insensitive because it assumes that the SBS power equals the pump[11] power. This also explains why Eq. (3.24) approximated somewhat higher power limits than the FEM solver. Furthermore, the Yb^{3+} doping concentrations from reference [99] used in the simulations were rather large and led to relatively short fiber lengths. This means that in practice longer fibers may be necessary that lead to even lower SBS power thresholds. Thus, the simulations possibly overestimated the achievable output power in the *off-band* regime. By contrast, SBS-free operation close to the simulated power limit was experimentally demonstrated with pump wavelengths from the *in-band* regime. For example, the absence of SBS was experimentally confirmed up to power levels of 207 W and 111 W through backward directed power monitoring or relative power noise measurements by Creeden *et al.* and Varona *et al.* [55, 56], respectively.

Temperature dependency

The 9xx nm pump band leads to an inherent quantum defect close to $\approx 40\,\%$. The generated heat grows with pump and seed power and is thus dependent on the location in the fiber. Fig. 3.2.7 shows the simulated temperature along the fiber for different pump wavelengths. The data shows that pump wavelengths with low absorption led to lower temperatures due to the spatially more distributed heat generation. It must be emphasized, however, that all simulated wavelengths resulted in temperatures close to the critical coating temperature of 80°C as per Sec. 2.2.2 [76] at already 200 W pump power. Pumping at 976 nm showed somewhat lower temperatures compared to 970 nm or 980 nm due to the increased generation of the Yb^{3+} ASE and the associated deceleration of the Yb^{3+}-to-Er^{3+} energy transfer.
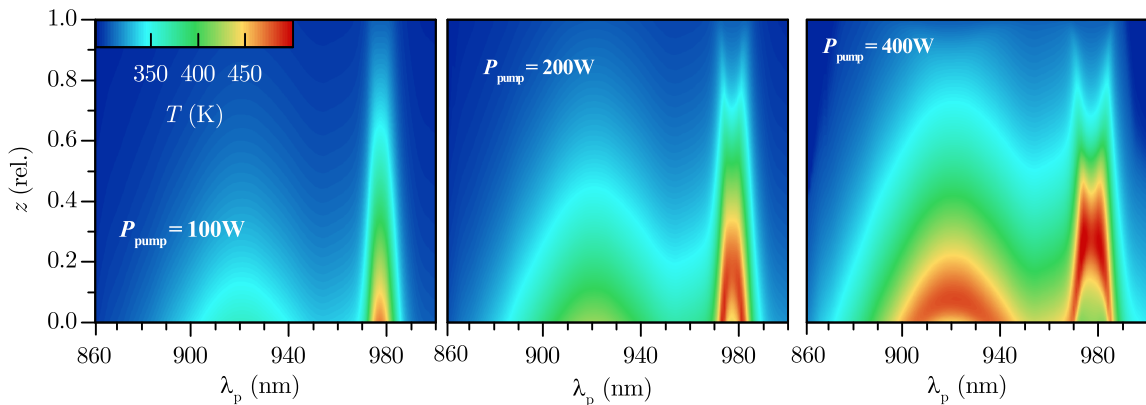

Figure 3.2.7: Temperature versus pump wavelength and fiber position from left to right at pump power levels of 100 W, 200 W and 400 W. Pump wavelengths with low absorption resulted in lower temperatures due to the spatially more distributed heat generation. The fiber temperature can peak distant from the pump end due to the Yb^{3+} ASE.

The consequences for the SBS power are discussed in the following. The temperature gradient spectrally detunes the SBS gain along the z-axis because the SBS frequency shift $\Delta f_0 \approx \nu_{\text{B}} + c_f \Delta T$ depends on the temperature. This reduces the overall SBS gain making the quantum defect advantageous in terms of SBS. The output spectrum of the SBS is shown in Fig. 3.2.6. The frequency

---

[11]In this context, the term *pump* refers to the signal at the seed wavelength because this is the one pumping the SBS.

chirp effectively broadened the SBS spectrum. The SBS center frequency Δf_0 and the average core temperature T_{avg} are plotted in the inset. The slope of the temperature, $\partial \Delta T_{\mathrm{avg}} / \partial P_{\mathrm{out}}$, increased above the SBS power threshold because of the signal depletion that required in total more pump power to scale the output power and thus resulted in more heat per W output power[12]. The simulated core temperatures, and thus severity of the spectral shift, depend on the choice of the simulation parameters, e.g. thermal conductivity k and convective heat transfer coefficient h. However, the parameters that were used in this work produced reasonable core temperatures, which supports the validity of their choice.

In total, pump wavelengths from the *off-band* regime are assessed as unsuited to scale the power of single-frequency EYDFAs because of the required long fiber lengths and the associated low SBS power thresholds. The SBS cannot be mitigated by the inherent quantum defect.

3.3 Conclusion

The trade-off between Yb^{3+} ASE suppression and SBS mitigation was numerically investigated for a single-frequency EYDFA pumped at 9xx nm. A typical LMA 25/300 Er^{3+}:Yb^{3+} doped double-cladding fiber was assumed. The fiber length corresponded to 10 dB pump light absorption. The Er^{3+} and Yb^{3+} ions were modelled as coupled 2- and 4-level systems that were linked by the Yb^{3+}-to-Er^{3+} energy transfer and described by the corresponding rate equations. The Yb^{3+} absorption band was segmented in *in-band* (880 nm $< \lambda_{\mathrm{p}} <$ 990 nm) and *off-band* ($\lambda_{\mathrm{p}} \leq$ 880 nm and $\lambda_{\mathrm{p}} \geq$ 990 nm) pump wavelengths. The simulated power was limited by the Yb^{3+} ASE in the *in-band* regime. The Yb^{3+}-to-Er^{3+} transfer efficiency was introduced as the ratio between the excited Yb^{3+} ions that transfer their energy to Er^{3+} ions and the Yb^{3+} ions that release their energy through the Yb^{3+} ASE. Pumping at 976 nm depleted the $^4I_{15/2}$ energy level and reduced the number of available Er^{3+} transfer partners. As a consequence, Yb^{3+} ions accumulated in the $^2F_{5/2}$ energy level. The Yb^{3+}-to-Er^{3+} transfer efficiency decreased therefore steeply at $\approx$60.2 W output power for the studied amplifier configuration. Pumping at 940 nm distributed the pump absorption along the fiber and increased the ASE power threshold to $\approx$220.6 W output power. The corresponding $^2F_{5/2}$ energy level was homogeneously populated between 5 % and 15 %.

SBS limited the output power in the *off-band* regime. The threshold was approximatable by Eq. (3.24) and decreased steeply with longer fiber lengths. Pump wavelengths at the edges of the Yb^{3+} absorption band resulted in powerful SBS. Er^{3+}'s large quantum defect shifted the center frequency of the SBS gain and broadened the SBS spectrum. However, the spectral chirp could not mitigate the SBS. Pump wavelengths from the *off-band* regime were considered as not suited to pump the EYDFA. The results, however, indicate that off-peak pumping at wavelengths from the *in-band* regime, in particular at 940 nm, may contribute greatly to further power scaling of EYDFAs around 1.55 μm.

---

[12]As a secondary reason, the SBS power also triggered the transition from the $^4I_{13/2}$ to the $^4I_{15/2}$ energy level near $z = L$ where the local signal power and thus W_{21} would be low otherwise. This increased the availability of Er^{3+} transfer partners in the $^4I_{15/2}$ energy level. Hence, the efficiency of the Yb^{3+}-to-Er^{3+} energy transfer and the rate of the phonon transition from the $^4I_{11/2}$ to the $^4I_{13/2}$ energy level increased resulting in additional heat.

Chapter 4

Estimation of interlock requirements for high-power EYDFAs

The most promising approach to meet the laser power requirements of GWDs around 1.5 µm is currently the use of double-cladding fibers with large pump power levels [56]. However, if the seed laser fails amid operation - e.g. by technical malfunction - parasitic lasing or uncontrolled Q-switching may damage the laser system; for example, the LIDT of the fiber ends is $22\,\mathrm{Jcm}^{-2}$ (1 ns pulses, $\lambda \approx 1\,\mathrm{\mu m}$) [140]. The implementation of an autonomous emergency-off (EMO) system can avoid potential fiber damage by interlocking the pumping process and therefore increase the ruggedness of the laser system. The EMO system must react fast enough before the unsaturated gain reaches a destructive level. The reaction time of the EMO system is therefore a critical design parameter. A direct measurement of the reaction time, however, would certainly lead to the destruction of the laser system and is therefore not feasible. Furthermore, a measurement at low power levels would produce a different outcome[1].

A combined numerical and experimental approach is proposed to estimate the EMO requirements for GWD-compatible EYDFAs by using core-pumped single-mode fibers. The approach is justified because core-pumping produces similar pump intensities in the fiber core as found in cladding-pumped architecture. It is therefore reasonable to assume that the build-up time of the gain would be similar. The associated power levels, however, are lower and less destructive[2].

The length-integrated populations were calculated from backward directed ASE transients of three single-mode fibers under test (FUTs) by a FEM solver. The transients were used to estimate the time interval until a typical cladding-pumped LMA fiber encounters parasitic lasing after a seed laser malfunction. Furthermore, a prototype EMO system in PCB[3] format was characterized. The chapter concludes with a summary of the key findings. The work has been partly published in reference [141].

4.1 FEM model

A modified FEM solver computed the optical power levels and populations of the Yb^{3+} and Er^{3+} energy levels by solving a system of partial differential equations (PDEs). The pump and seed input powers, i.e. $P_{\mathrm{pump}}(t) = I_{\mathrm{pump}}(t) \times \pi\omega^2$ and $P_{\mathrm{seed}}^{\pm}(t)$, formed a boundary-value-problem at the fiber ends. The computation principle is shown in Fig. 4.1.1. The optical power levels of pump, signal, Yb^{3+} ASE and Er^{3+} ASE are expressed as $P_{\mathrm{p}}(t,z)$, $P_{\mathrm{s}}^{\pm}(t,z)$, $P_{\mathrm{Yb}}^{\pm}(t,z)$ and $P_{\mathrm{Er}}^{\pm}(t,z)$. The pump

---

[1]The gain dynamic depends on the population in the laser-active energy levels and such depends largely on the net decrease of the pump intensity per unit time.

[2]The proposed approach only renders an estimation of the gain build-up time because the gain dynamic also depends on factors such as pump wavelength or doping concentrations.

[3]**P**rinted **c**ircuit **b**oard.

power propagated in the positive z direction without exception, whereas the seed, Yb^{3+} ASE and Er^{3+} ASE power propagated in the direction that is indicated by the superscript. The z-axis of the coordinate system was oriented parallel to the fiber. The SCD was used to approximate the power distribution in radial direction as explained in Chap. 3. The fiber lengths used for the computation were sufficiently short to omit SBS in the following as it was only at the µW-level (contrary to Chap. 3).
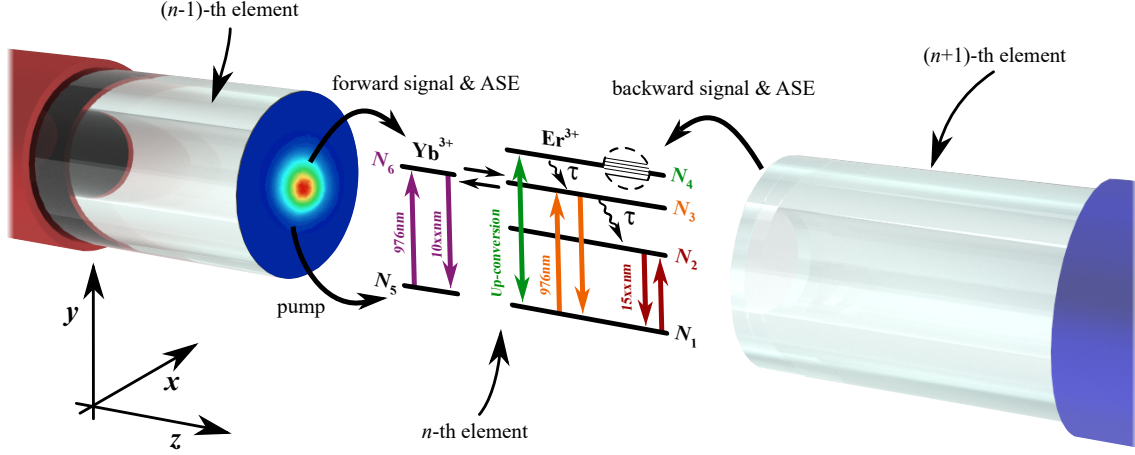

Figure 4.1.1: Working principle of FEM solver: the fiber was meshed in equidistant nodes labelled as (n-1), n, (n+1), etc. The populations were computed node-wise according to the local power levels and rate equations. The full energy level diagram is presented in Sec. 2.2.3. Seed, Yb^{3+} ASE and Er^{3+} ASE propagated bidirectionally; the pump power propagated in the positive z direction without exception. The optical power evolution was calculated from the transition rates and photon energies.

The evolution of the relevant energy levels was calculated from the optical power levels; the schematic energy level diagram can be found in Fig. 4.1.1 and more detailed in Sec. 2.2.3. As in Chap. 3, the ${}^4I_{15/2}$, ${}^4I_{13/2}$, ${}^4I_{11/2}$ and the ${}^4I_{9/2}$ energy levels of Er^{3+} are referred to as levels 1 to 4. The ${}^2F_{7/2}$ energy level of Yb^{3+} is denoted as level 5 and the ${}^2F_{5/2}$ energy level as level 6. The population in each level is described as follows. Small letters, $n_i(t,z)$, describe the normalized population of the energy levels. Because every ion must exist in either of the energy levels, the equation

$$\sum_i n_i(t,z) = 1 \tag{4.1}$$

holds for i from 1 to 4 and i from 5 to 6[4]. Capital letters, $N_i(t) = \int_0^L n_i(t,z)\partial z$, describe the length-integrals of the energy level populations[5]. The doping concentrations of the Er^{3+} and Yb^{3+} ions, denoted as N_{Er} and N_{Yb}, were calculated from the specified absorption of the FUTs. The optical gain that arises from the laser-active transitions, i.e. between the energy levels 1 and 2 and between 5 and 6, was calculated from the length-integrated populations:

$$g_{21}(\lambda, t) = N_{Er}\left[\sigma_{21}(\lambda)N_2(t) - \sigma_{12}(\lambda)N_1(t)\right], \tag{4.2}$$

$$g_{65}(\lambda, t) = N_{Yb}\left[\sigma_{65}(\lambda)N_6(t) - \sigma_{56}(\lambda)N_5(t)\right]. \tag{4.3}$$

The transfer rates between energy levels i and j were calculated similarly to Chap. 3; however, time dependence was considered:

$$\begin{aligned} W_{ij,p}(t,z) &= \frac{\Gamma\lambda_p\sigma_{ij}}{A_{core}hc}P_p(t,z), & W_{ij,Yb}^{\pm}(t,z) &= \frac{\Gamma\lambda_{Yb}\sigma_{ij}}{A_{core}hc}P_{Yb}^{\pm}(t,z), \\ W_{ij,s}^{\pm}(t,z) &= \frac{\Gamma\lambda_s\sigma_{ij}}{A_{core}hc}P_s^{\pm}(t,z), & W_{ij,Er}^{\pm}(t,z) &= \frac{\Gamma\lambda_{Er}\sigma_{ij}}{A_{core}hc}P_{Er}^{\pm}(t,z). \end{aligned} \tag{4.4}$$

---

[4] The energy level population was normalized to ease the computation process.

[5] The following will omit the calling of the parenthesized t, z to improve the readability.

The parameters λ_p, λ_s, λ_{Yb} and λ_{Er} are the pump, seed, Yb^{3+} ASE and Er^{3+} ASE wavelengths; h is the Planck constant and c the speed of light [99]. The parameters σ_{ij} represent the associated absorption and emission cross-sections. The Er^{3+} and Yb^{3+} ions were linked by a dipole-dipole interaction with bidirectional energy transfer. The Yb^{3+}-to-Er^{3+} transfer coefficient R_{63} was calculated from the Yb^{3+} doping concentration according to Eq. (2.33) to allow the comparison of different fibers[6]. The backtransfer coefficient R_{36} was chosen to be the same in accordance to the McCumber theory [142]. The lifetimes were approximated to $\tau_{21} = 8\,\text{ms}$ [72, 83], $\tau_{32} = 10\,\mu\text{s}$ [83], $\tau_{43} = 0.2\,\mu\text{s}$ [143] and $\tau_{65} = 1\,\text{ms}$ [56, 72, 131] similar to Chap. 3. The up-conversion coefficient C_{up} was computed as described by Federighi *et al.* [95]. The population of the energy levels evolved according to the rate equations established by Han *et al.* [99] and Karasek *et al.* [100]:

$$\frac{\partial n_1}{\partial t} = W_{21}n_2 + W_{31}n_3 - W_{12}n_1 - W_{13}n_1 + R_{36}N_{Yb}n_3n_5 - R_{63}N_{Yb}n_6n_1$$
$$+ C_{up}N_{Er}n_2^2 + \frac{n_2}{\tau_{21}}, \tag{4.5}$$

$$\frac{\partial n_2}{\partial t} = W_{12}n_1 - W_{21}n_2 - 2C_{up}N_{Er}n_2^2 + \frac{n_3}{\tau_{32}} - \frac{n_2}{\tau_{21}}, \tag{4.6}$$

$$\frac{\partial n_3}{\partial t} = W_{13}n_1 - W_{31}n_3 + R_{63}N_{Yb}n_6n_1 - R_{36}N_{Yb}n_5n_3 + \frac{n_4}{\tau_{43}} - \frac{n_3}{\tau_{32}}, \tag{4.7}$$

$$\frac{\partial n_4}{\partial t} = C_{up}N_{Er}n_2^2 - \frac{n_4}{\tau_{43}}, \tag{4.8}$$

$$\frac{\partial n_5}{\partial t} = W_{65}n_6 - W_{56}n_5 + R_{63}N_{Er}n_6n_1 - R_{36}N_{Er}n_5n_3 + \frac{n_6}{\tau_{65}}, \tag{4.9}$$

$$\frac{\partial n_6}{\partial t} = W_{56}n_5 - W_{65}n_6 - R_{63}N_{Er}n_6n_1 + R_{36}N_{Er}n_5n_3 - \frac{n_6}{\tau_{65}}. \tag{4.10}$$

In contrast to Chap. 3, time dependence i.e. non-equilibrium conditions were considered. The explicit quoting of (t, z), however, and the distinction between opposite propagation directions i.e. the superscript are omitted in this representation to ease the readability. As an example, W_{12} represents the sum of $W_{12,s}^+(t, z)$, $W_{12,s}^-(t, z)$, $W_{12,Er}^+(t, z)$ and $W_{12,Er}^-(t, z)$. The rate equations were solved by the Euler method $n_i(t + \Delta t) \approx n_i(t) + \partial n_i(t)/\partial t \times \Delta t$ using $\Delta t = 0.5\,\mu\text{s}$ and $\Delta L = 0.4\,\text{mm}$. The power of the pump and signal as well as the Yb^{3+} ASE and Er^{3+} ASE power evolved along the fiber according to the following equations:

$$\frac{\partial P_p(t, z)}{\partial z} = N_{Yb}\left[W_{65,p}(t, z)n_6(t) - W_{56,p}(t, z)n_5(t)\right]\frac{hc}{\lambda_p}, \tag{4.11}$$

$$\frac{\partial P_s^\pm(t, z)}{\partial z} = \pm N_{Er}\left[W_{21,s}^\pm(t, z)n_2(t) - W_{12,s}^\pm(t, z)n_1(t)\right]\frac{hc}{\lambda_s}, \tag{4.12}$$

$$\frac{\partial P_{Yb}^\pm(t, z)}{\partial z} = \pm N_{Yb}\left[W_{65,Yb}^\pm(t, z)n_6(t) - W_{56,Yb}^\pm(t, z)n_5(t)\right]\frac{hc}{\lambda_{Yb}} \pm \beta A_{Yb}(t, z)\frac{hc}{\lambda_{Yb}}, \tag{4.13}$$

$$\frac{\partial P_{Er}^\pm(t, z)}{\partial z} = \pm N_{Er}\left[W_{21,Er}^\pm(t, z)n_2(t) - W_{12,Er}^\pm(t, z)n_1(t)\right]\frac{hc}{\lambda_{Er}} \pm \beta A_{Er}(t, z)\frac{hc}{\lambda_{Er}}. \tag{4.14}$$

The terms in square brackets calculated the total stimulated transition rates between the energy levels i and j, i.e. "*photon emission rate minus photon absorption rate*", which was multiplied by the corresponding photon energy hc/λ. The ASE was initiated by spontaneous emission along the fiber, which was computed by the photon energies and spontaneous transition rates:

$$A_{Yb} = \frac{N_{Yb}n_6\Delta V}{\tau_{65}}, \qquad A_{Er} = \frac{N_{Er}n_2\Delta V}{\tau_{21}}. \tag{4.15}$$

---

[6] R_{63} was assumed to be constant in Chap. 3.

The factor β is the relative proportion of the spontaneous emission that is emitted within the cone of acceptable NAs ($\Theta < \Theta_{NA}$) and thus guided in the fiber core. β was calculated from the incident angle indicated by the NA.

Eq. (4.11) to Eq. (4.14) show that the backward directed ASE output power, i.e. $P_{Yb}^-(t,0)$ and $P_{Er}^-(t,0)$, depends on the population of the laser-active energy levels. Be f_i a function that associates $P_{Yb}^-(t,0)$ and $P_{Er}^-(t,0)$ to the length-integrated population of the corresponding i-th energy level:

$$f_i : \begin{cases} P_{Er}^-(t,0) \mapsto N_i(t) \text{ for } i \text{ from 1 to 4,} \\ P_{Yb}^-(t,0) \mapsto N_i(t) \text{ for } i \text{ from 5 to 6.} \end{cases}$$

For example, the functions f_1 and f_2 associate $P_{Er}^-(t,0)$ to $N_1(t)$ and $N_2(t)$ and the functions f_5 and f_6 associate $P_{Yb}^-(t,0)$ to $N_5(t)$ and $N_6(t)$. Fig. E.0.2, Appendix E shows the functions f_1 to f_6; the functions were numerically extracted from the model. The functions were reasonably robust against variations of the input parameters as depicted in Fig. E.0.1, Appendix E. The function outputs were therefore not significantly affected by the uncertainty of the input parameters. For example, the outputs of f_1, f_2, f_5 and f_6 deviated less than $\pm 5\,\%$ if the fiber length was varied by $\pm 20\,\%$. Moreover, a deviation of less than $\pm 5\,\%$ was found under variation of the doping concentrations within the specified error interval of the FUTs. Additionally, the functions f_1, f_2, f_5 and f_6 were reasonably robust against variations of the pump intensity. The function outputs were therefore not significantly affected by the uncertainty of such. Furthermore, the functions f_1, f_2, f_5 and f_6 were tested to be bijective by parameter sweeping. This means that these functions unambiguously assigned a distinct output to each function input. In contrast, the functions f_3 and f_4 depended greatly on the pump intensity (see Fig. E.0.2, Appendix E). However, f_3 and f_4 could be omitted for the following analysis because the ${}^4I_{11/2}$ and ${}^4I_{9/2}$ energy levels were mostly empty. The function inputs, i.e. $P_{Yb}^-(t,z)$ and $P_{Er}^-(t,z)$, were measured as described in the following.

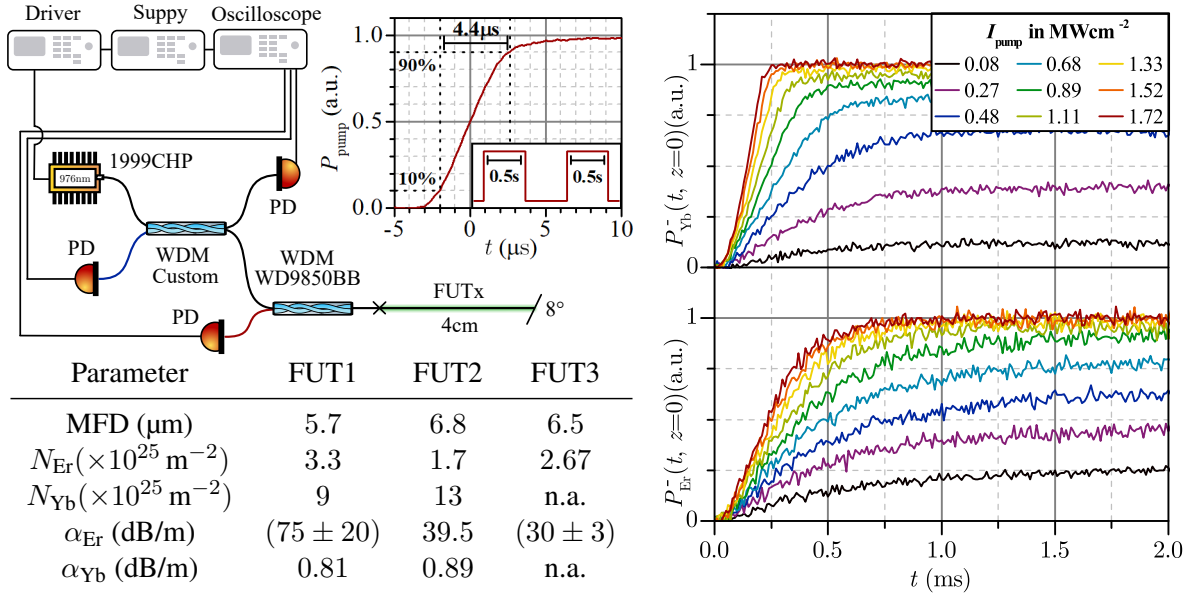| Parameter	FUT1	FUT2	FUT3
MFD (µm)	5.7	6.8	6.5
$N_{Er}(\times 10^{25}\,\mathrm{m}^{-2})$	3.3	1.7	2.67
$N_{Yb}(\times 10^{25}\,\mathrm{m}^{-2})$	9	13	n.a.
α_{Er} (dB/m)	(75 ± 20)	39.5	(30 ± 3)
α_{Yb} (dB/m)	0.81	0.89	n.a.

Figure 4.1.2: Top, left: experimental setup to measure $P_{Yb}^-(t,z)$ and $P_{Er}^-(t,z)$ with wavelength division multiplexers (WDM) to filter the Er^{3+} ASE and Er^{3+} ASE, FUTs and photo detectors (PD). The output power of the laser diode (1999CHP, *3SP Technologies S.A.S.*, $\lambda_p = 976\,\mathrm{nm}$) was modulated by a function generator (rectangular pulse shape). The rising edge of the pump pulse provided the time reference. Bottom, left: fiber parameters of FUTs. The mode-field diameter, α_{Er} and α_{Yb} were defined at $\lambda_s \approx 1.5\,\mu\mathrm{m}$ or $\lambda_p = 915\,\mathrm{nm}$. Right: Er^{3+} ASE and Yb^{3+} ASE transients of FUT1. The time scales of the Er^{3+} ASE transients were longer than the time scales of the Yb^{3+} ASE transients.

4.2 Experimental ASE transients from core-pumped fibers

The experimental setup is shown at the top left in Fig. 4.1.2; the setup allowed to imitate a seed laser malfunction, i.e. pumping without seed. A single-mode laser diode (1999CHP, *3SP Technologies S.A.S.*) delivered up to 0.35 W output power in quasi-cw mode (rectangular pulse shape) with a wavelength of 976 nm and a repetition rate of $f_{rep} = 1$ Hz. A 50 % duty cycle ensured excited state depletion between consecutive pulses, i.e. on-/off-time: 0.5 s. A set of 2x2 fiber-fused wavelength division multiplexers (WD9850BB, *Thorlabs Inc.* and custom, *LZH e.V.*)[7] separated the backward propagating Yb^{3+} ASE and Er^{3+} ASE power. The InGaAs photo detectors (DET10D/M, *Thorlabs Inc.*, 40 MHz bandwidth) were triggered at the pump pulse arrival (rise time: $\approx 4.4\,\mu s$). The arrival of the pump pulse represented the time of the seed laser malfunction; the time reference was measured at the idle port of the custom-made wavelength division multiplexer. The FUTs were 4 cm-long single-mode $Er^{3+}:Yb^{3+}$ or Er^{3+} doped fibers: TC1500Y(6/125)HD (FUT1, *Fibercore Ltd.*), SM-EYDF-6/125-HE (FUT2, *Nufern Inc.*) and Er30-4/125 (FUT3, *nLight Inc.*). The parameters of the FUTs are summarized in the table of the figure. Optical feedback from Fresnel reflection was prevented by slanting the fiber outputs with an 8° angle.
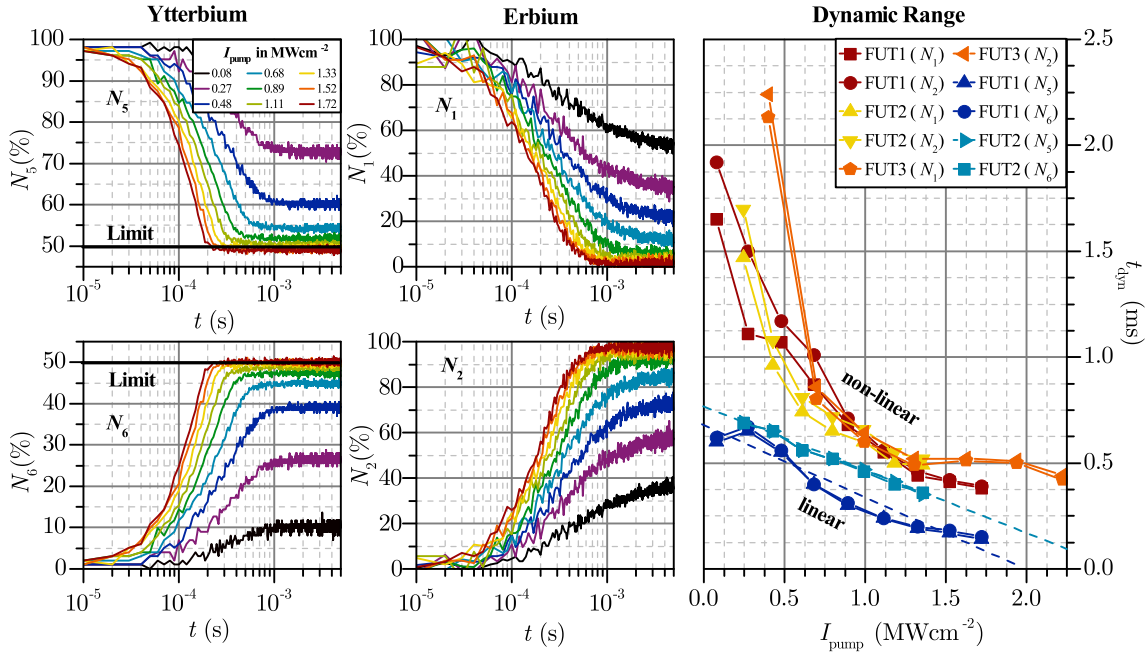

Figure 4.2.1: Left: transients $N_1(t)$, $N_2(t)$, $N_5(t)$ and $N_6(t)$ obtained from the backward directed ASE transients of FUT1. The pump pulse's rising edge was set to $t = 0\,\mu s$. The dynamic range of the Yb^{3+} ASE was between 0.14 ms and 0.69 ms; the dynamic of the Er^{3+} ASE ranged between 2.24 ms and 0.38 ms. The Yb^{3+} inversion saturated at $N_5 \approx N_6$ because of the quasi-2-level energy structure. Right: dynamic range of integrated population densities. The dynamic range was defined by the time between the 10 % and 90 % values of the rising or the falling edges. The dynamic range decreased with pump intensity and was shorter for the Yb^{3+} levels. The scaling with pump intensity seemed more linear for the Yb^{3+} levels.

Fig. 4.1.2 shows the ASE power transients from FUT1; the transients from the other FUTs are depicted in Fig. E.0.1, Appendix E. Fig. 4.2.1 shows the length-integrated populations of the energy levels 1, 2, 5 and 6 (calculated from FUT1). The laser-active energy levels 2 and 6 were populated at the beginning of the pump's on-cycle; the ground levels 1 and 5 depleted accordingly. The stimulus saturated as soon as the pumping process was compensated by the energy withdrawal from the ASE and/or energy transfer. The saturation level increased with pump intensity. Quenching of level 5 and 6

---

[7]The wavelength division multiplexers were designed for 1550 nm and 976 nm as well as 1040 nm and 976 nm.

was found near 50 % because the absorption and emission cross-sections are equal at $\lambda_p = 976$ nm. Fig. 4.2.1 also shows the duration of the transients (10 % to 90 % level). A duration between 0.69 ms to 0.14 ms accelerating with pump intensity was found for the Yb^{3+} ions. The pump dependency tended to be circa linear (see guide-to-the-eye in figure) because the Er^{3+}-to-Yb^{3+} backtransfer was negligible for the Yb^{3+} ions. Instead, the Yb^{3+} ions were primarily excited through direct pump absorption in a "*first-order excitation mechanism*". A similar time scale can be obtained from the Yb^{3+} doping concentration and pump flux by comparing the number of dopants with the pump photons per s. This comparison estimates the duration of the Yb^{3+} transients between 0.06 ms and 1.31 ms depending on pump intensity.

A longer duration was found for the transients of the Er^{3+} ions because of Er^{3+}'s smaller absorption cross-sections at 976 nm ($\sigma_{13} \approx 0.10 \times \sigma_{56}$). The (de-)population process of the $^4I_{15/2}$ and $^4I_{13/2}$ energy levels accelerated with pump intensity from 2.24 ms to 0.38 ms. The Er^{3+} ions were additionally populated through the Yb^{3+}-to-Er^{3+} energy transfer process, i.e. "*second-order excitation mechanism*"; the dependence on the pump intensity tended therefore to be less linear. The transients $N_1(t)$ and $N_2(t)$ were approximately mirror-symmetrical because the $^4I_{11/2}$ and $^4I_{9/2}$ energy levels were mostly empty. A total depletion of the $^4I_{15/2}$ energy level was possible because of the quasi-3-level structure of the energy scheme and the Yb^{3+}-to-Er^{3+} energy transfer.

4.3 Estimation of EMO requirements

This section identifies the requirements of the EMO system by using the results from Sec. 4.2. A cladding-pumped high-power EYDFA with 25/300 LMA fibers was assumed. The approach is justified for the following reasons. Firstly, the pump intensities applied in Sec. 4.2 are similar to typical pump intensity levels found in the fiber core of a cladding-pumped amplifier. As for example, the fiber in reference [56] was pumped with approximately 0.34 MWcm^{-2} at 940 nm; the FUTs from Sec. 4.2 were pumped between 0.08 MWcm^{-2} and 2.22 MWcm^{-2}. Secondly, the doping concentrations of the FUTs (see table in Fig. 4.1.2) were also similar. For example, the fiber in reference [56] was doped with Er^{3+} and Yb^{3+} doping concentrations of 3.7×10^{25} m^{-3} and 1.3×10^{26} m^{-3}, respectively. As such, it seems to be reasonable that the build-up time of the ASE power in double-cladding pump architecture would be at least similar in scale to the results from the core-pumped FUTs. Nonetheless, the following analysis can merely provide an estimation; the shortcomings are discussed in Sec. 4.5.

Parasitic lasing can occur if the optical gain exceeds the round-trip losses. Be g_{thr} the threshold gain to meet this requirement. The following gives an estimation of g_{thr}; the outcoupling loss at a perpendicular cleave is ≈ 15 dB loss per reflection[8] totalling to 30 dB loss per round-trip[9]. Scattering losses (passive fibers: 0.2 dB per km [61], Er^{3+}:Yb^{3+} doped fibers: 20 dB per km [132]) are negligible. Therefore, it seems reasonable to define g_{thr} as 30 dB per round-trip. The actual threshold, however, is difficult to specify because the actual losses depend on the configuration. Nonetheless, the results of this approach were only marginally affected by the actual choice of g_{thr}; the threshold definition therefore holds for a crude estimation. The time window from the seed laser malfunction i.e. pump pulse arrival in this case[10] to the beginning of the parasitic lasing specifies the reaction time requirement of the EMO system. Be t_{21} and t_{65} the time periods until the gain per round-trip exceeds 30 dB for the Er^{3+} and Yb^{3+} wavelength bands, respectively. t_{21} and t_{65} can be obtained by solving

---

[8] Assuming Fresnel reflections with $n_{air} \approx 1$ and $n_{glass} \approx 1.46$.

[9] Assuming two perpendicularly cleaved fiber ends i.e. free-space seed coupling.

[10] The validity of the assumption that a seed laser failure is equivalent to pumping an unseeded fiber is discussed in Sec. 4.5.

the following implicit relation for $t_{ij}(\lambda)$ by exhaustive searching:

$$g_{\text{thr}} \stackrel{!}{=} 10/\ln(10) \times g_{ij}(\lambda, t_{ij}) \times L_{10\text{dB}} \tag{4.16}$$

$$\Rightarrow 6.91 \stackrel{!}{=} N_{\text{Yb/Er}} \left[\sigma_{ij}(\lambda) N_i(t_{ij}) - \sigma_{ji}(\lambda) N_j(t_{ij}) \right]. \tag{4.17}$$

A fiber length of 1 m according to $\approx 10\,\text{dB}$ pump absorption for a pump wavelength of 976 nm was assumed. Moreover, $N_1(t)$, $N_2(t)$, $N_5(t)$ and $N_6(t)$ were substituted with the calculated length-integrals from Sec. 4.2.

Fig. 4.3.1 shows t_{21} and t_{65} versus the wavelength; the following results were found. More pump power accelerated the population process of the laser-active energy levels. Therefore, t_{21} and t_{65} decreased with pump intensity because g_{thr} was reached in less time. The dependency on the pump power quenched significantly above $\approx 1\,\text{MWcm}^{-2}$ because of the inverse proportionality of the excitation rate and saturation time, i.e if the pump absorption doubles, the laser-active energy levels are saturated in approximately half the time and vice versa. The *quenching limit*[11] of $\approx 1\,\text{MWcm}^{-2}$ gives a

FUT	Pump intensity	1033 nm	1531 nm
FUT1	$0.95\,\text{MWcm}^{-2}$	0.13 ms	0.43 ms
	$1.35\,\text{MWcm}^{-2}$	0.09 ms	0.29 ms
FUT2	$0.95\,\text{MWcm}^{-2}$	0.11 ms	0.49 ms
	$1.35\,\text{MWcm}^{-2}$	0.08 ms	0.39 ms
FUT3	$1.00\,\text{MWcm}^{-2}$	n.a.	2.06 ms
	$1.31\,\text{MWcm}^{-2}$	n.a.	0.58 ms
Total		$\gtrsim 0.1\,\text{ms}$	$\gtrsim 0.3\,\text{ms}$

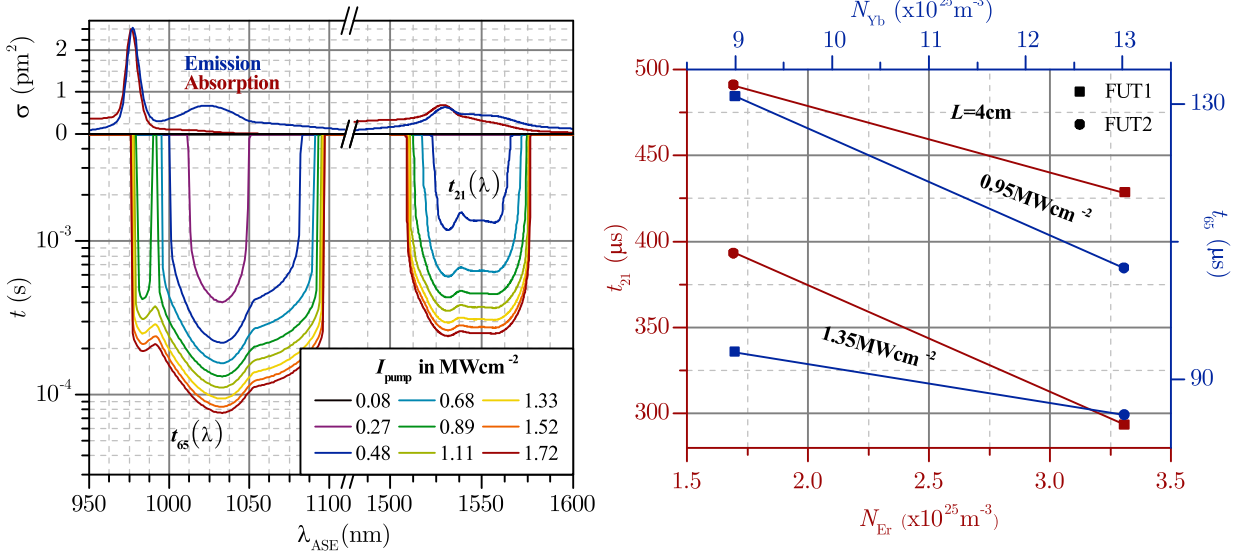**Table 4.1:** Minima of $t_{21}(\lambda)$ and $t_{65}(\lambda)$ at 1531 nm and 1033 nm.

cautious estimation of the time period that must be addressed by a potential EMO system. Moreover, the minima of t_{21} and t_{65} were found at $\approx 1033\,\text{nm}$ and $\approx 1531\,\text{nm}$ stipulating the wavelengths that probably encounter parasitic lasing first. Tab. 4.1 gives a list of t_{21} and t_{65} at 1033 nm and 1531 nm around $\approx 1\,\text{MWcm}^{-2}$ pump intensity showing that the EMO system ought to react faster than $\approx 100\,\mu\text{s}$ (and/or $\approx 300\,\mu\text{s}$). For FUT3, t_{21} was found to be larger than for FUT1 and FUT2 because the absence of Yb^{3+} resulted in the lowest pump absorption.

Figure 4.3.1: Top, left: Yb^{3+} and Er^{3+} emission and absorption cross-sections. Bottom, left: t_{21} and t_{65} for FUT1 at different pump intensities. Right: minimum of t_{21} and t_{65} versus doping concentration of corresponding dopant (Yb^{3+}: blue, Er^{3+}: red). t_{21} and t_{65} decreased with doping concentration because higher doped fibers provided more gain within a specific period of time.

---

[11]It must be noted that much shorter t_{21} or t_{65} are possible as a matter of principle. In practice, however, the laser diodes to provide the required pumping power are virtually unavailable.

The right plot in Fig. 4.3.1 shows the dependency on the Yb^{3+} and Er^{3+} doping concentrations, respectively; the results suggest that the processes accelerate with the concentration of the corresponding dopant. The reason may lie in the link between doping concentration and pump absorption because in heavily doped fibers more ions are excited within a specific period of time. In turn, more gain becomes available on a shorter time scale; the maximum gain also increases.

4.4 EMO prototype in PCB format

This section presents the characterization of an EMO system prototyped in PCB format. The setup is depicted in Fig. 4.4.1. The PCB contained a non-inverting Schmitt trigger (TLC372, *Texas Instruments Inc.*, delay: 0.2 µs [144]), high-speed buffer (BUF634, *Texas Instruments Inc.*) and MOSFET[12] (IXTH80N65X2, *IXYS Corporation Inc.*). The setup was toggled by a monitor signal generated from a photo detector, i.e. in practice a pick-off of the seed beam must be aligned to the photo detector. The monitor signal, however, was mimicked by a binary signal with sharp edge (on: 2.35 V, off: 0 V, fall time: ≈2.71 ns) to ease the characterization process. The output of the non-inverting Schmitt trigger was buffered by the BUF634 buffer and toggled the MOSFET. The D-S line of the MOSFET became conductive if the monitor signal falls to zero; the laser diode was short-circuited. The dissimilar on/off levels resulting from the hysteretic logic of the Schmitt trigger prevented shortterm AC-modulations around the toggle threshold to fast-switch the MOSFET. A laser diode (K976DN1RN, *BWT Ltd.*) capable to deliver up to 140 W at 976 nm was used for the characterization process.
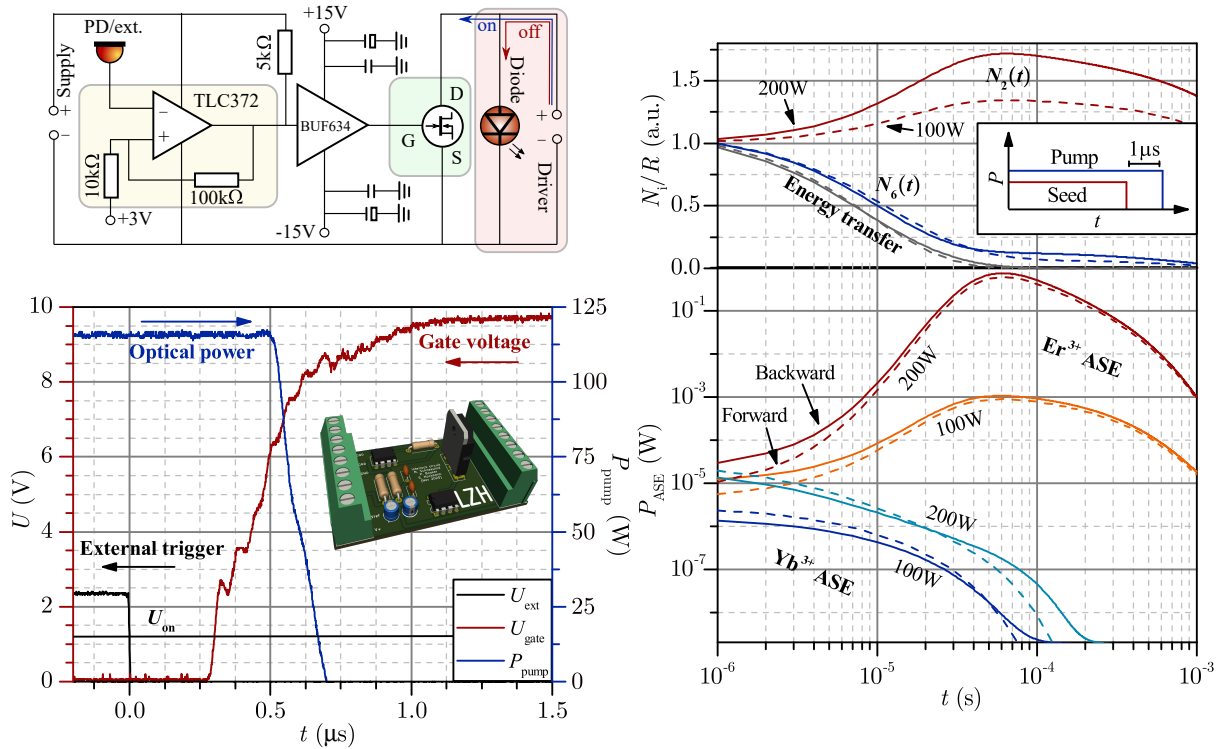

Figure 4.4.1: Top, left: EMO setup with MOSFET (green, IXTH80N65X2, *IXYS Corporation Inc.*) and pump diode (red, K976DN1RN, *BWT Ltd.*). The non-inverting Schmitt trigger (yellow, TLC372, *Texas Instruments Inc.*) toggled the MOSFET and interlocked the pumping process. The photo detector monitored the seed input power. Bottom, left: external trigger signal, voltage at MOSFET gate and output power of the laser diode versus time. The photo detector was replaced by an external signal generator. Top, right: normalized transients $N_1(t)$, $N_5(t)$ and energy transfer rate. The sequence of the pump and seed power is illustrated in the inset: the pump power was shutdown 1 µs after the simulated seed failure. Bottom, right: transients of forward and backward directed Yb^{3+} and Er^{3+} ASE. The simulation parameters were adopted from reference [56].

---

[12]**M**etal-**o**xide-**s**emiconductor **f**ield-**e**ffect **t**ransistor.

Fig. 4.4.1 also shows the transients of the binary signal and the output power of the laser diode. The optical power of the diode declined with a delay of $0.49 \pm 0.04 \, \mu s$ after the monitor signal's descend and approached zero after another $0.21 \pm 0.01 \, \mu s$[13]. The total shutdown time was much less than t_{21} or t_{65}, i.e. $0.70 \pm 0.05 \, \mu s$ versus $\approx 100 \, \mu s$ or $\approx 300 \, \mu s$. The EMO prototype therefore meets the requirements to protect a GWD-compatible EYDFA. The EMO prototype was used as part of the engineering-level amplifier prototype (see Chap. 6).

4.4.1 Verification of EMO prototype performance

The processes after a seed laser malfunction, e.g. optical power evolution and dynamics of the energy levels, that may occur regardless of a timely pump shutdown are analyzed in the following. The analysis was performed with the FEM solver. A 25/300 gain fiber with 0.09 NA was assumed; the total Er^{3+} and Yb^{3+} doping concentrations were $3.7 \times 10^{25} \, m^{-3}$ and $1.3 \times 10^{26} \, m^{-3}$ as the fiber in reference [56], respectively. The investigated pump power levels were 100 W and 200 W at a wavelength of 940 nm; the seed power was 2.0 W at a wavelength of 1556 nm. The optical power levels and energy level populations were pre-computed for 1 ms to meet steady-state conditions; only μW power levels were found for the Er^{3+} ASE and Yb^{3+} ASE because of the seeding process and ongoing Yb^{3+}-to-Er^{3+} energy transfer. Seed and pump input powers were sequentially set to zero with a delay of 1 μs to mimic the performance of the EMO prototype (see Fig. 4.4.1).
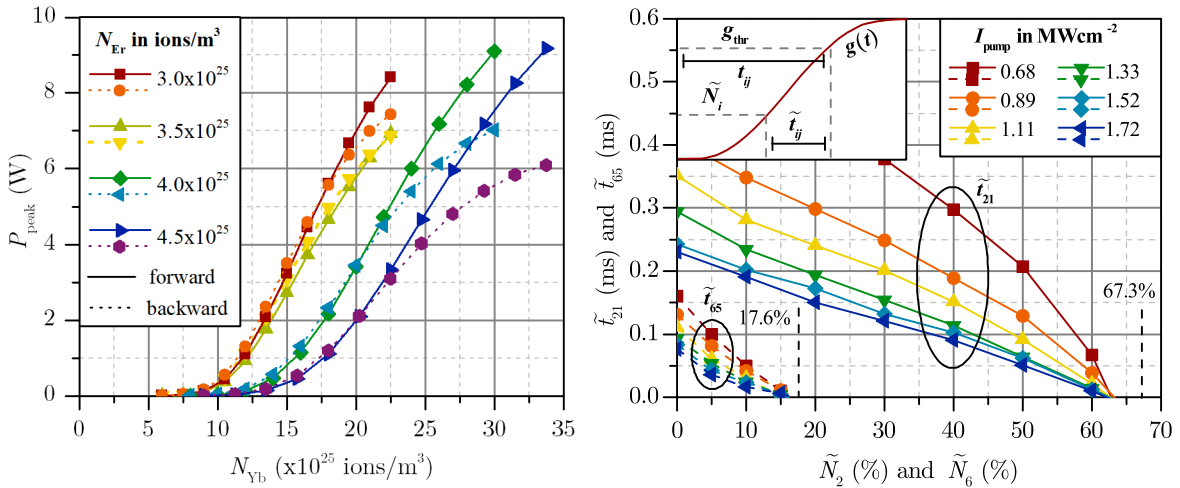

Figure 4.4.2: Left: peak power of the Er^{3+} ASE transients in forward and backward direction for various doping concentrations. The fiber parameters were adopted from reference [56]. Input powers were $P_{pump} = 200 \, W$ and $P_{seed} = 2.0 \, W$ with $\lambda_p = 940 \, nm$ and $\lambda_s = 1556 \, nm$. The pump light propagated in counter-propagation direction. Right: $\tilde{t}_{65}(\lambda)$ and $\tilde{t}_{21}(\lambda)$ versus starting population of laser-active levels. The inset illustrates the definition of t and $\tilde{t}$. The time to reach g_{thr} decreased towards higher starting populations. Above a certain population, g_{thr} was reached during regular steady-state operation.

The transients of the Yb^{3+} and the Er^{3+} ASE, the energy transfer rate and the populations of the laser-active energy levels are shown in Fig. 4.4.1; the transients of the forward (dashed) and backward (solid) directed ASE were similar. No significant excitation took place throughout the short unseeded time window before the EMO system reacted. The Yb^{3+} ASE decayed within $\approx 100 \, \mu s$, which is much faster than the spontaneous lifetime of the $^2F_{5/2}$ energy level ($\tau_{65} = 1 \, ms$). This was possible because the energy from the $^2F_{5/2}$ level was additionally withdrawn through the Yb^{3+}-to-Er^{3+} energy transfer. Moreover, the Yb^{3+}-to-Er^{3+} energy transfer continued to populate the $^4I_{13/2}$ energy level even without pumping. The Er^{3+} ASE therefore peaked after 60.1 μs with $\approx 0.75 \, W$ peak

---

[13]The error was defined as the duration of the slope transition.

power (200 W pump power). The peak power scaled with the ratio between the stored energy and the number of receiving Er^{3+} ions, and thus with the N_{Yb}-to-N_{Er} doping ratio as depicted in Fig. 4.4.2. More Yb^{3+} dopants could store more energy so the peak power increased. In contrast, the total energy required to provide a certain relative Er^{3+} inversion increases with the Er^{3+} doping concentration; the peak power of the Er^{3+} ASE therefore decreased with higher Er^{3+} doping concentrations if the Yb^{3+} doping concentration remained constant. The analysis indicated that only tolerable sub-W peak levels occurred for the assumed doping concentrations and pump power levels; highly Yb^{3+} doped fibers, however, might produce higher, and possibly more destructive, peak power levels.

4.5   Discussion of the combined experimental and numerical approach

The following discusses the shortcomings of the conducted approach. The FUTs in Sec. 4.2 were *unpumped* and *unseeded* at the time of the pump pulse arrival; the laser-active energy levels were therefore depleted. It is only reasonable to assume that the approach overestimated the minimum reaction time ($t_{65} \approx 100\,\mu s$ and $t_{21} \approx 300\,\mu s$) because less time would be required to exceed g_{thr} if the energy levels are non-depleted in the beginning. This means that the EMO requirements may be stricter than estimated. The following, however, shows that the consequence of the overestimation is rather insignificant.

Be $\tilde{t}_{21}$ and $\tilde{t}_{65}$ defined as the interval from the moment at which a certain starting population in the laser-active levels exists and the moment at which the FUTs exceed g_{thr}. Moreover, be $\tilde{N}_2$ and $\tilde{N}_6$ the corresponding starting populations of level 2 and 6. An illustration of these definitions can be found in the inset of Fig. 4.4.2. The right body of Fig. 4.4.2 shows the dependency of $\tilde{t}_{21}$ and $\tilde{t}_{65}$ on $\tilde{N}_2$ and $\tilde{N}_6$. An approximately linear decrease of $\tilde{t}_{21}$ and $\tilde{t}_{65}$ with $\tilde{N}_2$ and $\tilde{N}_6$ was found. Per definition, $\tilde{t}_{21}$ and $\tilde{t}_{65}$ must intersect the y-axis at the values of the non-modified t_{21} and t_{65}; the crossing of the x-axis was found at $\tilde{N}_2 = 62.7\,\%$ and $\tilde{N}_6 = 16.2\,\%$. The crossing points with the x-axis constitute the population levels at which g_{thr} would be exceeded without disruption of the seeding process; the amplifier system would therefore provide enough gain for the parasitic lasing process during regular steady-state operation. Values similar to the crossing points with the x-axis were also found by setting Eq. (4.2) and Eq. (4.3) to $g_{21} = 30\,dB$ and $g_{65} = 30\,dB$, respectively, and assuming depletion of the non-relevant energy levels, i.e. $N_1(t) = 1 - N_2(t)$ and $N_5(t) = 1 - N_6(t)$; values of $\approx 67.3\,\%$ and $\approx 17.6\,\%$ were found. In agreement to that, Fig. 3.2.2 shows that tremendous Yb^{3+} ASE power levels occur if the $^2F_{5/2}$ energy level is populated between 7 % and 36 % (pumping at 976 nm, lasing effects not included). Fig. 3.2.2, however, also shows that average populations of $\approx 52.4\,\%$ and $\approx 7.5\,\%$ (calculated from plotted data) can be expected during regular operation if the system is pumped at 940 nm. Referring to Fig. 4.4.2, this would lead to $\tilde{t}_{21} \approx 0.2 \times t_{21}$ and $\tilde{t}_{65} \approx 0.4 \times t_{65}$, which is at least similar in scale. Hence, the interlock requirements from Sec. 4.3 are assumed to hold as a crude estimation for a pump wavelength of 940 nm. Moreover, a reasonable margin of safety was demonstrated with the setup from Fig. 4.4.1.

Furthermore, the FUTs were pumped at a wavelength of 976 nm; off-peak pumping at 915 nm or 940 nm, however, is preferred as argued in Chap. 3. The longer gain fibers would contain more dopants on an absolute scale. The pump absorption rate, i.e. pump photons per s, would probably remain the same (x00 W pump power). This means that it would take more time (dopants per excitation rate) to populate the laser-active energy levels of an off-peak pumped fiber. Thus, t_{21} and t_{65} would increase; the investigated wavelength of 976 nm stipulates a *worst-case* estimate. The setup from Fig. 4.4.1 demonstrated that even in this *worst-case* scenario a considerable performance margin to the requirements from Sec. 4.3 was achieved, i.e. $0.70 \pm 0.05\,\mu s$ versus $\approx 100\,\mu s$ or $\approx 300\,\mu s$. The EMO prototype from Fig. 4.4.1 is therefore suited to be used for the following work.

4.6 Conclusion

The reaction time required to shutdown the pumping process after a seed laser failure has been studied by a combined numerical and experimental approach with ASE power transients from Er^{3+}:Yb^{3+} doped single-mode fibers. The backward directed ASE transients, separated by a set of 2x2 wavelength division multiplexers, were used to calculate the populations of the energy levels by a time-dependent FEM solver. The fibers were pumped in quasi-cw mode by a single-mode diode at a wavelength of 976 nm. The pump intensities and doping concentrations were in accordance with typical Er^{3+}:Yb^{3+} doped fibers as used in high-power cladding-pump architecture.

The transients of the Yb^{3+} energy levels lasted between 0.14 ms and 0.69 ms depending on the pump intensity. The Yb^{3+} inversion was limited to 50 % due to the quasi-2-level structure of the Yb^{3+} energy scheme. The transients of the Er^{3+} energy levels lasted between 0.38 ms and 2.24 ms; full inversion was reached due to the 3-level structure of the Er^{3+} energy scheme. The populations of the $^4I_{11/2}$ and $^4I_{9/2}$ energy levels were negligible.

It was estimated that a typical LMA fiber would exceed a critical gain of 30 dB in $\approx$100 μs (Yb^{3+} band at 1033 nm) or $\approx$300 μs (Er^{3+} band at 1531 nm) decreasing with pump intensity and concentration of the corresponding dopant because of the larger pump absorption. As a result, more ions were excited within a given period of time to the laser-active levels and, in turn, more gain was available on a shorter time scale.

An EMO prototype in PCB format has been successfully tested to interlock a 140 W pump diode with a wavelength of 976 nm in 0.70±0.05 μs. Nonetheless, it was found by simulations that the Yb^{3+}-to-Er^{3+} energy transfer continues after the shutdown of the pump diode; the population in Er^{3+}'s laser-active level was also found to continue increasing. The simulated Er^{3+} ASE therefore peaked 60.1 μs after the shutdown of the pump diode with 0.75 W peak power. It was found that large Yb^{3+}-to-Er^{3+} doping ratios might lead to W-level Er^{3+} ASE pulses.

Chapter 5

Laboratory-level EYDFA prototype

A non-exhaustive list of single-frequency EYDFAs compliant with the prospective GWD power requirements can be found in Tab. 5.1. Both the thermal stress and its impact on fiber coating degradation were detrimental to the robustness of the listed systems. Therefore, various thermal management concepts were used. Creeden *et al.* cooled the gain fiber by forming cold-contacted fiber spirals [55]. Varona *et al.* coiled the gain fiber on a water-cooled aluminum cylinder [56]. Matniyaz *et al.* even had to immerse the fiber directly into water but power scaling was still limited by a fiber fuse [57]. Additionally, non-PM fibers and free-space coupling of seed and/or pump were used that eventually led to instabilities of the seed/pump input power or its polarization. This makes it inevitable to implement the amplifier with PM fibers, preferably without any free-space part, if the amplifier is planned to be used as a GWD laser. In 2015, Bai *et al.* achieved 56.4 W output power from a PM fiber but had to implement the EYDFA with three amplification stages[1] [104]. Furthermore, GWD-compatible low-noise seed lasers[2], which are important because they can ease the post-stabilization procedure, typically operate only at low power levels. This must be factored into the design process. So far, there is no demonstration of the EYDFA technology in PM all-fiber format with low seed power. There are also no reports on any successful longterm operation ($>$1 day) at tens of W even of a non-PM setup.

Table 5.1: Overview of relevant EYDFA publications.

Authors	Power	Beam quality	Comments	Reference
Creeden *et al.*	207 W	$M^2 = 1.05$	non-PM fibers free-space seed coupling	[55]
Varona *et al.*	111 W	94.8 % TEM$_{00}$	non-PM fibers free-space seed coupling	[56]
Matniyaz *et al.*	302 W	$M^2_{x,y} = 1/1.08$ (244 W)	non-PM fibers free-space seed/pump coupling	[57]
Bai *et al.*	56.4 W	n.a.	three amplification stages	[104]

A laboratory-level two-stage single-frequency EYDFA with PM fibers and low seed input power matching to GWD-compatible seed lasers is presented herein. The two-stage amplifier consisted of a pre- and high-power amplifier and used the off-peak pumping technique. In the following, a custom pre-amplifier system is developed, although compatible pre-amplifier systems are procurable. A custom-made pre-amplifier has the advantage that it gives access to individual components, enables their exchangeability and therefore eases maintenance procedures. A detailed comparison with

---

[1]Carter *et al.* also demonstrated $\approx$21 W (38 % slope efficiency) output power from a PM fiber by pumping at 976 nm [67]. However, the reported power levels were far below the state-of-the-art and Carter *et al.* neither specified the beam quality nor used a low-power seed source.

[2]In 2021, Meylahn and Willke studied compatible seed laser candidates, i.e. an external cavity diode laser (ECDL, RIO3135-3-34-5, *Redfern Integrated Optics Inc.*) and an EDFL (Koheras Adjustik E15, *NKT Photonics Corp.*) [145].

commercially available laser systems is presented in Sec. 5.1.3. Furthermore, Sec. 5.1.3 contains a comparison of the pre-amplifier performance with conventional pumping mechanisms[3]. Moreover, Sec. 5.2 discusses the optical beam properties of the complete laboratory-level two-stage EYDFA. Additionally, an advanced system progressed to an intermediate engineering-level is presented in Chap. 6. The optical beam properties of the engineering-level amplifier and its longterm performance are discussed. Power degradation was observed that is discussed in the context of photodarkening. Furthermore, the fundamental mode power of the laser beam was analyzed with a 3-mirror-cavity. All systems shown hereafter were implemented with commercial off-the-shelf standard fibers making them easy to repair and/or replace. This work has been partially published in reference [146].

5.1 Pre-amplifier

The setup of the pre-amplifier - also referred to as SUT1 in Sec. 5.1.3 - is shown in Fig. 5.1.1. The pre-amplifier was seeded at 1556.65 nm by an 8/125 fiber-coupled single-frequency InGaS/InP multi-quantum-well laser diode with distributed feedback structure (AA1401, *Gooch & Housego Ltd.*, $\approx 25°C$) [147]. The laser diode was derated to 8 mW to match the output power of GWD-compatible seed laser sources. The power slope and optical spectrum of the laser diode are depicted in Fig. 5.1.2. To obtain the data at higher seed power levels, the diode was replaced by an off-the-shelf fiber laser (RFLSA-2000-3-1556.55-UNL-PM-N, *NP Photonics Inc.*, ≈ 2 W and < 10 kHz linewidth).
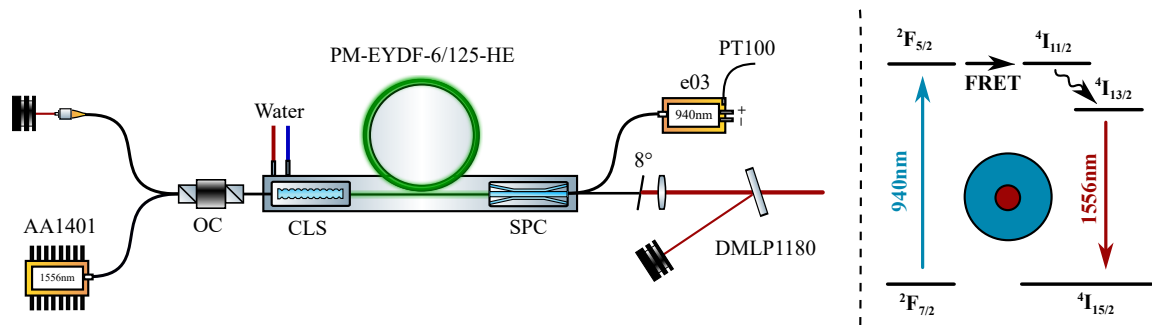

Figure 5.1.1: Setup of the pre-amplifier. The pre-amplifier was off-peak pumped through the $^2F_{5/2}$ energy level at 940 nm in counter-propagation configuration. The figure shows the seed laser diode (AA1401, *Gooch & Housego Ltd.*), the optical circulator (OC, CR-05-0766, *Advanced Fiber Resources Ltd.*), the cladding-light-stripper (CLS), the signal-pump-combiner (SPC), the pump diode (element e03, *nlight Inc.*, 35 W at 940 nm), the collimator lens and the long-pass filter (DMLP1180, *Thorlabs Inc.*). The pump mechanism is illustrated on the right side.

The laser diode was protected from spurious back reflections by an in-line optical circulator (OC, CR-05-0766, *Advanced Fiber Resources Ltd.*). The pre-amplifier was pumped in backward direction at 940 nm through the cladding. The backward pumping technique was used to increase the SBS threshold as demonstrated by Hildebrandt *et al.* [113]. The pump source was a high-brightness single-emitter laser diode (element e03, *nlight Inc.*, 35 W at 940 nm) launched through a matching (2+1)x1 signal-pump-combiner. The residual pump light was removed by a cladding-light-stripper fabricated inhouse by periodic micro-structuring of the fiber cladding with CO_2 laser irradiation. The micro-structured fiber was packaged with UV-curable adhesive for dust protection and stray light shielding. Details on the fabrication process can be found in reference [148]. The 5 m-long 6/125 Er^{3+}:Yb^{3+} doped PM fiber (PM-EYDF-6/125-HE, *Nufern Inc.*) was coiled on a V-grooved aluminum cylinder with 11 cm diameter. The fiber length corresponded to ≈ 10 dB pump absorption as determined by experimental cut-back[4]. The splices were carefully recoated with a low index UV-curable polymer

---

[3]The term *conventional pumping* refers to pumping at 976 nm, around 1480 nm or at 1530 nm.

[4]The cut-back was conducted on a forward pumped amplifier at 940 nm. The pump absorption in reverse direction was assumed to be similar.

resin. The optical fibers were contacted to the mechanics with ceramic-based thermal grease. The pre-amplifier was mounted on two water-cooled aluminum cold plates. The baseplate of the pre-amplifier was placed inside an aluminum enclosure for acoustic shielding and the enclosure was decoupled from the optical table with silicon dampers. The output fiber of the pre-amplifier was slanted with an $8°$ angle for the characterization process to suppress optical feedback from Fresnel reflections. The pre-amplifier was spliced after the characterization process to the high-power amplification stage as described in Sec. 5.2.
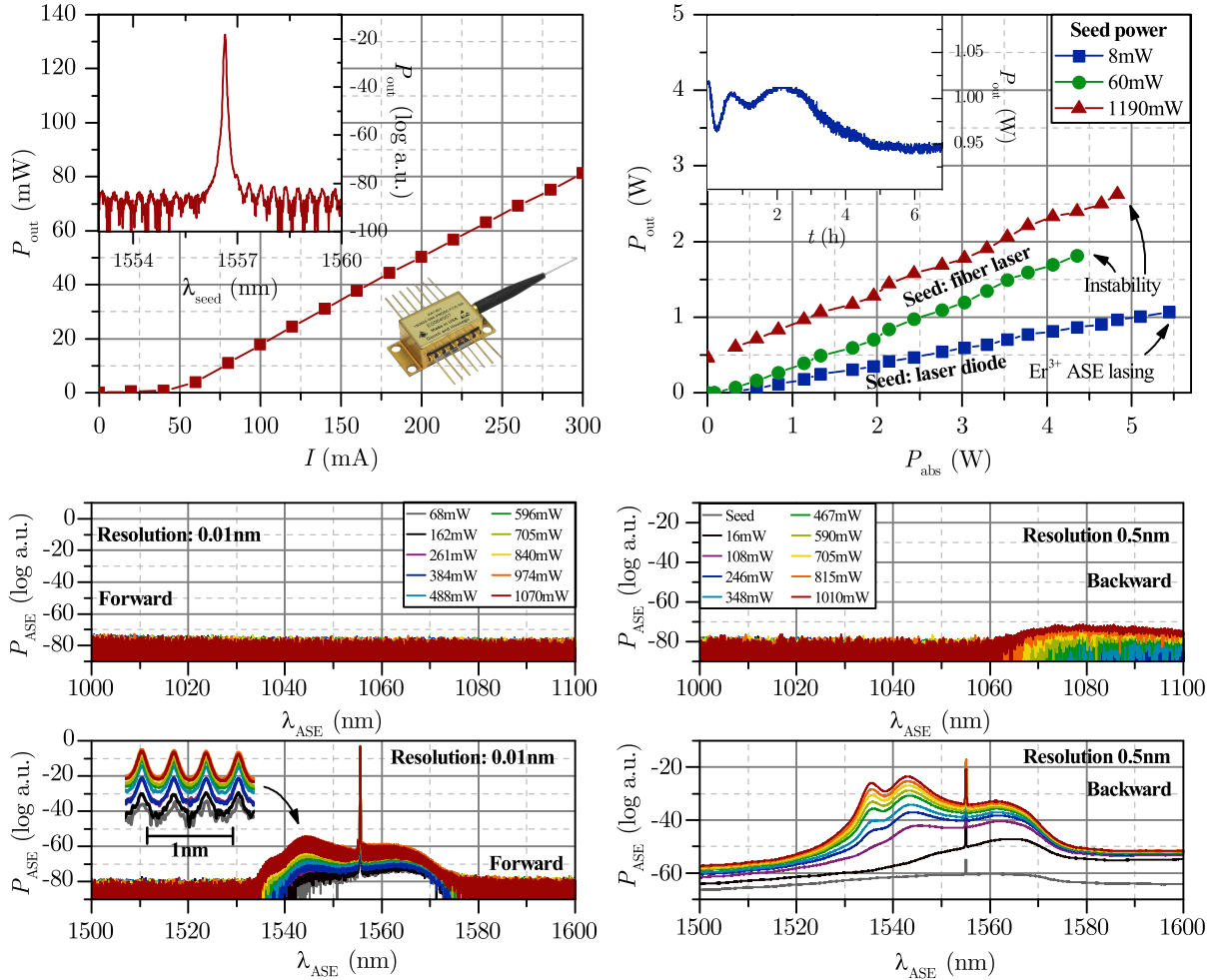
Figure 5.1.2: Power slopes and optical spectra of the pre-amplifier. Top, left: power slope of AA1401 laser diode. Inset: spectrum of AA1401 laser diode at room temperature. Top, right: power slopes of the pre-amplifier. Further power scaling was limited by lasing of the Er^{3+} ASE (8 mW seed power) or power instabilities (60 mW and 1190 mW seed power). Inset: midterm power measurement close to maximum output power at 8 mW seed power. Middle, left: forward directed Yb^{3+} ASE at 8 mW seed power. The long-pass filter was removed for the measurement of the forward directed Yb^{3+} ASE spectrum. Middle, right: backward directed Yb^{3+} ASE at 8 mW seed power. Bottom, left: forward directed Er^{3+} ASE at 8 mW seed power. Inset: zoom-in shows periodic pattern with ≈ 0.35 nm spacing. Bottom, right: backward directed Er^{3+} ASE at 8 mW seed power.

5.1.1 Amplifier slope and optical spectrum

The power slopes plotted in Fig. 5.1.2 were measured with thermopile power heads (LM-10, *Coherent Inc.* or 12A-V1-ROHS, *Ophir Optronics Solutions Ltd.* [149]) and their affiliated data acquisition systems (Fieldmaster, *Coherent Inc.* and Pulsar-4, *Ophir Optronics Solutions Ltd.*). The optical spectra in Fig. 5.1.2 were measured by dispersive grating spectroscopy (OSA, AQ6317C, *Ando Electric Co. Ltd.*). A dichroic long-pass optic (DMLP1180, *Thorlabs Inc.*) filtered the forward directed Yb^{3+}

ASE power. The long-pass filter, however, was removed before the optical spectra were measured. The power slopes were corrected by the losses through the long-pass filter and collimator lens. The absorbed pump power was calculated from the launched pump power and residual pump power[5]. The pre-amplifier was capable to deliver 1.07 W optical power (21.3 dB gain) with 8 mW seed power. Further power scaling was limited by lasing of the blue-sided Er^{3+} ASE around $\approx$1543 nm. The ASE showed a periodic pattern with $\approx$0.35 nm spacing that originated from the seed laser diode (see Fig. 5.1.2, inset of top left plot). The Yb^{3+} ASE was only scarcely notable due to the use of off-peak pumping. It must be added, however, that the fiber coupling to the spectrometer was optimized at 1.55 μm. Thus, the Yb^{3+} ASE power levels plotted in Fig. 5.1.2 may be slightly skewed by chromatic aberrations. The notable red shift of the optical spectra was owed to the 5 m-long fiber and bleached with higher pump and/or seed power. Thermal equilibrium was reached after $\approx$4 h of operation as shown in the inset, which was probably owed to the missing thermal stabilization of the pump diode. The polarization extinction ratio (PER) of the pre-amplifier was $\approx$18.3 dB after warm-up. An optical-to-optical efficiency of only 21.0$\pm$0.2 % was found by linear fitting that was far off the theoretical quantum limit of $\approx$60 %. The reason for this shortcoming was probably unmet seed saturation conditions that increased the effective lifetime in the $^4I_{13/2}$ energy level. The efficiency could be recovered to 42.3$\pm$0.6 % and 44.8$\pm$0.4 % with 1.81 W and 2.67 W output power by using 60 mW and 1.190 W seed power from the fiber laser, respectively. The recovered efficiencies tie in well to a very similar configuration examined by the fiber manufacturer [150]. Further power scaling with the fiber laser seed, however, was discontinued to avoid any damage to the pre-amplifier.

5.1.2 Relative intensity noise and stimulated Brillouin scattering

The knowledge on the relative intensity noise (RIN) is necessary to design a potential power stabilization system for the pre-amplifier, for example via fast pump power control as shown by Thies *et al.* [48]. Furthermore, GWDs use modulated side-bands in the MHz frequency domain for the length and alignment stabilization procedures, which is a second reason why low noise operation at MHz frequencies is required [151]. The RIN was therefore measured as follows. The pre-amplified beam was attenuated by a set of fixed and tunable neutral density filters. The attenuated beam was pointed to an InGaAs photo detector (PDA10CF-EC, *Thorlabs Inc.*). The photo detector was connected to one of two spectrum analyzer instruments (SR785[6], *Stanford Research Systems Inc.* and E4440A, *Agilent Technologies Inc.*), which were used to obtain the radio-frequency spectra from 1 Hz to 102.4 kHz (SR785) and from 1 Hz to 100 MHz (E4440A). The rms, "***root mean square***", of the optical power noise was calculated from the power spectral density as follows:

$$(\text{rms})^2 = \int_f^\infty \left[\mathcal{S}(\text{Hz}/\sqrt{\text{Hz}}) \right]^2 \partial f. \tag{5.1}$$

It was found that the RIN from 1 Hz to 102.4 kHz decreased with output power as plotted in Fig. 5.1.3 possibly due to excess pump noise and the effective low-pass behavior of the pump-to-signal transfer function [152]. This explanation ties in well with the fact that a broad peak was notable around 1.35 kHz at 68 mW output power at which the pump diode operated close to its threshold current. The RIN of the pre-amplified beam was relatively uniform from $\approx$10 Hz to $\approx$2.85 kHz. A single peak around $\approx$10 kHz contributed significantly to the total rms of $\approx$0.32 % at the maximum power level. The narrow peaks at multiples of 50 Hz matched the utility frequency and therefore originated probably from the electronics.

---

[5]The residual pump power was measured with a forward pumped setup and may thus differ slightly in backward configuration.

[6]The RIN was measured in sections from 1 Hz to 25 Hz, to 200 Hz, to 1.6 kHz, to 12.8 kHz and to 102.4 kHz with 3, 5, 30, 80 and 100 averages. The curves were joined by a LabVIEW script.
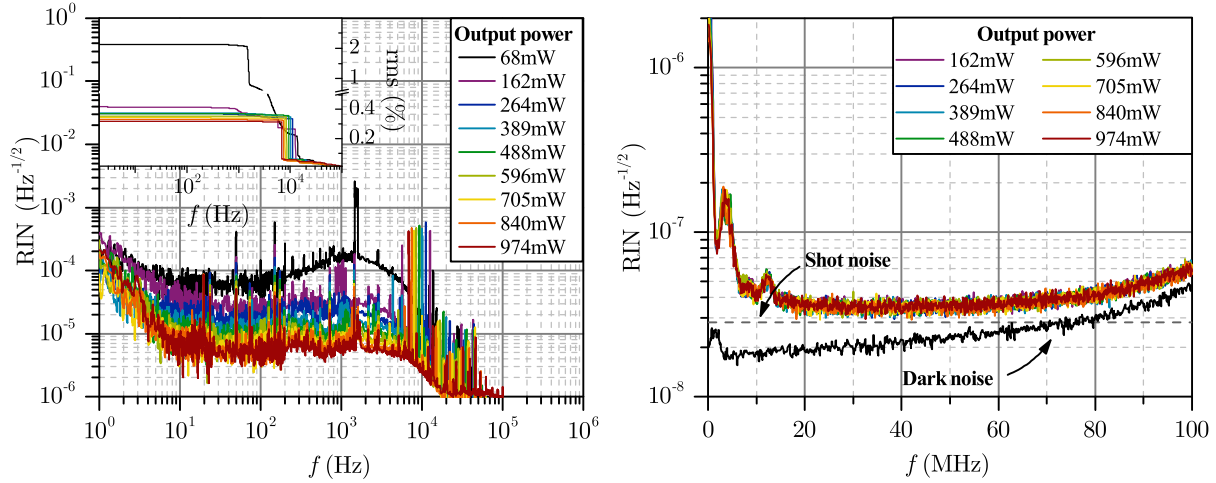
Figure 5.1.3: Radio-frequency spectra of the pre-amplifier. Left: spectrum up to 102.4 kHz measured with SR785 instrument. The excess noise at low power levels was probably caused by excess pump noise. Right: radio-frequency spectrum up to 100 MHz measured with E4440A instrument. The RIN curves coincided and approached the shot noise limit. The dark noise of the photo detector dominated the RIN above 60 MHz.

The onset of SBS imprints a broadband intensity noise on the signal (see Sec. 2.3.1). Thus, the onset and build-up of SBS can be monitored by detecting the RIN in the MHz regime for a power dependent noise increase [113]. The relative shot noise level has been calculated as in reference [56] from the 4 V DC-level on the photo detector and its transimpedance gain $T = 1 \times 10^4$ VA^{-1} to be

$$ S_S = \sqrt{\frac{2eT}{V}} = 2.83 \times 10^{-8}\,\text{Hz}^{-1/2}. \tag{5.2} $$

The relative shot noise is depicted as a grey line in the right plot of Fig. 5.1.3 showing that the RIN of the pre-amplifier approached the shot noise limit in the range between ≈ 20 MHz and ≈ 60 MHz. Above ≈ 60 MHz, the RIN was dominated by the dark noise of the photo detector. The peaks below ≈ 20 MHz originated from the seed laser diode. The coinciding of the RIN curves confirms that the pre-amplifier operated SBS-free at the studied power levels. The theoretical SBS threshold was 22.64 W, which supports this conclusion. The parameters $K_B = 1.5$, $A_{eff} = 36.3\,\mu\text{m}^2$ (MFD = 6.8 μm), $g_0 = 5 \times 10^{-11}$mW^{-1} and $L_{eff} = 1.01$ m and Eq. (2.41) were used for the calculation. Thus, the pre-amplifier yielded much more power scaling potential in the perspective of SBS, particularly because no SBS suppression techniques were used.

5.1.3 Assessment of pre-amplifier performance

The output power of the pre-amplifier - hereafter labelled as system under test (SUT) 1 - is well below commercial off-the-shelf laser systems with GWD-compatible beam properties (see Tab. 5.2). Nonetheless, the use of SUT1 has the following advantages; firstly, as per Fig. 3.2.3, SUT1 provided enough seed power to seed saturate a subsequent 25/xxx fiber; thus, the benefits of higher seed power are diminished. Secondly, SUT1 was fabricated from standard fibers and standard fiber components. Hence, individual fiber components can be replaced easily if damaged. Thirdly, the design of SUT1 contains a single amplification stage only making SUT1 less complex. Fourthly, coupling losses from SUT1 to a subsequent high-power amplification stage can be reduced by fiber splicing; neither free-space coupling nor fiber-to-fiber connections are necessary. The integrability of commercial pre-amplifier systems depends greatly on their optical interface if the device must not be damaged. Fifthly, the performance of SUT1, i.e. PER, noise properties and beam quality, can be accessed where necessary. Thus, information on the performance of individual components can be obtained.

Table 5.2: Overview of commercially available single-frequency PM laser sources at 1.5 μm.

Product model	Type	Supplier	Output power	Reference
Koheras Boostik HP	Laser source	*NKT Photonics A/S*	15 W	[153]
The Rock/RFLSA	Laser source	*NP Photonics Inc.*	5 W	[154]
HOPA-1550	Laser amplifier	*Cybel LLC*	25 W	[155]
CEFL-KILO	Laser source	*Lumibird S.A.*	15 W	[156]
LRL2	Laser source	*RPMC Lasers Inc.*	1 W	[157]

In the following, the performance of SUT1 is benchmarked against alternative amplifier configurations labelled as SUT 2 to 5. The SUTs include direct and indirect pumping of the $^2F_{5/2}$[7] (SUT1, SUT2), $^4I_{11/2}$ (SUT3) and $^4I_{13/2}$ (SUT4, SUT5) energy levels. Details on SUT2 to SUT5 can be found in Appendices A to D. The results are summarized in Tab 5.3 and can also be found partly in reference [146]. The following conclusions can be drawn.

Pumping at 940 nm offers lower ASE power levels than pumping at 976 nm and therefore more power scaling potential as evident from a direct comparison of SUT1 and SUT2. The relative Er^{3+} and Yb^{3+} ASE power levels can be found in Tab. 5.3. When evaluated at maximum output power, the Er^{3+} ASE levels from SUT1 were still 32.77 dB lower compared to SUT2 despite the fact that SUT1 delivered approximately twice the power. The Yb^{3+} ASE was at least 24.46 dB lower but obscured by the sensitivity of the analyzer instrument. The differing ASE levels could not be caused by spectroscopic differences of the used gain fibers because SUT1 and SUT2 were both implemented with the same type of gain fiber from the same batch. For both SUTs, further power scaling was limited by parasitic lasing around ≈1.53 μm. The greatly differing ASE power levels underline the efficacy of the off-peak pumping technique and are in agreement with previous findings from Sec. 3.2.1 and references [55], [56] and [128].

Pumping at 1475 nm, which was used in SUT4, reduces Er^{3+}'s energy level scheme to a quasi-2-level system, which resulted in the lowest Er^{3+} ASE power levels from all SUTs without the risk of detrimental Yb^{3+} ASE. Additionally, the power noise of SUT4 was exceptionally low. Pumping at 1475 nm might therefore become of great interest as a future line to investigate in the scope of GWD-compatible laser sources.

All SUTs had in common that their slope efficiencies were far off the theoretical quantum limit for the used pump and seed wavelengths because of the low seed input power. It was found accordingly for all SUTs that this shortcoming can be remedied by increasing the seed power as per Sec. 5.1.1, Sec. A.1, Sec. B.1, Sec. C.1 and Sec. D.1.

The investigated SUTs showed acceptable noise levels with the sole exception of SUT5 due to its technical shortcomings as discussed in Appendix D. On the contrary, the power noise of SUT4 was exceptionally low.

The SUTs - including SUT1 - operated free of SBS. The long gain fiber used in SUT1 is therefore acceptable in the view of SBS. Indeed, no SBS suppression techniques were used for all SUTs. Additionally, the achieved power levels were well below the theoretical SBS thresholds. Therefore, all SUTs could deliver more power in the view of SBS. It must be added, however, that SBS-free operation of SUT5 could not be verified experimentally.

---

[7]Only possible if the fiber is sensitized with Yb^{3+} ions.

Table 5.3: Overview of the pumping strategies investigated in this work.

System under test	SUT1	SUT2	SUT3	SUT4	SUT5
Pumped energy level	$^2\mathbf{F}_{5/2}$	$^2\mathbf{F}_{5/2}$	$^4\mathbf{I}_{11/2}$	$^4\mathbf{I}_{13/2}$	$^4\mathbf{I}_{13/2}$
Pump wavelength	940 nm	976 nm	976 nm	1475 nm	1530 nm
Pumping technique	cladding	cladding	core	core	core
Pumping direction	counter-propagating		co-propagating	counter-propagating	co-propagating
Fiber type	PM-EYDF-6/125-HE		EDF50-PM EC	TCF1500Y(11/125)HD	Er80-8/125
Manufacturer	*Nufern Inc.*		*OFS Fitel LLC*	*Fibercore Ltd.*	*nLight Inc.*
Fiber doping	Er^{3+}:Yb^{3+}		Er^{3+}	Er^{3+}:Yb^{3+}	Er^{3+}
Mode-field diameter at 1.55 μm	6.8 μm		5.4 μm	10.8 μm	9.5 μm
Fiber length	5.0 m	3.5 m	1.0 m	1.5 m	1.5 m
Pump absorption	10 dB	7.2 dB	10 dB	10 dB	10 dB
Seed source	InGaS/InP laser diode	RFLSA-2000-3-1556.55-UNL-PM-N		InGaS/InP laser diode	
Seed power	8 mW	8 mW	8 mW	8 mW	8 mW
Seed wavelength	1556.65 nm	1556.55 nm		1556.65 nm	
Achievable power	1070 mW	633 mW	141 mW	159.5 mW	119 mW
Gain	21.3 dB	19.0 dB	12.5 dB	13.0 dB	11.7 dB
Slope efficiency	21.0±0.2 %	27.1 %±0.8 %	30.4 %±0.8 %	44.5±0.5 %	25.8±1.2 %
PER	18.3 dB	18.7 dB	25.8 dB	21.0 dB	6.0 dB
Scaling limitation	Parasitic lasing		Available pump power		Pump saturation
Er^{3+} ASE to carrier	-51.43 dB (1070 mW)	-18.66 dB (596 mW)	-36.67 dB (141 mW)	-58.41 dB (159.5 mW)	-13.56 dB (111 mW)
Yb^{3+} ASE to carrier	less than -72 dB (1.07 W)	-47.54 dB (0.60 W)	n.a.	n.a.	n.a.
Stimulated Brillouin scattering	SBS-free operation				n.a.
Calculated SBS threshold	22.64 W	28.93 W	43.89 W	121.22 W	86.16 W
%rms (1 Hz to 102.4 kHz)	0.32 %	0.51 %	n.a.	0.01 %	3.60 %
Reference chapter	5.1	A	B	C	D
Comments	Used as pre-amplifier	Free-space seed coupling		Non-PM fibers	Non-PM fibers

Moreover, the cladding pumping technique appears preferable in technological terms as per comparison of SUT1 and SUT2 with SUT3 to SUT5 because suitable single-mode pump sources that deliver multi-W power levels were unavailable in the scope of this work. A non-exhaustive list of pump sources available on the market is depicted in Tab. 5.4; for example, Raman laser modules (*OFS Fitel LLC*) can provide high power levels around 1480 nm with single-mode beam quality. Nevertheless, Raman lasers have a high degree of complexity[8], which might conflict with the idea of easy maintainability and robustness of potential GWD laser sources. On the contrary, the 976 nm multi-stage master oscillator (MO) power amplifier (PA) laser system from the IR Series (*Azur Light Systems S.A.S.*) is advertised with *maintenance free - long life* [158]. Core-pumping at 976 nm, however, appears to be only a moderately suited pump strategy because of the larger ASE power levels as per results of SUT3.

Table 5.4: Overview of high-brightness (top) and single-mode (bottom) pump modules.

Product model	Supplier	Output power	Wavelength	Reference
D4F1J22	*Dilas Diodenlaser GmbH*	100 W	9xx nm	[136]
ST Series	*Lumentum LLC*	140 W	908 nm - 950 nm,	[135]
K976BN1RN-140.0W	*BWT Ltd.*	140 W	976 nm,	[159]
e18 Series	*nLight Inc.*	>135 W	9xx nm,	[160]
LM976B200GAAF1	*ADC Tel. Inc.*	0.20 W	976 nm	[161]
S30 Series	*JDSU Ltd.*	0.66 W	976 nm	[162]
LC962UF74P-20R	*II-VI Inc.*	0.68 W	976 nm	[163]
AC1409	*Gooch & Housego Ltd.*	0.70 W	976 nm	[164]
BL976-PAG900	*Thorlabs Inc.*	0.90 W	976 nm	[165]
1999CVX	*3SP Technologies S.A.S.*	0.95 W	976 nm	[166]
IR Series	*Azur Light Systems S.A.S.*	10 W	976 nm	[158]
AF4B Series (C)	*Anritsu Corp.*	0.40 W	1480 nm	[167]
S36 Series	*Lumentum LLC*	0.60 W	1470 nm	[168]
Raman laser module	*OFS Fitel LLC*	100 W	1480 nm	[169]

In conclusion, the comparison demonstrates the benefits of 940 nm cladding pumping as implemented in SUT1. The results, however, also suggest that pumping at 1475 nm as used for SUT4 might be suited as well if a multi-W pump source is available. SUT1 was used as a pre-amplifier in the following.

5.2 High-power amplifier

The setup of the two-stage amplifier is shown in Fig. 5.2.1. A description of a similar non-PM setup can be found in reference [56]. The description of the pre-amplifier can be found in Sec. 5.1. The pre-amplifier was operated at 1.07 W output power[9] for at least ≈4 h warm-up time before characterization. The pre-amplifier was protected from spurious back reflections by an optical Faraday isolator (IO-J-1550, *Thorlabs Inc.*). The mode-field-adapter fitted the LP_{01} mode from a passive 10/125 PM fiber to a 25/300 LMA PM fiber. The cladding-light-stripper was fabricated into the very same piece of passive fiber by the method described in Sec. 5.1 to avoid the additional splice. The heat was removed from the housing of the cladding-light-stripper by a water-cooled aluminum heat sink. The 4.5 m-long 25/300 Er^{3+}:Yb^{3+} doped LMA PM fiber (PLMA-EYDF-25P/300-HE, *Nufern Inc.*)

---

[8]Raman lasers are typically pumped by Yb^{3+} lasers that are red-shifted in multiple conversion steps to 1480 nm (≈13.2 THz per step). Hence, Raman lasers include at least pump diodes and fiber Bragg gratings for the Yb^{3+} laser, a Raman cavity, the auxiliary fiber components and the electronics required to operate the system.

[9]Maximum pre-amplified power without onset of parasitic lasing, see Sec. 5.1 for details.

has a 44.7 μm×43.2 μm index pedestal around the fiber core (extracted from end-view images). The doped fiber was contacted with ceramic-based thermal grease to a V-grooved aluminum spool with 19 cm diameter. Two 106.5/125 fiber-coupled pump diodes (ST940B, *Lumentum LLC*) delivered up to 2×140 W pump power at 935 nm[10]; the diodes were stabilized to 298 K by Peltier elements. The pump light was launched in counter-propagation configuration through a matching (4+1)x1 signal-pump-combiner made by the side-fuse technique. Already Matniyaz *et al.* found that the splice surroundings are the critical weak points with respect to the thermal load; the splice of the gain fiber and the matching passive fiber of the signal-pump-combiner was therefore cooled on a separate V-grooved water-cooled heat sink. A sample splice of the passive and active fiber was furthermore examined by X-ray microscopy. The images are depicted in Fig. G.0.1, Appendix G and confirm the accurate alignment of the fiber stress rods with no indication of fiber damage, air or particle inclusions. The splices were recoated to avoid pump light leakage and to protect the fiber from particle contaminations. The cladding-light-stripper at the output was implemented to remove forward propagating cladding light, which would otherwise deteriorate the optical beam quality. The output fiber was slanted with an 8° angle to suppress optical feedback from Fresnel reflections. The optical beam was collimated by an aspherical lens (A397TM-C, *Thorlabs Inc.*) with a focal length of 11 mm. The reflections from a wedged glass window were used in the following to analyze the optical beam properties.
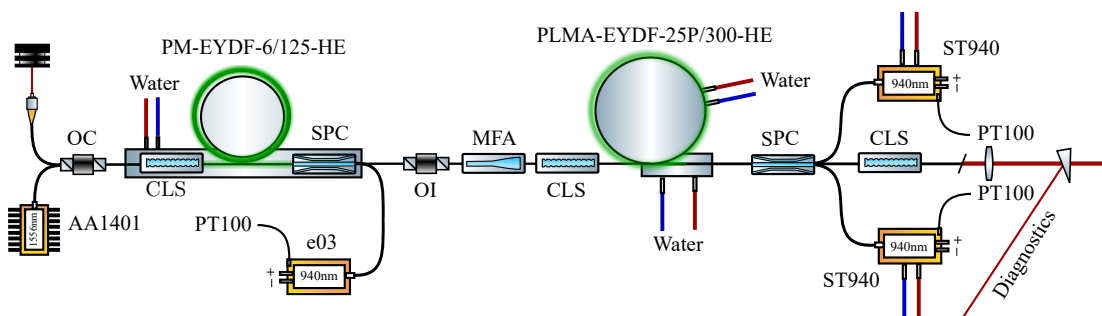
Figure 5.2.1: Setup of GWD-compatible two-stage EYDFA system with pre- and high-power amplifier. The figure contains the pre-amplifier, optical isolator (OI, IO-J-1550, *Thorlabs Inc.*), mode-field-adapter (MFA), cladding-light-stripper (CLS, *FiberBridge Photonics GmbH*), signal-pump-combiner (SPC), pump diodes (ST940B, *Lumentum LLC*), collimator lens and wedged glass window (BSF2550, *Thorlabs Inc.*).

5.2.1 Amplifier slope and optical spectrum

The power slope of the two-stage amplifier shown in Fig. 5.2.2 was measured by a thermopile power head (FL300A-SH, *Ophir Optronics Solutions Ltd.*) and the affiliated data acquisition system (Pulsar-4, *Ophir Optronics Solutions Ltd.*). The optical spectra plotted in Fig. 5.2.3 were measured by dispersive grating spectroscopy (OSA, AQ6317C, *Ando Electric Co. Ltd.*). The absorbed pump power was calculated by assuming a cladding light attenuation of ≈2.17 dB per m at 940 nm as calculated from reference [130] and assuming 90 % coupling efficiency of the pump light. The power slopes were corrected by the losses due to the glass wedge and the collimator lens. The two-stage amplifier delivered up to 110 W optical power. A slope efficiency of 44.4±0.3 % was found by a linear fit. The slope efficiency was close to the theoretical quantum limit of ≈60 % for the used seed and pump wavelengths and similar to references [55], [56] and [57]. In fact, the efficiency was higher than achieved, for example, by Yb^{3+} ASE suppression through a co-pump-propagating Yb^{3+}-band auxiliary signal [170]. A slight kink appeared in the power slope around ≈50 W output power after turning-on the second pump diode, which is probably a calibration error of the actual launched pump power. The optical spectra plotted in Fig. 5.2.3 confirm that the amplifier operated free of parasitic

---

[10]See Sec. 3.2.1 for details.

lasing. The Er^{3+} ASE showed a periodic pattern with ≈ 0.35 nm spacing that originated from the seed laser diode. The extinction ratio of the Er^{3+} ASE was 48.34 dB at 110 W, while the power of the Yb^{3+} ASE was negligible. This underlines the Yb^{3+} ASE suppression effectiveness of the off-peak pumping technique.
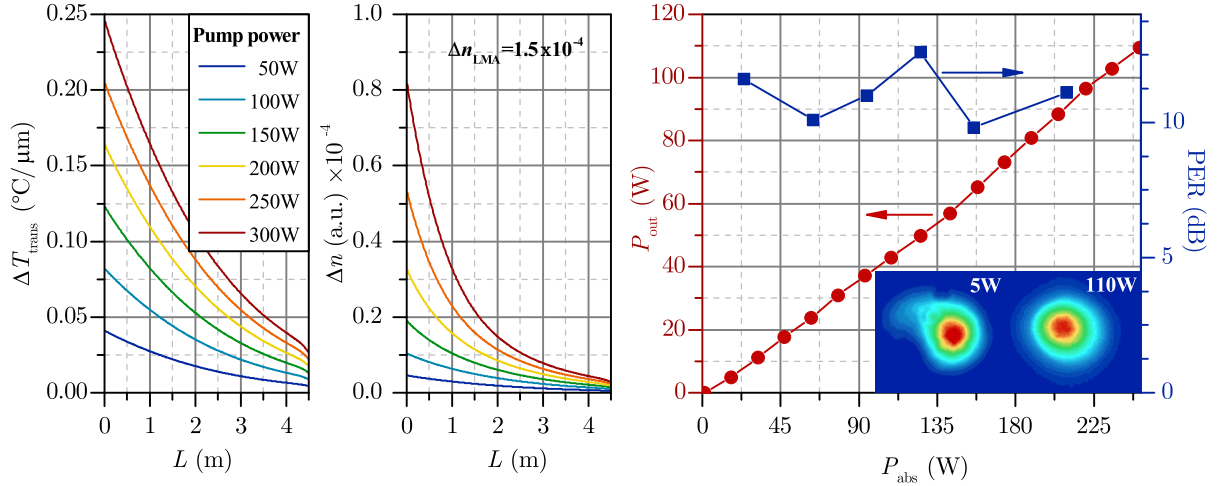

Figure 5.2.2: Left: simulated transverse temperature gradient in the core of a 25/300 Er^{3+}:Yb^{3+} fiber and the resulting birefringence. Right: power slope (left axis) and PER (right axis) of two-stage EYDFA system. The power scaling was limited by a fiber-burn at the splice between the signal-pump-combiner and gain fiber of the high-power amplifier. The beam images were measured at 5 W and 110 W output power.

A fiber-burn in the gain fiber limited further power scaling; the fiber-burn occurred ≈ 10 cm away from the pump end similar to references [57] and [171][11]. The applied pump power at 110 W (power limit) matches the findings from Fig. 3.2.7 showing that the simulated fiber heated to more than 80 °C, which is a critical temperature for the coating, already at around 200 W pump power i.e. ≈ 100 W output power. The simulations further indicated that the fiber temperature may peak slightly distant from the pump end if the Yb^{3+} ASE is considered. In contrast, 207 W output power was achieved by reference [55] with the non-PM counterpart of the gain fiber and a similar cooling approach.
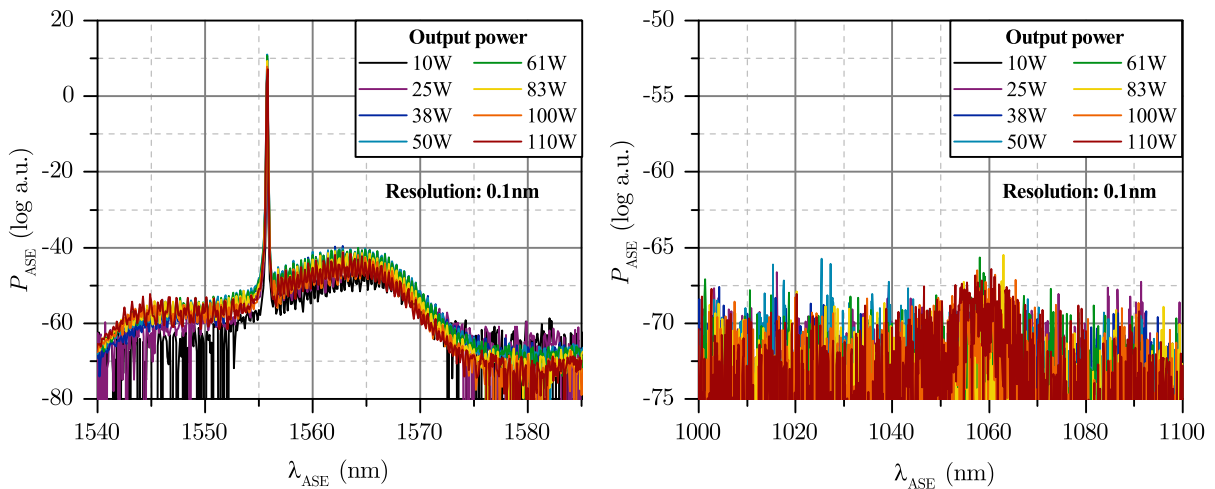
Figure 5.2.3: Optical spectra of two-stage EYDFA. Left: forward directed Er^{3+} ASE. The periodic pattern originated from the seed laser diode. Right: forward directed Yb^{3+} ASE. The colors correspond to different output power levels. The data were measured with an optical spectrum analyzer (OSA, AQ6317C, *Ando Electronics Co. Ltd.*).

---

[11]Reference [171] studied Yb^{3+} doped fibers.

Furthermore, the output beam appeared to be of low beam quality at lower power levels as can be seen on the images obtained from a phosphor-coated IR-camera (SP503U-1550, *Ophir Spiricon LLC*). The beam quality with this particular fiber is further discussed in Sec. 6.3.

The PER shown on the right axis of Fig. 5.2.2 ranged from 9.8 dB to 12.6 dB. Similar values were reported by Varona *et al.*[12] defying the fact that Varona *et al.* used non-PM fibers [56]. The authors, however, reduced the elliptical component of the beam's polarization with a $\lambda/4$-rotator in front of the polarization measurement. In contrast, Bai *et al.* demonstrated 21 dB PER using the very same PM fiber as herein. The following steps were taken to recover the polarization. A deterioration of the polarization from component fabrication flaws was unlikely; the fiber components including the optical isolator (PER: ≈ 26 dB), the combined cladding-light-stripper and mode-field-adapter module (PER: ≈ 27 dB) and the signal-pump-combiner (PER: >18 dB at 1064 nm) were independently tested to maintain the optical polarization. The correct angular alignment of the stress rods was confirmed by the X-ray images of the splice sample (see Fig. G.0.1) showing no indication of misalignment during the splicing process. Furthermore, the PM properties of the fiber chain were verified as follows. A ≈ 94.3 mW probe beam at 1616.9 nm (FPL1054P-SP1, *Thorlabs Inc.*, PER: >20 dB) was injected at the input end of the high-power amplifier; no pre-amplifier was used. The absorption cross-sections of Er^{3+} are ≈ 14 times smaller at that wavelength compared to 1556.65 nm making it possible to measure the PER of the unpumped fiber chain. This technique therefore eliminates any influence of thermal stress and/or the amplification process. The transmitted 1616.9 nm signal showed an acceptable polarization of ≈ 15.1 dB. It was therefore assumed that the polarization deterioration arose either from thermal stress and/or unwanted gain of the light in orthogonal polarization e.g. from scattering at the splice. It was found moreover with the three-term temperature-dependent Sellmeier equation that the birefringence resulting from the transverse temperature gradient across the fiber core amid operation (see Fig. 5.2.2) was close to the inherent birefringence value of the PM fiber, which is 1.5×10^{-4} [130]. The Sellmeier coefficients were extrapolated from reference [172] and the transverse temperature gradient was found by the FEM solver from Chap. 3. Therefore, thermo-optical processes could have influenced the PM properties of the fiber. Similar unsatisfying polarization properties were also found with a thulium-doped pedestal fiber (PLMA-TDF-25P/400-HE, *Nufern Inc.*) [173], which also raises the possibility that the problem was associated with the pedestal. At the time of submission, the origin of the unsatisfying polarization properties of this particular fiber is not completely understood. Further investigations of this PM fiber are therefore necessary, albeit the promising results from its non-PM counterpart [56].

5.2.2 Relative intensity noise and stimulated Brillouin scattering

The RIN of the two-stage amplifier was measured by the procedure from Sec. 5.1.2 as follows. A pick-off beam attenuated by a variable grey filter (NDC-50C-4, *Thorlabs Inc.*) was pointed to an InGaAs photo detector (PDA10CF-EC, *Thorlabs Inc.*). The photo detector was connected to one of the two spectrum analyzer instruments (SR785, *Stanford Research Systems Inc.* and E4440A, *Agilent Technologies Inc.*), which were used as explained in Sec. 5.1.2. The RIN plotted in Fig. 5.2.4 decreased from $\approx 10^{-3}$ Hz$^{-1/2}$ (1 Hz) to $\approx 10^{-6}$ Hz$^{-1/2}$ (102.4 kHz). The peak at 870.59 Hz with 668.11 Hz full-width-half-maximum contributed greatly to the rms power noise of ≈ 0.36 % (calculated as described in Sec. 5.1.2). The RIN from ≈ 5 MHz to ≈ 50 MHz was dominated by the shot noise (calculated as described in Sec. 5.1.2) and above ≈ 50 MHz by the dark noise of the photo detector. The overlapping of the RIN curves at the shot noise level without any power dependent excess noise indicates SBS-free operation of the amplifier. This conclusion is supported by the theoretical SBS power threshold of 214.08 W from Eq. (2.41), which is far higher than the achieved output power of the amplifier. The used parameters were $K_B = 1.5$, $A_{eff} = 327 \, \mu m^2$, $L_{eff} = 0.96$ m ($L = 4.5$ m and 1.07 W to 110 W signal evolution) and $g_0 = 5 \times 10^{-11}$ mW^{-1}.

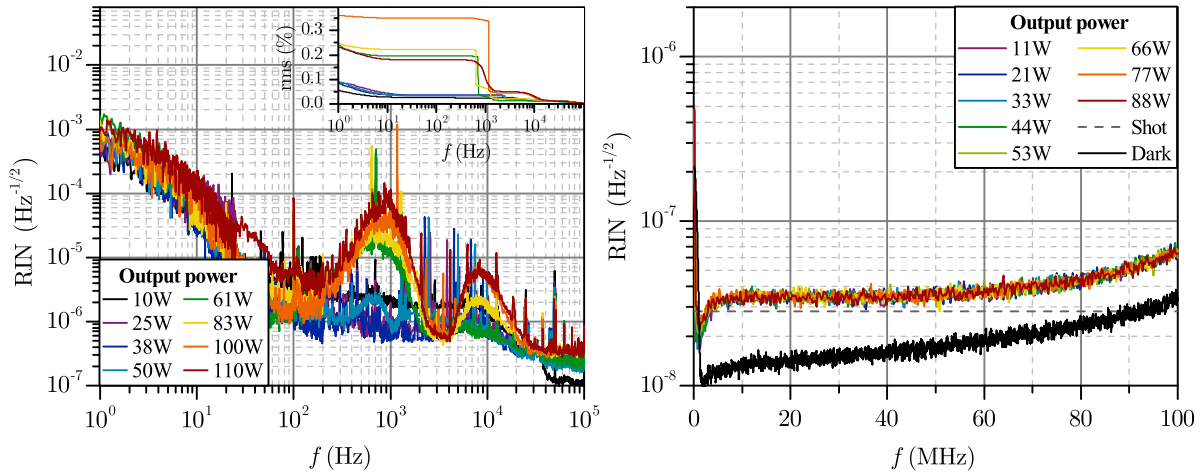[12]The authors demonstrated an average PER of 12.8 dB over the course of 1 h from a non-PM fiber.

Figure 5.2.4: Radio-frequency spectra of two-stage EYDFA. Left: spectrum up to 102.4 kHz measured with SR785 instrument. The rms power noise is shown in the inset. A peak appeared around 870.59 Hz. Right: spectrum up to 100 MHz measured with E4440A instrument. The overlapping of the curves at the shot noise level from 5 MHz to 50 MHz indicates SBS-free operation of the amplifier.

It must be noted that the two-stage amplifier was implemented without any SBS suppression techniques besides backward pumping [113]; for example artificial thermal gradients [113, 115] can be integrated without modifying the fundamental design. In contrast, the application of mechanical stress [116], phase modulations [117] or doping variations [118] may require major modifications. However, the linearity of the power slope, the optical-to-optical efficiency in line with the literature [55, 56] and the absence of the Yb^{3+} ASE indicate further power scaling potential of the two-stage amplifier. A further developed prototype with improved thermal management is therefore under development at *LZH e.V.* as described in Chap. 6.

Chapter 6

Engineering-level EYDFA prototype

The setup of an engineering-level prototype - developed from the system from Sec. 5.2 - is depicted in Fig. 6.0.1 and described in the following. The system was on an advanced engineering-level and featured a revised cooling concept to mitigate thermal fiber damage. Nonetheless, the characterization has been carried out at an intermediate power level of 50 W to guarantee failure-free operation during the characterization process. Two types of suitable gain fibers have been tested, hereinafter referred to as *Nufern* (0.7 wt% Er, 4.9 wt% Yb) and *iXblue* fiber (1.0 wt% Er, 5.4 wt% Yb)[1].
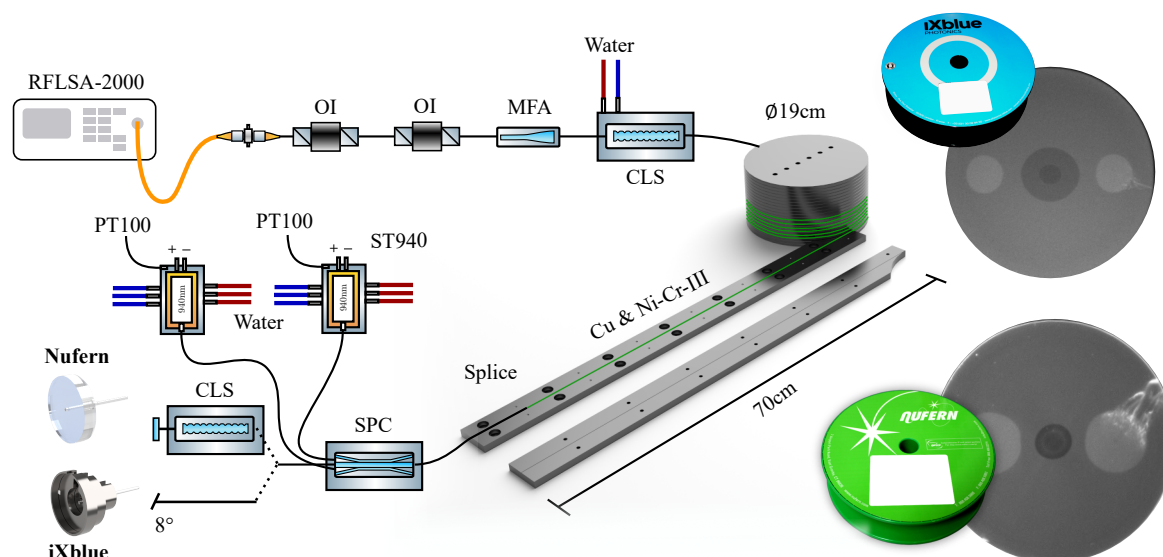
Figure 6.0.1: Setup of the engineering-level prototype. The setup was implemented with a commercial off-the-shelf seed laser (RFLSA-2000-3-1556.55-UNL-PM-N, *NP Photonics Inc.*), optical isolators (OI, IO-J-1550, *Thorlabs Inc.*), water-cooled cladding-light-stripper (CLS), signal-pump-combiner (SPC) and pump diodes (ST940, *Lumentum LLC*, 2×140 W at 940 nm). The fiber chain was terminated with an AR-coated Corning-7980-0F glass window (*Nufern* fiber) or by cleaving with an $8°$ angle (*iXblue* fiber). The gain fibers were coiled on Ni-Cr-III-coated Cu mechanics. Right: images of used gain fibers; the *Nufern* and *iXblue* fibers are 25/300 and 25/250 Er^{3+}:Yb^{3+} doped LMA fibers, respectively. The *iXblue* fiber provides more pump absorption per unit length because of its smaller cladding diameter.

The setup was seeded with a commercial off-the-shelf fiber laser (RFLSA-2000-3-1556.55-UNL-PM-N[2], *NP Photonics Inc.*) derated to 1.71 W. The seed laser featured a power stabilization system based on internal feedback loops and an integrated noise suppressor. Moreover, mode-hopping amid operation was prevented by piezoelectrical actuation of the laser oscillator length. The laser wavelength was tuned to 1556.55 nm by heating the laser oscillator to 73.5 °C. The seed powers launched

---

[1]Obtained by energy-dispersive X-ray spectroscopy with Quanta 400 FEG (*FEI Company Inc.*) instrument.
[2]Specifications: 2 W at 1.55 μm with <10 kHz linewidth.

into the gain fibers were 0.95 W (*Nufern*) and 0.92 W (*iXblue*) with an rms and PER of 0.13 % and 19.3 dB, respectively. The seed powers were sufficient to omit further pre-amplification leading to less complexity compared to the setup from Sec. 5.2[3]. The connection between the seed laser and amplifier was established via FC/APC connectors to maintain the operability of the seed laser for future experiments. The seed laser was additionally protected against backward propagating power by a second optical Faraday isolator (IO-J-1550, *Thorlabs Inc.*)[4]. As in Sec. 5.2, a mode-field-adapter was used to excite only the LP_{01} mode at the input of the amplifier. The mode-field-adapter and Faraday isolators were mounted on a vibration decoupled breadboard to increase the power stability of the coupled seed power. The cladding-light-stripper was fabricated as described in Sec. 5.2 and mounted on a water-cooled cold plate. One of two different 25/xxx Er^{3+}:Yb^{3+} doped LMA PM fibers was used: a 4.5 m-long piece of PLMA-EYDF-25P/300-HE (*Nufern Inc.*) or a 4.2 m-long piece of IXF-2CF-EY-PM-25-250 (*iXblue S.A.S.*).

The front-end of the *Nufern* fiber relative to the amplifier output was prone to thermal damage as per Sec. 5.2.1; the cooling concept has therefore been revised as follows. The front-end of the *Nufern* fiber (50 cm-long, including splice) was enclosed between two straight 70 cm-long V-grooved Cu cold plates to increase the fiber's physical contact with the cooling interface. The front-end of the *iXblue* fiber was embedded on the base plate only without cover to reduce the risk of mechanical breakage and because thermal breakdown was not observed with that fiber yet. The remainders of the gain fibers were coiled on a V-grooved Cu cylinder with 19 cm diameter. The thermal conductivity of Cu is 240 $Wm^{-1}K^{-1}$ to 380 $Wm^{-1}K^{-1}$ [174, 175]; the heat flow within the revised cooling mechanics was therefore larger than in the Al-based mechanics (205 $Wm^{-1}K^{-1}$ [175]) used in Sec. 5.2. The Cu mechanics have been furthermore coated with a Ni-Cr-III layer to prevent corrosion and increase their mechanical robustness. The gain fibers were contacted to the cold plates/cylinder by highly-conductive Al-nanoparticle-based thermal paste ($k = 14.2$ $Wm^{-1}K^{-1}$). The revised cooling mechanics were placed on a 17 °C water-cooled breadboard.

The pump power was launched into the gain fibers through matching signal-pump-combiners (*Nufern*: (4+1)x1, *iXblue*: (2+1)x1) made from passive fibers. The pump diodes (ST940, *Lumentum LLC*, 2×140 W) were heated to 30 °C to reduce the thermal load per unit length compared to the system from Sec. 5.2[5].

The setup was equipped with the EMO system from Sec. 4.4; the system mitigated the risk for total destruction amid operation by interlocking the pump diodes if strong output power degradations would have occurred. Furthermore, a cladding-light-stripper was integrated close to the output end of the *Nufern* fiber to remove residual cladding light, for example from spontaneous emission, and to increase the beam quality. Additionally, a Corning-7980-0F glass window with 12.7 mm×6 mm dimensions was spliced with a CO_2 laser to the output end of the *Nufern* fiber. A picture of the glass window is depicted in Fig. G.0.2, Appendix G. The glass window was coated with an anti-reflectance (AR) coating that reduces residual back reflections at 1.0 µm and 1.5 µm to less than 0.2 % and 0.15 %, respectively. The output end of the *iXblue* fiber was slanted with an 8° angle and glued with UV-curable adhesive in a custom-made 1-inch adapter as depicted in the setup figure.

6.1 Amplifier slope and power stability

The characterization of the engineering-level prototype included a 2-week period of continuous operation. The system's beam properties were recorded at the beginning and at the end of that 2-week

---

[3]The benefits of using SUT1 as outlined in Sec. 5.1.3 were not deemed important enough to outweigh the use of the commercial seed laser.

[4]The total attenuation of the backward propagating power was ≈46 dB and 77.6 dB around 1.0 µm and 1.5 µm, respectively.

[5]The pump wavelengths (Yb^{3+} absorption cross-sections) of the engineering- and laboratory-level prototypes were 937 nm (5.12×10^{-25} m^2) and 935 nm (5.39×10^{-25} m^2).

period. The output power was measured with a FL300A-SH power head and the affiliated Pulsar-4 (*Ophir Optronics Solutions Ltd.*) data acquisition system. The seed power was monitored by a photo detector integrated in the laser device. The 2-week operation period with the *Nufern* fiber was split in three operation cycles, i.e. two 24 h-cycles and one 10-day cycle. The second operation cycle was terminated due to a failure of the laboratory's climate control system; the 10-day operation cycle was shutdown intendedly. The *iXblue* fiber was tested in a continuous 13-day operation cycle without interruption. The experimental results are summarized in Tab. G.1, Appendix G. No deterioration of the optical beam properties with the sole exception of the optical efficiency was observed at the 50 W level during the operation period(s) of both fibers. The results are discussed in the following.
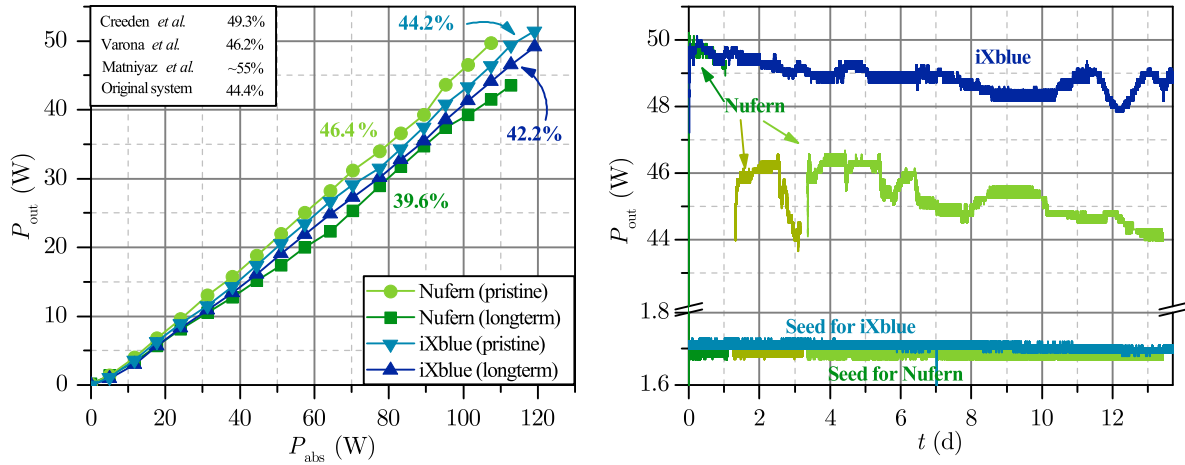
Figure 6.1.1: Left: power slopes of engineering-level prototype with *Nufern* and *iXblue* gain fibers. The slope efficiencies were 46.4±0.5 % and 39.6±0.6 % (*Nufern*) as well as 44.2±0.4 % and 42.2±0.4 % (*iXblue*). The slope efficiencies of the *Nufern* and *iXblue* fibers deteriorated during the longterm test by 14.7±2.2 % and 4.5±0.8 %, respectively. Right: output power during 2-week period. The 2-week period was split for the *Nufern* fiber in three measurement cycles. The first and third operation cycle was terminated intentionally; the second operation cycle was terminated due to a failure of the laboratory's climate control system to protect the amplifier. The *iXblue* fiber was tested over 13 days without interruption.

The slope efficiencies were 46.4±0.5 % (*Nufern*, pristine) and 39.6±0.6 % (*Nufern*, longterm) as well as 44.2±0.4 % (*iXblue*, pristine) and 42.2±0.4 % (*iXblue*, longterm); the slope efficiencies degraded over the 2-week period by 14.7±2.2 % (*Nufern*) and 4.5±0.8 % (*iXblue*) despite being operated only at the intermediate 50 W level. The efficiency loss was permanent in both fibers and could not be recovered by a temporary system cool-down. At the time of writing, the reasons for this growing power loss are not completely understood. Pump diode degradation or damage to the optical isolators were ruled out as the problem because the optical properties of both components were found intact in the final component inspection process. Furthermore, a degradation of the signal-pump-combiner is unlikely at the 50 W level ($\approx$135 W total pump power) because its durability was successfully tested at 405 W throughput power (maximum 150 W per port at 976 nm [176]). The efficiency loss was most probably caused by a gradually growing attenuation in the fiber - called photodarkening - that is induced by intense light irradiation or ionizing radiation. Koponen *et al.* [177] pointed out that photodarkening can be explained on the atomic level by the generation of structural deformations of the glass or the formation of color centers as described by Glebov [178]. The phenomenon was comprehensively studied in Yb^{3+} doped fibers but is also known to exist in Ce^{3+} [179], Pr^{3+} [180], Eu^{3+} [180], Tb^{3+} [181] or Tm^{3+} [182] fibers. It is well known from these studies that the rate and magnitude of the photodarkening process depend on the glass composition of the fiber [183] and the population inversion [184, 185]. It is also known that photodarkening occurs primarily at high power levels. Photodarkening in Er^{3+}:Yb^{3+} fibers was first observed by Robin *et al.* [186]. The process was attributed to the formation of P1 type color centers (PO_3^{2-}) that form from phospho-

65

rous oxygen hole centers (POHC, $PO_4{}^{2-}$ [187]). This process accelerates at high temperatures [188], which would explain why the power loss tends to be more severe at high power levels as reported in references [186, 189]. Robin *et al.* argued that the proposed formation mechanism is supported by the well-known existence of POHCs in X- or γ-ray irradiated phosphorous doped silica [188]. It is also well known by optical spectroscopy investigated by Regnier *et al.* that the absorption band of the P1 color centers lies at 1620 nm [190]. Robin *et al.*, however, emphasized that further spectroscopic analysis is necessary to provide evidence. Moreover, the power stability of the engineering-level amplifier up to the 100 W level is also not known.

6.1.1 Assessment of P1/POHC hypothesis

The following presents evidence that the growing power loss was indeed caused by photodarkening as proposed by Robin *et al*. A more detailed examination of the underlying physical photodarkening mechanism in these particular Er^{3+}:Yb^{3+} fibers, however, is out of the scope of this work.

Firstly, the characteristics of the power loss observed herein are similar to the work of Robin *et al.* [186]. For example, the time scale of the process ties in well to last from a few days to months (herein: $14.7 \pm 2.2\%$ per 13 days for the *Nufern* fiber). Furthermore, the power loss occurred at $15.21\,\mathrm{MWcm^{-2}}$ (*Nufern*) and $15.17\,\mathrm{MWcm^{-2}}$ (*iXblue*) signal intensity. In reference [186], the photodarkening process already started around $6\,\mathrm{MWcm^{-2}}$ to $9\,\mathrm{MWcm^{-2}}$ but no later than $17.7\,\mathrm{MWcm^{-2}}$ (derived from publication). Reference [189] found evidence in another study that the photodarkening process may not start below $\approx 21\,\mathrm{MWcm^{-2}}$. However, only a time period of $\approx 4\,\mathrm{h}$ was recorded without covering longterm degradations from days to weeks like in reference [186]. Moreover, the fiber burn of the laboratory system in Sec. 5.2 occurred at $\approx 33.6\,\mathrm{MWcm^{-2}}$; therefore, it may be possible that the photodarkening process played a crucial role in the damaging process.

Secondly, the atomic composition was analyzed by energy dispersive X-ray spectroscopy revealing 13.6 wt% of P in the *Nufern* fiber[6]; 2.8 wt% of Al and 11.8 wt% of P were found in the *iXblue* fiber. The lower P content may have led to less P-related defects, which would explain why the growing power loss was less evident with the *iXblue* fiber. Moreover, the Al doping in the *iXblue* fiber reduces the phosphorous-oxygen double-bonds, which act as POHC precursor sites [191]. The Al doping therefore decreases the P-related defect susceptibility as argued by Girard *et al.* [191]. The incorporation mechanism of the Al in the phosphosilicate lattice can be found in reference [192].

Thirdly, a growing attenuation at 1556.55 nm was found for two phosphosilicate fibers - including the *iXblue* fiber - in Appendix F. This finding supports the proposed POHC-to-P1 formation mechanism through heat.

Fourthly, reference [57] suspected coating degradation as the origin of the fiber damage. In this work, however, no visible coating degradation was found. Additionally, a $\approx 5\,\mathrm{dB}$ lower core transmission, which cannot be affected by the coating condition, was found without pumping. The transmitted power, however, was only some tens of mW, which is close to the minimal resolvable power of the FL300A-SH power head. Furthermore, the observed attenuation of the unpumped fiber might have been further skewed by the strong small signal absorption of Er^{3+}.

6.2 Optical spectra and PER

The optical spectra are shown in Fig. 6.2.1. The optical spectra from both fibers were free of parasitic lasing up to 50 W output power. The Er^{3+} ASE extinction ratio was 48.59 dB (pristine), 50.82 dB (longterm) for the *Nufern* fiber and 51.16 dB (pristine) and 51.54 dB (longterm) for the *iXblue* fiber. The Er^{3+} ASE from both fibers held more power at shorter wavelengths compared to the system from Sec. 5.2 due to the omission of the pre-amplifier. The total Yb^{3+} ASE power levels from spectral

---

[6]The non-PM fiber showed 1.6 wt% of Al and only 9.1 wt% of P [57] which may explain why much higher power levels of 302 W were possible with that fiber.

integration can be found in Fig. 6.4.2. An Yb^{3+} ASE extinction ratio of 60.02 dB (pristine), 58.77 dB (longterm) was found for the *Nufern* fiber; 42.19 dB (pristine) and 39.88 dB (longterm) was found for the *iXblue* fiber. The somewhat lower Yb^{3+} ASE extinction ratios from the *iXblue* fiber were probably a result of the fiber's larger pump absorption (*Nufern*: 2.9±0.5 dB per m at 915 nm, *iXblue*: 3.9±0.7 dB per m at 915 nm) that distributed the pump energy less homogeneously along the *iXblue* fiber and diminished the benefits of the off-peak pumping technique.
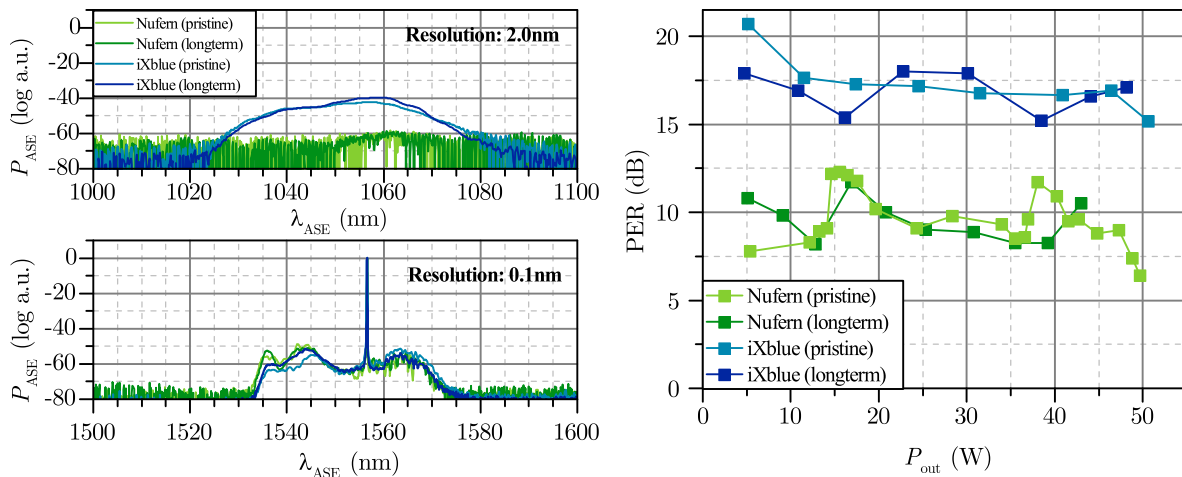
Figure 6.2.1: Left: optical spectra of *Nufern* (green) and *iXblue* (blue) fibers at 50 W output power. The spectra were measured with the AQ6317C (*Ando Electric Co. Ltd.*) spectrum analyzer instrument; the resolution bandwidths were 2.0 nm and 0.1 nm. The spectra were normalized to the signal peak at maximum output power. Right: PER from the *Nufern* and *iXblue* fibers measured with $\lambda/2$ rotator and polarizing beam splitter.

The PER is shown in Fig. 6.2.1. The beam from the *Nufern* fiber was polarized between 6.4 dB and 12.3 dB; the range was similar to the results from Sec. 5.2.1 i.e. a range between 9.8 dB and 12.6 dB. This was probably a result of the beam's low fundamental mode power as per Sec. 6.3. The output from the *iXblue* fiber was acceptably polarized between 15.2 dB and 20.7 dB.

6.3 Beam characterization by diagnostic breadboard

A GWD-compatible laser source must provide excellent beam quality. This characteristic is not guaranteed from LMA fibers because their V-number is larger than 2.405 (see Sec. 2.1). This has the consequence that - even if the seed light is perfectly launched in the LP$_{01}$ mode at the fiber input - microscopic defects, environmental perturbations or ASE can transfer energy from the fundamental mode into HOMs. The M^2 parameter can be used to characterize the beam quality if it is important for the application. The M^2 parameter compares the divergence of the laser beam with the divergence of an ideal fundamental mode. Wielandy, however, demonstrated that single-mode operation is not guaranteed even for low M^2 parameters of 1.1 [194]. Also Kwee *et al.* pointed out that the
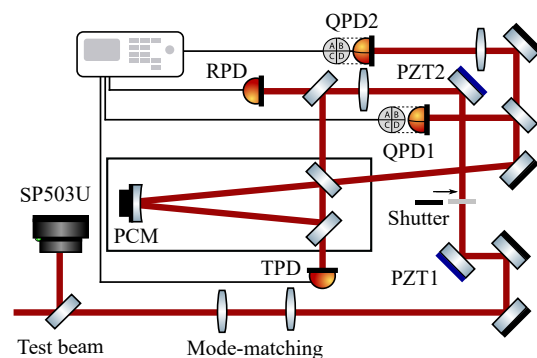

Figure 6.3.1: Setup of the DBB instrument with 3-mirror optical ring resonator, photo detectors RPD, TPD, QPD1 and QPD2 and piezo-tiltable mirrors PZT1 and PZT2 [193]. The resonator can be *scanned* by a piezo-controllable mirror called PCM. The transverse beam profile was imaged with an IR-camera (SP503U-1550, *Ophir Spiricon LLC*).

fundamental mode power[7] is a better criterion to characterize the beam quality in some fields of applications [193]. Therefore, the power in the fundamental mode is used in this work.

The fundamental mode power was analyzed by the *Diagnostic Breadboard* (DBB) instrument developed at the Albert-Einstein-Institute, Hanover. The setup is shown in Fig. 6.3.1; details of a similar instrument for a wavelength of 1064 nm can be found in reference [193]. The instrument contains a non-confocal 3-mirror optical ring resonator with finesse $\mathcal{F} = 250$ for p-polarization and a free spectral range of 714 MHz. The instrument also contains four germanium-based (quadrant) photo detectors to measure the optical properties of the laser beam, labelled as RPD, TPD, QPD1 and QPD2.

The fundamental mode content was obtained with the *mode scan* procedure. The laser beam was expanded in the optical ring resonator into the Hermite-Gaussian transverse electro-magnetic (TEM) modes[8]. The optical ring resonator therefore acted as a selective mode filter because each TEM mode has a different resonance frequency. Additionally, a phosphor-coated IR-camera (SP503U-1550, *Ophir Spiricon LLC*) was used for beam imaging.

The pointing and frequency noise was obtained as follows. The round-trip length of the optical ring resonator was stabilized to the laser frequency of the fundamental mode by dithering the piezo-controllable mirror labelled PCM [195]. The resulting phase-modulated laser beam was superposed on QPD1 with the unmodulated input beam. The demodulated signal from QPD1 was used to actuate the PCM mirror. The two tiltable piezo-actuated mirrors, namely PZT1 and PZT2, were used for the alignment and pointing stabilization procedure. The optical ring resonator was used as a pointing reference. The associated servo loop signals from QPD1 and QPD2 were used to acquire the pointing noise data. More details on all measurement procedures can be found in references [193, 195].

The fundamental mode content is shown in Fig. 6.3.2. The fundamental mode content from the *Nufern* fiber recovered partly from 49.0 % at 5.38 W to 73.0 % at 49.68 W. The low fundamental mode power is also clearly reflected in the beam images. The mode scan showed that significant power was confined to the TEM modes of higher order despite careful optimization of the mode-matching. Kwee *et al.*, however, already pointed out that the manual mode-matching procedure cannot arbitrarily reduce the measured power of modes that originate from astigmatism and/or ellipticity of the laser beam [196, 193]. Moreover, the cladding-light-stripper at the fiber output failed to recover the fundamental mode power; parasitic cladding modes can hence be dismissed as the origin. Nonetheless, the origin of the unsatisfying fundamental mode content

Figure 6.3.2: Fundamental mode power of *Nufern* and *iXblue* gain fibers with beam images.

from the *Nufern* fiber is unknown at the time of submission. It has been shown, however, that the non-PM counterpart can provide acceptable beam quality. For example, Varona *et al.* demonstrated a fundamental mode content of 94.8 % (111 W, 1556 nm) from the non-PM fiber [125]. Creeden *et al.* also showed with the same non-PM fiber that an M^2 parameter of 1.05 is possible at 207 W [55]; however, no mode decomposition was performed. Matniyaz *et al.* reported an M^2 parameter of 1.40 with the non-PM fiber at 50 W (ISO11146 standard) [57]. Matniyaz *et al.* also reconfirmed that M^2 parameters close to 1 are possible at higher power levels. Kuhn *et al.* achieved 85 % fundamental
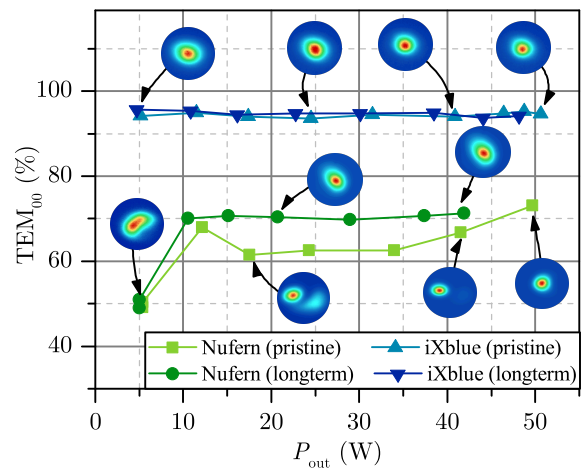
---

[7]The fundamental mode content is the power in the fundamental mode compared to the total power.

[8]The spatial mode at the fiber output is intrinsically an LP_{01} mode, which is close but not identical to a Gaussian TEM_{00} mode.

mode content from the non-PM fiber around 1 W output power at 1535 nm [197]. It is furthermore reasonable to assume that the unsatisfying polarization from the *Nufern* fiber was linked to the low fundamental mode power from that fiber. The *Nufern* fiber is therefore not suited to be used in a GWD-compatible laser source. The fundamental mode content from the *iXblue* fiber ranged between 93.5 % and 95.7 % at the investigated power levels; the fundamental mode content was thus similar to that of the non-PM counterpart of the *Nufern* fiber (see reference [56]).

Fig. 6.3.3 shows the relative pointing noise of the laser beam from the *iXblue* fiber; no relevant dependency on the output power was found. Indeed, the fiber baseline revealed somewhat less pointing noise than the free-space amplifier system of the aLIGO detectors taken from reference [198]. Because vibrations of the free-floating fiber end can contribute greatly to the pointing noise, the following improvement measures are feasible. Firstly, the susceptibility to mechanical disturbances can be mitigated by splicing a glass window to the fiber output. With this technique, Wellmann *et al.* demonstrated that Yb^{3+} doped fiber amplifiers are capable to provide pointing noise levels of $\approx 10^{-4}$ $Hz^{-1/2}$ around 1 Hz at a wavelength of 1064 nm [199]. Secondly, Kwee *et al.* noted that the pointing noise below 20 Hz is dominated by the characterization environment [195]. Further improvements of the pointing performance may therefore be achievable by insulation measures.

Fig. 6.3.3 shows the frequency noise of the laser beam from the *iXblue* fiber; no relevant impact of the amplification process was found by comparing to the frequency noise of the RFLSA-2000-3-1556.55-UNL-PM-N laser (taken from reference [56]). The laser linewidth was calculated as described in reference [189] by the following equation:

$$(\Delta f)^2 = \int_{f_0}^{\infty} [\mathrm{FN}(\mathrm{Hz}/\sqrt{\mathrm{Hz}})]^2 \, \partial f. \tag{6.1}$$

f_0 is the inverse time at which the linewidth is specified and FN the measured frequency noise spectrum. The calculated laser linewidth (120 μs delay time) is shown in the inset of the figure and ties in well with the manufacturer specification of less than 10 kHz obtained from a self-heterodyne measurement (120 μs delay time).
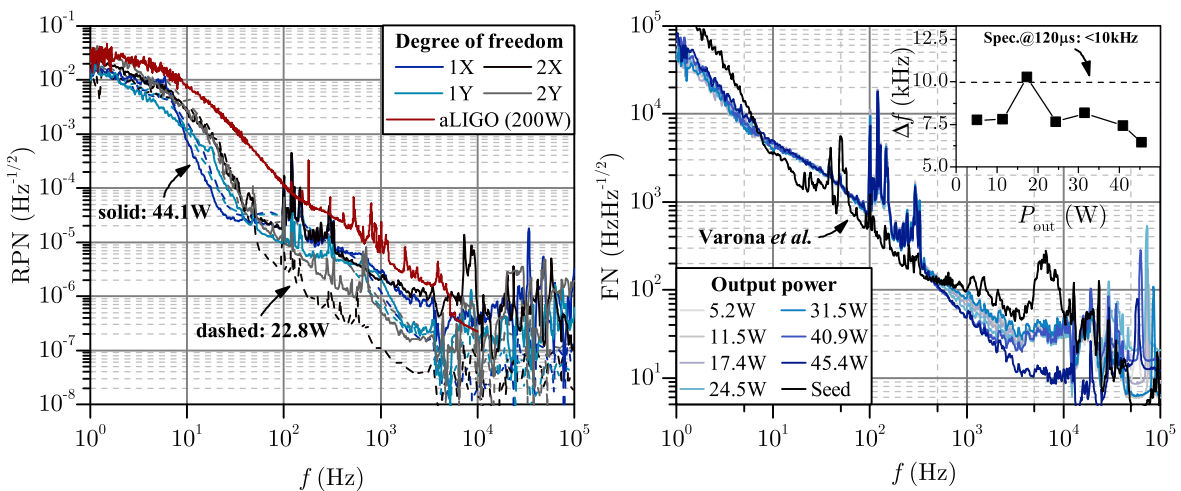

Figure 6.3.3: Left: relative pointing noise of the laser beam from the *iXblue* fiber at 22.8 W (dashed) and 44.1 W (solid) output power. The pointing noise of the aLIGO high-power oscillator was taken from reference [198]. Right: frequency noise of the laser beam from the *iXblue* fiber. No excess noise was added by the amplification process. The corresponding laser linewidth is shown in the inset and in agreement with the specifications from the seed laser manufacturer (<10 kHz, 120 μs delay time).

6.4   Relative intensity noise and stimulated Brillouin scattering

The radio-frequency spectra are shown in Fig. 6.4.1. The method described in Sec. 5.1.2 and Sec. 5.2.2 was used to test for SBS; the curves coincided in the MHz frequency regime at all investigated power levels without any power dependent excess noise. This is a strong indication that the engineering-level prototype operated free of SBS. This result was indeed expected given the findings from Sec. 5.2.2 (similar fiber and length) and ties in well with the theoretical SBS thresholds that are $184.60\,\mathrm{W}$ (*Nufern*) and $208.89\,\mathrm{W}$ (*iXblue*). The theoretical thresholds were calculated from Eq. (2.41) with $K_\mathrm{B} = 1.5$, $g_0 = 5 \times 10^{-11}\mathrm{mW^{-1}}$ and $A_\mathrm{eff} = 326.9\,\mathrm{\mu m^2}$ (*Nufern*) or $A_\mathrm{eff} = 339.8\,\mathrm{\mu m^2}$ (*iXblue*); effective lengths of $1.12\,\mathrm{m}$ and $1.02\,\mathrm{m}$ were found with Eq. (2.42) for the *Nufern* and *iXblue* fibers, respectively.
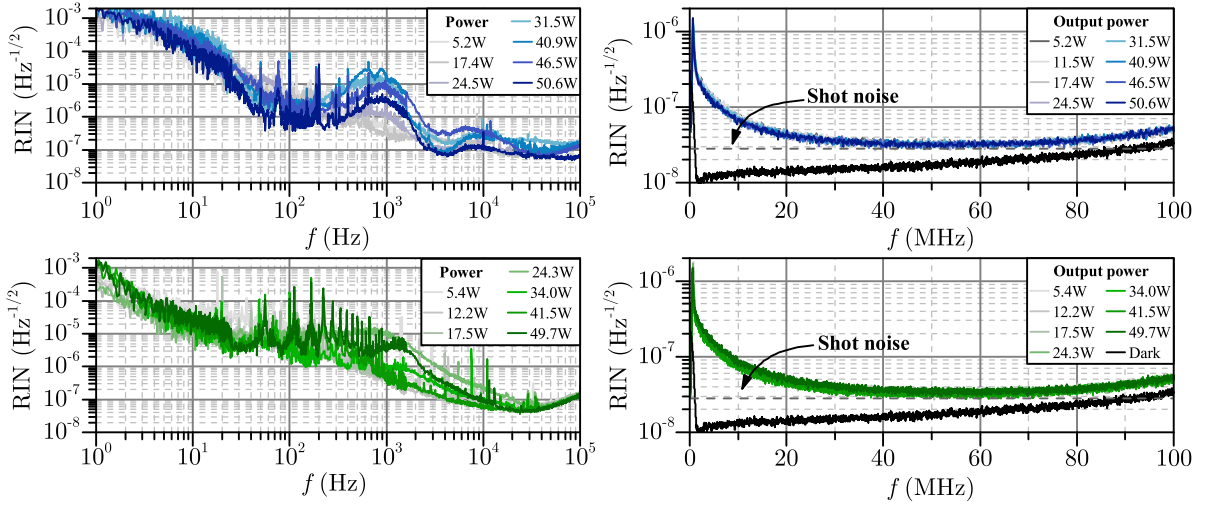
Figure 6.4.1: Radio-frequency spectra of the laser beams from the *Nufern* and *iXblue* fibers. Left: spectra up to 102.4 kHz measured with SR785 instrument. A peak appeared around 850 Hz. Right: spectra up to 100 MHz measured with E4440A instrument. The overlapping of the curves in the range from 5 MHz to 60 MHz at the shot noise level indicates SBS-free operation of the amplifier.

A peak ($\approx$850 Hz, full-width-half-maximum of 556 Hz) emerged in the radio-frequency spectrum of the laser beam from the *iXblue* fiber. The peak appeared as well with the *Nufern* fiber (904 Hz, full-width-half-maximum of 723 Hz) but only above $\approx$50 W output power (see Sec. 5.2.2). The peak was also notable in the radio-frequency spectrum of SUT2 at $\approx$783 Hz with 143 Hz full-width-half-maximum (see Appendix A). The following observations tentatively imply a link to the Yb^{3+} ASE. At the time of submission, further investigation is needed to identify the underlying physical mechanism.

Firstly, the peak's onset power was $\approx$50 W for the *Nufern* fiber and $\approx$25 W for the *iXblue* fiber, which ties in well with the respective onset power of the Yb^{3+} ASE shown in the top left plot of Fig. 6.4.2. Moreover, SUT2 also produced the highest Yb^{3+} ASE output of all SUTs.

Secondly, the peak magnitude was counter-correlated to the coupled seed power as shown in the bottom left plot of Fig. 6.4.2; the peak magnitude increased if the seed power decreased and vice versa. This supports the hypothesis that the Yb^{3+} ASE was responsible for the peak because less seed power also means more Yb^{3+} ASE and vice versa.

Thirdly, a wavelength division multiplexer was added between the mode-field-adapter and optical isolators to co-seed the setup with a fiber-coupled single-mode laser diode (BF-A64-0180-SSF, *Sheaumann Laser, Inc.*). The laser diode provided $\approx$180 mW at a wavelength of 1064 nm. The laser diode was protected from spurious back reflections by a fiber isolator. More details on the auxiliary seeding technique can be found in reference [123]. Fig. 6.4.2 shows that the peak was also suppressed by the co-seed injection. It is also well known that auxiliary seeding reduces the Yb^{3+} ASE, which further supports the link between the noise peak and the Yb^{3+} ASE.

Lastly, Fig. 6.3.3 clearly shows no excess pointing noise around 850 Hz e.g. from the suspended fiber end. This observation was supported by a simplified numerical FEM analysis of a one-end fixed suspended fiber carried out by CATIA software; the first eigenfrequencies were found at 2013 Hz, thus apart from the peak's center frequency. Pointing noise can therefore be ruled out as the origin.
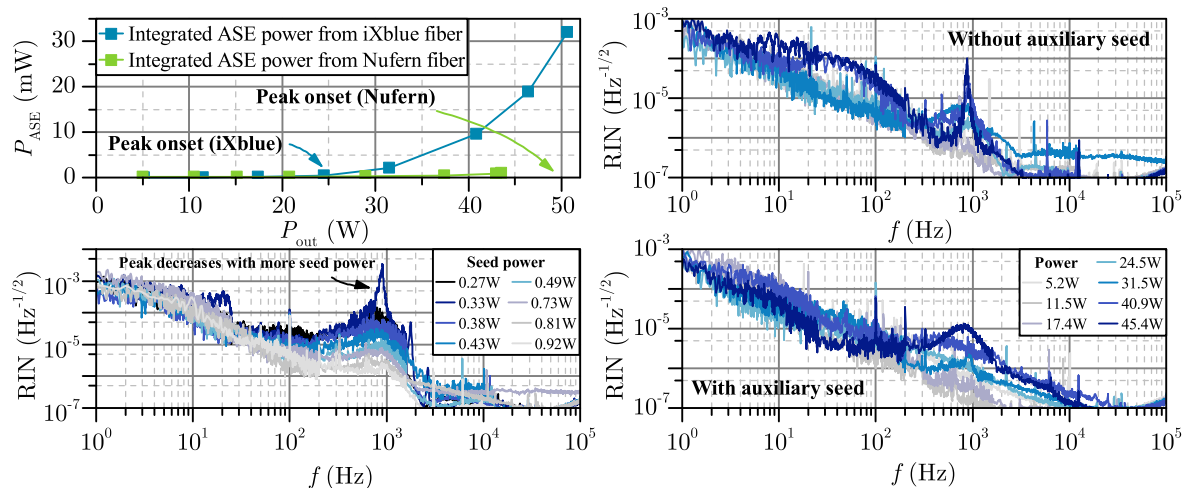

Figure 6.4.2: Radio-frequency spectra of the laser beam. Top, left: forward directed Yb^{3+} ASE power integrated from spectra. Bottom, left: radio-frequency spectrum of the laser beam obtained from *iXblue* fiber. The plot shows that the peak at ≈ 850 Hz increased at lower seed input power and vice versa. Top and bottom, right: radio-frequency spectra of the laser beam from the *iXblue* fiber excluding (top) or including (bottom) the co-seed injection. The peak at ≈ 850 Hz was suppressed by the co-seed injection.

6.5 Conclusion

A high-power single-frequency EYDFA with a wavelength of 1.55 μm in all-fiber PM format has been developed on a laboratory- and advanced engineering-level. The laboratory-level system consisted of a pre- and high-power amplifier; both were pumped off-peak at 940 nm in backward direction. The pre-amplifier provided 1.07 W output power free of parasitic lasing and SBS. The pre-amplifier showed the most power scaling potential benchmarked against conventional pumping mechanisms. The high-power amplifier was implemented with an $Er^{3+}:Yb^{3+}$ doped 25/300 PM fiber from *Nufern*. The laboratory-level system provided 110 W output power with 44.4±0.3 % slope efficiency. The amplifier operated free of SBS with low ASE power levels. The PER, however, only ranged from 9.8 dB to 12.6 dB. Moreover, beam images revealed unsatisfying beam quality at low power levels. Further power scaling was limited by thermal fiber damage ≈ 10 cm away from the pump end.

The advanced engineering-level amplifier was also off-peak pumped at 940 nm; the pre-amplifier could be omitted by seeding with a commercial off-the-shelf laser source. The engineering-level amplifier featured a refined thermal management; nonetheless, the characterization has been carried out at an intermediate power level of 50 W to guarantee failure-free operation during the characterization process. The performance of the system was tested based on the original *Nufern* and an alternative *iXblue* fiber. The *iXblue* fiber performed reliably at the 50 W level without significant power loss; thus, the *iXblue* fiber seemed more heat resilient under operation than the *Nufern* fiber. The noise properties of the *iXblue* fiber were also acceptable. Furthermore, the PER was recovered to up to 20.7 dB with the *iXblue* fiber and the beam quality was improved to up to 95.7 %. Moreover, the Er^{3+} and Yb^{3+} ASE power levels were low and no indication of SBS was found. It is concluded that the *iXblue* fiber is suited to be used in a GWD-compatible laser source; the characterization on the 100 W power level has to be still carried out.

Chapter 7

Summary and outlook

In 2015, the space-time distortion caused by GW150914 was found - a pivotal event that inaugurated the era of interferometric gravitational wave astronomy. As of today, gravitational wave observations are routinely made with proper sky localization by the world-wide operating detector network of the second generation. The audio-band sensitivity of today's detectors is limited by the quantum[1] and coating thermal noise. The quantum noise can be suppressed by frequency dependent squeezing and higher laser powers. The coating thermal noise can be mitigated by cooling the detector to cryogenic temperatures. Cryogenically cooled detectors, however, must use optics made of materials other than fused silica, e.g. crystalline silicon. Crystalline silicon is opaque at the currently used laser wavelength of 1064 nm but transparent around 1.55 μm. Er^{3+}-based fiber amplifiers - the workhorse devices for optical power amplification at 1.55 μm - may therefore play an important role in the next detector generation.

Up-conversion processes within clustered Er^{3+} ions and/or non-linear effects can limit the achievable output power of purely Er^{3+} doped single-frequency fiber amplifiers. The cluster formation can be prevented by codoping the Er^{3+} fibers with Yb^{3+} ions. The Yb^{3+} ions also provide strong pump absorption at 9xx nm and transfer the absorbed energy to the Er^{3+} ions via the Yb^{3+}-to-Er^{3+} energy transfer. The energy transfer can stagnate at high power levels; then, Yb^{3+} ASE can occur, which reduces the efficiency of the device. Pumping at wavelengths with low absorption suppresses the Yb^{3+} ASE but requires longer gain fibers; hence, further power scaling might be limited by SBS at some point.

This work found by numerical simulations that the achievable output power is limited by the Yb^{3+} ASE for pump wavelengths from 880 nm to 990 nm; SBS limits the output power for pump wavelengths shorter than 880 nm or longer than 990 nm. Pumping at 940 nm was found to provide good power scalability; suitable pump diodes can be procured as off-the-shelf products with proven reliability.

Catastrophic Yb^{3+} or Er^{3+} ASE power levels, e.g. during a seed laser failure, can damage the amplifier; the implementation of a protective EMO system is therefore necessary. This work identified the reaction time that a potential EMO system must comply with by using a combined numerical and experimental approach with ASE transients from single-mode fibers. It was found that the EMO system must react within ≈100 μs and/or ≈300 μs to prevent catastrophic Yb^{3+} and/or Er^{3+} ASE power levels. An EMO prototype in PCB format was developed; the prototype had a reaction time of 0.70±0.05 μs and was found capable to meet this requirement. The EMO prototype was installed as part of the engineering-level amplifier.

A GWD-compatible single-frequency EYDFA made with PM fibers[2] from *Nufern* was presented

---

[1] The quantum noise is dominated by radiation pressure noise at low frequencies; photon shot noise dominates the quantum noise at high frequencies.

[2] The latest progress on high-power single-frequency EYDFAs was made using non-PM fibers which makes the latest systems unsuited as GWD laser sources.

in Chap. 5. The system was on a laboratory-level and consisted of a pre- and high-power amplifier; both amplifiers were pumped off-peak at 940 nm in backward direction. The pre-amplifier provided 1.07 W output power with low ASE power levels and operated free of SBS. A comparison of different pumping mechanisms showed that pumping at 940 nm provided the highest output power under the criteria of comparison. The high-power amplifier delivered up to 110 W output power at 1.55 μm with 44.4±0.3 % optical-to-optical efficiency. The amplifier operated SBS-free; the ASE power levels were low emphasizing the efficacy of off-peak pumping. Further power scaling was limited by thermal fiber damage assumed to originate from photodarkening; further evidence, however, must be provided. Moreover, the polarization of the system was only ≈11 dB probably owed to deficient polarization properties of the used *Nufern* fibers.

An engineering-level amplifier was characterized in Chap. 6. The amplifier featured a refined cooling concept and was implemented with a fiber from *iXblue*; the fiber performed reliably at the 50 W level without significant power loss. Thus, the fiber seemed more heat resilient under operation than the *Nufern* fiber. Furthermore, the noise properties were acceptable, the Er^{3+} and Yb^{3+} ASE power levels were low and no indication of SBS was found. Additionally, the PER recovered to up to 20.7 dB with that fiber. The beam quality improved to up to 95.7 %. The *iXblue* fiber is therefore suited to be used in a GWD-compatible laser source. The promising results highly motivate to follow-up with the characterization at higher power levels.

As shown and argued throughout Chap. 6, the optical beam properties from the *iXblue* fiber are in line with the foreseeable laser requirements of the third detector generation. The thermal stress and/or fiber coating degradation, however, remain challenging obstacles for further power scaling; the quantum defect between the $^4I_{11/2}$ and $^4I_{13/2}$ energy levels is the main heat source and thus constitutes an inherent shortcoming of the 9xx nm pump band. Furthermore, a growing power loss associated with thermal stress has been observed; the mechanism may play a crucial role for catastrophic fiber damage at high power levels. Therefore, it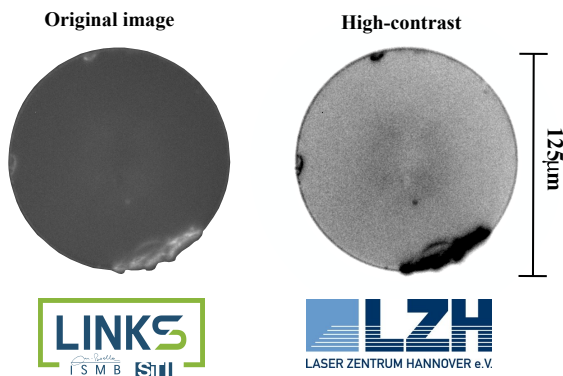 seems only reasonable to investigate pump wavelengths with smaller quantum defect in future activities. For example, a pump wavelength of 1480 nm has a quantum defect of only ≈5 %; moreover, no Yb^{3+} ASE can occur thanks to the lack of Yb^{3+} absorption at 1480 nm.

At the time of writing, the following high-power pump sources are available at 1480 nm: Raman lasers with ≈100 W output power and single-mode beam quality (see reference [169]) as well as laser diode stacks with ≈40 W output power[3] from 200/220 fibers (see reference [200]).

Er^{3+}'s low absorption at 1480 nm can be compensated by using non-standard fibers with higher Er^{3+} doping limits. For example, the *LZH e.V.* has conducted a research collaboration with Fondazione LINKS, Turin (formerly *Istituto Superiore Mario Boella - ISMB*) in 2018 to develop a 12/125 phosphate glass fiber with 0.09 NA. The phosphate glass fiber was doped with 2.60×10^{26} Er^{3+} ions per m^3 (2.0 mol%) without notable lifetime quenching i.e. cluster formation [201, 202]. A picture of the delivered fiber is shown in Fig. 7.0.1.

In total, the availability of non-standard fibers with high Er^{3+} doping concentrations and suitable pump sources strongly motivates to study pumping at 1480 nm as a second line of investigation.

Original image **High-contrast**

125μm

Figure 7.0.1: Image of 12/125 Er^{3+} doped phosphate glass fiber made by Fondazione LINKS, Turin. The contrast of the fiber cross-section was increased with image post-processing showing a potential glass inhomogeneity around the fiber core.

---

[3]A total pump power of ≈160 W can be achieved if used with a (4+1)x1 signal-pump-combiner.

Appendix A

Conventional pump strategy - cladding pumping at 976 nm

SUT2 to SUT5 are investigated in the following; the chapters contain the setups of the SUTs, their power slopes as well as optical spectra and noise properties. The pump strategies include pumping of the $^2F_{5/2}$ (SUT2), $^4I_{11/2}$ (SUT3) and $^4I_{13/2}$ (SUT4, SUT5) energy levels. The key results can be found in Tab. 5.3 and partly in reference [146].
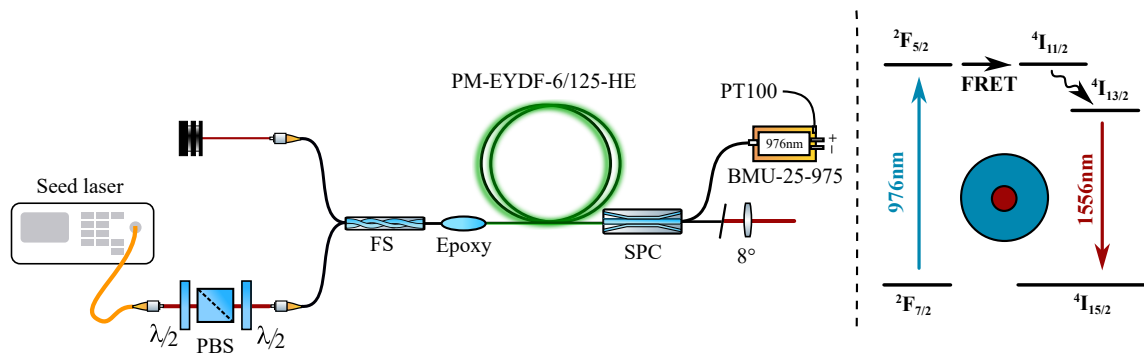

Figure A.0.1: Setup of SUT2. The commercial off-the-shelf seed laser (RFLSA-2000-3-1556.55-UNL-PM-N, *NP Photonics Inc.*) was attenuated by a $\lambda/2$-rotator and polarizing beam splitter (PBS). The system consisted of 2x2 fiber splitter (FS, 1 % splitting ratio), cladding-light-stripper (CLS), Er^{3+}:Yb^{3+} doped gain fiber (PM-EYDF-6/125-HE, *Nufern Inc.*), (2+1)x1 signal-pump-combiner (SPC) and pump diode (BMU-25-975-01-R, *Oclaro Inc.*). Right: illustration of the pumping mechanism with Yb^{3+}-to-Er^{3+} energy transfer using the cladding pumping technique.

The setup of the system presented herein - also referred to as SUT2 - is shown in Fig. A.0.1. The system was seeded at 1556.55 nm by a derated commercial off-the-shelf single-frequency fiber laser (RFLSA-2000-3-1556.55-UNL-PM-N, *NP Photonics Inc.*, 1.69 W with <10 kHz linewidth). A full description of the seed laser can be found in Chap. 6. Free-space seed coupling was used to be able to reuse the seed laser for future experiments. A combination of a tunable $\lambda/2$-rotator and a polarizing beam splitter cube was used to set the seed power. A second $\lambda/2$-rotator was used to align the seed input polarization to the PM-axis of the fiber chain. A 2x2 fiber splitter (1 % splitting ratio) allowed throughout monitoring of the coupled seed power amid operation of the system. If not explicitly specified otherwise, the results presented hereafter were obtained by using 8 mW seed power. The 3.5 m-long 6/125 Er^{3+}:Yb^{3+} PM gain fiber (PM-EYDF-6/125-HE, *Nufern Inc.*) was coiled on the optical table with a diameter of 10 cm. The Er^{3+}:Yb^{3+} energy system was pumped at 976 nm using the cladding pumping technique. The fiber length of SUT2 was relatively short in comparison to SUT1 because of Yb^{3+}'s high absorption at 976 nm. A single emitter based 105/125 fiber-coupled laser diode (BMU-25-975-01-R, *Oclaro Inc.*, 25 W at 976 nm) placed on a 52.4 °C Peltier-controlled heat sink was used as a pump source. Backward pumping was used to increase the SBS threshold

as it was already demonstrated by Hildebrandt *et al.* [113]. The pump light was coupled into the fiber cladding through an in-house manufactured (2+1)x1 signal-pump-combiner. The pump light absorption was determined by experimental cut-back to be 81±5%, which was somewhat less than that of SUT1 from Sec. 5.1. All fiber components were carefully spliced with a fusion splice station (S183P, *Furukawa Electronic Co. Ltd.* or FFS-2000, *Vytron LLC*). The fiber splices were recoated with the sole exception of the splice between the Er^{3+}:Yb^{3+} fiber and the 2x2 splitter, which was submersed in refractive index matching epoxy glue to remove residual pump light from the cladding. The output fiber of the system was cleaved with an 8° angle to suppress optical feedback from Fresnel reflections. The output beam was collimated by an $f = 8.0\,$mm lens (C240TME-C, *Thorlabs Inc.*) and spectrally filtered by a dichroic long-pass optic (DMLP1180, *Thorlabs Inc.*). The optical spectra of the system were measured by optical grating spectroscopy (OSA, AQ6317C, *Ando Electric Co. Ltd.* [203]) without the long-pass filter.
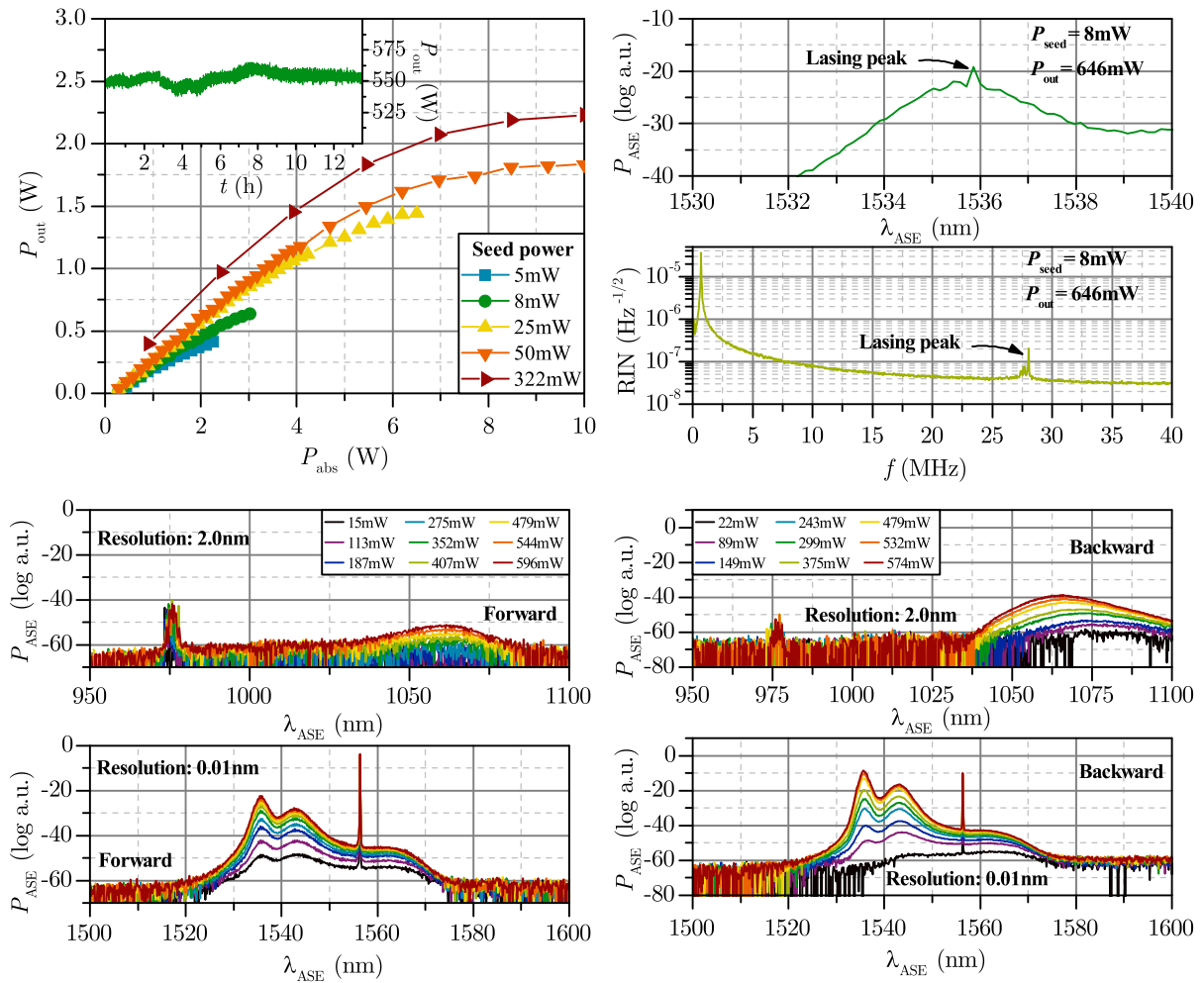

Figure A.0.2: Power slopes and optical spectra of SUT2. Top, left: power slopes of SUT2. The results are color-coded from blue to red according to the used seed power. The power slopes show a saturation pattern due to the generation of the Er^{3+} ASE. The inset shows the longterm performance of the system with 8 mW seed power. Top, right: optical and radio-frequency spectra at 633 mW output power (lasing threshold). Bottom, left: optical spectra in forward direction showing the Er^{3+} and Yb^{3+} ASE. Bottom, right: optical spectra in backward direction. The colors correspond to different output power levels. The backward propagating ASE was measured at the idle port of the fiber splitter. The spectra were measured with an optical spectrum analyzer (OSA, AQ6317C, *Ando Electric Co. Ltd.*). The fiber coupling to the instrument was optimized at 1556 nm.

A.1 Amplifier slope and optical spectrum

The power slopes of SUT2 were measured with a thermopile power head (LM-10, *Coherent Inc.*) and its affiliated data acquisition system (Fieldmaster, *Coherent Inc.*, total accuracy of $\approx 3\%$ [149]). The acquired data was corrected for the 5.2% signal loss through the long-pass optic and lens to represent the output power at the fiber end. The power slopes plotted in Fig. A.0.2 showed a significant saturation pattern, which was probably due to gain depletion through the Er^{3+} ASE, which was apparent in the optical spectra. It is hence only reasonable that further power scaling of SUT2 was limited by parasitic lasing of the blue-sided Er^{3+} ASE near 1536 nm as evident in the top right plot of Fig. A.0.2. The lasing was also apparent in the radio-frequency spectrum at 28.05 MHz corresponding to a total round-trip length of 10.71 m, which roughly accords to twice the length of the gain fiber and the passive fibers. A fit to the linear part of the power slope gave $27.1\pm0.8\%$ slope efficiency[1], which deviated from the theoretical quantum limit of $\approx 62.7\%$ for the pump and seed wavelengths of 976 nm and 1556 nm. The slope efficiency was somewhat similar to the efficiency achieved with SUT1 and also recovered to $34.7\pm1.7\%$ by increasing the seed input power to 322 mW. The maximum lasing-free output power of SUT2 was 633 mW[2] (19.0 dB gain), and thus less compared to SUT1. SUT2 was operated over a period of 12 h without any sign of power degradation as evident in the inset. Further power scaling potential might be achievable by using a longer gain fiber. This would also help to increase the overall efficiency of SUT2, although such was not of interest in this analysis. The reduction of the SBS threshold associated with a longer gain fiber would be acceptable in the view of the achieved power levels and the theoretical SBS threshold (see Sec. A.2). The Yb^{3+} ASE arose at relatively long wavelengths, i.e. ≈ 1060 nm in forward direction and ≈ 1080 nm in backward direction, probably due to re-absorption in the seed-sided end of the gain fiber. More pump power bleached the signal absorption and thus shifted the backward ASE towards shorter wavelengths. The Yb^{3+} ASE power was ≈ 30 dB lower than the Er^{3+} ASE power; therefore, the Yb^{3+} ASE was not the reason for the decay of the slope efficiency. It must be noted, however, that the beam coupling to the spectrometer was optimized at 1556 nm. Thus, the Yb^{3+} ASE power levels may be affected by chromatic aberrations or the wavelength dependent properties of the fiber splitter leading to different absolute power levels at the spectrometer input. The PER of SUT2 was 18.7 dB comparable to SUT1 pumped at 940 nm.

A.2 Relative intensity noise and stimulated Brillouin scattering

The RIN of the free-running SUT2 system is important to design the feedback loops required for potential post-stabilization systems. Thus, the RIN of SUT2 was characterized as described in the following. The reflection from an 8° wedged glass window was aligned to an InGaAs photo detector (PDA10CF-EC, *Thorlabs Inc.*)[3]. The power level of the reflected beam was attenuated by a tunable neutral density filter wheel (NDC-50C-4, *Thorlabs Inc.*) to a constant $V_{DC} \approx 9$ V DC-level on the photo detector. The power spectral density of the beam's AC-signal was analyzed by an electrical spectrum analyzer instrument (SR785, *Stanford Research Systems Inc.* and E4440A, *Agilent Technologies Inc.*) similar to Sec. 5.1.2. All spectra shown hereafter were averaged to eliminate low-frequency fluctuations of the DC level. The rms noise level was also calculated by Eq. (5.1) as described in Sec. 5.1.2.

The RIN of the SUT2 system is shown in Fig. A.2.1. The seed noise was notably damped by one order of magnitude around tens of Hz. This damping behavior is typical for the Er^{3+}:Yb^{3+} amplifica-

---

[1]Referring to the linear part of the power slope at 8 mW seed power.

[2]A maximum output power of 409 mW (19.1 dB gain) and 2.25 W (8.4 dB gain) was possible with 5 mW and 322 mW seed power.

[3]The photo detector is sensitive in the wavelength regime from 800 nm to 1700 nm and for frequencies of up to 150 MHz [204].

tion mechanism because of the effective high-pass behavior of the seed-to-output transfer function as reported by Steinke *et al.* [152] and explains why the amplified beam showed a somewhat lower rms noise than the seed at lower power levels. The comb-like pattern around hundreds of Hz originated from the internal power stabilization of the seed laser. A peak appeared at 782.56 Hz that narrowed down with increasing pump power; the peak probably arose from fluctuations of the Yb^{3+} ASE power. A more detailed discussion on the origin of that peak can be found in Chap. 6. The peak contributed notably to the rms noise level of $\approx 0.51\%$ making the resulting total noise larger than that of SUT1 with an rms noise level of $\approx 0.32\%$. Hence, the occurrence of the peak appears to be a disadvantage of SUT2 when compared to the off-peak pumped SUT1 system. The peak near at 699.7 kHz originated from the relaxation oscillation of the seed laser [56] as explained by Varona *et al.*, who used the same seed laser [56]. The peaks at multiple of 50 Hz were a result of the electrical utility frequency but contributed only insignificantly to the total rms noise of the output beam.
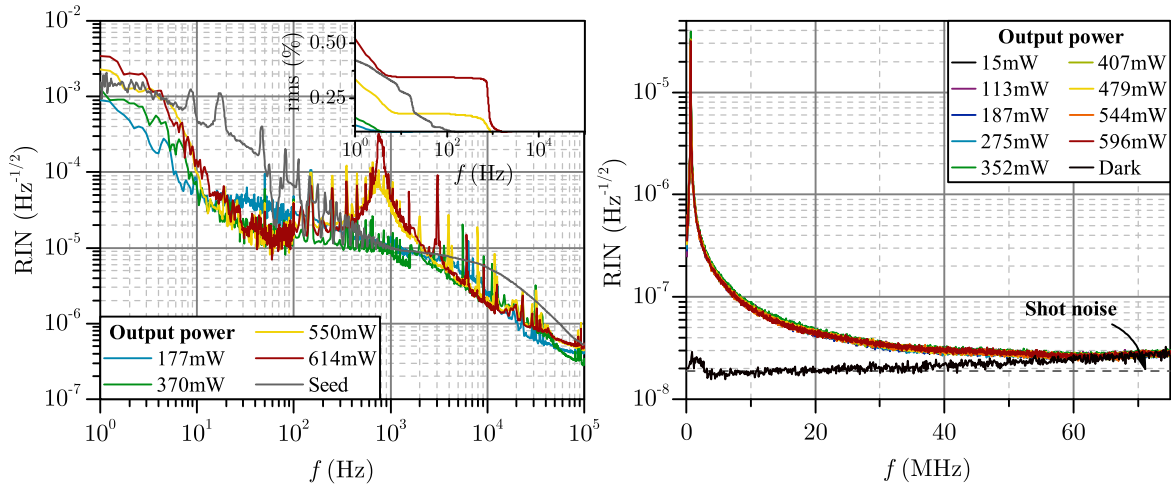

Figure A.2.1: Radio-frequency spectra of SUT2. Left: spectrum up to 102.4 kHz. The inset shows the rms noise obtained by integrating the power spectral density. Right: spectrum up to 75 MHz. The data were measured with an InGaAs photo detector and E4440A instrument. The origin of the peak at 782.56 Hz is discussed in Chap. 6. The absence of excess noise indicates SBS-free operation of SUT2.

The RIN approached the shot noise limit - depicted in the right plot of Fig. A.2.1 as the dashed line - up to ≈ 50 MHz but was dominated by the dark noise of the photo detector at higher frequencies. The relative shot noise level was calculated as in Sec. 5.1.2. All spectra coincided well at all power levels without excess noise indicating that no SBS was present at the studied power levels. This conclusion is supported by the fact that no backward propagating Stokes peak was observed in the optical spectrum. The theoretical SBS threshold was calculated to be 28.93 W with Eq. (2.41) using $K_B = 1.5$, $A_{eff} = 36.3\,\mu m^2$ (MFD = 6.8 μm), $L_{eff} = 0.79$ m ($L = 3.5$ m and 8 mW to 633 mW signal evolution) and $g_0 = 5 \times 10^{-11} mW^{-1}$, which significantly exceeds the power levels achieved herein and supports the conclusion that no SBS was present at the studied power levels. This result is not a considerable advantage against SUT1 because SUT1 also operated SBS-free. It is also worth noticing that no SBS mitigation technique was applied; thus, there is further potential for power scaling of SUT2 in the view of SBS.

A.3 Summary

The amplifier system presented herein was pumped at 976 nm in backward direction using the cladding pumping technique. The system was seeded by a commercial off-the-shelf fiber laser at 1556.55 nm. The seed power was attenuated to 8 mW by a free-space power tuning stage. The system showed

higher ASE power levels than SUT1 from Sec. 5.1, which used the off-peak pumping technique. A slope efficiency of 27.1$\pm$0.8 % was achieved deviating from the theoretical quantum limit of 62.7 % for the pump and seed wavelengths of 976 nm and 1556 nm. The efficiency recovered by increasing the seed power to 322 mW. Further power scaling was limited by parasitic lasing of the blue-sided Er^{3+} ASE near 1536 nm. The PER of SUT2 was 18.7 dB. The RIN followed a damped high-pass behavior at hundreds of Hz as expected from the Er^{3+}:Yb^{3+} amplification mechanism. A peak appeared in the radio-frequency spectrum at 782.56 Hz contributing to the overall rms of the output beam. The RIN was close to the shot noise limit in the MHz regime and coincided well at all power levels. The absence of any power dependent excess noise indicates SBS-free operation of SUT2. This conclusion is in agreement with the theoretical SBS threshold of 28.93 W. In conclusion, a single-frequency backward cladding pumped amplifier at 976 nm can provide 633 mW (19.0 dB gain) output power with 8 mW seed input power without the onset of SBS or lasing of the Yb^{3+} and/or Er^{3+} ASE. Therefore, this concept is regarded as moderately suited as a pre-amplifier, although it could not provide the same or higher power levels as achieved with the SUT1 system pumped at 940 nm.

Appendix B

Conventional pump strategy - core pumping at 976 nm

The setup of the system shown in Fig. B.0.1 - also referred to as SUT3 - is described herein and discussed in the following. The system was seeded at 1556.55 nm by a commercial off-the-shelf single-frequency free-space coupled fiber laser (RFLSA-2000-3-1556.55-UNL-PM-N, *NP Photonics Inc.*). The seed laser - described in more detail in Chap. 6 - was derated to 1.69 W and further attenuated by a combination of a tunable $\lambda/2$-rotator and a polarizing beam splitter cube. The coupled seed power was monitored throughout the characterization process at the idle port of a wavelength division multiplexer. Unless explicitly stated in the text, all results presented hereafter were obtained by using 8 mW seed power. A second $\lambda/2$-rotator was used to align the input polarization to the PM-axis of the fiber chain. Using free-space coupling between the seed laser and SUT3 made it possible to use the seed laser without splicing and thus maintained the reusability of the device.
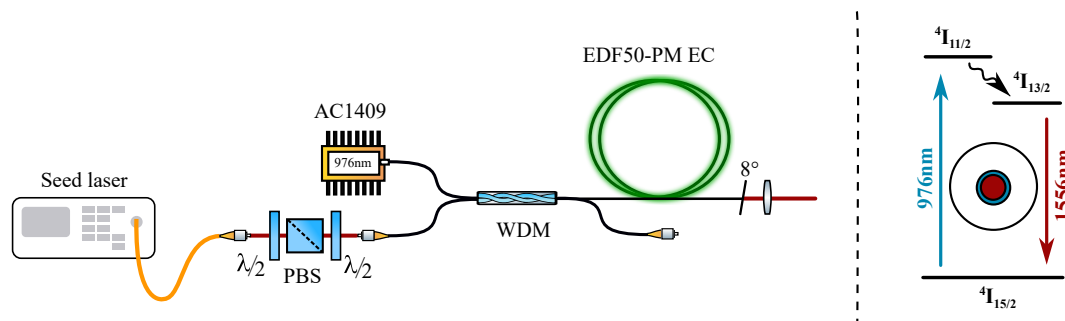

Figure B.0.1: Setup of SUT3. The commercial off-the-shelf seed laser (RFLSA-2000-3-1556.55-UNL-PM-N, *NP Photonics Inc.*) was attenuated by a $\lambda/2$-rotator and polarizing beam splitter (PBS) cube. The amplifier system consisted of an in-house fabricated wavelength division multiplexer (WDM), purely Er^{3+} doped fiber (EDF50-PM EC, *OFS Fitel LLC*) and pump diode (AC1409, *Gooch & Housego Ltd.*). The pump mechanism is illustrated on the right side and was implemented with the core pumping technique.

SUT3 was pumped at 976 nm using the core pumping technique, which led to relatively short fiber lengths. Thus, a co-propagating configuration of seed and pump light could be implemented because SBS was not expected in this configuration. This avoided the necessity to remove residual backward propagating pump light, which reduced the overall complexity of the system. A single-mode 7/125 PM fiber-coupled laser diode (AC1409-0600-0980-PM, *EM4 Inc.*, 540 mW at 980 nm) operating at 298 K was used as a pump source. An in-house fabricated 2x2 fiber-fused wavelength division multiplexer (custom, *LZH e.V.*) was used to combine the pump and seed light. The 1 m-long purely Er^{3+} doped fiber (EDF50-PM EC[1], *OFS Fitel LLC*) was coiled on the optical table with a diameter of 10 cm. The fiber length was optimized in a cut-back experiment to correspond to 90±1 %

---

[1]The fiber has an elliptically shaped core and a mode-field diameter of 5.4 µm at 1530 nm [205].

pump light absorption. The fiber was much shorter than the fiber used for the 940 nm pumped SUT1 thanks to the 976 nm pump wavelength and use of the core pumping technique. The end of the gain fiber was cleaved with an angle of 8° to suppress optical feedback from Fresnel reflections. The output beam was collimated by an $f = 8.0$ mm lens (C240TME-C, *Thorlabs Inc.*). The residual pump light was filtered with a dichroic long-pass optic (DMLP1180, *Thorlabs Inc.*).

B.1 Amplifier slope and optical spectrum

The power slopes of SUT3 were measured with a thermopile power head and its affiliated data acquisition system (LM-10 and Fieldmaster, *Coherent Inc.*). The optical spectra referred to hereafter were measured by optical grating spectroscopy (AQ6317C, *Ando Electric Co. Ltd.*). The power slopes plotted in Fig. B.1.1 showed a mild saturation pattern probably due to pump saturation. Gain depletion through the Er^{3+} ASE was ruled out because the Er^{3+} ASE power levels showed a linear behavior at the investigated power levels as evident in the inset of Fig. B.1.1; moreover, the Er^{3+} ASE power levels were generally much lower for example compared to SUT2. Nevertheless, the relative ASE power levels were still somewhat higher compared to SUT1, which was pumped at 940 nm, making the pump configuration used for SUT3 disadvantageous with respect to the Er^{3+} ASE. No statement, however, can be made on the backward directed Er^{3+} ASE of SUT3 due to the system's lacking accessibility to the backward propagating power. It must be noted that the different ASE power levels, albeit depending on the used pump strategy, might also have originated from spectroscopic differences of the used fibers. The maximum achievable output power was 141 mW (12.5 dB gain) limited by available pump power[2]. Linear fitting of the power slope found 30.4±0.8 % slope efficiency, which is less than the theoretical quantum limit of ≈62.7 % for the pump and seed wavelengths of 976 nm and 1556 nm. The same shortcoming was observed with the 940 nm pumped SUT1. The different efficiencies of the power slopes at 5 mW and 8 mW, however, suggest that this shortcoming can be recovered by increasing the seed input power. The PER of the system was 25.8 dB; thus, the PER was comparable to the SUT1 system pumped at 940 nm.
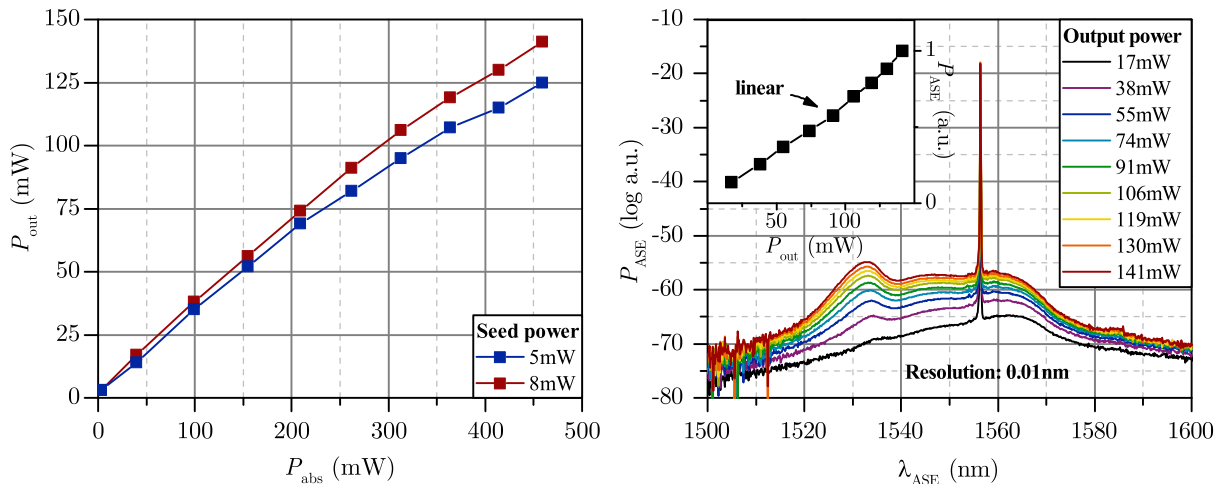

Figure B.1.1: Power slopes and optical spectrum of SUT3. Left: power slopes of the system showing that the efficiency declined at higher output powers due to pump saturation. The different slope efficiencies at 5 mW and 8 mW suggest that the efficiency can be recovered by using sufficient seed power. Right: forward directed optical spectrum measured with AQ6317C (*Ando Electric Co. Ltd.*) at different output power levels from 17 mW to 141 mW. The relative ASE power levels of SUT3 were higher compared to the SUT1 system presented in Sec. 5.1.

---

[2] A maximum output power of 125 mW (11.9 dB gain) was achieved by using 5 mW seed power.

B.2 Relative intensity noise and stimulated Brillouin scattering

The RIN of a free-running laser system is required for the design of the servo loops for potential post-stabilization systems. The RIN of SUT3 was therefore characterized similar to Sec. 5.1.2 in the following way. The output beam was pointed to an InGaAs photo detector (PDA10CF-EC, *Thorlabs Inc.*)[3]. The laser power was attenuated by neutral density filter glasses and a tunable neutral density filter wheel (NDC-50C-4, *Thorlabs Inc.*) to correspond to ≈ 9 V on the photo detector. The power spectral density of the AC-signal was obtained with the electrical spectrum analyzer E4440A (*Agilent Technologies Inc.*). Each power spectral density curve shown hereafter is the result from averaging over hundred individual spectra to eliminate low-frequency power fluctuations. The relative shot noise level was calculated from $V_{DC} = 9$ V and the detector's transimpedance gain $T = 1 \times 10^4$ VA^{-1} as in Sec. 5.1.2 to be 1.88×10^{-8} Hz$^{-1/2}$.

The peak at 699.7 kHz resulted from the relaxation oscillation of the seed laser as explained by Varona *et al.* [56]. The RIN was dominated by the dark noise of the photo detector above ≈ 50 MHz, which limited the detectable power noise. Nevertheless, no excess noise was observed that is a clear indication that no SBS was present in SUT3 at the power levels studied herein. This result is indeed anticipated because the fiber length used herein was as short as $\approx 20\%$ of the length that was used for SUT1, which also operated free of SBS; furthermore, the power levels herein were also much lower. No statement can be made on the presence of backward propagating Stokes scattering due to the unavailability of the optical spectrum in backward direction. The theoretical SBS threshold was calculated to be 43.89 W according to Eq. (2.41) using $K_B = 1.5$, $A_{eff} = 22.9$ µm^2 (MFD $= 5.4$ µm), $L_{eff} = 0.33$ m ($L = 1.0$ m

Figure B.2.1: Radio-frequency spectrum of SUT3. The spectrum was measured with InGaAs photo detector and E4440A instrument. The absence of excess noise at MHz frequencies indicated that SUT3 operated SBS-free.

and 8 mW to 141 mW signal evolution) and $g_0 = 5 \times 10^{-11}$ mW^{-1}; thus, the theoretical SBS threshold is much larger than the investigated power levels. This supports the conclusion that no SBS was present. The absence of SBS, however, is not a considerable advantage against the 940 nm pumped SUT1 system because SUT1 also operated SBS-free. It is worth noticing that no SBS mitigation technique was used so that SUT3 has much more power scaling potential in the view of SBS. Albeit no characterization of the power noise is available in the low-frequency range for this particular system, the Albert-Einstein-Institute found excellent noise properties of less than $\approx 10^{-6}$ Hz$^{-1/2}$ in this regime by investigating a resembling system developed by the *LZH e.V.* [145], i.e. similar seed power levels and implemented with the same gain fiber.
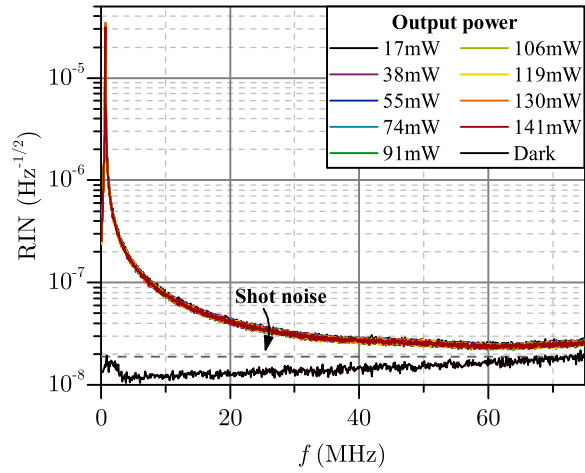
B.3 Summary

The amplifier presented herein, denoted as SUT3, was core pumped at 976 nm in co-propagation configuration. The setup was seeded by a commercial off-the-shelf single-frequency fiber laser at 1556.55 nm with 8 mW seed power obtained by free-space attenuation of the laser beam. The system showed somewhat higher ASE power levels than SUT1 from Sec. 5.1, which used the off-peak

---

[3]The detector is sensitive in the wavelength regime from 800 nm to 1700 nm and frequencies up to 150 MHz [204].

pumping technique. The power slopes showed a mild saturation pattern due to pump saturation. Gain depletion through the Er^{3+} was ruled out because the Er^{3+} ASE power levels showed a linear behavior and were generally low. The maximum achievable output power was 141 mW (12.5 dB gain) with 30.4 ± 0.8 % slope efficiency; further power scaling was limited by the available pump power. The PER of the system was 25.8 dB, which was similar to that of SUT1. The noise spectrum indicated that SUT3 operated free of SBS. Albeit no characterization of SUT3's power noise is available for the low-frequency regime, the Albert-Einstein-Institute found excellent noise properties by investigating a similar system developed by the *LZH e.V.* Nevertheless, power scaling into the W range is not expected with SUT3; therefore, the system is assessed as not suited as a pre-amplifier for a GWD laser source.

Appendix C

Conventional pump strategy - core pumping at 1475 nm

The setup of the system characterized herein - also referred to as SUT4 - is shown in Fig. C.0.1 and described in the following. The system was seeded at 1556.65 nm by an InGaS/InP multi-quantum-well laser diode with integrated distributed feedback structure (AA1401, *Gooch & Housego Ltd.*, 60 mW, sub-MHz linewidth, spectrum in Sec. 5.1). The diode was protected from back reflections by a fiber-based optical isolator (OI, IO-J-1550, *Thorlabs Inc.*). A fiber-fused 2x2 fiber splitter (PN1550R1A2, *Thorlabs Inc.*, 1 % splitting ratio) allowed throughout monitoring of the seed power amid operation. The amplifier system was pumped at 1475 nm leading to a quantum defect of only ≈5.2 %. Furthermore, the core pumping technique was used, which led to relatively short fiber lengths without the risk of SBS occurring. A single-mode fiber-coupled laser diode (AF4B140CD75L type C, *Anritsu Corp.*, 400 mW at 1475 nm) with built-in isolation was used as a pump source. A 2x2 fiber-fused wavelength division multiplexer from *SIFAM Fibre Optics Ltd.* was used to combine the pump and seed light. The 1.5 m-long 11/125 Er^{3+}:Yb^{3+} codoped triple-clad fiber (TCF1500Y(11/125)HD, *Fibercore Ltd.*) was coiled on the optical table with 10 cm diameter; the fiber length corresponded to 10 dB pump absorption. It must be noted that the fiber was a non-PM fiber and must be substituted with a suitable PM fiber if SUT4 is integrated as a pre-amplifier in the GWD laser. The output end of the gain fiber was cleaved with an 8° angle to suppress feedback from optical Fresnel reflections. The output beam was collimated by an $f = 8.0$ mm lens (C240TME-C, *Thorlabs Inc.*) and filtered from residual pump light by a dichroic long-pass optic (FF01-1535/LP-25, *Semrock Inc.*).
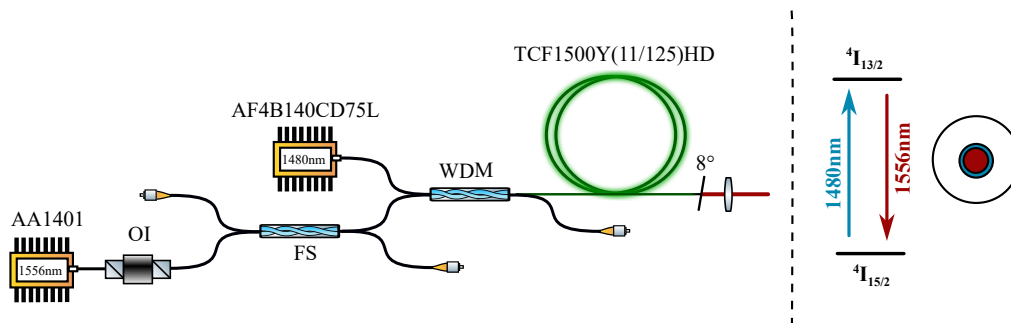

Figure C.0.1: Setup of SUT4. The system was seeded by a distributed feedback laser diode (AA1401, *Gooch & Housego Ltd.*). The diode was protected by an optical isolator (OI, IO-J-1550, *Thorlabs Inc.*). The seed power was monitored through a 2x2 fiber splitter (FS, PN1550R1A2, *Thorlabs Inc.*, 1 % splitting ratio). A single-mode diode (AF4B140CD75L, *Anritsu Corp.*) was used as a pump source. The pump and seed powers were combined by a 2x2 wavelength division multiplexer (WDM, *SIFAM Fibre Optics Ltd.*). A 1.5 m-long 11/125 Er^{3+}:Yb^{3+} codoped triple-clad fiber (TCF1500Y(11/125)HD, *Fibercore Ltd.*) was used; the fiber was non-PM. The pump mechanism is illustrated on the right and exploits the core pumping technique.

C.1 Amplifier slope and optical spectrum

The power slopes of the system were measured with a thermopile power head (3A-FS, *Ophir Optronics Solutions Ltd.*) and its affiliated data acquisition system (Pulsar-4, *Ophir Optronics Solutions Ltd.*). All results presented hereafter were obtained with 8 mW seed power if not noted otherwise. SUT4 performed with the lowest Er^{3+} ASE power levels (see Fig. C.1.1) out of all systems investigated in this work. It must be noted that these low ASE power levels - albeit depending on the used pump strategy - might also have originated from spectroscopic differences of the used fibers. The power slopes plotted in Fig. C.1.1 showed a linear behavior at the power levels investigated without notable saturation. The maximum output power was 159.5 mW (8 mW seed power, 13.0 dB gain) limited by available pump power. Linear fitting found 44.5±0.5 % slope efficiency, which increased to 52.6±0.4 % with 25 mW seed power. This was the highest efficiency of all tested systems and in particular higher compared to SUT1. This is especially astonishing considering that the used fiber has the largest mode-field area of all studied fibers, which led to the lowest seed intensity; the quantum defect, however, was only ≈5.2%. The output beam was polarized with an extinction ratio of 21.0 dB, which is a fairly good result given that a non-PM fiber was used. These findings and the low quantum defect suggest that the system has far more power scaling potential.
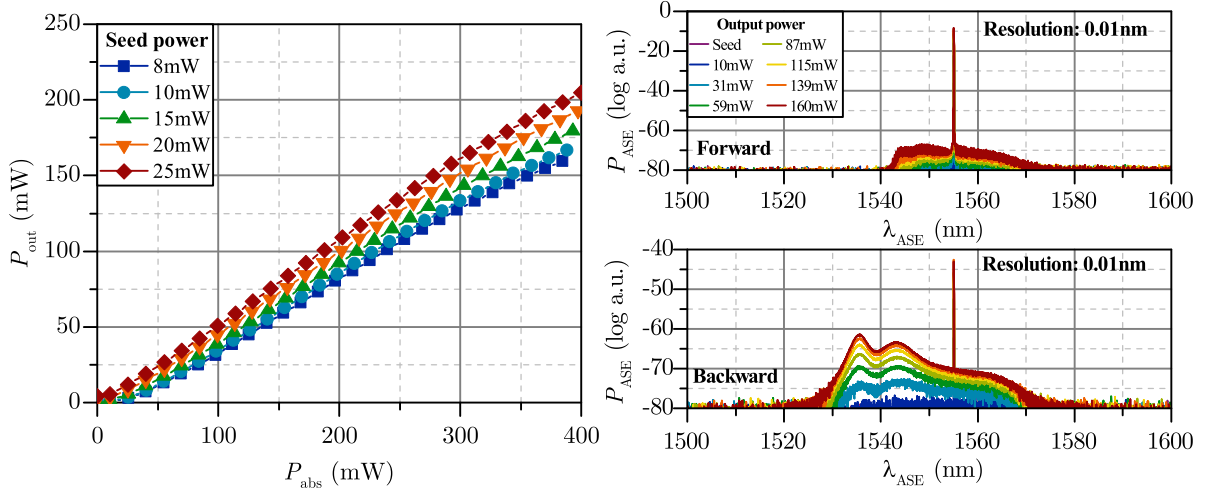

Figure C.1.1: Power slopes and optical spectra of SUT4. Left: the power slopes show a linear behavior; the slope efficiencies were the highest out of all systems investigated in this work ranging from 44.5±0.5 % to 52.6±0.4 %. Right: optical spectra of the Er^{3+} ASE power measured with optical spectrum analyzer (OSA, AQ6317C, *Ando Electric Co. Ltd.*). The Er^{3+} ASE power levels were the lowest of all SUTs.

C.2 Relative intensity noise and stimulated Brillouin scattering

The RIN of SUT4 is an important characteristic for the design of potential post-stabilization systems. Thus, the output beam of SUT4 was attenuated by a set of fixed and tunable neutral density filters and pointed to an InGaAs photo detector (PDA10CF-EC, *Thorlabs Inc.*) connected to a spectrum analyzer instrument (E4440A, *Agilent Technologies Inc.*). All spectra shown hereafter are the result of averaging over hundred individual spectra to eliminate low-frequency fluctuations of the DC-level. The system herein showed the lowest RIN levels in the low-frequency range of all SUTs, particularly somewhat lower than the RIN of SUT1, which is probably a consequence of SUT4's low ASE levels. Thus, the system herein proved promising in terms of its noise properties. The rms level of the beam's power noise was calculated as in Sec. 5.1.2; the rms noise was 0.14 ‰ at maximum output power and therefore the lowest of all SUTs. The narrow peak(s) at (multiple of) 50 Hz matched the utility frequency and originated probably from the electronics. Additional noise, however, was observed up

to $\approx 10\,\text{kHz}$ at low output power levels. The peaks between $\approx 10\,\text{kHz}$ and $\approx 20\,\text{MHz}$ were also present in the spectrum of the seed diode.

The relative shot noise was calculated as in Sec. 5.1.2 to be $2.83 \times 10^{-8}\,\text{Hz}^{-1/2}$. No excess power noise was observed in the MHz range that indicated SBS-free operation of the system, although the power noise was somewhat limited by the dark noise of the photo detector towards higher frequencies. The absence of SBS ties well with the theoretical SBS threshold of 121.22 W calculated by Eq. (2.41) with $K_B = 1.5$, $A_{\text{eff}} = 91.6\,\mu\text{m}^2$ (MFD $= 10.8\,\mu\text{m}$), $L_{\text{eff}} = 0.48\,\text{m}$ ($L = 1.5\,\text{m}$ and $8\,\text{mW}$ to $159.5\,\text{mW}$ amplification) and $g_0 = 5 \times 10^{-11}\,\text{mW}^{-1}$. Therefore, SUT4 also showed further power scaling potential with respect to SBS.
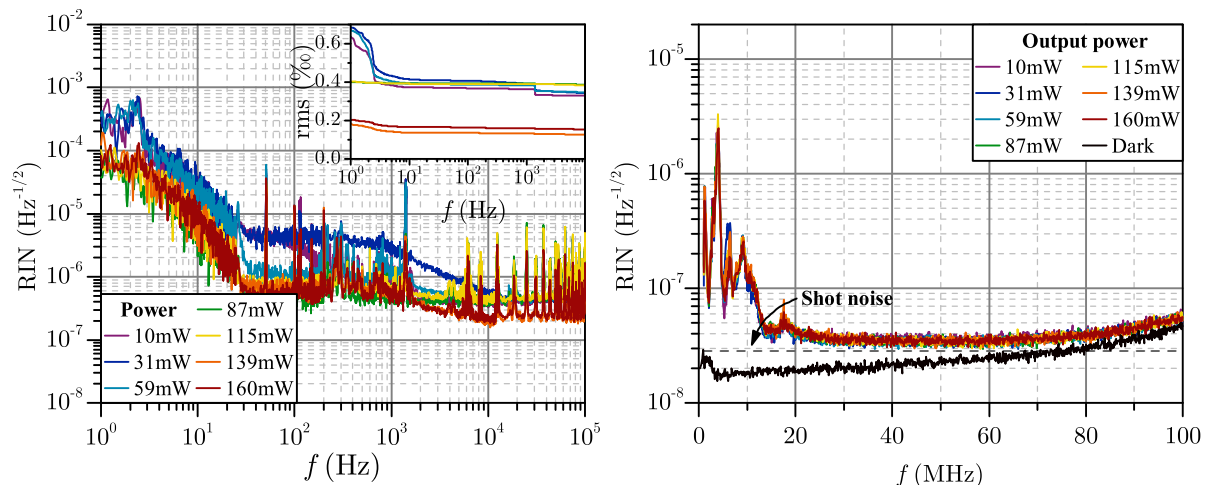

Figure C.2.1: Radio-frequency spectra of SUT4. Left: spectrum up to $102.4\,\text{kHz}$. The inset shows the rms noise obtained by integrating the power spectral density. Right: spectrum up to $100\,\text{MHz}$. The data were measured with an InGaAs photo detector and E4440A (*Agilent Technologies Inc.*) spectrometer. The absence of excess noise indicates SBS-free operation.

C.3 Summary

The system investigated herein was pumped in co-propagation direction at 1475 nm by using the core pumping technique. The system was seeded by a distributed feedback laser diode (AA1401, *Gooch & Housego Ltd.*) at 1556.65 nm with sub-MHz linewidth. The system performed with the lowest Er^{3+} ASE power levels out of all systems studied in this work. The maximum output power was 159.5 mW with $44.5 \pm 0.5\,\%$ slope efficiency; further power scaling was limited by available pump power. SUT4 showed the highest efficiency of all tested systems. Furthermore, SUT4 proved promising in terms of its noise properties without excess noise in the MHz range that indicates that the system operated SBS-free. This ties well with the theoretical SBS power threshold of 121.22 W. This pumping strategy is therefore highly interesting for a pre-amplifier, although it could not provide the same or higher power levels as achieved with the SUT1 system pumped at 940 nm because of the limited pump power.

Appendix D

Conventional pump strategy - core pumping at 1530 nm

The setup of the system presented herein - also referred to as SUT5 - is shown in Fig. D.0.1. The system was seeded at 1556.65 nm by an InGaS/InP multi-quantum-well laser diode with distributed feedback structure (AA1401, *Gooch & Housego Ltd.*, 60 mW, sub-MHz linewidth, spectrum in Sec. 5.1). The optical isolator protected the laser diode from spurious back reflections. The 2x2 fiber splitter (1 % splitting ratio) allowed monitoring of the coupled seed power during operation of the system. The system was pumped at the absorption maximum of Er^{3+} around 1530 nm by using the core pumping technique. An in-house developed monolithic fiber laser was used as a pump source; more details
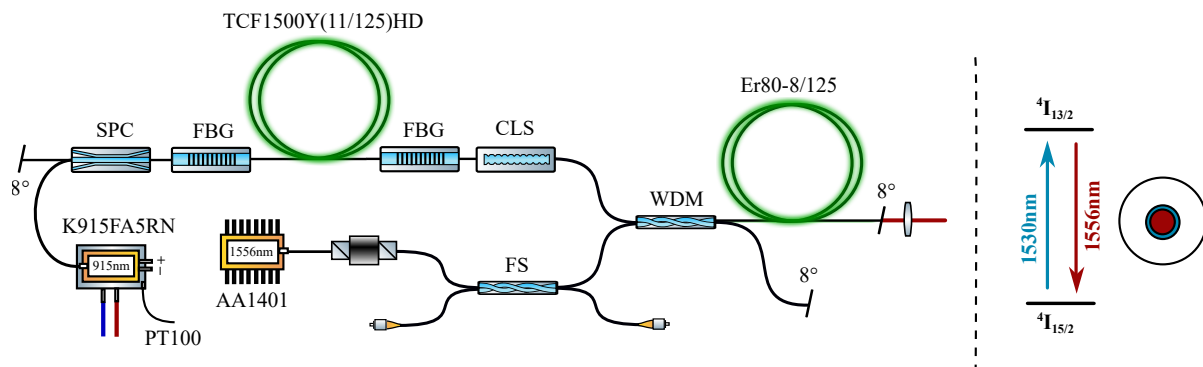

Figure D.0.1: Setup of SUT5. The pump laser was in-house fabricated from an TC1500Y(11/125)HD fiber and two fiber Bragg gratings with 99.997 % and 5 % reflectivity near 1530 nm. The pump laser was pumped at 915 nm through a signal-pump-combiner (SPC) and the residual pump light was removed by a cladding-light-stripper (CLS). The amplifier was seeded by a laser diode (AA1401, *Gooch & Housego Ltd.*). The wavelength division multiplexer (WDM), which was spliced to the Er^{3+} doped fiber (Er80-8/125, *nLight Inc.*), combined the pump and seed light. The 2x2 fiber splitter (FS, 1 % splitting ratio) allowed throughout monitoring of the coupled seed power. The pump mechanism is illustrated on the right using the core pumping technique.

can be found in reference [206]. A 4.2 m-long piece of the 11/125 Er^{3+}:Yb^{3+} doped triple-clad fiber (TC1500Y(11/125)HD, *Fibercore Ltd.*) was coiled on a water-cooled aluminum cylinder with 12 cm diameter. The fiber was pumped by a 105/125 fiber-coupled laser diode at 915 nm (K915FA5RN-70W, *BWT Beijing Ltd.*, 70 W at 915 nm) through a (2+1)x1 signal-pump-combiner. The laser process was enforced by two fiber Bragg gratings (P59272 and P325509, *TeraXion Inc.*, 99.997 % and 5 % reflectivity near 1530 nm). The residual pump light was removed by a CO_2 laser micro-structured cladding-light-stripper. The pump laser provided 15.7 W single-mode output power at 1530 nm with 42.5±1.0 % slope efficiency. The power stability of the pump laser was successfully tested over a 3 h period. The pump and seed light was combined by an in-house fabricated fiber-fused 2x2 wavelength division multiplexer. A 1.5 m-long 8/125 Er^{3+} doped fiber (Er80-8/125, *nLight Inc.*) coiled on an

aluminum cylinder with 10 cm diameter was used as a gain fiber. The fiber was a non-PM fiber and must be substituted by a suitable PM counterpart if the system is integrated in a GWD laser source. The fiber ends were either terminated with FC/APC connectors or cleaved with an angle of 8° to suppress optical feedback from Fresnel reflections. A long-pass optic (FF01-1535/LP-25, *Semrock Inc.*) was used to filter residual pump power.

D.1 Amplifier slope and optical spectrum

The power slopes of the system plotted in Fig. D.1.1 were measured with a thermopile power head (3A-FS, *Ophir Optronics Solutions Ltd.*) and its affiliated data acquisition system (Pulsar-4, *Ophir Optronics Solutions Ltd.*). The achievable output power was limited by pump saturation at 119 mW (11.7 dB gain) with $25.8 \pm 1.2\%$ slope efficiency[1]. Therefore, further optimization of the fiber length is required. The slope efficiency was one of the lowest of all systems investigated in this work and far off the theoretical quantum limit of $\approx 98\%$ for the used pump and seed wavelengths. This was a consequence of the quasi 2-level structure of the Er^{3+} energy levels and the almost identical emission and absorption cross-sections ($\sigma_{21}/\sigma_{12} \approx 0.93$) at 1530 nm. This limited the achievable inversion to $\approx 50\%$ and poses a fundamental drawback of this pumping strategy. This shortcoming could be remedied with increasing seed power but did not recover for the seed power levels investigated herein. Additionally, parasitic lasing was observed in the optical spectra at 1561.40 nm at all power levels probably because of insufficient isolation between the amplifier and the pump laser. The lasing was also apparent in the radio-frequency spectrum at 18.64 MHz corresponding to a total round-trip length of 16.09 m; the total length of the fiber chain i.e. half the round-trip length was ≈ 8 m. The parasitic lasing probably originated from a spurious reflection from a fiber component or splice inside the pump laser chain. Adding an optical isolator between the pump laser and the amplifier could solve the lasing issue; however, further investigations were not performed due to the prospective poor power scalability of SUT5. The PER of SUT5 was 6.0 dB confirming that the use of a PM fiber is necessary.
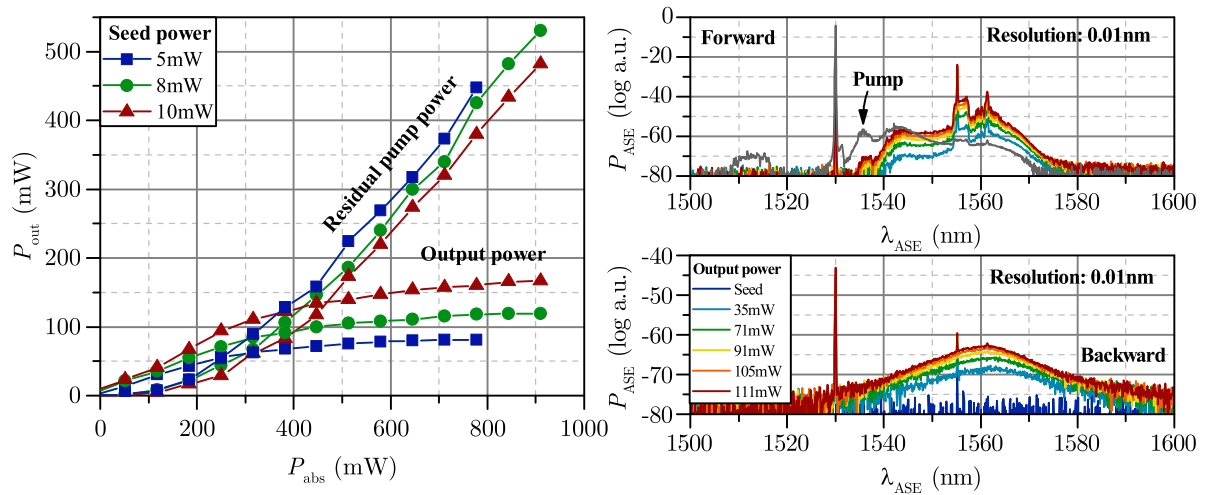

Figure D.1.1: Power slope and optical spectra of SUT5. Left: power slopes and residual pump power showing strong pump saturation particularly notable at lower seed power. This shortcoming did not recover with the seed power levels investigated in this work. Right: optical spectra in forward and backward direction. Parasitic lasing was observed in the optical spectra at 1561.40 nm at all investigated power levels. The relative ASE power levels were higher compared to SUT1, which is presented in Sec. 5.1. The grey curve is the optical output spectrum of the pump source.

---

[1]Maximum output powers of 81 mW (10.1 dB gain) and 167 mW (13.2 dB gain) with $21.2 \pm 0.8\%$ and $33.1 \pm 1.4\%$ slope efficiencies were achieved with 5 mW and 10 mW seed power.

D.2 Relative intensity noise and stimulated Brillouin scattering

The RIN of SUT5 was characterized in the following way. The beam was attenuated by a set of fixed and tunable neutral density filters and focused on an InGaAs photo detector (PDA10CF-EC, *Thorlabs Inc.*). The photo detector was connected to one of two spectrum analyzer instruments (SR785, *Stanford Research Systems Inc.* and E4440A, *Agilent Technologies Inc.*). The spectra shown hereafter were obtain by averaging to equalize low-frequency fluctuations of the DC-level. The rms noise level was calculated by Eq. (5.1) as described in Sec. 5.1.2.

The radio-frequency spectra depicted in Fig. D.2.1 showed severe rms noise of $\approx 3.60\%$ at 119 mW output power and numerous peaks around 100 Hz as a consequence of the parasitic lasing process, which was observed in Sec. D.1. The peaks at multiple of 18.64 MHz can also be explained by the lasing process. The relative shot noise depicted as a dashed line was calculated as in Sec. 5.1.2 to be 2.83×10^{-8} Hz$^{-1/2}$. The RIN laid significantly above the shot noise level; thus, any noise caused by SBS might not be detectable. However, the theoretical SBS threshold was calculated by Eq. (2.41) to be $P_{\text{thr}} = 86.16$ W with $K_B = 1.5$, $A_{\text{eff}} = 70.9\,\mu\text{m}^2$ (MFD = 9.5 μm), $L_{\text{eff}} = 0.52$ m ($L = 1.5$ m and 8 mW to 119 mW signal evolution) and $g_0 = 5 \times 10^{-11}$mW^{-1}. Therefore, it is reasonable to assume that the system operated free of SBS; this assumption is consistent with the results from Appendices A to C and Sec. 5.1.

Nonetheless, the noise characteristics of SUT5 were not compliant with the requirements of a GWD laser system. The excessive noise was probably caused by missing optical isolation between SUT5 and the pump laser. This shortcoming was therefore probably of technical origin and independent of the investigated pump strategy. The shortcoming was not remedied because of SUT5's lack of prospective power scalability.
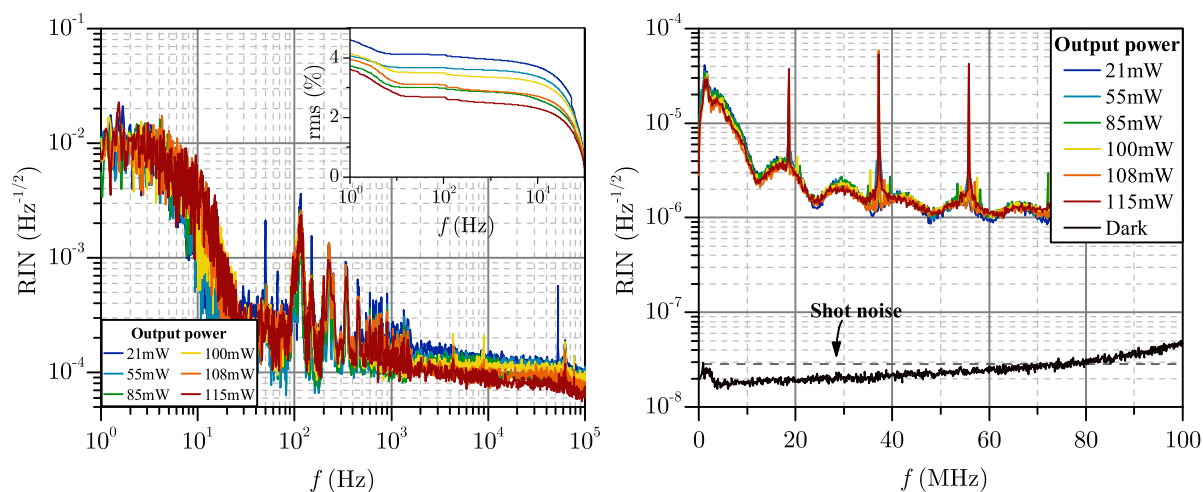

Figure D.2.1: Radio-frequency spectra of SUT5. Left: spectrum up to 102.4 kHz. The inset shows the rms noise obtained by integrating the power spectral density. SUT5 showed the highest RIN of all SUTs, which was probably caused by missing isolation between the pump laser and the amplifier. Right: spectrum up to 100 MHz. The excess noise obstructed any noise originating from SBS.

D.3 Summary

The system investigated herein was pumped at 1530 nm in co-propagation direction by an in-house assembled pump laser and by using the core pumping technique. The pump laser was implemented with a 4.2 m-long Er^{3+}:Yb^{3+} doped triple-clad fiber pumped by a 105/125 fiber-coupled laser diode at 915 nm and fiber Bragg gratings with 99.997 % and 5 % reflectivity. The system was seeded by a distributed feedback laser diode (AA1401, *Gooch & Housego Ltd.*) at 1556.65 nm with sub-MHz

linewidth. A maximum output power of 119 mW (11.7 dB gain) and a slope efficiency of 25.8±1.2 % was achieved. The PER was only 6.0 dB probably owed to the use of a non-PM fiber. Parasitic lasing was observed in the optical spectra at 1561.40 nm, which caused considerable noise; the noise obstructed the detection of any noise originating from SBS. Nevertheless, it was concluded from the theoretical SBS threshold that the system probably operated SBS-free. Albeit SUT5's technical shortcomings, e.g. missing isolation and non-PM fiber, may be remedied, the pump strategy is unsuited to be used in a GWD laser system because of its low power scaling capability, particularly compared to the SUT1 system pumped at 940 nm.

Appendix E

ASE transients and mapping functions

Fig. E.0.1 shows the Er^{3+} and Yb^{3+} (if applicable) ASE transients of FUT2 and FUT3. The bottom right plot shows the relative deviation of each mapping function (see color code) versus relative change of doping concentrations or fiber length. For example, a black data point at $(x, y) = (1.1, 2.8\%)$ means that the mapping function f_1 (black) deviates by 2.8% when the fiber length changes by 10%. The mapping functions are shown in Fig. E.0.2.
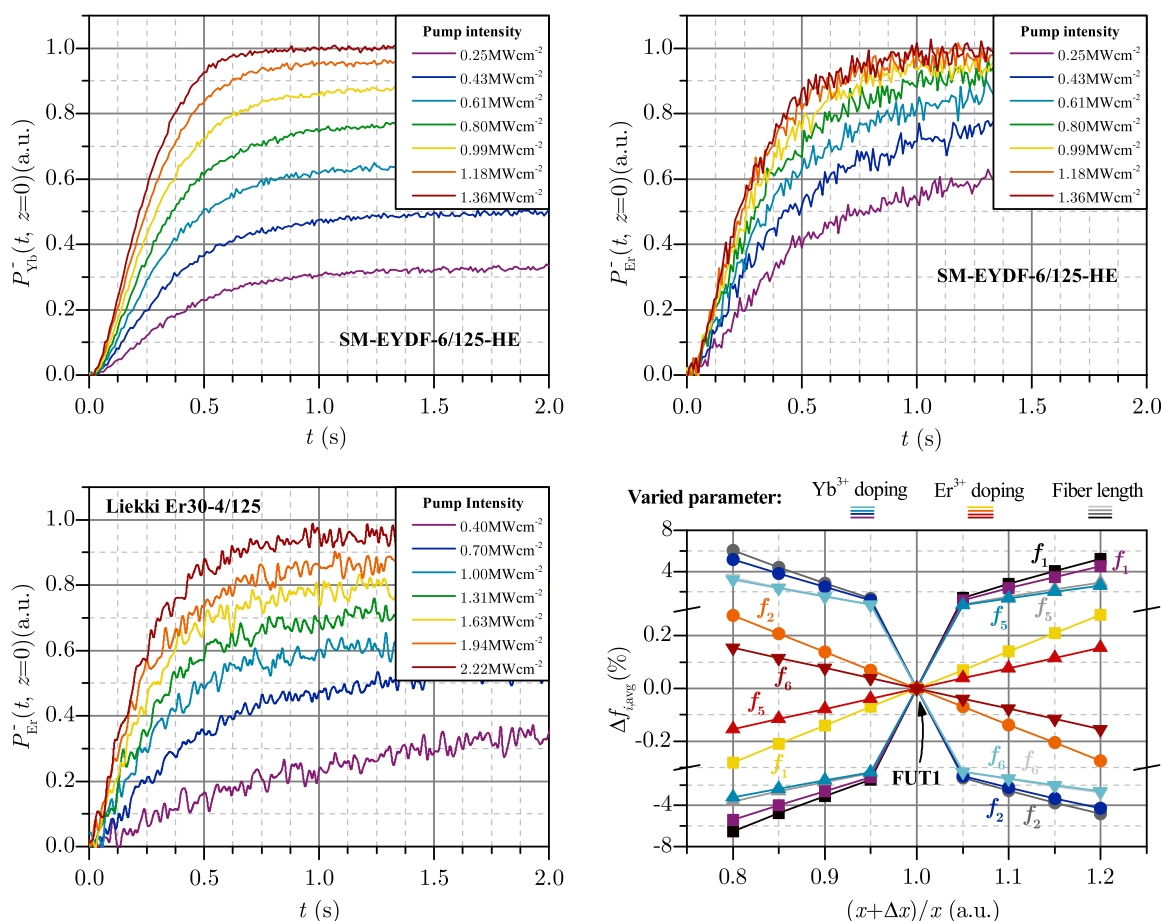

Figure E.0.1: Top, left: Yb^{3+} ASE transients of FUT2. Top, right: Er^{3+} ASE transients of FUT2. Bottom, left: Er^{3+} ASE transients of FUT3. Bottom, right: relative mean deviation of the six mapping functions f_i under variation of decisive simulation parameters such as the Yb^{3+} and Er^{3+} doping concentrations or the fiber length. The colors correspond to the parameter that was varied. For example, the purple curve corresponds to the mean difference of f_1 under variation of the Yb^{3+} doping concentration. The mean deviation is zero if no parameters are changed, namely $(x + \Delta x)/x = 1.0$.
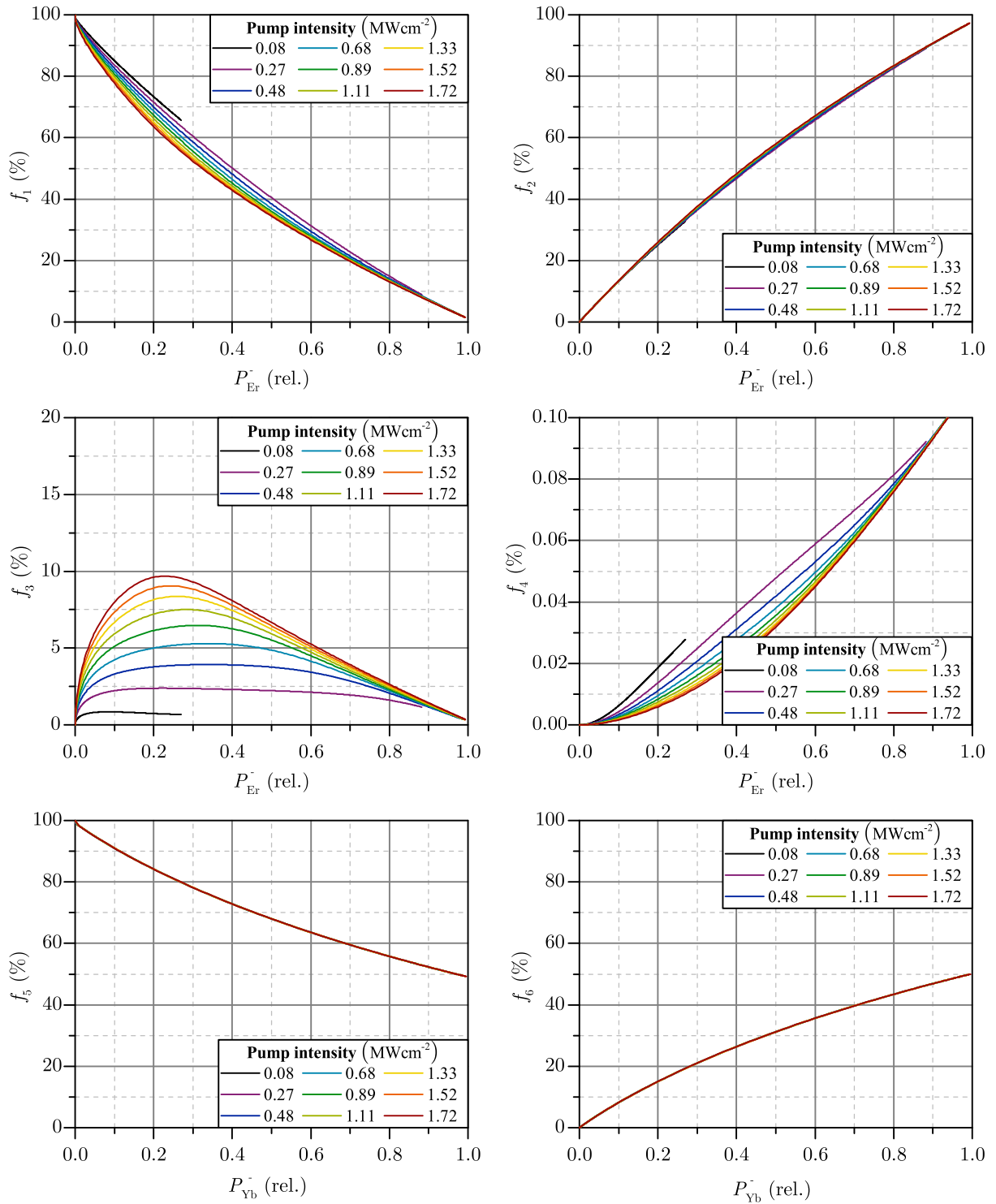
Figure E.0.2: Population of relevant energy levels versus corresponding ASE power. Top, left: $^4I_{15/2}$ level. Top, right: $^4I_{13/2}$ level. Middle, left: $^4I_{11/2}$ level. Middle, right: $^4I_{9/2}$ level. Bottom, left: $^2F_{7/2}$ level. Bottom, right: $^2F_{5/2}$ level.

Appendix F

Thermal effects in phosphosilicate fibers

The following presents the thermal degradation of two Er^{3+}:Yb^{3+} doped phosphosilicate fibers. The test setup is shown in the inset of Fig F.0.1. Samples from a single-mode fiber (TC1500Y(6/125)HD, *Fibercore Ltd.*) and LMA fiber (IXF-2CF-EY-PM-25-250, *iXblue S.A.S.*) of 1 m and 0.5 m length were tested. The fibers revealed 12.3 wt% and 11.8 wt% of P by energy dispersive X-ray spectroscopy, respectively. Furthermore, 2.8 % of Al was found in the LMA fiber; the single-mode fiber showed no evidence of Al. The test fibers were contacted with thermal grease on a 300 °C heat plate (PZ-28-1T, *Harry Gestigkeit GmbH*). The light from a commercial off-the-shelf fiber laser (RFLSA-2000-3-1556.55-UNL-PM-N, *NP Photonics Inc.*) with 1.25 W at 1556.55 nm was launched into the test fibers. The laser was connected via FC/APC connection to maintain the operability of the device. The transmitted power was recorded with a 3A-SH power head and the affiliated Pulsar-4 (*Ophir Optronics Solutions Ltd.*) data acquisition device. A mode-field-adapter was added for the LMA fiber to only excite the fundamental mode in that fiber. The coupling to the fundamental mode was prone to be affected by external thermal influences; the measurement period of the LMA fiber was therefore limited to a ≈5 h window where the temperature was constant within the day-night cycles of the laboratory's climate control system. Instead, the experiment with the LMA fiber was performed thrice to increase its conclusiveness. Any spurious cladding light was reduced by embedding the fiber tips in high-index liquid. The fiber ends were slanted with an 8° angle to prevent optical feedback from Fresnel reflections. The test setup was placed in an aluminum enclosure for environmental shielding.
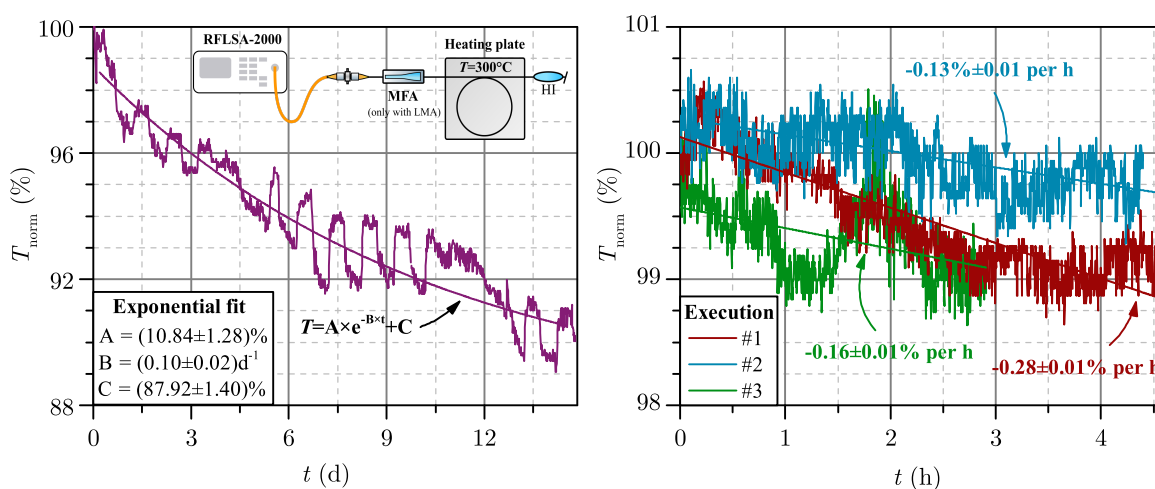

Figure F.0.1: Normalized throughput power of test fibers. The test setup is shown in the inset. The fibers were heated to 300 °C during the measurement period. Left: measurement with TC1500Y(6/125)HD fiber. Right: measurement with IXF-2CF-EY-PM-25-250 fiber (repeated thrice).

A growing power loss was observed while heating; an exponential fit to the transmittance gave a decay constant of $B = 0.10 \pm 0.02\,\mathrm{d^{-1}}$ for the single-mode fiber i.e. a loss of 0.02 % to 0.04 % per hour. The loss rate was somewhat similar to Fig. 6.1.1, where $\approx$0.05 % and $\approx$0.01 % loss per hour was found for the *Nufern* and *iXblue* fibers, respectively. It must be added, however, that a direct comparison to Fig. 6.1.1 is obstructed due to unknown parameters such as the absolute core temperatures and/or the thermal distribution.

The power through the LMA fiber decreased immediately after heating by $\approx$15 % (not shown), which can be explained by the well-known increase of the Er^{3+} absorption cross-sections around 1.55 μm at high temperatures [207]. The transmittance was approximated by linear fitting (no exponential fit for LMA fiber) because of the short measurement period. The linear fit revealed a power loss of 0.13$\pm$0.01 % to 0.28$\pm$0.01 % per hour.

The growing power loss can be explained by the heat-induced formation of P1 type color centers (PO_3^{2-}) from phosphorous oxygen hole centers (POHC, PO_4^{2-} [187]). This mechanism is supported by the well-known existence of POHCs in X- or γ-ray irradiated phosphorous doped silica [188]. The absence of Al made in fact the single-mode fiber particularly prone to POHC precursors [191]; nonetheless, a lower loss rate was found for that fiber. Both magnitude and time scale of the power loss tie in well with the observations from Chap. 6. This suggests that - if the underlying loss mechanisms were the same - the fiber cores in Chap. 6 exhibited severe temperatures despite the vigorous cooling approach. The results reinforce the proposed loss mechanism; further spectral analysis[1] can likely provide additional support for this theory.

---

[1]The absorption of POHCs is centered around 540 nm; the absorption of P1 type color centers is centered around 1620 nm [190].

Appendix G

Miscellaneous

Table G.1: Comparison of alternative gain fibers at 50 W output power.

Fiber	PLMA-EYDF-25P/300-HE	IXF-2CF-EY-PM-25-250
Pump absorption at 915 nm	2.9 dBm^{-1}	3.6 dBm^{-1}
Length	4.5 m	4.2 m
Mode-field radius at 1.55 µm	10.2 µm	10.4 µm
Seed source	RFLSA-2000-3-1556.55-UNL-PM-N	
Seed power	0.95 W	0.92 W
Slope efficiency	Pristine: 46.4±0.5 %	Pristine: 44.2±0.4 %
	Longterm: 39.6±0.6 %	Longterm 42.2±0.4 %
PER	6.4 dB to 12.3 dB	15.2 dB to 20.7 dB
Er^{3+} ASE to carrier	Pristine: 48.59 dB	Pristine: 51.16 dB
	Longterm: 50.82 dB	Longterm: 51.54 dB
Yb^{3+} ASE to carrier	Pristine: 60.02 dB	Pristine: 42.19 dB
	Longterm: 58.77 dB	Longterm: 39.88 dB
Stimulated Brillouin scattering	SBS-free	
Calculated SBS threshold	184.60 W	208.89 W
rms noise	≈0.1 %	≈0.2 %
Fundamental mode content	73.0 %	94.6 %

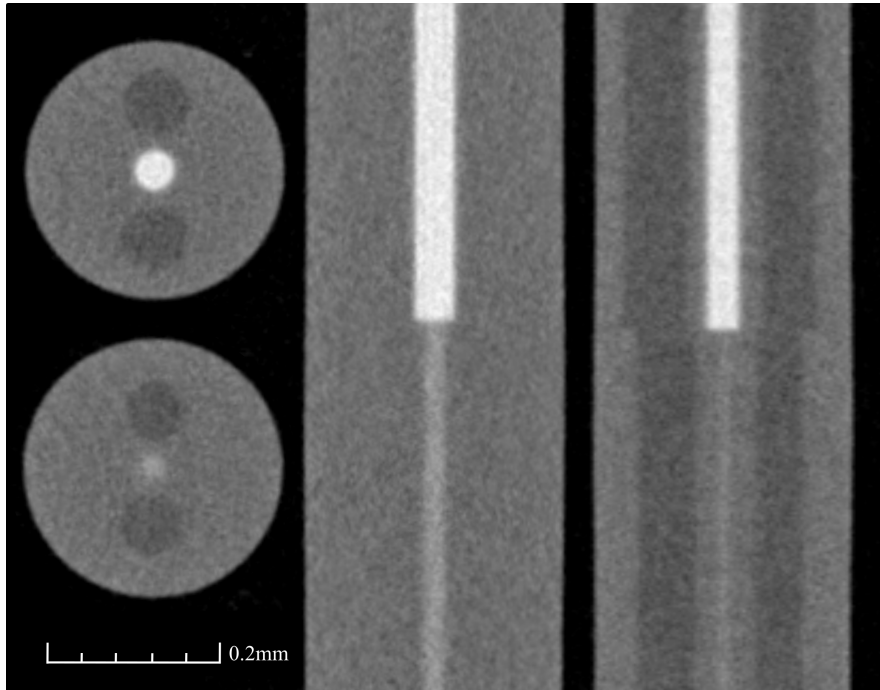**Figure G.0.1:** X-ray microscopy image of fiber splice between the PLMA-EYDF-25P/300-HE (top) and PLMA-GDF-25/300 (bottom) fibers. Left: cross-sections through the xy-plane confirming the accurate alignment of the stress rods. Right: cross-sections through the xz-/yz-plane. The bright region is the fiber pedestal.

Figure G.0.2: Corning-7980-0F glass window spliced to the PLMA-EYDF-25P/300-HE fiber with a CO_2 laser.

Appendix H

Publications

[1] O. Varona, W. Fittkau, P. Booker, T. Theeg, M. Steinke, D. Kracht, J. Neumann, and P. Wessels. Single-frequency fiber amplifier at 1.5 µm with 100 W in the linearly-polarized TEM_{00} mode for next-generation of gravitational wave detectors. *Opt. Express*, 25(21): 24880-24892, 2017.

[2] M. Steinke, H. Tnnermann, V. Kuhn, T. Theeg, M. Karow, O. de Varona, P. Jahn, P. Booker, J. Neumann, P. Wessels, and D. Kracht. Single-frequency Fiber Amplifiers for Next-Generation Gravitational Wave Detectors. *IEEE J. Sel. Top. Quantum Electron.*, 24(3): 3100613, 2018.

[3] P. Booker, O. Varona, P. Wessels, M. Steinke, J. Neumann, and D. Kracht. Numerical investigations of off-resonant pumped Er^{3+}:Yb^{3+}-codoped fibre amplifiers. *European Conference on Lasers and Electro-Optics*, CJ_P_12, 2017.

[4] F. Wellmann, P. Booker, S. Hochheim, T. Theeg, O. Varona, W. Fittkau, L. Overmeyer, M. Steinke, P. Wessels, J. Neumann, and D. Kracht. Recent progress on monolithic fiber amplifiers for next generation of gravitational wave detectors. *Proc. SPIE 10512, Fiber Lasers XV: Technology and Systems*, 105120I, 2018.

[5] P. Booker, R. Caspary, J. Neumann, D. Kracht, and M. Steinke. Pump wavelength dependence of ASE and SBS in single-frequency EYDFAs. *Opt. Lett.*, 43(19): 4647-4650, 2018.

[6] P. Booker, F. Kranert, P. Wessels, M. Steinke, J. Neumann, and D. Kracht. Numerical investigations on ASE and SBS in Er^{3+}:Yb^{3+}-codoped fiber amplifiers. *SPIE Photonics Europe*, 2018.

[7] S. Hochheim, F. Wellmann, T. Theeg, O. de Varona, P. Booker, P. Wessels, M. Steinke, J. Neumann, and D. Kracht. Monolithic fiber amplifiers for the next generation of gravitational wave detectors. *Proc. SPIE 10683, Photonics Europe*, 1068320, 2018.

[8] P. Booker, M. Dürbeck, N. G. Boetti, D. Pugliese, S. Abrate, D. Milanese, M. Steinke, J. Neumann, and D. Kracht. Single-frequency Er^{3+} doped phosphate fiber MOPA. *European Conference on Lasers and Electro-Optics*, CJ_P_17, 2019.

[9] P. Booker on behalf of M. Steinke and the LZH/AEI Hanover laser team. Fiber-based laser systems for 3G-detectors. *13th Edoardo Amaldi Conference on Gravitational Waves*, 2019.

[10] P. Booker, O. Varona, M. Steinke, P. Wessels, J. Neumann, and D. Kracht. Experimental and numerical study of interlock requirements for high-power EYDFAs. *Opt. Express*, 28(21): 31480-31486, 2020.

[11] P. Booker, O. Varona, P. Wessels, J. Neumann, and D. Kracht. Experimental and Numerical Results of High-power EYDFA Interlock Requirements. *OSA Advanced Photonics Congress*, SoTu3H.3, 2020.

[12] P. Booker, O. Varona, M. Steinke, P. Wessels, J. Neumann, and D. Kracht. Two-stage fully monolithic single-frequency Er:Yb fiber amplifiers at 1556 nm for next-generation of gravitational wave detectors. *Proc. SPIE 11665, Fiber Lasers XVIII: Technology and Systems*, 116650O, 2021.

[13] P. Booker, K. Kruska, M. Steinke, B. Willke, P. Wessels, J. Neumann, and D. Kracht. Recent Progress on Single-Frequency EYDFAs for Gravitational Wave Detection. *Conference on Lasers and Electro-Optics*, SF2M.4, 2022.

LVK publications

[1] P. Booker, F. Wellmann, S. Hochheim, T. Theeg, O. Varona, W. Fitkau, M. Steinke, P. Wessels, J. Neumann, and D. Kracht. Update on fiber amplifier prototypes at 1064 nm and 1550 nm. *LVC March meeting*, 2018.

[2] P. Booker, F. Wellmann, M. Steinke, F. Thies, N. Bode, P. Oppermann, B. Willke, L. Overmeyer, J. Neumann, and D. Kracht. Characterization of the Monolithic Fiber Amplifier Engineering Prototype for the Next Generation of Gravitational Wave Detectors. *LVC March meeting*, 2019.

[3] P. Booker, S. Hochheim, F. Wellmann, N. Bode, B. Willke, P. Wessels, J. Neumann, and D. Kracht. Fiber amplifiers for next generation of gravitational wave detectors. *LVK March meeting*, 2021.

Bibliography

[1] A. Einstein. Die Grundlage der allgemeinen Relativitätstheorie. *Annalen der Physik*, 354(7):769 – 822, 1916.

[2] M. Bailes et al. Gravitational-wave physics and astronomy in the 2020s and 2030s. *Nat. Rev. Phys.*, 3:344–366, 2021.

[3] GWIC, GWIC-3G, and GWIC-3G-SCT-Consortium. Gravitational-Wave Astronomy with the Next-Generation Earth-Based Observatories - Exploring the Universe from Planck to Hubble Scales. *GWIC publication*, 2019.

[4] E. Hubble. A relation between distance and radial velocity among extra-galactic nebulae. *Proc. N.A.S.*, 15(3):168 – 173, 1929.

[5] J. Weber. Detection and Generation of Gravitational Waves. *Phys. Rev.*, 117(306):306 – 313, 1960.

[6] D. J. Gretz. Early History of Gravitational Wave Astronomy: The Weber Bar Antenna Development. *Hist. Phys. Newsletter*, 13(6):5–16, 2018.

[7] J. H. Taylor, L. A. Fowler, and P. M. McCulloch. Measurement of general relativistic effects in the binary pulsar PSR1913+16. *Nature*, 277:437 – 440, 1979.

[8] V. D. Sabbata, P. Fortini, C. Gualdi, and S. Petralia. A Proposal for Combined Efforts Regarding Geophysical Research and Detection of Gravitational Waves. *Annals of Geophysics*, 23(1):21 – 25, 1970.

[9] R. Weiss. Electromagnetically Coupled Broadband Gravitational Antenna. *Quart. Progress Report, Research Laboratory of Electronics MIT*, 1972.

[10] LIGO Scientific Collaboration. Advanced LIGO Reference Design. *LIGO Document Control Center*, M060056-v2, March 2011.

[11] Coherent Inc. *Datasheet - Mephisto/Mephisto S*, December 2017.

[12] P. Kwee, C. Bogan, K. Danzmann, M. Frede, H. Kim, P. King, J. Pöld, O. Puncken, R. L. Savage, F. Seifert, P. Wessels, L. Winkelmann, and B. Willke. Stabilized high-power laser system for the gravitational wave detector advanced LIGO. *Opt. Express*, 20(10):10617 – 10634, 2012.

[13] N. Bode, F. Meylahn, and B. Willke. Sequential high power laser amplifiers for gravitational wave detection. *Opt. Express*, 28(20):29469–29478, 2020.

[14] N. A. Robertson et al. Quadruple suspension design for Advanced LIGO. *Class. Quantum Gravity*, 19(15):4043, 2002.

[15] F. Matichard et al. Advanced LIGO two-stage twelve-axis vibration isolation and positioning platform. Part 1: Design and production overview. *Precision Engineering*, 40(1):273 – 286, 2015.

[16] K. Tsubono. TAMA300 laser interferometer for gravitational wave detection. *Proc. SPIE 3744, Interferometry: Techniques and Technologies*, 1999.

[17] S. Miyoki et al. CLIO Cryogenic Laser Interferometer Observatory. 28th *International Cosmic Ray Conference*, 5:3073–3076, 2003.

[18] B. Willke et al. The GEO 600 gravitational wave detector. *Class. Quantum Gravity*, 19(7):1377 – 1387, 2002.

[19] P. Fritschel. Second generation instruments for the Laser Interferometer Gravitational Wave Observatory (LIGO). *Proc. SPIE 4856, Gravitational-Wave Detection*, 2002.

[20] T. Accadia et al. Virgo: a laser interferometer to detect gravitational waves. *J. Instrum.*, 7(03):P03012, 2012.

[21] P. Barriga et al. AIGO: A southern hemisphere detector for the worldwide array of ground-based interferometric gravitational wave detectors. *Class. Quantum Grav.*, 27(8):084005, 2010.

[22] M. Frede and B. Willke. Advanced LIGO PSL Front End Amplifiers vs Oscillator. *LIGO Document Control Center*, T060235-x0, 2006.

[23] E. Hirose, D. Bajuk, G. Billingsley, T. Kajita, B. Kestner, N. Mio, M. Ohashi, B. Reichman, H. Yamamoto, and L. Zhang. Sapphire mirror for the KAGRA gravitational wave detector. *Phys. Rev. D*, 89(6):062003, 2014.

[24] K. Takeno, T. Ozeki, S. Moriwaki, and N. Mio. 100 W, single-frequency operation of an injection-locked Nd:YAG laser. *Opt. Lett.*, 30(16):2110 – 2112, 2005.

[25] KAGRA Collaboration. Overview of KAGRA: Detector design and construction history. *Prog. Theor. Exp. Phys.*, 2021(5):05A101, 2020.

[26] B. P. Abbott et al. Observation of Gravitational Waves from a Binary Black Hole Merger. *Phys. Rev. Lett.*, 116(6):061102, 2016.

[27] B. P. Abbott et al. GW170817: Observation of Gravitational Waves from a Binary Neutron Star Inspiral. *Phys. Rev. Lett.*, 119(16):161101, 2017.

[28] B. P. Abbott et al. Multi-messenger Observations of a Binary Neutron Star Merger. *Astrophys. J.*, 848(2):L12, 2017.

[29] M. R. Drout et al. Light curves of the neutron star merger GW170817/SSS17a: Implications for r-process nucleosynthesis. *Science*, 358(6370):1570 – 1574, 2017.

[30] B. P. Abbott et al. GWTC-1: A Gravitational-Wave Transient Catalog of Compact Binary Mergers Observed by LIGO and Virgo during the First and Second Observing Runs. *Phys. Rev. X*, 9(3):031040, 2019.

[31] B. P. Abbott et al. GWTC-2: Compact Binary Coalescences Observed by LIGO and Virgo during the First Half of the Third Observing Run. *Phys. Rev. X*, 11(021053), 2021.

[32] L. McCuller, C. Whittle, D. Ganapathy, K. Komori, M. Tse, A. Fernandez-Galiana, L. Barsotti, P. Fritschel, M. MacInnis, F. Matichard, K. Mason, N. Mavalvala, R. Mittleman, H. Yu, M.E. Zucker, and M. Evans. Frequency-Dependent Squeezing for Advanced LIGO. *Phys. Rev. Lett.*, 124, 2020.

[33] G. M. Harry, H. Armandula, E. Black, D. R. M. Crooks, G. Cagnoli, J. Hough, P. Murray, S. Reid, S. Rowan, P. Sneddon, M. M. Fejer, R. Route, and S. D. Penn. Thermal noise from optical coatings in gravitational wave detectors. *Appl. Opt.*, 45(7):1569 – 1574, 2006.

[34] A. Schroeter, R. Nawrodt, R. Schnabel, S. Reid, I. Martin, S. Rowan, C. Schwarz, T. Koettig, R. Neubert, M. Thürk, W. Vodel, A. Tünnermann, K. Danzmann, and P. Seidel. On the mechanical quality factors of cryogenic testmasses from fused silica and crystalline quartz. *arXiv*, 2007.

[35] R. Adhikari et al. A Cryogenic Silicon Interferometer for Gravitational-wave Detection. *Class. Quantum Gravity*, 37(16), 2020.

[36] M. J. Keevers and M. A. Green. Absorption edge of silicon from solar cell spectral response measurements. *Appl. Phys. Lett.*, 66(2):174 – 176, 1995.

[37] D. Engin, B. Mathason, and M. Storm. Efficient, space-based, PM 100W thulium fiber laser for pumping Q-switched 2µm Ho:YLF for global winds and carbon dioxide lidar. *Proc. SPIE 10406, Lidar Remote Sensing for Environmental Monitoring*, 104060B-1, 2017.

[38] M. Meleshkevich, N. Platonov, D. Gapontsev, A. Drozhzhin, V. Sergeev, and V. Gapontsev. 415W Single-Mode CW Thulium Fiber Laser in all-fiber format. *Proc. IEEE, European Conference on Lasers and Electro-Optics and the International Quantum Electronics Conference*, CP2_3, 2007.

[39] G. D. Goodno, L. D. Book, and J. E. Rothenberg. Low-phase-noise, single-frequency, single-mode 608W thulium fiber amplifier. *Opt. Lett.*, 34(8):1204 – 1206, 2009.

[40] A. Hemming, N. Simakov, A. Davidson, M. Oermann, L. Corena, D. Stepanov, N. Carmody, J. Haub, R. Swain, and A. Carter. Development of high-power holmium-doped fibre amplifiers. *Proc. SPIE 8961, Fiber Lasers XI: Technology, Systems, and Applications*, 89611A, 2014.

[41] J. Steinlechner, W. Martin, A. S. Bell, J. Hough, M. Fletcher, P. G. Murray, R. Robie, S. Rowan, and R. Schnabel. Silicon-Based Optical Mirror Coatings for Ultrahigh Precision Metrology and Sensing. *Phys. Rev. Lett.*, 120(26):263602, 2018.

[42] A. D. Bristow, N. Rotenberg, and H. M. van Driel. Two-photon absorption and Kerr coefficients of silicon for 850 - 2200 nm. *Appl. Phys. Lett.*, 90(19):191104, 2007.

[43] P. Klipstein, O. Klin, S. Grossman, N. Snapi, I. Lukomsky, D. Aronov, M. Yassen, A. Glozman, T. Fishman, E. Berkowicz, O. Magen, I. Shtrichman, and E. Weiss. XBn barrier photodetectors based on InAsSb with high operating temperatures. *Opt. Eng.*, 50(6):061002, 2011.

[44] LIGO Scientific Collaboration. GWTC-3: Compact Binary Coalescences Observed by LIGO and Virgo During the Second Part of the Third Observing Run. *LIGO Document Control Center*, P2000318-v8, 2021.

[45] LIGO Scientific Collaboration. Instrument Science White Paper 2020. *LIGO Document Control Center*, T2000407-v3, 2020.

[46] LIGO Scientific Collaboration. LIGO Voyager Upgrade: Design Concept. *LIGO Document Control Center*, T1400226-v9, 2017.

[47] ET Science Team. Einstein gravitational wave Telescope Conceptual Design Study. 2011.

[48] F. Thies, N. Bode, P. Oppermann, M. Frede, B. Schulz, and B. Willke. Nd:YVO$_4$ high-power master oscillator power amplifier laser system for second-generation gravitational wave detectors. *Opt. Lett.*, 44(3):719 – 722, 2019.

[49] E. Snitzer and R. Woodcock. Yb^{3+}-Er^{3+} Glass Laser. *Appl. Phys. Lett.*, 6(3):45 – 46, 1965.

[50] E. V. Zharikov, V. I. Zhekov, L. A. Kulevskii, T. M. Murina, V. V. Osiko, A. M. Prokhorov, A. D. Savel'ev, V. V. Smirnov, B. P. Starikov, and M. I. Timoshechkin. Stimulated emission from Er^{3+} ions in yttrium aluminum garnet crystals at $\lambda = 2.94$ μ. *Sov. J. Quantum Electron.*, 4(8):1039, 1975.

[51] N. Barnes, R. Allen, L. Esterowitz, E. Chicklis, M. Knights, and H. Jenssen. Operation of an Er:YLF laser at 1.73 μm. *IEEE J. Quantum Electron.*, 22(2):337 – 343, 1986.

[52] M. Weber, M. Bass, T. Varitimos, and D. Bua. Laser action from Ho^{3+}, Er^{3+}, and Tm^{3+} in YAlO3. *IEEE J. Quantum Electron.*, 9(11):1079 – 1086, 1973.

[53] E. Kifle, P. Loiko, C. Romero, J. R. V. de Aldana, A. Ródenas, V. Jambunathan, V. Zakharov, A. Veniaminov, A. Lucianetti, T. Mocek, M. Aguiló, F. Díaz, U. Griebner, V. Petrov, and X. Mateos. Fs-laser-written erbium-doped double tungstate waveguide laser. *Opt. Express*, 26(23):30826 – 30836, 2018.

[54] N. Ter-Gabrielyan, V. Fromzel, T. Lukasiewicz, W. Ryba-Romanowski, and M. Dubinskii. Nearly quantum-defect-limited efficiency, resonantly pumped, Er^{3+}:YVO$_4$ laser at 1593.5nm. *Opt. Lett.*, 36(7):1218 – 1220, 2011.

[55] D. Creeden, H. Pretorius, J. Limongelli, and S. D. Setzler. Single frequency 1560nm Er:Yb fiber amplifier with 207W output power and 50.5% slope efficiency. *Proc. SPIE 9728, Fiber Lasers XIII: Technology, Systems, and Applications*, 2016.

[56] O. Varona, W. Fittkau, P. Booker, T. Theeg, M. Steinke, D. Kracht, J. Neumann, and P. Wessels. Single-frequency fiber amplifier at 1.5 μm with 100 W in the linearly-polarized TEM$_{00}$ mode for next-generation gravitational wave detectors. *Opt. Express*, 25(21):24880 – 24892, 2017.

[57] T. Matniyaz, F. Kong, M. T. Kalichevsky-Dong, and L. Dong. Record 302W single-mode power from an Er/Yb fiber MOPA. *Opt. Lett.*, 45(10):2910 – 2913, 2020.

[58] D. J. Richardson, J. Nilsson, and W. A. Clarkson. High power fiber lasers: current status and future perspectives. *J. Opt. Soc. Am. B*, 27(11):B63 – B92, 2010.

[59] D. Marcuse. *Theory of Dielectric Optical Waveguides*. Academic Press, 1991.

[60] J. Ballato and P. Dragic. Materials Development for Next Generation Optical Fiber. *Materials*, 7(6):4411 – 4430, 2014.

[61] F. Mitschke. *Glasfasern - Physik und Technologie*. Elsevier GmbH, 2005.

[62] D. Kouznetsov, J. Moloney, and E. M. Wright. Efficiency of pump absorption in double-clad fiber amplifiers. I. Fiber with circular symmetry. *J. Opt. Soc. Am. B*, 18(6):743 – 749, 2001.

[63] D. Kouznetsov and J. V. Moloney. Efficiency of pump absorption in double-clad fiber amplifiers. II. Broken circular symmetry. *J. Opt. Soc. Am. B*, 19(6):1259 – 1263, 2002.

[64] H. Po, E. Snitzer, R. Tumminelli, L. Zenteno, F. Hakimi, N.M. Cho, and T. Haw. Double Clad High Brigthness Nd Fiber Laser pumped by GaAlAs phased Array. *Optical Fiber Communication Conference, Vol. 5 of OSA Technical Digest Series*, PD7, 1989.

[65] C.-A. Bunge et al. *Polymer Optical Fibres - Fibre Types, Materials, Fabrication, Characterisation and Applications*. Elsevier Ltd., 2017.

[66] J. P. Koplow, D. A. V. Kliner, and L. Goldberg. Single-mode operation of a coiled multimode fiber amplifier. *Opt. Lett.*, 25(7):442 – 444, 2000.

[67] A. Carter. Highly efficient, Large Mode Area (LMA) fibers for use in high power eye-safe wavelength lasing applications. *Nufern Inc. Library*, 2007.

[68] J. A. Buck. *Fundamentals of Optical Fibers*. Wiley - Interscience, 2004.

[69] T.S. Izumitani. *Optical Glass*. American Inst. of Physics, 1986.

[70] T. Yamashita, S. Amano, I. Masuda, T. Izumitani, and A. J. Ikushima. Nd- and Er-doped phosphate glass liber lasers. *Proc. OSA Technical Digest, Conference on Lasers and Electro-Optics*, THH2, 1988.

[71] D. Keck, P. Schultz, and F. Zimar. U.S. patent US3737292A - Method of forming optical waveguide fibers. *USPTO*, 1972.

[72] M. J. F. Digonnet. *Rare-Earth-Doped Fiber Lasers and Amplifiers*. Marcel Dekker, Inc., 2001.

[73] S. R. Nagel, J. B. MacChesney, and K. L. Walker. An Overview of the Modified Chemical Vapor Deposition (MCVD) Process and Performance. *IEEE Transactions on Microwave Theory and Techniques*, 30(4):305–322, 1982.

[74] J. B. MacChesney, P. B. O'Connor, F. V. DiMarcello, J. R. Simpson, and P. D. Lazay. Preparation of low loss optical fibers using simultaneous vapor phase deposition. *Int. Congr. Glass*, 6:40–44, 1974.

[75] J. E. Townsend, S. B. Poole, and D. N. Payne. Solution-doping technique for fabrication of rare-earth-doped optical fibres. *Electron. Lett.*, 23(7):329 – 331, 1987.

[76] M.-A. Lapointe, S. Chatigny, M. Pich, M. Cain-Skaff, and J.-N. Maran. Thermal effects in high-power CW fiber lasers. *Proc. SPIE 7195, Fiber Lasers VI: Technology, Systems, and Applications*, 71951U, 2009.

[77] Fibercore Ltd. Fiberpaedia - Coating. 2020. `https://fibercore.humaneticsgroup.com/services-support/fiberpaedia/c/coating`.

[78] OFS Fitel LLC. What is a Fiber Optic Cable Jacket? 2020. `https://www.ofsoptics.com/optical-fiber-coatings/`.

[79] B. R. Judd. Optical Absorption Intensities of Rare-Earth Application. *Phys. Rev.*, 127(3):750 – 761, 1962.

[80] G. S. Ofelt. Intensities of Crystal Spectra of Rare-Earth Ions. *J. Chem. Phys.*, 37(3):511 – 520, 1962.

[81] N. Mavalvala, D. E. McClelland, G. Mueller, D. H. Reitze, R. Schnabel, and B. Willke. Lasers and optics: looking towards third generation gravitational wave detectors. *Gen. Relativ. Gravit.*, 43:569 – 592, 2011.

[82] P. C. Becker, N. A. Olsson, and J. R. Simpsons. Erbium-Doped Fiber Amplifiers: Fundamentals and Technology. *Academic Press Inc.*, 1999.

[83] O. Varona, M. Steinke, D. Kracht, J. Neumann, and P. Wessels. Influence of the third energy level on the gain dynamics of EDFAs: analytical model and experimental validation. *Opt. Express*, 24(22):24833 – 24895, 2016.

[84] J. W. Nicholson, M. F. Yan, P. Wisk, J. Fleming, F. DiMarcello, E. Monberg, T. Taunay, C. Headley, and D. J. DiGiovanni. Raman fiber laser with 81 W output power at 1480 nm. *Opt. Lett.*, 35(18):3069 – 3071, 2010.

[85] V. R. Supradeepa and J. W. Nicholson. Power scaling of high-efficiency 1.5 μm cascaded Raman fiber lasers. *Opt. Lett.*, 38(14):2538 – 2541, 2013.

[86] A. Fujisaki, S. Matsushita, K. Kasai, M. Yoshida, T. Hirooka, and M. Nakazawa. An 11.6W output, 6kHz linewidth, single-polarization EDFA-MOPA system with a $^{13}C_2H_2$ frequency stabilized fiber Laser. *Opt. Express*, 23(2):1081 – 1087, 2015.

[87] V. R. Supradeepa, J. W. Nicholson, and K. Feder. Continuous wave Erbium-doped fiber laser with output power of >100 W at 1550 nm in-band core-pumped by a 1480nm Raman fiber laser. *Proc. OSA Technical Digest, CLEO/Europe-EQEC*, 2012.

[88] J. Zhang, V. Fromzel, and M. Dubinskii. Resonantly cladding-pumped Yb-free Er-doped LMA fiber laser with record high power and efficiency. *Opt. Express*, 19(6):5574 – 5578, 2011.

[89] J. D. Minelly, W. L. Barnes, R. I. Laming, P. R. Morkel, J. E. Townsend, S. G. Grubb, and D. N. Payne. Diode-array pumping of $Er^{3+}Yb^{3+}$ Co-doped fiber lasers and amplifiers. *IEEE Photonics Technol. Lett.*, 5(3):301 – 303, 1993.

[90] K. Tankala, B. Samson, A. Carter, J. Farroni, D. Machewirth, N. Jacobson, U. Manyam, A. Sanchez, M.-Y. Chen, A. Galvanauskas, W. Torruellas, and Y. Chen. New developments in high power eye-safe LMA fibers. *Proc. SPIE 6102, Fiber Lasers III: Technology, Systems, and Applications*, 610206, 2006.

[91] V. Kuhn, D. Kracht, J. Neumann, and P. Wessels. Yb-free Er-doped 980 nm Pumped Single-Frequency Fiber Amplifier with Output Power of 54 W and Near-Diffraction Limited Beam Quality. *Proc. OSA Technical Digest, CLEO/Europe-EQEC*, CJ7_5, 2011.

[92] V. Kuhn, D. Kracht, J. Neumann, and P. Wessels. Er-doped photonic crystal fiber amplifier with 70 W of output power. *Opt. Lett.*, 36(16):3030 – 3032, 2011.

[93] L. V. Kotov, M. E. Likhachev, M. M. Bubnov, O. I. Medvedkov, M. V. Yashkov, A. N. Guryanov, J. Lhermite, S. Février, and E. Cormier. 75 W 40% efficiency single-mode all-fiber erbium-doped laser cladding pumped at 976 nm. *Opt. Lett.*, 38(13):2230 – 2232, 2013.

[94] Q. Zhao, J. Zhang, Y. Luo, J. Wen, and G.-D. Peng. Energy transer enhanced near-infrared spectral performance in bismuth/erbium codoped aluminosilicate fibers for broadband application. *Opt. Express*, 26(14):17889 – 17898, 2018.

[95] M. Federighi and F. D. Pasquale. The effect of pair-induced energy transfer on the performance of silica waveguide amplifiers with high Er^{3+}/Yb^{3+} concentrations. *IEEE Photonics Technol. Lett.*, 7(3):303 – 305, 1995.

[96] B. J. Ainslie. A review of the fabrication and properties of erbium-doped fibers for optical amplifiers. *J. Light. Technol.*, 9(2):220 – 227, 1991.

[97] WebElements Ltd. and University of Sheffield. Online periodic table - Ytterbium and Erbium. 2020. `https://www.webelements.com/`.

[98] I. Medintz and N. Hildebrandt. *FRET - Förster Resonance Energy Transfer*. Wiley-VCH Verlag GmbH & Co. KGaA, 2013.

[99] Q. Han, J. Ning, and Z. Sheng. Numerical Investigation of the ASE and Power Scaling of Cladding-Pumped Er-Yb Codoped Fiber Amplifier. *IEEE J. Quantum Electron.*, 46(11):1535 – 1541, 2010.

[100] M. Karasek. Optimum Design of Er^{3+}-Yb^{3+} Codoped Fibers for Large-Signal High-Pump-Power Applications. *IEEE J. Quantum Electron.*, 33(10):1699 – 1705, 1997.

[101] M. A. Jebali, J. N. Maran, and S. LaRochelle. 264W output power at 1585nm in Er-Yb codoped fiber laser using in-band pumping. *Opt. Lett.*, 39(13):3974 – 3977, 2014.

[102] Y. Jeong, J. K. Sahu, D. B. S. Soh, C. A. Codemard, and J. Nilsson. High-power tunable single-frequency single-mode erbium:ytterbium codoped large-core fiber master-oscillator power amplifier source. *Opt. Lett.*, 30(22):2997 – 2999, 2005.

[103] Y. Jeong, S. Yoo, C. A. Codemard, J. Nillson, J. K. Sahu, D. N. Payne, R. Horley, P. W. Turner, L. Hickey, A. Harker, M. Lovelady, and A. Piper. Erbium:Ytterbium Codoped Large-Core Fiber Laser with 297-W Continuous-wave Output Power. *IEEE J. Sel. Top. Quantum*, 13(3):573 – 579, 2007.

[104] X. Bai, Q. Sheng, H. Zhang, S. Fu, W. Shi, and J. Yao. High-Power All-Fiber Single-Frequency Erbium-Ytterbium Co-Doped Fiber Master Oscillator Power Amplifier. *IEEE Photonics Journal*, 7(6):7103106, 2015.

[105] C. Alegria, Y. Jeong, C. Codemard, J. K. Sahu, J. A. Alvarez-Chavez, L. Fu, M. Ibsen, and J. Nilsson. 83-W single-frequency narrow-linewidth MOPA using large-core erbium-ytterbium Co-doped Fiber. *IEEE Photonics Technol. Lett.*, 16(8):1825 – 1827, 2004.

[106] W. Demtröder. *Experimentalphysik 2 - Elektrizität und Optik*. Springer-Verlag Berlin Heidelberg, 2013.

[107] R. W. Boyd. *Nonlinear Optics*. Elsevier Inc., 2008.

[108] L. Brillouin. Diffusion de la lumière et des rayons X par un corps transparent homogène. *Ann. Phys.*, 9(17):88–122, 1922.

[109] A. Kobyakov, M. Sauer, and D. Chowdhury. Stimulated Brillouin scattering in optical Optical. *Adv. Opt. Photonics*, 2(1):1–59, 2010.

[110] D. R. Lide. *CRC Handbook of Chemistry and Physics*. CRC Press LLC, 2005.

[111] R. M. Shelby, M. D. Levenson, and P.W. Bayer. Resolved forward Brillouin scattering in optical fibers. *Phys. Rev. Lett.*, 54(9):939–942, 1985.

[112] M. Horowitz and A. R. Chraplyvy R. W. Tkach J. L. Zyskind. Broad-Band Transmitted Intensity Noise Induced by Stokes and Anti-Stokes Brillouin Scattering in Single-Mode Fibers. *IEEE Photonics Technol. Lett.*, 9(1):124 – 126, 1997.

[113] M. Hildebrandt, S. Büsche, P. Wessels, M. Frede, and D. Kracht. Brillouin scattering spectra in high-power single-frequency ytterbium doped fiber amplifiers. *Opt. Express*, 16(20):15970 – 15979, 2008.

[114] R. G. Smith. Optical Power Handling Capacity of Low Loss Optical Fibers as Determined by Stimulated Raman and Brillouin Scattering. *Appl. Opt.*, 11(11):2489 – 2494, 1972.

[115] J. Hansryd, F. Dross, M. Westlund, P. A. Adrekson, and S. N. Knudsen. Increase of the SBS Threshold in a Short Highly Nonlinear Fiber by Applying a Temperature distribution. *J. Light. Technol.*, 19(11):1691, 2001.

[116] N. Yoshizawa and T. Imai. Stimulated Brillouin scattering suppression by means of applying strain distribution to fiber with cabling. *J. Light. Technol.*, 11(10):1518 – 1522, 1993.

[117] J. B. Coles, B. P.-P. Kuo, N. Alic, S. Moro, C.-S. Bres, J. M. C. Boggio, P. A. Adrekson, M. Karlsson, and S. Radic. Bandwidth-efficient phase modulation techniques for Stimulated Brillouin Scattering suppression in fiber optic parametric Amplifiers. *Opt. Express*, 18(17):18138 – 18150, 2010.

[118] M. Takahashi, M. Tadakuma, R. Sugizaki, and T. Yagi. SBS suppression techniques in highly nonlinear fibers. *Proc. IEEE Photonics Society Summer Topicals*, 149-150, 2010.

[119] R. Menzel. *Photonics - Linear and Nonlinear Interactions of Laser Light and Matter*. Springer, 2007.

[120] V. Kuhn, P. Wessels, J. Neumann, and D. Kracht. Stabilization and power scaling of cladding pumped Er:Yb-codoped fiber amplifier via auxiliary signal at 1064 nm. *Opt. Express*, 17(20):18304 – 18311, 2009.

[121] V. Kuhn, D. Kracht, J. Neumann, and P. Wessels. Dependence of Er:Yb-codoped 1.5μm amplifier on wavelength-tuned auxiliary seed signal at 1μm wavelength. *Opt. Lett.*, 35(24):4105 – 4107, 2010.

[122] D. Sliwinska, P. Kaczmarek, G. Sobon, and K. M. Abramski. Double-Seeding of Er/Yb Co-Doped Fiber Amplifiers for Controlling of Yb-ASE. *J. Light. Technol.*, 31(21):3381 – 3386, 2013.

[123] M. Steinke, A. Croteau, C. Par, H. Zheng, P. Laperle, A. Proulx, J. Neumann, D. Kracht, and P. Wessels. Co-seeded Er^{3+}:Yb^{3+} single frequency fiber amplifier with 60 W output power and over 90% TEM_{00} content. *Opt. Express*, 22(14):16722 – 16730, 2014.

[124] Q. Han, Y. He, Z. Sheng, W. Zhang, J. Ning, and H. Xiao. Numerical characterization of Yb-signal-aided cladding-pumped Er:Yb-codoped fiber amplifiers. *Opt. Lett.*, 36(9):1599 – 1601, 2011.

[125] O. Varona, M. Steinke, J. Neumann, and D. Kracht. All-fiber, single-frequency, and single-mode Er^{3+}:Yb^{3+} fiber amplifier at 1556nm core-pumped at 1018nm. *Opt. Lett.*, 43(11):2632 – 2635, 2018.

[126] S. Wang, Z. Liu, Z. Zhao, S. Qu, Y. Xie, X. Gao, and Z. Cong. 18 W single-frequency 1550 nm Er:Yb co-doped fiber amplifier cladding-pumping at 1018 nm. *Opt. Commun.*, 464, 2020.

[127] A. Shirakawa, H. Suzuki, M. Tanisho, and K. Ueda. Yb-ASE-Free Er Amplification in Short-Wavelength Filtered Er:Yb Photonic-Crystal Fiber. *Proc. Optical Fiber Communication Conference (OSA)*, OThN2, 2008.

[128] P. Booker, R. Caspary, J. Neumann, D. Kracht, and M. Steinke. Pump wavelength dependence of ASE and SBS in single-frequency EYDFAs. *Opt. Express*, 43(19):4647 – 4650, 2018.

[129] D.C. Brown and H. J. Hoffman. Thermal, stress, and thermo-optic effects in high average power double-clad silica fiber lasers. *IEEE J. Quantum Electron.*, 37(2):207 – 217, 2001.

[130] Coherent Inc. *Product catalog*, 2020.

[131] R. Paschotta, J. Nilsson, P. R. Barber, J. E. Caplen, A. C. Tropper, and D. C. Hanna. Lifetime quenching in Yb-doped fibres. *Opt. Commun.*, 136(5-6):375 – 378, 1997.

[132] G. Canat, J.-C. Mollier, J.-P. Bouzinac, G. M. Williams, B. Cole, L. Goldberg, Y. Jaouën, and G. Kulcsar. Dynamics of high-power erbium-ytterbium fiber amplifiers. *J. Opt. Soc. Am. B*, 22(11):2308 – 2318, 2005.

[133] C. R. Giles and E. Desurvire. Modeling Erbium-Doped Fiber Amplifiers. *J. Light. Technol.*, 9(2):271 – 283, 1991.

[134] D. Marcuse. Gaussian approximation of the fundamental modes of graded-index fibers. *J. Opt. Soc. Am.*, 68(1):103 – 109, 1978.

[135] Lumentum LLC. *Datasheet - ST Series*, September 2020.

[136] Dilas Diodenlaser GmbH. *Datasheet - D4F1J22*, September 2020.

[137] L. Dong, T. Matniyaz, M. T. Kalichevsky-Dong, J. Nilsson, and Y. Jeong. Modeling Er/Yb fiber lasers at high powers. *Opt. Express*, 28(11):16244–16255, 2020.

[138] M. F. S. Ferreira. *Nonlinear Effects in Optical Fibers*. A John Wiley & Sons, 2011.

[139] M. O. van Deventer and A. J. Boot. Polarization properties of stimulated Brillouin scattering in single-mode fibers. *J. Light. Technol.*, 12(4):585 – 590, 1994.

[140] W. Koechner. *Solid-State Laser Engineering*. Springer-Verlag Berlin Heidelberg, 2006.

[141] P. Booker, O. Varona, M. Steinke, P. Wessels, J. Neumann, and D. Kracht. Experimental and numerical study of interlock requirements for high-power EYDFAs. *Opt. Express*, 28(21):31480 – 31486, 2020.

[142] D. E. McCumber. Einstein Relations Connecting Broadband Emission and Absorption Spectra. *Phys. Rev.*, 136(4A):A954, 1964.

[143] J. Thøgersen, N. Bjerre, and J. Mark. Multiphoton absorption and cooperative upconversion excitation in Er^{3+}-doped fibers. *Opt. Lett.*, 18(3):197 – 199, 1993.

[144] Texas Instruments Inc. *Datasheet - TLC372*, October 2021.

[145] F. Meylahn and B. Willke. Stabilized laser systems at 1550 nm wavelength for future gravitational wave detectors. *arXiv*, 2112.03792, 2021.

[146] P. Booker, O. Varona, M. Steinke, P. Wessels, J. Neumann, and D. Kracht. Two-stage fully monolithic single-frequency Er:Yb fiber amplifier at 1556 nm for next-generation of gravitational wave detectors. *Proc. 11665 Fiber Lasers XVIII: Technology and Systems*, 116650O-1, 2021.

[147] Gooch & Housego Ltd. *Datasheet - AA1401*, September 2020.

[148] M. Wysmolek, C. Ottenhues, T. Pulzer, T. Theeg, H. Sayinc, M. Steinke, U. Morgner, J. Neumann, and D. Kracht. Microstructured fiber cladding light stripper for kilowatt-class laser systems. *Appl. Opt.*, 57(23):6640 – 6644, 2018.

[149] *Coherent Inc. Fieldmaster$^{\text{TM}}$ - Power/Energy Meter - User Manual.*

[150] Nufern Inc. Tutorial - Selecting the Optimal Er/Yb Doped Optical Fiber: Design Considerations and System Performances. 2015. `https://www.coherent.com/resources/application-note/components-and-accessories/specialty-optical-fibers/er-yb-doped-optical-fiber-consideration-performance.pdf`.

[151] K. Izumi and D. Sigg. Advanced LIGO: length sensing and control in a dual recycled interferometric gravitational wave antenna. *Class. Quantum Grav.*, 34(1):015001, 2017.

[152] M. Steinke, J. Neumann, D. Kracht, and P. Wessels. Gain dynamics in Er^{3+}:Yb^{3+} co-doped fiber amplifiers. *Opt. Express*, 23(11):14946 – 14959, 2015.

[153] NKT Photonics A/S. *Datasheet - Koheras Boostik HP*, February 2022.

[154] NP Photonics Inc. *Datasheet - The Rock*, February 2022.

[155] Cybel LLC. *Datasheet - HOPA-1550*, February 2022.

[156] Lumibird S.A. *Datasheet - CEFL-KILO*, February 2022.

[157] RPMC Lasers Inc. *Datasheet - LRL2*, February 2022.

[158] Azur Light Systems S.A.S. *Datasheet - IR Series*, September 2020.

[159] BWT Ltd. *Datasheet - K976BN1RN-140.0W*, September 2020.

[160] nLight Inc. *Datasheet - e18 Series*, August 2022.

[161] ADC Telecommunications Inc. *Datasheet - LM976B200GAAF1*, September 2020.

[162] JDSU Ltd. *Datasheet - S30 Series*, September 2020.

[163] II-VI Inc. *Datasheet - LC962UF74P-20R*, September 2020.

[164] Gooch & Housego Ltd. *Datasheet - AC1409 Series*, September 2020.

[165] Thorlabs Inc. *Datasheet - BL976-PAG900*, September 2020.

[166] 3SP Technologies S.A.S. *Datasheet - 1999CVX*, September 2020.

[167] Anritsu Corp. *Datasheet - AF4B Series type C*, September 2020.

[168] Lumentum LLC. *Datasheet - S36 Series*, September 2020.

[169] OFS Fitel LLC. *Datasheet - OFS Raman Fiber Laser Module*, September 2020.

[170] Q. Han, Y. Yao, Y. Chen, F. Liu, T. Liu, and H. Xiao. Highly efficient Er/Yb codoped fiber amplifier with an Yb-band fiber Bragg grating. *Opt. Lett.*, 40(11):2634 – 2636, 2015.

[171] J. Boullet, Y. V. Bardin, M. Bérisset, and C. Pierre. Optimization of kW-class fiber splices and packages for ultra-high-power applications. *Proc. SPIE 11667, Components and Packaging for Laser Systems*, 116670I-1, 2021.

[172] D. B. Leviton and B. J. Frey. Temperature-dependent absolute refractive index measurements of synthetic fused silica. *Proc. SPIE 6273, Optomechanical Technologies for Astronomy*, 62732K-1, 2006.

[173] W. Fittkau, P. Wessels, and J. Neumann. Internal results acquired in POFILASE project. *Laser Zentrum Hannover e.V.*, 2021.

[174] H.-J. Bargel. *Werkstoffkunde*. Springer-Verlag Berlin Heidelberg, 2008.

[175] H. D. Young and R. A. Freedman. *University Physics*. Pearson Education Ltd., 1992.

[176] FiberBridge Photonics GmbH. *Test Report - (4+1)x1 signal-pump-combiner*, 2020.

[177] J. Koponen, M. Söderlund, H. J. Hoffman, D. Kliner, and J. Koplow. Photodarkening Measurements in Large-Mode-Area Fibers. *Proc. SPIE 6453, Fiber Lasers IV: Technology, Systems, and Applications*, 64531E-1, 2007.

[178] L. B. Glebov. Linear and Nonlinear Photoionization of Silicate Glasses. *Glasstech. Ber. Glass Sci. Technol.*, 75(C2):1, 2002.

[179] M. M. Broer, R. L. Cone, and J. R. Simpson. Ultraviolet-induced distributed-feedback gratings in Ce^{3+}-doped silica optical fibers. *Opt. Lett.*, 16(18):1391 – 1393, 1991.

[180] E. G. Behrens, R. C. Powell, and D. H. Blackburn. Characteristics of laser-induced gratings in Pr^{3+}- and Eu^{3+}-doped silicate glasses. *J. Opt. Soc. Am. B*, 7(8):1437 – 1444, 1990.

[181] G. R. Atkins and A. L. G. Carter. Photodarkening in Tb^{3+}-doped phosphosilicate and germanosilicate optical fibers. *Opt. Lett.*, 19(12):874 – 876, 1994.

[182] M. M. Broer, D. M. Krol, and D. J. DiGiovanni. Highly nonlinear near-resonant photodarkening in a thulium-doped aluminosilicate glass fiber. *Opt. Lett.*, 18(10):799 – 801, 1993.

[183] S. Jetschke, S. Unger, A. Schwuchow, M. Leich, and J. Kirchhof. Efficient Yb laser fibers with low photodarkening by optimization of the core composition. *Opt. Express*, 16(20):15540–15545, 2008.

[184] J. Koponen, M. Laurila, and M. Hotoleanu. Inversion behavior in core- and cladding-pumped Yb-doped fiber photodarkening measurements. *Appl. Opt.*, 47(25):4522–4528, 2008.

[185] N. Li, S. Yoo, X. Yu, D. Jain, and J. K. Sahu. Pump Power Depreciation by Photodarkening in Ytterbium-Doped Fibers and Amplifiers. *IEEE Photonics Technol. Lett.*, 26(2):115–118, 2014.

[186] T. Robin, T. Gotter, A. Barnini, P. Guitton, R. Montron, G. Mélin, C. Ranger, A. Laurent, and B. Cadier. Evidence of photo-darkening in co-doped erbium-ytterbium double-clad fibers operated at high-output power. *Proc. SPIE 10528, Optical Components and Materials*, 1052815-1, 2018.

[187] S. Girard, C. Marcandella, A. Morana, J. Perisse D. Di Francesca, P. Paillet, J.-R. Macé, A. Boukenter, M. Léon, M. Gaillardin, N. Richard, M. Raine, S. Agnello, M. Cannas, and Y. Ouerdane. Combined High Dose and Temperature Radiation Effects on Multimode Silica-Based Optical Fibers. *IEEE Transactions on Nuclear Science*, 60(6):4305 – 4313, 2013.

[188] D. L. Griscom, E. J. Friebele, K. J. Long, and J. W. Fleming. Fundamental defect centers in glass: Electron spin resonance and optical absorption studies of irradiated phosphorus-doped silica glass and optical fibers. *J. Appl. Phys.*, 54(7):3743–3762, 1983.

[189] O. de Varona. PhD thesis: Fiber Amplifiers at 1.5 µm for Laser Sources in Next-Generation Gravitational Wave Detectors. *Leibniz Universität Hannover*, 2018.

[190] E. Regnier, I. Flammer, S. Girard, F. Gooijer, F. Achten, and G. Kuyt. Low-Dose Radiation-Induced Attenuation at InfraRed Wavelengths for P-Doped, Ge-Doped and Pure Silica-Core Optical Fibres. *IEEE Transactions on Nuclear Science*, 54(4):1115–1119, 2007.

[191] S. Girard, Y. Ouerdane, B. Tortech, C. Marcandella, T. Robin, B. Cadier, J. Baggio, P. Paillet, V. Ferlet-Cavrois, A. Boukenter, J.-P. Meunier, J. R. Schwank, M. R. Shaneyfelt, P. E. Dodd, and E. W. Blackmore. Radiation Effects on Ytterbium- and Ytterbium/Erbium-Doped Double-Clad Optical Fibers. *IEEE Transactions on Nuclear Science*, 56(6):3293 – 3299, 2009.

[192] G. G. Vienne, W. S. Brocklesby, R. S. Brown, Z. J. Chen, J. D. Minelly, J. E. Roman, and D. N. Payne. Role of Aluminum in Ytterbium-Erbium Codoped Phosphoaluminosilicate Optical Fibers. *Opt. Fiber Technol.*, 2(4):387 – 393, 1996.

[193] P. Kwee, F. Seifert, B. Willke, and K. Danzmann. Laser beam quality and pointing measurement with an optical resonator. *Rev. Sci. Instrum.*, 78(7):073103, 2007.

[194] S. Wielandy. Implications of higher-order mode content in large mode area fibers with good beam quality. *Opt. Express*, 15(23):15402–15409, 2007.

[195] P. Kwee and B. Willke. Automatic laser beam characterization of monolithic Nd:YAG nonplanar ring lasers. *Appl. Opt.*, 47(32):6022 – 6032, 2008.

[196] P. Kwee. PhD thesis: Charakterisierung von Lasersystemen für Gravitationswellendetektoren. *Leibniz Universität Hannover*, 2005.

[197] V. Kuhn, S. Unger, S. Jetschke, D. Kracht, J. Neumann, J. Kirchhof, and P. Wessels. Experimental Comparison of Fundamental Mode Content in Er:Yb-Codoped LMA Fibers With Multifilament- and Pedestal-Design Cores. *J. Light. Technol.*, 28(22):3212 – 3219, 2010.

[198] L. Winkelmann, O. Puncken, R. Kluzik, C. Veltkamp, P. Kwee, J. Poeld, C. Bogan, B. Willke, M. Frede, J. Neumann, P. Wessels, and D. Kracht. Injection-locked single-frequency laser with an output power of 220 W. *Applied Physics B*, 102(3):529 – 538, 2011.

[199] F. Wellmann, M. Steinke, F. Meylahn, N. Bode, B. Willke, L. Overmeyer, J. Neumann, and D. Kracht. High power, single-frequency, monolithic fiber amplifier for the next generation of gravitational wave detectors. *Opt. Express*, 27(20):28523 – 28533, 2019.

[200] nlight Inc. *Datasheet - pearl p14*, 2021.

[201] Fondazione LINKS. *Report - ISMB - LZH Research collaboration program U08/18/D*, 2018.

[202] D. Pugliese, N. G. Boetti, J. Lousteau, E. Ceci-Ginistrelli, E. Bertone, F. Geobaldo, and D. Milanese. Concentration quenching in an Er-doped phosphate glass for compact optical lasers and amplifiers. *J. Alloys Compd.*, 657:678 – 683, 2016.

[203] *Ando Electric Co. Ltd. Optical Spectrum Analyzer AQ6317, year unknown.*

[204] *Thorlabs Inc. PDA10CF(-EC) InGaAs Amplified Detector - User Guide, 2017.*

[205] *OFS Fitel LLC. RightWave Erbium-Doped Optical Fiber - Catalog*, 2020.

[206] M. S. G. Dürbeck. Master thesis: Single-mode fiber laser at 1530nm for resonant Er^{3+} core-pumping. *Leibniz Universität Hannover*, 2020.

[207] N. Kagi, A. Oyobe, and K. Nakamura. Temperature dependence of the gain in erbium-doped fibers. *J. Light. Technol.*, 9(2):261 – 265, 1991.

Declaration of Authorship

I hereby confirm that I have authored this thesis independently and without use of others than the indicated sources. All passages which are literally or in general matter taken out of publications or other sources are marked as such.

Hanover, November 14, 2022

Phillip Booker

Curriculum Vitae

Personal Data

Name	Phillip Booker
Date of birth	21.10.1992 (Mettingen)
Nationality	German

Education

1999 - 2003	Grundschule Wissingen
2003 - 2004	Orientierungsstufe Bissendorf
2004 - 2011	Gymnasium Carolinum

University Education

2011 - 2014	B.Sc. Physik, Universität Osnabrück Thesis: *Stationärer Einfluss von Polaronen auf die OH^--Streckschwingung in LiNbO$_3$*
2014 - 2016	M.Sc. Physik, Universität Osnabrück Thesis: *Dynamik freier Polaronen in LiNbO$_3$*

Professional Affiliations

2016 - present	Research scientist Solid-State Lasers Group Laser Development Department Laser Zentrum Hannover e.V.